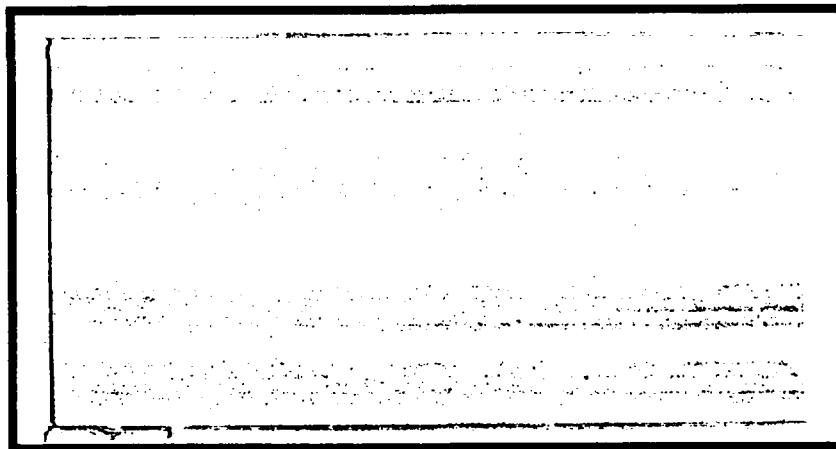
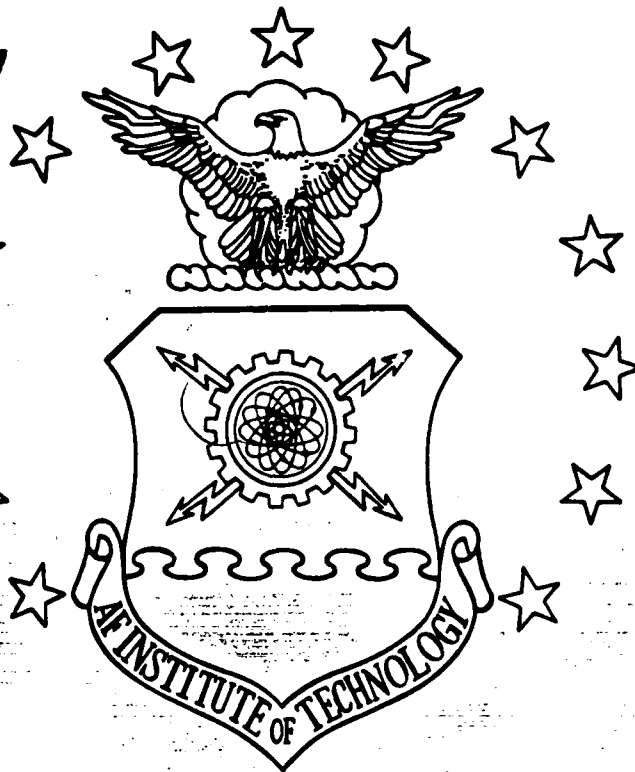


DTIC FILE COPY

AD-A216 410



DISTRIBUTION STATEMENT A

Approved for public release;
Distribution Unlimited

DEPARTMENT OF THE AIR FORCE
AIR UNIVERSITY

AIR FORCE INSTITUTE OF TECHNOLOGY

Wright-Patterson Air Force Base, Ohio

90 01 02 103

DTIC
ELECTE
JAN 03 1990
S
D
CS

AFIT/GAE/ENY/89D-20

⑤

DTIC
ELECTE
JAN 03 1990
S D D

ECCENTRICITY EFFECTS OF SQUARE CUTOUTS ON THE
NATURAL FREQUENCIES AND MODE SHAPES OF
CURVED RECTANGULAR COMPOSITE PANELS

THESIS

Vincent J. Levraea, Jr.
Captain, US Air Force

AFIT/GAE/ENY/89D-20

Approved for public release; distribution unlimited

THESIS

Presented to the Faculty of the School of Engineering
of the Air Force Institute of Technology

Air University

In Partial Fulfillment of the
Requirements for the Degree of
Master of Science in Aeronautical Engineering

Vincent J. Levraea, Jr.

Captain, US Air Force

December 1989



Accession For	
NTIS	CRA&I <input checked="" type="checkbox"/>
DTIC	T&B <input type="checkbox"/>
Unannounced	<input type="checkbox"/>
Justification	
By	
Distribution	
Availability Codes	
Dist	Availability for Special
A-1	

Preface

The primary objective of this thesis was to investigate the eccentricity effects of square cutouts on the dynamic response of curved composite panels. Documented research concerning the vibration analysis of curved composite panels with eccentrically located cutouts is limited. It is hoped that this study will not only make a useful contribution to the research community, but will also encourage additional work in similar areas.

The author would like to acknowledge his appreciation to those individuals whose support and contributions have made the completion of this thesis possible. A special thanks to my thesis advisor, Dr. Anthony Palazotto, and my thesis committee members, Major Ronald Hinrichsen and Captain Howard Gans, whose continuous support and advice guided me through this effort. In addition, I want to thank Mr. Gene Maddux for allowing me to invade his laboratory to conduct the holographic analysis of the panels. I will be ever grateful to Mr. Maddux for his selflessness and invaluable contributions. His extensive knowledge and insights were indispensable to the completion of this thesis. I also extend my gratitude to Mr. Jack Smith, Mr. Nick Yardich, and Mr. Jay Anderson for their technical support and assistance.

Most of all, I want to express my extreme appreciation to my lovely wife, Nancy, and my wonderful children, Maeghan, Ryan, and Trey for their support and sacrifice over the past eighteen months. Their patience, love, and understanding provided the strength necessary for me to complete this thesis. They are my inspiration.

Vincent J. Levraea, Jr.

Table of Contents

	Page
Preface	ii
List of Figures	vi
List of Tables	x
Abstract	xii
I. Introduction	1-1
A. Background	1-2
B. Objectives	1-3
C. Approach	1-4
(1) Outline of Experimental Investigation	1-4
(2) Outline of Numerical Investigation	1-5
II. Theory	2-1
A. Assumptions	2-1
B. Composite Material Properties	2-2
C. Finite Element Method	2-13
D. Holographic Interferometry	2-22
III. Composite Panels	3-1
IV. Experimental Analysis	4-1
A. Equipment	4-1
(1) Test Fixture	4-1
(2) Holography Equipment and Setup	4-5
B. Holography Procedure	4-8
C. Retroreflective Coating Effects	4-9
D. Contamination	4-12

Table of Contents (Cont'd)

	Page
V. Finite Element Analysis	5-1
A. STAGSC-1 Program	5-1
B. Element Selection	5-4
C. Convergence Study	5-5
D. Panel Modeling	5-10
VI. Results and Discussion	6-1
A. Panel 1	6-8
B. Panels with 2" Square Cutouts	6-17
(1) Panel 2	6-17
(2) Panels 3 and 4	6-25
(3) Panels 5 and 6	6-38
C. Panels with 4" Square Cutouts	6-48
(1) Panel 7	6-48
(2) Panels 8 and 9	6-57
(3) Panels 10 and 11	6-68
D. STAGSC-1's Performance	6-77
E. Panels with 3" and 5" Square Cutouts	6-80
(1) Panels 12 Through 16	6-81
(2) Panels 17 Through 21	6-86
F. Summary	6-91
(1) Summary of Cutout Effects	6-92
(2) Summary of Eccentricity Effects	6-96
(2.1) Circumferential Eccentricity	6-96
(2.2) Tangential Eccentricity	6-99
VII. Conclusions	7-1
VIII. Recommendations	8-1
Bibliography	BIB-1

Table of Contents (Cont'd)

	Page
Appendix A: Eigenvalue Problem Solution Algorithms	A-1
Appendix B: Comparison of Holography Techniques	B-1
Appendix C: Sample Input Files	C-1
Appendix D: Orthographic Views of Mode Shapes for Panels 1 and 7	D-1
Vita	V-1

List of Figures

Figure	Page
2-1. Body Coordinates (x,y,z) versus Material Coordinates (1,2,3) . . .	2-5
2-2. Force and Moment Resultants on Laminate [23:153] . . .	2-9
2-3. Geometry of an N-layered Laminate [23:154] . . .	2-10
2-4. Split-Beam Holographic Interferometry Setup . . .	2-24
2-5. Effect of Light Wave Interference [24:7] . . .	2-24
2-6. Recording of Hologram [19:2.7] . . .	2-25
2-7. Hologram Reconstruction [19:2.8] . . .	2-26
2-8. Relative Displacements Which Cause Fringe Formation . . .	2-27
3-1. Panel Dimensions and Coordinate System . . .	3-4
3-2. Panel Boundary Conditions . . .	3-4
3-3. Description of Cutout Locations . . .	3-5
4-1. Front View of Test Fixture . . .	4-3
4-2. Back View of Test Fixture . . .	4-3
4-3. Improvement to Test Fixture Clamp . . .	4-4
4-4. Schematic of Typical Video Holography Setup . . .	4-6
4-5. Video Holography Setup . . .	4-6
5-1. Degrees of Freedom for STAGSC-1 410 QUAF Element . . .	5-5
5-2. Typical Element Mesh Used for Finite Element Models (22 x 24) . . .	5-9
5-3. Orthographic View of Finite Element Mesh (22 x 24) . . .	5-9
6-1. First Mode Shape for Panel 1 . . .	6-9
6-2. Second and Third Mode Shapes for Panel 1 . . .	6-10
6-3. Fourth and Fifth Mode Shapes for Panel 1 . . .	6-11
6-4. Orthographic View of the Third Mode Shape for Panel 1 . . .	6-12

List of Figures (Cont'd)

Figure	Page
6-5. Orthographic View of the Fourth Mode Shape for Panel 1	6-12
6-6. Frequency versus Mode for Panel 1	6-13
6-7. First and Second Mode Shapes for Panel With $[0/+45/-45/90]_c$ Layup .	6-16
6-8. Third and Fourth Mode Shapes for Panel With $[0/+45/-45/90]_s$ Layup .	6-16
6-9. First Mode Shape for Panel 2	6-18
6-10. Second and Third Mode Shapes for Panel 2	6-19
6-11. Fourth and Fifth Mode Shapes for Panel 2	6-20
6-12. Frequency versus Mode for Panel 2	6-21
6-13. Experimental Frequency versus Mode for Panels 1, 2, 3, 4, 5, and 6 .	6-22
6-14. Analytical Frequency versus Mode for Panels 1, 2, 3, 4, 5, and 6 .	6-23
6-15. First Mode Shape for Panel 3	6-26
6-16. Second and Third Mode Shapes for Panel 3	6-27
6-17. Fourth and Fifth Mode Shapes for Panel 3	6-28
6-18. First Mode Shape for Panel 4	6-29
6-19. Second and Third Mode Shapes for Panel 4	6-30
6-20. Fourth and Fifth Mode Shapes for Panel 4	6-31
6-21. Frequency versus Circumferential Eccentricity for 2" Square Cutout .	6-34
6-22. First Mode Shape for Panel 5	6-39
6-23. Second and Third Mode Shapes for Panel 5	6-40
6-24. Fourth and Fifth Mode Shapes for Panel 5	6-41
6-25. First Mode Shape for Panel 6	6-42
6-26. Second and Third Mode Shapes for Panel 6	6-43
6-27. Fourth and Fifth Mode Shapes for Panel 6	6-44
6-28. Frequency versus Tangential Eccentricity for 2" Square Cutout . .	6-46

List of Figures (Cont'd)

Figure	Page
6-29. First Mode Shape for Panel 7	6-49
6-30. Second and Third Mode Shapes for Panel 7	6-50
6-31. Fourth and Fifth Mode Shapes for Panel 7	6-51
6-32. Frequency versus Mode for Panel 7	6-52
6-33. Experimental Frequency versus Mode for Panels 1, 7, 8, 9, 10, and 11 .	6-53
6-34. Analytical Frequency versus Mode for Panels 1, 7, 8, 9, 10, and 11 .	6-54
6-35. Cutout Effects on Mode Shape	6-56
6-36. First Mode Shape for Panel 8	6-58
6-37. Second and Third Mode Shapes for Panel 8	6-59
6-38. Fourth and Fifth Mode Shapes for Panel 8	6-60
6-39. First Mode Shape for Panel 9	6-61
6-40. Second and Third Mode Shapes for Panel 9	6-62
6-41. Fourth and Fifth Mode Shapes for Panel 9	6-63
6-42. Frequency versus Circumferential Eccentricity for 4" Square Cutout .	6-65
6-43. First Mode Shape for Panel 10	6-69
6-44. Second and Third Mode Shapes for Panel 10	6-70
6-45. Fourth and Fifth Mode Shapes for Panel 10	6-71
6-46. First Mode Shape for Panel 11	6-72
6-47. Second and Third Mode Shapes for Panel 11	6-73
6-48. Fourth and Fifth Mode Shapes for Panel 11	6-74
6-49. Frequency versus Tangential Eccentricity for 4" Square Cutout . .	6-76
6-50. Analytical Frequency versus Mode for Panels 1, 12, 13, 14, 15, and 16 .	6-82
6-51. Frequency versus Circumferential Eccentricity for 3" Square Cutout .	6-84

List of Figures (Cont'd)

Figure	Page
6-52. Frequency versus Tangential Eccentricity for 3" Square Cutout . . .	6-85
6-53. Analytical Frequency versus Mode for Panels 1, 17, 18, 19, 20, and 21 .	6-87
6-54. Frequency versus Circumferential Eccentricity for 5" Square Cutout .	6-89
6-55. Frequency versus Tangential Eccentricity for 5" Square Cutout . . .	6-90
6-56. Frequency versus Percent Mass Removed By Cutout	6-93
A-1. Subspace Iteration Algorithm	A-4
B-1. Conventional Holography Test Setup (Front)	B-3
B-2. Conventional Holography Test Setup (Back)	B-4
B-3. First Mode Shape for Panel 7	B-8
B-4. Second Mode Shape for Panel 7	B-8
B-5. Third Mode Shape for Panel 7	B-9
B-6. Fourth Mode Shape for Panel 7	B-9
B-7. Fifth Mode Shape for Panel 7	B-10
D-1. First Mode Shape for Panel 1	D-1
D-2. Second Mode Shape for Panel 1	D-1
D-3. Third Mode Shape for Panel 1	D-2
D-4. Fourth Mode Shape for Panel 1	D-2
D-5. Fifth Mode Shape for Panel 1	D-2
D-6. First Mode Shape for Panel 7	D-3
D-7. Second Mode Shape for Panel 7	D-3
D-8. Third Mode Shape for Panel 7	D-3
D-9. Fourth Mode Shape for Panel 7	D-4
D-10. Fifth Mode Shape for Panel 7	D-4

List of Tables

Table	Page
3-1. Material Properties of Composite Panels	3-2
3-2. Panel Numbers for Original 11 Panels	3-6
3-3. Panel Numbers for Additional 10 Panels	3-7
5-1. Comparison of the 410 and 411 Elements for Panel 1	5-6
5-2. Resulting Frequencies (Hz) from Convergence Study for Panel 1	5-7
5-3. Resulting Frequencies (Hz) from Convergence Study for Panel 9	5-7
5-4. Resulting Frequencies (Hz) from Convergence Study for Panel 11	5-8
6-1. Comparison of Experimental and Analytical Resonant Frequencies for Panel 1	6-9
6-2. Comparison of Experimental and Analytical Resonant Frequencies for Panel 2	6-18
6-3. Comparison of Experimental and Analytical Resonant Frequencies for Panel 3	6-26
6-4. Comparison of Experimental and Analytical Resonant Frequencies for Panel 4	6-29
6-5. Comparison of Experimental and Analytical Resonant Frequencies for Panel 5	6-39
6-6. Comparison of Experimental and Analytical Resonant Frequencies for Panel 6	6-42
6-7. Comparison of Experimental and Analytical Resonant Frequencies for Panel 7	6-49
6-8. Comparison of Experimental and Analytical Resonant Frequencies for Panel 8	6-58
6-9. Comparison of Experimental and Analytical Resonant Frequencies for Panel 9	6-61
6-10. Comparison of Experimental and Analytical Resonant Frequencies for Panel 10	6-69
6-11. Comparison of Experimental and Analytical Resonant Frequencies for Panel 11	6-72

List of Tables (Cont'd)

Table	Page
6-12. Normalized Frequencies for Panel 1	6-79
6-13. Normalized Frequencies for Panel 2	6-79
6-14. Normalized Frequencies for Panel 7	6-80
6-15. Natural Frequencies for Panels 12 Through 16	6-81
6-16. Natural Frequencies for Panels 17 Through 21	6-86

Abstract

The purpose of this study was to investigate the eccentricity effects of square cutouts on the natural frequencies and mode shapes of circular, cylindrical composite panels. A video holographic interferometry technique was used to determine the first five natural frequencies and mode shapes of the panels. Analytically, predictions for this same data were obtained using the STAGSC-1 finite element program. The primary objective was to examine how cutout eccentricity altered the dynamic characteristics of the panels. A secondary objective was to continue the verification of the dynamic analysis capabilities of the STAGSC-1 program.

The panels examined were constructed of Graphite/Epoxy (Gr/Ep) and had an arclength, height, and radius of curvature of 12 inches, 11 inches, and 12 inches, respectively. A $[0/-45/+45/90]_s$ ply layup was used, which resulted in a panel thickness of 0.04 inches. A clamped-free-clamped-free boundary condition was selected for this study. Cutouts eccentrically located in both the circumferential and tangential directions were considered. Experimentally, 2 inch and 4 inch square cutouts were studied, while the analytical analysis included 2 inch, 3 inch, 4 inch, and 5 inch square cutouts. Only the frequencies are presented for the panels with 3 inch and 5 inch cutouts.

It was observed that, in general, eccentrically located cutouts caused small frequency variations when compared to centered cutouts. The amount of variation observed tended to increase with cutout sizes. Primarily, eccentricity caused variations in frequency by changing the cutout's location with respect to node lines and antinodes. Also, frequency variation was observed when eccentricity moved cutouts towards or away from regions experiencing relatively large bending moments within the panel.

The experimental and analytical results were compared and the natural frequencies were found to correlate well. The percent differences between the experimental and

analytical frequencies were in all cases less than 10%. STAGSC-1 did an excellent job of predicting the mode shapes observed experimentally. For this study, STAGSC-1 proved to be a very useful engineering tool.

ECCENTRICITY EFFECTS OF SQUARE CUTOUTS ON THE NATURAL FREQUENCIES AND MODE SHAPES OF CURVED RECTANGULAR COMPOSITE PANELS

I. Introduction

Composite materials have gained widespread acceptance in many advanced technology applications. One area of primary concern is the use of composites in aerospace structures. The ever increasing use of composite materials in aerospace applications is due mainly to their superior strength-to-weight and stiffness-to-weight ratios, as compared to traditional metal alloys [19:1.2]. Another advantage of composite materials is that a laminate can be designed to satisfy a particular need; that is, the layup can be "tailored" to meet the strength and stiffness requirements of the application. As aircraft performance requirements increase, so do the demands placed on the materials from which they are manufactured. Often, composite laminates are anisotropic and exhibit extremely complex behavior due to coupling between extension, bending, and twisting. Therefore, for designers to take full advantage of their benefits, an understanding of the behavior of composite materials is crucial.

Composite shell structures are common in aerospace applications. In aircraft, the use of composite materials for the construction of wing skins, fuselage panels, and fairings is rapidly growing. These structures are usually representative of thin-shell geometries. Often their dynamic behavior can be just as or more important than their static behavior. Excessive vibration of these structures could result in fatigue failure and significantly shorten their useful service life. The dynamic analysis of shell structures constructed of composite materials represents a formidable task in most cases, if traditional solution

methods are used. Therefore, the designer must rely on experimental data or a proven numerical technique such as a finite element method.

A. Background

The dynamic response of circular, cylindrical composite panels has been investigated by previous researchers. In 1985, Walley [42] studied the dynamic behavior of a curved Graphite/Epoxy (Gr/Ep) panel with fully clamped boundary conditions and centered cutouts (2" x 2", 2" x 4", 4" x 4"). Using similar composite panels, Cyr [13] investigated the effect of cutout orientation (0° , 90° , and $\pm 45^\circ$ angles) on the panel's natural frequencies and mode shapes. Both Walley and Cyr used holographic interferometry and the Structural Analysis of General Shells (STAGSC-1) finite element program to perform there experimental and analytical analyses, respectively. In 1988, Goodwin [19] extended Cyr's work and investigated the effects of aircraft battle damage repairs on the natural frequencies and mode shapes of curved composite panels. Goodwin studied the same panel geometries as Cyr, except aluminum patches (simulated repairs) had been fastened over the cutouts. Also in 1988, Bicos and Springer [10] studied cantilevered (clamped along arclength of one edge) semicircular composite panels with interior cutouts. Their analysis included panels with single and dual cutouts; however, the cutouts were always located such that the panel's geometry remained symmetric with respect to an axis system aligned with the panel's edges and located at its center. Based on the literature search performed, no documented research was found concerning the eccentricity effects of interior cutouts on the natural frequencies and mode shapes of a curved composite panel. Thus, this area was selected as a logical extension of previous research.

The original focus of this study was to extend the efforts of Walley and Cyr. Therefore, panels similar to those used by Walley and Cyr were selected. However, due to

limitations of the available test fixture, a clamped-free-clamped-free (free along the arclength edges and clamped along the clamped axial edges) boundary condition was used instead of a fully clamped condition as used by Walley and Cyr. The panels studied had an arclength, height, and radius of curvature of 12 inches, 11 inches, and 12 inches, respectively. They were 0.04 inches thick and constructed of Gr/Ep with a $[0/-45/45/90]_s$ ply layup. Circumferential and tangential eccentricities were investigated for both 2 inch and 4 inch square cutouts.

B. Objectives

The primary objective of this thesis was to investigate the eccentricity effects of square cutouts on the natural frequencies and mode shapes of curved composite panels. Both experimental and analytical analyses were performed. A video holography technique was used to obtain the experimental data and STAGSC-1 was used to obtain the analytical predictions. When considering the dynamic behavior of a structure, the response of the lower modes is most important because they contain the most energy and cause the most fatigue failure [26]. For purposes of this study, the first five modes were investigated. The first five modes were selected because they were sufficient to study cutout effects yet limited the computer time required to perform the analytical analysis.

The literature search conducted uncovered no previous work which had been documented concerning the eccentricity effects of cutouts on a curved composite panel's dynamic response. Thus, this study was undertaken to make a contribution to this area of research. Also, no prior data was available which considered the vibration analysis of a curved panel with the clamped-free-clamped-free condition. Therefore, the behavior of the solid panel, as well as the panels with centered cutouts were also of considerable interest. A secondary objective was to further verify STAGSC-1's performance in predicting the

natural frequencies and mode shapes of curved composite panels with interior cutouts. The STAGSC-1 program had been successfully used in the past by Walley [42] and Cyr [13]. However, their work had only considered centered cutouts. Also, they had only examined the fully clamped boundary condition. Therefore, STAGSC-1's ability to handle eccentrically located cutouts and free edge boundary conditions had not been investigated for vibration problems. STAGSC-1's performance was evaluated by comparison to the experimental data.

C. Approach

(1) Outline of Experimental Investigation. A video holography technique was used to obtain the natural frequencies and mode shapes of the curved Gr/Ep panels. Holography (holographic interferometry) is capable of detecting extremely small displacements and is therefore very useful for vibration analysis. The video holography technique used in this study was a convenient, relatively simple experimental technique. Frequency sweeps were made of the panels and the first five resonant frequencies and mode shapes were recorded. A solid panel was used as a baseline against which the cutout effects could be compared. Two inch and four inch square cutouts were investigated experimentally. Eccentricities of 1 inch and 2 inches were considered in the circumferential and tangential directions for both cutout sizes. Chapter III details the panel geometries and boundary conditions investigated and Chapter IV discusses the experimental analysis performed.

A single panel was tested using a conventional split-beam holography system so that a comparison between the video holography and conventional holography techniques could be performed. Appendix B contains the comparison of the two holography techniques.

(2) Outline of Numerical Investigation. The numerical analysis was conducted using the C-1 version of the Structural Analysis of General Shells (STAGSC-1) finite element program which was written by the Lockheed Palo Alto Research Laboratory. The program was located on the Air Force Institute of Technology (AFIT) Vax 11/785 computer system.

Previous vibration analyses at AFIT have been successfully conducted using STAGSC-1 [13; 42]. STAGSC-1 was selected for use in this study to continue verification of the dynamic capabilities of the program. STAGSC-1 contains a built in grid generator which was used to generate all of the finite element meshes required for this study. The same cutout sizes and eccentricity values which were tested experimentally were also investigated analytically. In addition, 3 inch and 5 inch square cutouts were also investigated using STAGSC-1. As with the experimental analysis, the first five natural frequencies and mode shapes were obtained for the panels with 2 inch and 4 inch square cutouts. Due to time constraints, only natural frequencies were obtained for the panels with 3 inch and 5 inch square cutouts. The analytical analysis is discussed in detail in Chapter V. Chapter VI contains a comparison of the analytical and experimental results.

II. Theory

The theoretical background required for this thesis follows. This chapter is divided into four sections: A. Assumptions, B. Composite Material Properties, C. Finite Element Analysis, and D. Holographic Interferometry. In the first section, the assumptions for thin shell analysis and lamination theory are outlined. The macromechanical properties of a lamina and classical lamination theory are summarized in the second section. Also presented is an expression for the internal strain energy of a laminate. The third section discusses the finite element technique which the STAGSC-1 program uses to solve the free vibration eigenvalue problem. STAGSC-1 is the latest version of the STAGS family of computer programs developed specifically for the analysis of general thin shell structures. Finally, the fourth section reviews the theory of holographic interferometry.

A. Assumptions

Based on the Kirchhoff-Love hypothesis for small displacements and on classical lamination theory the following assumptions were made.

1. The ratio of shell thickness, h , to radius of curvature, R , is much less than unity ($h/R \ll 1$) [34:592; 41:122]. This ratio is 1:300 for the composite panels studied.
2. Deformations are small compared to the shell thickness [34:592]. The thickness of the composite panels used is 0.04 inches, while the free vibration displacements were on the order of 50.0 microinches.
3. Planes originally normal to the mid-surface remain planar after deformation and normal to the mid-surface. They also undergo no extension. In effect, all strains in planes perpendicular to the mid-surface are negligible [25:6; 34:592]. In equation form this becomes, $\epsilon_z = \gamma_{xz} = \gamma_{yz} = 0$.

4. The transverse normal stress is negligible compared to other normal stresses [25:6]. This along with Assumption 1 implies that a state of plane stress exists.
5. The laminate is constructed of perfectly bonded laminae. That is, the bonds are infinitesimally thin and non-shear deformable. Therefore the lamina do not slip relative to each other allowing for continuous displacements across bonds [23:149].
6. Each lamina is orthotropic [23:45].

B. Composite Material Properties

This section describes the macromechanical properties of a composite lamina and classical lamination theory. Resultant forces and moments are developed for a laminate in terms of middle surface extensional strains and curvatures. Using these relationships an expression for internal strain energy is obtained.

The strain-stress relation for an orthotropic lamina is given by [23:36]

$$\begin{Bmatrix} \epsilon_1 \\ \epsilon_2 \\ \epsilon_3 \\ \gamma_{23} \\ \gamma_{31} \\ \gamma_{12} \end{Bmatrix} = \begin{bmatrix} S_{11} & S_{12} & S_{13} & 0 & 0 & 0 \\ S_{12} & S_{22} & S_{23} & 0 & 0 & 0 \\ S_{13} & S_{23} & S_{33} & 0 & 0 & 0 \\ 0 & 0 & 0 & S_{44} & 0 & 0 \\ 0 & 0 & 0 & 0 & S_{55} & 0 \\ 0 & 0 & 0 & 0 & 0 & S_{66} \end{bmatrix} \begin{Bmatrix} \sigma_1 \\ \sigma_2 \\ \sigma_3 \\ \tau_{23} \\ \tau_{31} \\ \tau_{12} \end{Bmatrix} \quad (2.1)$$

where $[S]$ is the compliance matrix, ϵ_i are the extensional strains, γ_{ij} are the shearing strains, σ_i are normal stresses, and τ_{ij} are the shearing stresses. In terms of engineering constants Equation 2.1 becomes [23:38]

$$\begin{Bmatrix} \epsilon_1 \\ \epsilon_2 \\ \epsilon_3 \\ \gamma_{23} \\ \gamma_{31} \\ \gamma_{12} \end{Bmatrix} = \begin{bmatrix} \frac{1}{E_1} & \frac{-v_{21}}{E_2} & \frac{-v_{31}}{E_3} & 0 & 0 & 0 \\ \frac{-v_{12}}{E_1} & \frac{1}{E_2} & \frac{-v_{32}}{E_3} & 0 & 0 & 0 \\ \frac{-v_{13}}{E_1} & \frac{-v_{23}}{E_2} & \frac{1}{E_3} & 0 & 0 & 0 \\ 0 & 0 & 0 & \frac{1}{G_{23}} & 0 & 0 \\ 0 & 0 & 0 & 0 & \frac{1}{G_{31}} & 0 \\ 0 & 0 & 0 & 0 & 0 & \frac{1}{G_{12}} \end{bmatrix} \begin{Bmatrix} \sigma_1 \\ \sigma_2 \\ \sigma_3 \\ \tau_{23} \\ \tau_{31} \\ \tau_{12} \end{Bmatrix} \quad (2.2)$$

where E_i are the Young's moduli, v_{ij} are the Poisson's ratios, and G_{ij} are the shear moduli. Symmetry of the compliance matrix leads to the following reciprocal relationship [23:38].

$$\frac{v_{ji}}{E_i} = \frac{v_{ij}}{E_j} \quad i, j = 1, 2, 3 \quad (2.3)$$

This reciprocal relationship represents the conventional notation and is emphasized here because STAGSC-1 uses a notation which is opposite to Equation 2.3. From Assumption 4, a state of plane stress exist within the lamina. For this condition, the strain-stress relation in Equation 2.2 can be reduced to [23:45-46]

$$\begin{Bmatrix} \epsilon_1 \\ \epsilon_2 \\ \gamma_{12} \end{Bmatrix} = \begin{bmatrix} \frac{1}{E_1} & \frac{-v_{21}}{E_2} & 0 \\ \frac{-v_{12}}{E_1} & \frac{1}{E_2} & 0 \\ 0 & 0 & \frac{1}{G_{12}} \end{bmatrix} \begin{Bmatrix} \sigma_1 \\ \sigma_2 \\ \tau_{12} \end{Bmatrix} \quad (2.4)$$

The stress-strain equation can now be obtained by inverting Equation 2.4 which, using contracted notation, gives [23:33,46]

$$\begin{Bmatrix} \sigma_1 \\ \sigma_2 \\ \tau_{12} \end{Bmatrix} = \begin{bmatrix} Q_{11} & Q_{12} & 0 \\ Q_{12} & Q_{22} & 0 \\ 0 & 0 & Q_{66} \end{bmatrix} \begin{Bmatrix} \epsilon_1 \\ \epsilon_2 \\ \gamma_{12} \end{Bmatrix} \quad (2.5)$$

where $[Q]$ is the reduced stiffness matrix, and its coefficients are defined as:

$$\begin{aligned} Q_{11} &= \frac{E_1}{1-\nu_{12}\nu_{21}} & Q_{12} &= \frac{\nu_{12}E_2}{1-\nu_{12}\nu_{21}} = \frac{\nu_{21}E_1}{1-\nu_{12}\nu_{21}} \\ Q_{22} &= \frac{E_2}{1-\nu_{12}\nu_{21}} & Q_{66} &= G_{12} \end{aligned} \quad (2.6)$$

Equation 2.5 establishes the stress-strain relationship for a lamina in the material coordinate system. Often the principal material coordinates (1, 2, 3) are not coincident with the principal body coordinates (x, y, z). The material coordinate system is related to the body coordinate system through a transformation dependant upon the angle, θ , as shown in Figure 2-1. Usually, stress and strain are desired in the body coordinate system but the stiffness matrix, $[Q]$ is known relative to the material coordinates. Applying the appropriate transformation, the stiffness matrix can be transformed into the body system by the expression [23:50]

$$[\bar{Q}] = [T]^{-1} [Q] [[T]^{-1}]^T \quad (2.7)$$

where $[\bar{Q}]$ is the transformed reduced stiffness matrix and

$$[T] = \begin{bmatrix} m^2 & n^2 & 2mn \\ n^2 & m^2 & -2mn \\ -mn & mn & m^2 - n^2 \end{bmatrix} \quad (2.8)$$

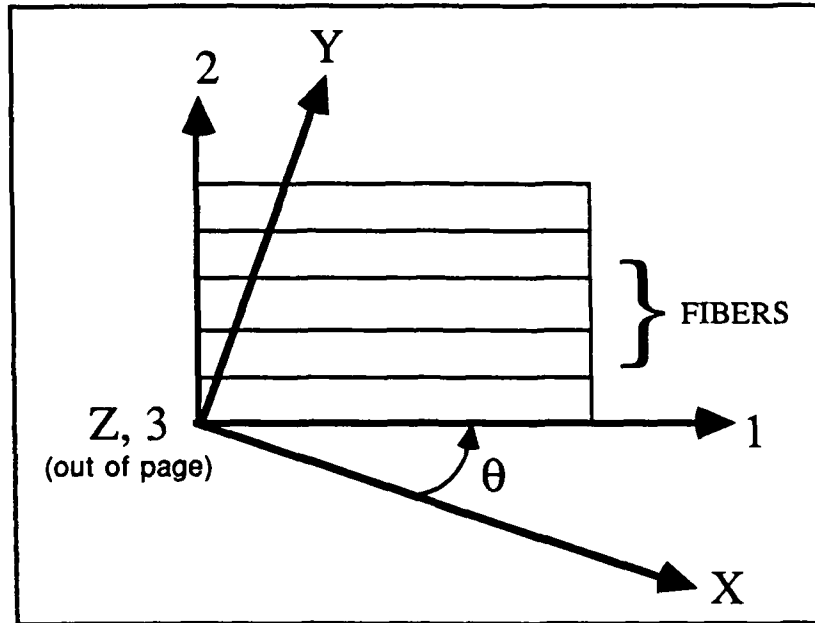


Figure 2-1. Body Coordinates (x,y,z) versus Material Coordinates (1,2,3)

Here, $m = \cos(\theta)$ and $n = \sin(\theta)$ and θ is positive measured from body axis to material axis (Figure 2.1). The stress-strain relation for a lamina of arbitrary orientation in body coordinates becomes [23:51]

$$\begin{Bmatrix} \sigma_x \\ \sigma_y \\ \tau_{xy} \end{Bmatrix} = \begin{bmatrix} \bar{Q}_{11} & \bar{Q}_{12} & \bar{Q}_{16} \\ \bar{Q}_{12} & \bar{Q}_{22} & \bar{Q}_{26} \\ \bar{Q}_{16} & \bar{Q}_{26} & \bar{Q}_{66} \end{bmatrix} \begin{Bmatrix} \epsilon_x \\ \epsilon_y \\ \gamma_{xy} \end{Bmatrix} \quad (2.9)$$

in which,

$$\begin{aligned}
\bar{Q}_{11} &= Q_{11}m^4 + 2(Q_{12} + 2Q_{66})n^2m^2 + Q_{22}n^4 \\
\bar{Q}_{12} &= (Q_{11} + Q_{22} - 4Q_{66})n^2m^2 + Q_{12}(n^4 + m^4) \\
\bar{Q}_{22} &= Q_{11}n^4 + 2(Q_{12} + 2Q_{66})n^2m^2 + Q_{22}m^4 \\
\bar{Q}_{16} &= (Q_{11} - Q_{12} - 2Q_{66})nm^3 + (Q_{12} - Q_{22} + 2Q_{66})n^3m \\
\bar{Q}_{26} &= (Q_{11} - Q_{12} - 2Q_{66})n^3m + (Q_{12} - Q_{22} + 2Q_{66})nm^3 \\
\bar{Q}_{66} &= (Q_{11} + Q_{22} - 2Q_{12} - 2Q_{66})n^2m^2 + Q_{66}(n^4 + m^4)
\end{aligned} \tag{2.10}$$

STAGSC-1 uses flat plate elements to model the curved shell surface. Consequently, the program does not directly use kinematic relations from any popular shell theory. STAGSC-1 uses modified plate theory relations which include in-plane rotation to adequately model shell behavior [6:2-10,6-37,39; 37:12]. These relations appear to be an extension of Von Kármán's plate theory equations. STAGSC-1 was designed primarily to be a nonlinear finite element program. Modifications were made to the STAGSC-1 code to allow for linear analysis. Two of these modifications dealt with separating the stiffness matrix and the strain-displacement relations, used by STAGSC-1, into linear and nonlinear parts. When the linear analysis option is selected, the nonlinear portions of the stiffness matrix and the strain-displacement relations are suppressed. The following discussion assumes that the nonlinear portions have been suppressed and only attempts to represent the linear relations present in STAGSC-1.

Similar to both thin plate and thin shell theories and based on the Kirchhoff-Love hypothesis, STAGSC-1 expresses total strain as a linear variation of the extensional and bending strains at the mid-surface. The mid-surface strains, for a linear analysis, are of the form

$$\begin{aligned}
\epsilon_x^0 &= u_{,x} \\
\epsilon_y^0 &= v_{,y} \\
\gamma_{xy}^0 &= u_{,y} + v_{,x}
\end{aligned}
\tag{2.11}$$

where the comma indicates partial differentiation with respect to the variable that follows. Based on the assumptions previously mentioned, the resulting total strains within the plate elements are given by [23:151]

$$\begin{aligned}
\epsilon_x &= \epsilon_x^0 - z w_{,xx} \\
\epsilon_y &= \epsilon_y^0 - z w_{,yy} \\
\gamma_{xy} &= \gamma_{xy}^0 - 2z w_{,xy}
\end{aligned}
\tag{2.12}$$

Denoting the middle surface curvatures as,

$$\begin{Bmatrix} \kappa_x \\ \kappa_y \\ \kappa_{xy} \end{Bmatrix} = - \begin{Bmatrix} w_{,xx} \\ w_{,yy} \\ 2w_{,xy} \end{Bmatrix}
\tag{2.13}$$

allows Equation 2-12 to be written as [23:151]

$$\begin{Bmatrix} \epsilon_x \\ \epsilon_y \\ \gamma_{xy} \end{Bmatrix} = \begin{Bmatrix} \epsilon_x^0 \\ \epsilon_y^0 \\ \gamma_{xy}^0 \end{Bmatrix} + z \begin{Bmatrix} \kappa_x \\ \kappa_y \\ \kappa_{xy} \end{Bmatrix}
\tag{2.14}$$

Equation 2.14 is the relationship used in the STAGSC-1 program and represents the strain variation through the thickness of the laminate. Substituting Equation 2.14 into Equation 2.9 yields [23:152]

$$\begin{Bmatrix} \sigma_x \\ \sigma_y \\ \tau_{xy} \end{Bmatrix}_k = \begin{bmatrix} \bar{Q}_{11} & \bar{Q}_{12} & \bar{Q}_{16} \\ \bar{Q}_{12} & \bar{Q}_{22} & \bar{Q}_{26} \\ \bar{Q}_{16} & \bar{Q}_{26} & \bar{Q}_{66} \end{bmatrix}_k \left\{ \begin{Bmatrix} \epsilon_x^o \\ \epsilon_y^o \\ \gamma_{xy}^o \end{Bmatrix} + z \begin{Bmatrix} \kappa_x \\ \kappa_y \\ \kappa_{xy} \end{Bmatrix} \right\} \quad (2.15)$$

Equation 2.15 is applicable to the k^{th} lamina of a multilayered laminate. Therefore to obtain the laminate resultant forces and moments (per unit length) the lamina stress in Equation 2.15 must be integrated through the laminate thickness. These force and moment resultants are respectively given by [23:153]

$$\begin{Bmatrix} N_x \\ N_y \\ N_{xy} \end{Bmatrix} = \int_{-t/2}^{t/2} \begin{Bmatrix} \sigma_x \\ \sigma_y \\ \tau_{xy} \end{Bmatrix} dz = \sum_{k=1}^N \int_{z_{k-1}}^{z_k} \begin{Bmatrix} \sigma_x \\ \sigma_y \\ \tau_{xy} \end{Bmatrix}_k dz \quad (2.16)$$

and

$$\begin{Bmatrix} M_x \\ M_y \\ M_{xy} \end{Bmatrix} = \int_{-t/2}^{t/2} \begin{Bmatrix} \sigma_x \\ \sigma_y \\ \tau_{xy} \end{Bmatrix} z dz = \sum_{k=1}^N \int_{z_{k-1}}^{z_k} \begin{Bmatrix} \sigma_x \\ \sigma_y \\ \tau_{xy} \end{Bmatrix}_k z dz \quad (2.17)$$

where N is the total number of plies in the laminate, k is the ply number, t is the laminate thickness, and z is measured from the laminate middle surface. The sign convention for the force and moment resultants is shown Figure 2-2 and laminate geometry is presented in Figure 2-3. The transformed reduced stiffness matrix is constant within a lamina and therefore Equation 2.9 can be substituted into Equations 2.16 and 2.17 to yield [23:154]

$$\begin{Bmatrix} N_x \\ N_y \\ N_{xy} \end{Bmatrix} = \sum_{k=1}^N [\bar{Q}]_k \left\{ \int_{z_{k-1}}^{z_k} \begin{Bmatrix} \epsilon_x^o \\ \epsilon_y^o \\ \gamma_{xy}^o \end{Bmatrix} dz + \int_{z_{k-1}}^{z_k} \begin{Bmatrix} \kappa_x \\ \kappa_y \\ \kappa_{xy} \end{Bmatrix} z dz \right\} \quad (2.18)$$

$$\begin{Bmatrix} M_x \\ M_y \\ M_{xy} \end{Bmatrix} = \sum_{k=1}^N [\bar{Q}]_k \left\{ \int_{z_{k-1}}^{z_k} \begin{Bmatrix} \epsilon_x^o \\ \epsilon_y^o \\ \gamma_{xy}^o \end{Bmatrix} z dz + \int_{z_{k-1}}^{z_k} \begin{Bmatrix} \kappa_x \\ \kappa_y \\ \kappa_{xy} \end{Bmatrix} z^2 dz \right\} \quad (2.19)$$

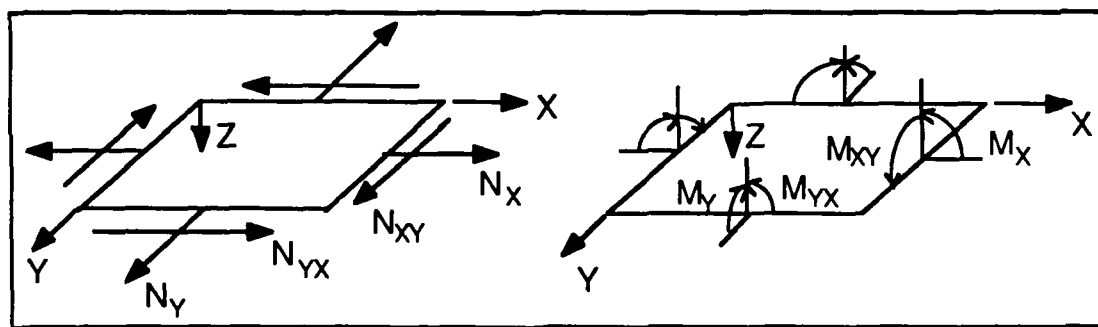


Figure 2-2. Force and Moment Resultants on Laminate [23:153]

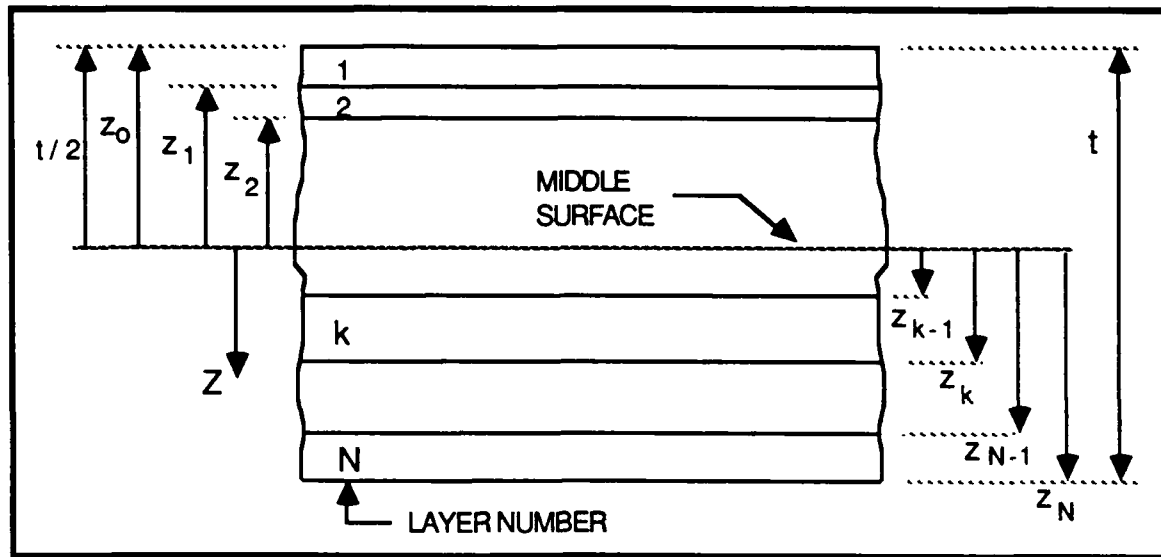


Figure 2-3. Geometry of an N-layered Laminate [23:154]

If one performs the indicated integrations and notes that the middle surface strains and curvatures are not a function of z , the following equations are obtained [23:154]

$$\begin{Bmatrix} N_x \\ N_y \\ N_{xy} \end{Bmatrix} = \begin{bmatrix} A_{11} & A_{12} & A_{16} \\ A_{12} & A_{22} & A_{26} \\ A_{16} & A_{26} & A_{66} \end{bmatrix} \begin{Bmatrix} \epsilon_x^0 \\ \epsilon_y^0 \\ \gamma_{xy}^0 \end{Bmatrix} + \begin{bmatrix} B_{11} & B_{12} & B_{16} \\ B_{12} & B_{22} & B_{26} \\ B_{16} & B_{26} & B_{66} \end{bmatrix} \begin{Bmatrix} \kappa_x \\ \kappa_y \\ \kappa_{xy} \end{Bmatrix} \quad (2.20)$$

$$\begin{Bmatrix} M_x \\ M_y \\ M_{xy} \end{Bmatrix} = \begin{bmatrix} B_{11} & B_{12} & B_{16} \\ B_{12} & B_{22} & B_{26} \\ B_{16} & B_{26} & B_{66} \end{bmatrix} \begin{Bmatrix} \epsilon_x^0 \\ \epsilon_y^0 \\ \gamma_{xy}^0 \end{Bmatrix} + \begin{bmatrix} D_{11} & D_{12} & D_{16} \\ D_{12} & D_{22} & D_{26} \\ D_{16} & D_{26} & D_{66} \end{bmatrix} \begin{Bmatrix} \kappa_x \\ \kappa_y \\ \kappa_{xy} \end{Bmatrix} \quad (2.21)$$

$$\begin{aligned}
 \text{where} \quad A_{ij} &= \sum_{k=1}^N (\bar{Q}_{ij})_k (z_k - z_{k-1}) & B_{ij} &= \frac{1}{2} \sum_{k=1}^N (\bar{Q}_{ij})_k (z_k^2 - z_{k-1}^2) \\
 D_{ij} &= \frac{1}{3} \sum_{k=1}^N (\bar{Q}_{ij})_k (z_k^3 - z_{k-1}^3)
 \end{aligned} \tag{2.22}$$

[A], [B], and [D] are the Extensional Stiffness, Coupling Stiffness, and Bending Stiffness Matrices, respectively. For laminates symmetric in both geometry and material properties about the middle surface, the coupling stiffness coefficients are zero ([B] = 0). Therefore, the laminate does not exhibit coupling between bending and extension. The panels studied in this thesis were constructed of a symmetric, $[0/-45/+45/90]_s$ ply layup. Using a short form notation, Equations 2.20 and 2.21 are commonly written as [23:173]

$$\begin{Bmatrix} N \\ M \end{Bmatrix} = \begin{bmatrix} [A] & [B] \\ [B] & [D] \end{bmatrix} \begin{Bmatrix} \epsilon^0 \\ \kappa \end{Bmatrix} \tag{2.23}$$

The total strain energy of the body is given by

$$U_T = \int_V U \, dV \tag{2.24}$$

where U is strain energy density. Using the formula of Clapeyron the strain energy density is given by [34:206,207]

$$U = \frac{1}{2} \sigma_{ij} \epsilon_{ij} \tag{2.25}$$

Based on the assumptions previously mentioned ($\epsilon_z = \gamma_{xz} = \gamma_{yz} = 0$), Equation 2.25 simplifies to

$$U = \frac{1}{2} (\sigma_x \epsilon_x + \sigma_y \epsilon_y + \tau_{xy} \gamma_{xy}) \quad (2.26)$$

If one substitutes Equation 2.26 into Equation 2.24, the total strain energy becomes

$$U_T = \int_V \frac{1}{2} (\sigma_x \epsilon_x + \sigma_y \epsilon_y + \tau_{xy} \gamma_{xy}) = \int_A \int_t \frac{1}{2} (\sigma_x \epsilon_x + \sigma_y \epsilon_y + \tau_{xy} \gamma_{xy}) dz dA \quad (2.27)$$

where t is the laminate thickness and dA is differential area. Defining $\{\epsilon\}$ as a vector whose components are the middle surface strains and curvatures and recalling that the middle surface strains and curvatures are not a function of z , the above equation in matrix notation becomes

$$U_T = \frac{1}{2} \int_A \int_t \{\epsilon\}^T [\sigma] dz dA = \frac{1}{2} \int_A \{\epsilon\}^T \left(\int_t [\sigma] dz \right) dA \quad (2.28)$$

Relating the integration through the thickness in Equation 2.28 with that previously performed and considering Equation 2.23, the total strain energy can be written in the form

$$U_T = \frac{1}{2} \int_A \left\{ \begin{matrix} \epsilon^0 \\ - \\ \kappa \end{matrix} \right\}^T \left\{ \begin{matrix} N \\ - \\ M \end{matrix} \right\} dA \quad (2.29)$$

or in final form as [13:18]

$$U_T = \frac{1}{2} \int_A \left\{ \begin{matrix} \epsilon^o \\ \kappa \end{matrix} \right\}^T \begin{bmatrix} [A] & [B] \\ [B] & [D] \end{bmatrix} \left\{ \begin{matrix} \epsilon^o \\ \kappa \end{matrix} \right\} dA \quad (2.30)$$

This is the form of the strain energy equation used by STAGSC-1 and will be used to develop the element stiffness matrix. The next section discusses the theory for solving eigenvalue problems by finite element methods.

C. Finite Element Method

This section provides an overview of the finite element technique, which is incorporated in the STAGSC-1 program, for solving free vibration problems. The primary emphasis is on using a finite element approach to solve eigenvalue problems arising from free undamped vibration of a structure. STAGSC-1 is the latest version of a family of computer programs developed by Lockheed Palo Alto Research Laboratory specifically for the analysis of general thin shell structures [37:1,2]. STAGSC-1 uses thin, flat plate elements to model shell geometries. Therefore, the actual curved shell surface is approximated by a multifaceted surface generated by the triangular or quadrilateral elements. Since no curved elements are available, a direct application of any shell theory cannot be part of the element formulation [37:12]. When flat elements are used to model curved surfaces inevitable compatibility problems exist. "The 410 (QUAF) elements were specifically developed to remove the displacement incompatibility which exists when flat shell elements do not lie in one plane" [37:45]. The shape function for in-plane displacements must be of the same order as the transverse function if edge displacements

are to be compatible. The transverse displacement function is usually cubic to account for the necessary second derivatives resulting from bending; therefore the in-plane functions must also be cubic. The 410 element includes the normal rotation at the four corners to achieve cubic in-plane functions [6:6-37,40; 37:45]. In effect, to enforce displacement compatibility, the displacement components normal to the element's edge must experience cubic variation in order to match the transverse cubic variation of displacement due to bending [37:15]. The STAGSC-1 Theory Manual [6] contains further information on the element shape functions and formulation. Additional information concerning plate elements modeling a cylindrical surface is presented in the STAGSC-1 Theory Manual [6] and is also discussed by Egan [15].

The governing equations for the dynamic behavior of a continuous system, derived from Newton's Second Law, is [29:9]

$$m \ddot{X}(t) + c \dot{X}(t) + kX(t) = f(t) \quad (2.31)$$

where	m = system mass	$X(t)$ = displacement
	c = system damping	$\dot{X}(t)$ = velocity
	k = system stiffness	$\ddot{X}(t)$ = acceleration
	t = time	$f(t)$ = external forcing function

For free vibration there are no applied forces and therefore $f(t) = 0$. Structural damping is based on the energy losses caused by internal friction as the panel deforms and is proportional to the amplitude of displacement [29:72]. The displacements experienced by the composite panels investigated were on the order of 50.0 microinches (1/800 of the panel thickness). These extremely small displacements and the nature of high stiffness, low mass materials justified the neglecting of damping effects ($C = 0$). Also, the effect of the surrounding air mass was negligible. Ignoring damping effects was further warranted

by modal behavior observed during testing, in particular the behavior of the fundamental mode. The first mode was "sharp" and apparent over a very narrow frequency range which is characteristic of a lightly damped structure [36:199]. Thus Equation 2.31 becomes

$$m \ddot{X}(t) + k X(t) = 0 \quad (\text{continuous system}) \quad (2.32)$$

The finite element method requires the discretization of a continuous system into small pieces (elements) in which the deformed geometry is represented by displacements at selected locations (nodes) within the body. Taking this into account, for a discretized system Equation 2.32 takes the form

$$[M] \{ \ddot{d} \} + [K] \{ d \} = 0 \quad (\text{discrete system}) \quad (2.33)$$

where $[M]$ = mass matrix $\{ d \}$ = nodal displacement vector
 $[K]$ = stiffness matrix $\{ \ddot{d} \}$ = nodal acceleration vector

The $[K]$ matrix can be determined considering the strain energy relation derived in the previous section (Equation 2.30). The strain energy for an element is given by [12:83]

$$U = \frac{1}{2} \{ d \}^T [k] \{ d \} \quad (2.34)$$

where $[k]$ is the desired element stiffness matrix. From finite element theory, the strains and curvatures in Equation 2.30 can be expressed in terms of nodal displacements by the strain-displacement matrix, $[\beta]$. This expression is of the form [12:82]

$$\{\epsilon\} = [\beta] \{d\} \quad (2.35)$$

where $[\beta]$ is defined as

$$[\beta] = [G][N] \quad (2.36)$$

Here, $[N]$ is the element shape function matrix and $[G]$ is an operator matrix populated by partial derivatives. Substituting Equation 2.36 into Equation 2.30 yields

$$U_T = \frac{1}{2} \int_A \{d\}^T [\beta]^T \begin{bmatrix} [A] & [B] \\ [B] & [D] \end{bmatrix} [\beta] \{d\} dA \quad (2.37)$$

Comparing Equations 2.37 and 2.30, and noticing that the nodal displacement are not dependent on area and can therefore be removed from within the integral, it becomes apparent that the element stiffness matrix for an element modeling a composite material becomes

$$[k] = \int_A [\beta]^T \begin{bmatrix} [A] & [B] \\ [B] & [D] \end{bmatrix} [\beta] dA \quad (2.38)$$

The global stiffness matrix, $[K]$ is assembled from the element stiffness matrices, a method called the Direct Stiffness Method, by adding the appropriate number of zero rows and columns to the element stiffness matrices then summing [12:28].

A consistent mass matrix is given by [47:531]

$$[M] = \int_v [N]^T \rho [N] dV \quad (2.39)$$

where $[N]$ is again the shape function matrix and ρ is mass per unit volume (density). The consistent mass formulation results in a fully populated, positive definite mass matrix. A lumped mass matrix is formulated by evenly distributing the total element mass among the translational degrees of freedom (DOF) of the element. This results in a diagonal matrix which is positive semidefinite since the diagonal coefficients corresponding to the rotational DOF are zero. Due to the poor quality of the STAGSC-1 Theory Manual, it is unclear precisely how the STAGSC-1 mass matrix is formulated. However, the manual does state that a diagonal matrix is used. It appears that this diagonal matrix is not a "traditional" lumped mass matrix, but is more sophisticated and represents somewhat of an average between the lumped and consistent formulations. The coefficients on the diagonal corresponding to rotational DOF (rotatory inertia terms) appear to be filled using the corresponding values which would be obtained from a consistent mass matrix approach. The coefficients associated with the translational DOF are then determined so that the remaining mass is evenly distributed and total element mass is preserved. A diagonal matrix created in this form introduces an additional approximation but allows each DOF to maintain some value of associated mass (translational DOF) or inertia (rotational DOF) while reducing the number of computations required to solve the system of equations [6:7-4,33]. Cook [12:306] outlines a possible approach to generating this type of mass matrix.

The simplifications made to the mass matrix in no way affects the formulation of the elemental stiffness matrix, which remains a fully populated symmetric matrix.

For harmonic vibration it is assumed that all nodal DOF are in phase and that $\{d\}$ in Equation 2.33 is given by [12:308; 47:545]

$$\{d\} = \{d_o\}e^{i\omega t} \quad (2.40)$$

where d_o is displacement amplitude, ω is circular natural frequency, and t is time.

Substituting into the differential equation (Equation 2.33) gives

$$[K]\{d_o\} - \omega^2 [M]\{d_o\} = 0 \quad (2.41)$$

Rearranging and changing notation yields

$$[K - \lambda_i M] \{\phi_i\} = 0 \quad (2.42)$$

where $\lambda_i = \omega_i^2$ ((rad/sec)²) and the brackets have been dropped off of K and M for convenience (K and M are still matrices.). For linear vibration analysis, K and M are independent of displacement and frequency. λ_i is the eigenvalue and $\{\phi_i\}$ is the eigenvector (mode shape) for the i^{th} mode. Each eigenvector will represent a unique shape but with arbitrary amplitude. Generally the eigenvector is normalized by setting the maximum displacement equal to one and the remaining displacements scaled accordingly. STAGSC-1 uses this method to handle eigenvectors [6:7-17]. Equation 2.42 represents

the generalized eigenvalue problem for linear free undamped vibration [8:517]. If K and M are $(n \times n)$ matrices then the solution of Equation 2.42 yields λ_i and $\{\phi_i\}$ for $i=1,2,3,\dots,n$. The eigenvectors are independent and thus form a basis for the eigenspace [8:49]. The eigenvectors can be arranged into a $(n \times n)$ modal matrix given by

$$\Phi = [\{\phi_1\} \ \{\phi_2\} \ \dots \{\phi_n\}] \quad (2.43)$$

where the columns of the modal matrix are the eigenvectors of the system. This allows Equation 2.42 to be rewritten as [8:558; 29:80]

$$K\Phi = M\Phi\Lambda \quad (2.44)$$

Here, Λ is a diagonal matrix of eigenvalues, λ_i 's (or λ_{ii}) and their location along the diagonal is determined by $\lambda_{11} < \lambda_{22} < \dots < \lambda_{nn}$. The location of $\{\phi_i\}$ within Φ must be consistent with the location of λ_{ii} in Λ ; that is, $\{\phi_i\}$ is the corresponding vector for λ_{ii} .

To solve eigenvalue problems STAGSC-1 uses a subspace iteration scheme [37:50]. The objective of subspace iteration is to solve for the "p" lowest eigenvalues and eigenvectors which satisfy Equation 2.44 [8:675]. Here, "p" is the number of modes desired. Using subspace iteration the reduced number of "p" eigenvectors are simultaneously obtained. The procedure implemented in STAGSC-1 is based on the subspace iteration method developed by Bathe [8:672-682] but with some modifications. These modifications include using Chebyshev polynomials and spectral shifting to enhance convergence. The STAGSC-1 manual did not elaborate on the implementation of Chebyshev polynomials used and due to their extensive nature, they will not be discussed

here. Hornbeck [20] provides additional information on Chebyshev polynomials. Spectral shifting is used to accelerate the calculations of the required eigensystem which overall reduces the number of iterations required to obtain convergence. Also, spectral shifting is useful to avoid a singular K matrix, if rigid body modes are present. If a spectral shift, σ , is defined such that

$$\lambda_i = \sigma + \lambda_{si} \quad (2.45)$$

where λ_i is the same as given in Equation 2.42 and λ_{si} is the eigenvalue obtained from the "shifted" eigenvalue problem. Substituting Equation 2.45 into Equation 2.42 yields

$$[(K - \sigma M) - \lambda_{si} M] \{\phi_i\} = 0 \quad (2.46)$$

or

$$[\bar{K} - \lambda_{si} M] \{\phi_i\} = 0 \quad (2.47)$$

where $\bar{K} = [K - \sigma M]$. Equation 2.47 is solved for λ_{si} and $\{\phi_i\}$. After λ_{si} is found then the "true" system eigenvalue, λ_i , is obtained from Equation 2.45. The spectral shift does not alter the eigenvectors obtained. For purposes of illustration, assume that an inverse power method is being used and that the eigenvalue corresponding to the fundamental mode is desired. If the dominance ratio, r , is defined as

$$r = \left| \frac{\lambda_{s1}}{\lambda_{s2}} \right| \quad (2.48)$$

where $\lambda_{s1} < \lambda_{s2}$ and $\lambda_{s1} = \lambda_1$ for σ equal zero. The convergence rate of the inverse power method improves as r moves further from 1. Therefore shifting both λ_1 and λ_2 by a constant subsequently shifts λ_{s1} and λ_{s2} which reduces the dominance ratio and improves the convergence rate [20:232,233].

Subspace iteration reduces a $(n \times n)$ eigensystem into a $(n \times p)$ system where "p" is as defined before. The subspace refers to the space spanned by the reduced set of eigenvectors. If the subspace which is spanned by the "true" reduced eigenvectors is denoted E_∞ , then the starting iteration vector can be thought of as spanning the E_1 subspace. As iterations are performed, the E_k ($k = 1, 2, \dots, \infty$) space approaches the E_∞ space. The E_∞ space is in effect spanned when the desired accuracy has been obtained.

The following gives an outline of the eigensolution technique used by STAGSC-1. First, a preliminary set of independent vectors is chosen which spans a subspace of the complete set of eigenvectors. Next, an inverse power method (inverse iteration) with shifting is performed. This transforms the E_k space into the E_{k+1} space. Now the projections of K and M are found on the new reduced eigenspace (subspace E_{k+1}) yielding K_{k+1} and M_{k+1} respectively [8:675,678]. The resulting reduced $(n \times p)$ eigenvalue problem is solved using Householder's Method with a LR algorithm [6:7-21]. (A description of Householder's Method and the LR algorithm are presented in the next paragraph.) Finally, a check for convergence of the eigenvalues is made and the process repeated until adequate convergence has been obtained. The criteria for determining convergence was not explicitly defined. It is believed that the "k+1" iteration eigenvalues are compared to the "k" iteration eigenvalues and if the relative error is below a predetermined threshold then convergence is assumed.

Householder's Method is an effective technique which uses orthogonal transformations to tridiagonalize a $(n \times n)$ symmetric matrix. This results in a large number of zero coefficient in the matrix which makes it easier to decompose. The LR algorithm refers to a procedure in which the tridiagonal matrix produced by Householder's Method is decomposed into a lower triangular matrix (L or Left) and an upper triangular matrix (R or Right). These two new matrices are used in similarity transformations which produce the eigenvalues. The original matrix is transformed into a matrix containing the eigenvalues along the main diagonal [20:241,246]. A description of the subspace iteration method, Householder's Method and the LR algorithm are presented in Appendix A. Figure A-1 presents a flow chart of the subspace iteration algorithm developed by Bathe.

This section developed the finite element method used in the STAGSC-1 program (as best as could be determined) to solve the undamped, free vibration eigenvalue problem. The approach presented here may not be the exact implementation in STAGSC-1, but after research of available documentation, is offered to provide the reader insight into the algorithms which appear to be used by STAGSC-1. The next section presents the theory of holographic interferometry.

D. Holographic Interferometry

This sections reviews the basic theory of holographic interferometry. First, conventional split-beam holography is presented. This is followed by a discussion on video holography. Finally some reasons for the success of holographic interferometry are presented.

Holographic interferometry (HI) is a optical, nondestructive testing technique which uses the wave properties of coherent light for measuring minute deformations of a structure. HI requires no physical contact with the structure being tested. A laser is used

to provide the monochromatic, coherent light source required for holography. The unit of measurement in holography is the wavelength of the laser light used [16:156]. Typically a Helium-Neon (HeNe) laser is used and its wavelength is 6328 \AA (24.913 microinches) [44:24]. Therefore HI is an extremely sensitive measuring technique. The most common form of HI is split-beam holographic interferometry which produces three-dimensional images called holograms. These holograms are stored on an optical recording medium such as a thermoplastic plate.

Split-beam holography is a two step process. In the first step the hologram of the object is recorded and in the second it is reconstructed to make a visible image of the object. Figure 2-4 gives a typical layout of a split-beam holography setup. Split-beam holography is based on the splitting of a single laser beam into two separate, mutually coherent (in phase) beams. The two separate beams are called the object beam and the reference beam (Figure 2-4). The reference beam illuminates the holographic plate and is used for hologram reconstruction. The object beam illuminates the diffuse object which scatters the light, some of which is directed towards the holographic plate. Both object beam and reference beam are expanded just prior to illumination of the object and holographic plate, respectively. It is imperative that the object and reference beams remain coherent after separation. This requires that the distance traveled by each beam be within approximately a few centimeters of each other. The reference beam will possess the same wave form as the original laser beam. The object beam, once reflected off the object, will become a complex wave of light which contains all the information about the shape of the object [16:157]. When the object and reference beams are superimposed at the holographic plate, a phenomena called interference occurs and a new wave front is produced [24:4]. The principle is analogous to the behavior of waves in water. Figure 2-5 shows the interference of two wave fronts, similar to what occurs near the holographic plate. The two basic types of interference are constructive interference and destructive interference. If the crests

of the first wave meet in phase with the crests of the second wave then constructive interference occurs and a new wave is created with amplitude greater than the previous two waves. However, if the crests of the first wave are aligned with the troughs of the second wave then destructive interference occurs and the amplitude of the new wave is reduced. Therefore, the interference pattern created by the object and reference beams contains areas of light and darkness which establishes the relative phase relationship between the two waves [24:4,8; 39:319,321]. This interference pattern, which is recorded on the holographic plate, is called the hologram (Figure 2-6).

Holography is not a photographic technique. Photography records only object intensities but the hologram contains both phase and amplitude (intensity) data on the total wave reflected from the object [16:158]. The hologram consists of very small fringes (tiny light and dark spots). These fringes are on the order of 1000 lines/mm and are not detectable by the unaided eye [16:161]. To reconstruct the hologram the reference beam alone is allowed to illuminate the developed holographic plate (Figure 2-7). Note, the

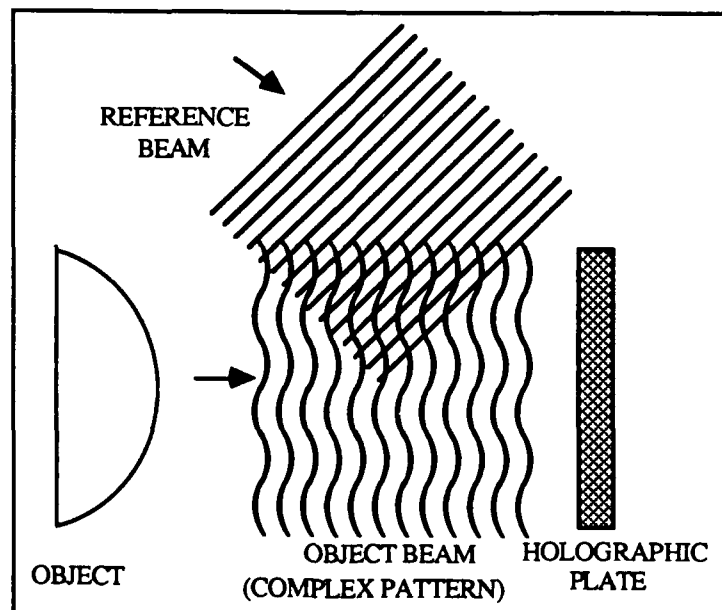


Figure 2-6. Recording of Hologram [19:2.7]

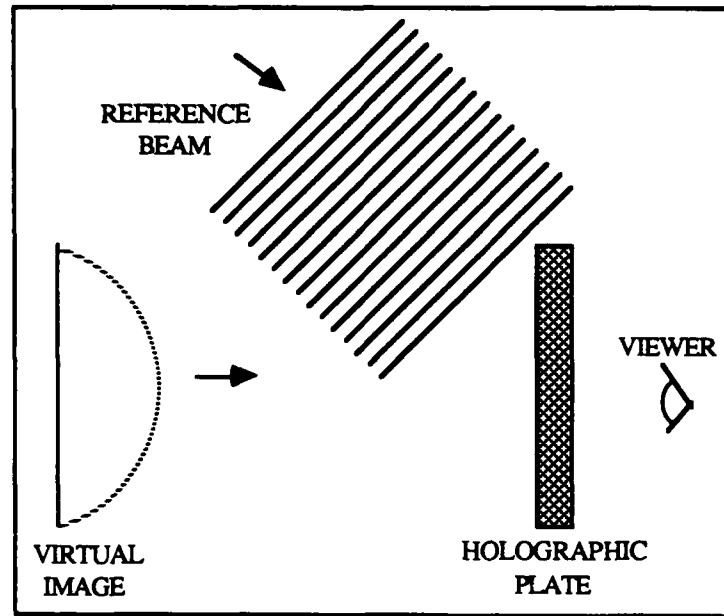


Figure 2-7. Hologram Reconstruction [19:2.8]

developed plate already contains the recorded hologram or interference fringes. When illuminated by the reference beam, the dark spots on the hologram act as barriers while the light areas diffract the light as it passes through. The diffracted waves reconstruct the original interference pattern (all the characteristics of phase and amplitude originally present) which created the hologram from the object [39:327]. The product is a virtual image of the object. When holography is applied to vibration analysis, this virtual image represents the mode shape of the object. The two most common methods of holography used in vibration analysis are real-time and time-average holography.

To perform real-time holography, a hologram is first taken of the object at rest. Without altering the setup the object is now excited. A virtual image of the object, produced by the hologram (undeformed geometry), is now superimposed on top of the vibrating object. As the excitation frequency is varied the reflected wave front from the object is continually changing. The interaction of the interference pattern created by the vibrating objects and the virtual image causes an interferometric fringe pattern to form. The

fringe pattern can be viewed in real time, thus the name real-time holography [45:95,97]. The fringes correspond to lines of constant vibration amplitude (displacement). For real time holography, the amount of displacement required to form a fringe line is one half the wavelength, λ , of the laser light [16:166]. For a HeNe laser $\lambda = 24.913$ microinches. Thus, each successive fringe represent an additional displacement of about 12.46 microinches. This displacement is relative to the undeformed object and therefore represent a peak displacement (Figure 2-8). The overall fringe pattern produced resembles a type of contour map of the object from which the mode shape can be visualized.

To perform time-average holography, a hologram is recorded as the object undergoes deformation. This is accomplished by recording a hologram of the interference pattern produced while the object is vibrating at one of its natural modes. The result is a hologram which records the time-average displacement of each point on the body during a vibration cycle (records deformed geometry). The exposure time of the hologram should be long in comparison to the period of excitation [45:90,95]. Due to the cyclic nature of the objects motion, the velocity is near zero at times of maximum displacement. The object thus spends most of the time at the two extreme amplitudes of its vibration cycle. This causes the interference patterns at the two extremes to contribute the most to the holographic exposure [26]. Therefore, the displacement detected during time-average holography is a peak-to-peak displacement (Figure 2-8). A fringe is formed for a peak-to-peak

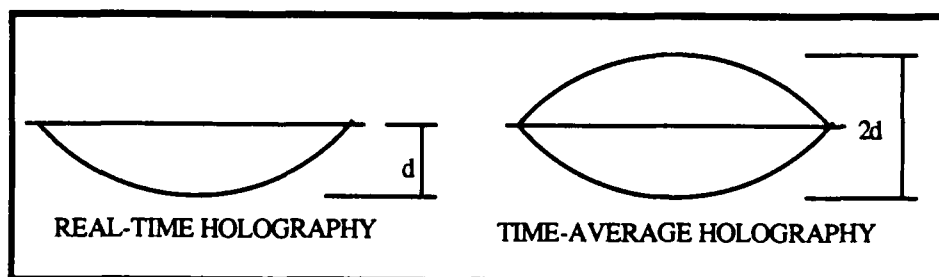


Figure 2-8. Relative Displacements Which Cause Fringe Formation

displacement of 12.46 microinches or a peak displacement of 6.23 microinches. For the same amplitude of vibration, time-average holography will result in more fringes and better resolution. Modal analysis generally involves a combination of real-time and time-average holography. Real-time holography is recommended for making initial frequency sweeps of an object to determine locations of resonant frequency. Time-average holography is then used for making the actual recording of the desired mode shapes.

Video holography is based on the same principles as conventional holography. A laser beam is split into two distinct beams and one is used as a reference beam and the other illuminates the object. However, the interference pattern formed is now recorded by the sensor of a video camera instead of a holographic plate. The interference pattern is integrated over 1/30 of a second which is the frame rate of the camera. The result is displayed by a television monitor for viewing [26]. Mode shapes are recorded using a Polaroid Freeze Frame unit connected to the video signal.

Holographic interferometry has many attributes which have contributed to its success as an experimental technique for performing modal analysis. HI is a relatively easy technique to apply and is highly effective for determining the natural frequencies and mode shapes of structures. HI is an extremely sensitive technique and therefore is capable of detecting small deformations. It is nondestructive and requires no physical contact with the structure being investigated. Although the physics behind holography is very complex, the application of holography is straight forward and only requires a basic understanding of optics. Also, HI requires no time consuming or extensive data reduction. The frequencies and mode shapes are immediately available and the mode shapes can be recorded for future analysis.

This chapter reviewed the theoretical material required for this study. The next chapter (Chapter III) presents the composite panel characteristics.

III. Composite Panels

The panel material properties and the panel geometries considered are presented in this chapter. Eleven panels were investigated both experimentally and analytically as part of the original effort. An additional ten panels were investigated only analytically after the original study was completed. All panels were constructed of the same graphite/epoxy (Gr/Ep) material and subjected to the same boundary condition. The panels were manufactured by the Flight Dynamics Laboratory Composite Shop, Wright-Patterson Air Force Base, Ohio. Cyr [13:31,34] documents the technique used to cut the holes in the composite panels.

The panels were constructed of AS4/3501-6 Gr/Ep twelve inch preimpregnated (prepreg) tape. For consistency with previous work at AFIT [13; 19; 42] a quasi-isotropic $[0/-45/+45/90]_s$ ply layup was selected. Each ply was 0.005 inches thick resulting in a panel thickness of 0.04 inches. Gr/Ep tensile test coupons consisting of $[0]_8$, $[90]_{16}$, and $[\pm 45]_{2s}$ layups were used to determine panel material properties. These coupons were manufactured with the panels. Table 3-1 lists the material properties which resulted from the coupon tests. These properties are relative to the material coordinate system and represent ply properties as opposed to laminate properties. Three 1 inch square specimens were cut from an extra panel and used to determine the density of the Gr/Ep. The mass of each specimen was measured using an electronic balance and its volume found by measuring water displacement in a graduated cylinder. The value listed in Table 3-1 represents an average of the three specimens. The mass density was converted to weight density to satisfy the STAGSC-1 input format. No other material properties were necessary as input to the STAGSC-1 program.

Circular cylindrical Gr/Ep panels were studied in this thesis. Excluding interior cutouts, the basic geometry of each panel was the same. For all panels the radius of curvature was 12 inches, the arclength was 16 inches, and the height was 11 inches. Two

Table 3-1. Material Properties of Composite Panels

E_1	=	20.46×10^6	psi
E_2	=	1.34×10^6	psi
G_{12}	=	8.638×10^5	psi
ν_{12}	=	0.3131	
ν_{21}	=	0.0205	
ρ	=	0.0583	lb _f /in ³

inches along the straight sides of the panel was used as a clamping surface to satisfy the desired boundary condition. Therefore, the effective panel arclength was 12 inches. For purposes of this thesis, the effective panel dimensions are defined as the dimensions of that portion of the panel free to vibrate. The remainder of this thesis will refer to the panels as having a 12 inch radius, 12 inch arclength, and 11 inch height, in effect ignoring the clamping portion. The panel dimensions and an appropriate coordinate system are presented in Figure 3-1. A Clamped-Free-Clamped-Free (CFCF) boundary condition was used and is shown in Figure 3-2. No previous analysis using the CFCF boundary condition was found in the literature. As used herein, a clamped boundary condition is defined by setting the three translations (u , v , w) and the three rotations (θ_x , θ_y , θ_z) at the panel's edge identically equal to zero. For the experimental analysis, the clamped condition could only be approximated as best as possible.

A solid panel (no cutout), five panels with 2 inch square cutouts, and five panels with 4 inch square cutouts were investigated as part of the original effort. All cutouts followed the contour of the surface, that is, the cutout dimensions were measured in the surface coordinate system. The solid panel provided a baseline to compare cutout effects against. Centered cutouts provided a baseline for comparison against eccentricity effects. Upon

completion of the original thesis effort, it was decided to also investigate five panels with 3 inch square cutouts and five panels with 5 inch square cutouts. The 3 inch cutouts provided data in between the two cutout sizes investigated experimentally and was helpful for confirming trends observed in the data. The 5 inch cutout was investigated to extend the previously obtained experimental data.

The eccentricity was introduced in two normal directions. For all cutout sizes, eccentricities of 1 inch and 2 inches in both the circumferential (y) and tangential (x) directions were examined. Figure 3-3 describes the cutout locations examined. The panels were assigned numbers so that they could conveniently be distinguished between for discussion purposes. Table 3-2 presents the panel numbering for the original eleven panels. Table 3-3 presents the panel numbering for the additional panels studied. Hereafter, individual panels will be referred to by the panel numbers assigned in these tables.

The panel characteristics cited in this chapter were used to create the finite element models. The next chapter (Chapter IV) describes the experimental analysis conducted.

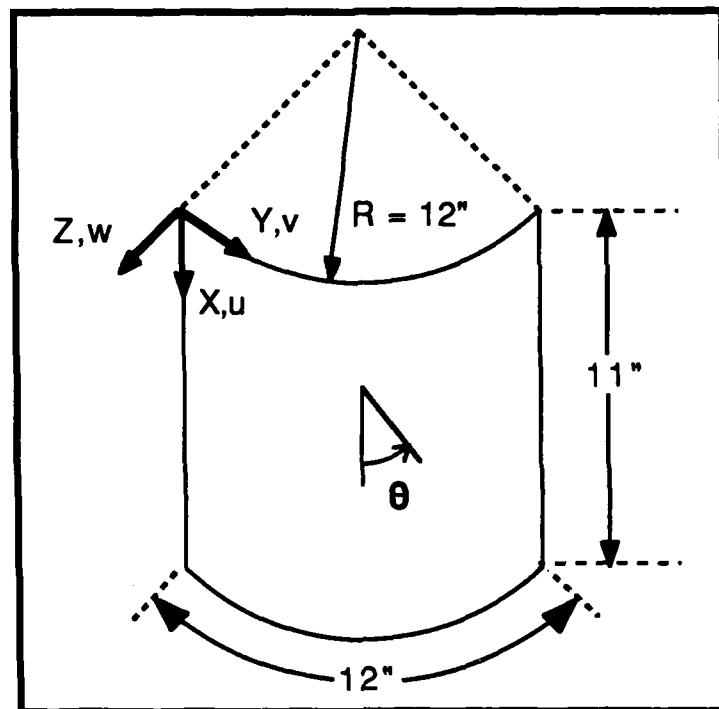


Figure 3-1. Panel Dimensions and Coordinate System

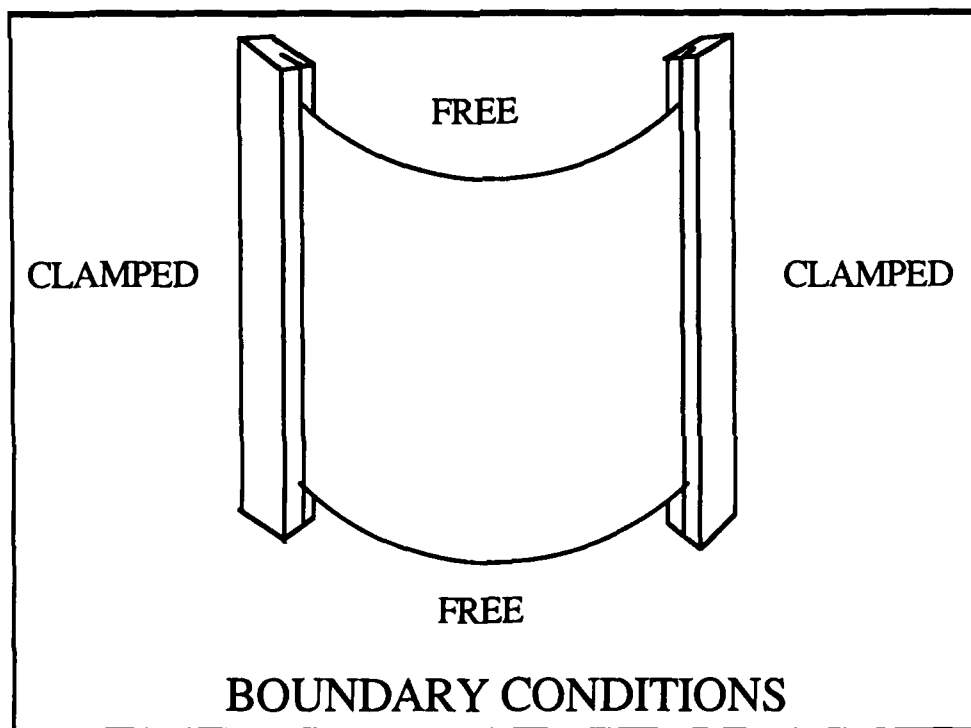


Figure 3-2. Panel Boundary Conditions

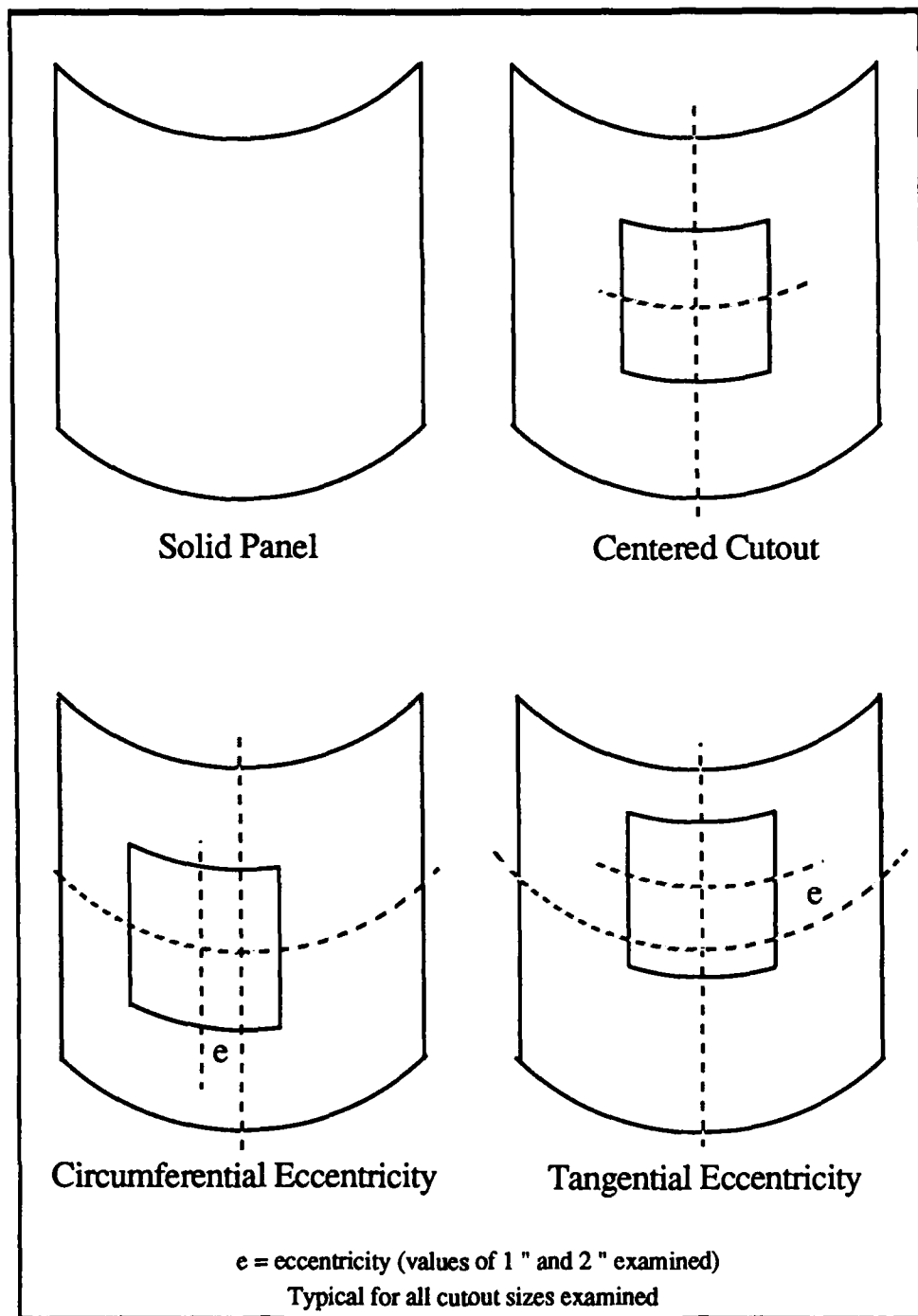


Figure 3-3. Description of Cutout Locations

Table 3-2. Panel Numbers for Original 11 Panels

PANEL NUMBER	CUTOUT SIZE	ECCENTRICITY *	
		AMOUNT	DIRECTION
1	No Cutout	—	—
2	2" x 2"	0"	—
3	2" x 2"	1"	C
4	2" x 2"	2"	C
5	2" x 2"	1"	T
6	2" x 2"	2"	T
7	4" x 4"	0"	—
8	4" x 4"	1"	C
9	4" x 4"	2"	C
10	4" x 4"	1"	T
11	4" x 4"	2"	T

* "C" indicates circumferential eccentricity (along y)
 "T" indicates tangential eccentricity (along x)

Table 3-3. Panel Numbers for Additional 10 Panels

PANEL NUMBER	CUTOUT SIZE	ECCENTRICITY *	
		AMOUNT	DIRECTION
12	3" x 3"	0"	—
13	3" x 3"	1"	C
14	3" x 3"	2"	C
15	3" x 3"	1"	T
16	3" x 3"	2"	T
17	5" x 5"	0"	—
18	5" x 5"	1"	C
19	5" x 5"	2"	C
20	5" x 5"	1"	T
21	5" x 5"	2"	T

* "C" indicates circumferential eccentricity (along y)
 "T" indicates tangential eccentricity (along x)

IV. Experimental Analysis

This chapter describes the procedures used to determine the experimental resonant frequencies and mode shapes for the Gr/Ep panels. Information is also provided on the equipment used and on the application of holography to vibration (modal) analysis. The experimental analysis was conducted using video-holography equipment provided by the Flight Dynamics Laboratory, Wright Patterson Air Force Base, Ohio. One panel (panel 7) was also tested using conventional split-beam holography in which the hologram is recorded on a thermoplastic plate. This was done so that a comparison could be made between video holography and conventional split-beam holography. Appendix B contains a comparison of these two holography methods concerning their application to modal analysis. The procedures for using both methods along with advantages and disadvantages for each method are presented.

A. Equipment

(1) **Test Fixture.** The test fixture used to perform the holographic testing was basically the same fixture first used by Walley [42] and subsequently used by Cyr [13] and Goodwin [19]. Recall from Chapter II, that holographic interferometry is capable of detecting displacements on the order of microinches. Therefore it is necessary that the fixture provide adequate isolation from the local environment and not allow any interferometrically detectable rigid body motion of the panels. Any movement of the fixture would be superimposed on to the panel and would obscure the panel's response. The fixture should also accurately simulate the desired boundary condition without interfering with the natural response of the panels. The fixture previously used [13; 19; 42] provided a proven method for satisfying these conditions. The fixture was made of solid steel and had proved massive and stiff enough for holographic vibration analysis. The fixture was originally

designed to provide clamped boundary conditions on all four sides of the panel. In the original design, a top plate weighing approximately 80 lbs was used to provide the clamped boundary along the upper edge of the panel. The top plate was supported by the sides of the fixture but had to be carefully lowered onto the upper edge of the panel. This task proved extremely awkward and virtually impossible to perform without bending the panel. If bending occurred it resulted in an undesirable prestress condition. For ease of experimentation it was decided that the Clamped-Free-Clamped-Free (CFCF) boundary condition (Figure 3-2) would be examined. Also no previous documentation concerning the analysis of the CFCF boundary condition was found in the literature. To simulate the CFCF boundary condition required only a minor modification to the fixture. Also an improvement was made on the original design to reduce the stresses introduced by the clamp.

The test fixture used in this thesis is shown in Figure 4-1 and 4-2. As mentioned, the top plate required to obtain the fully clamped boundary condition was not necessary. However, a steel bar was added to give support and rigidity to vertical supports. The base was made from 22 inch wide by 10 inch deep by 3 inch thick steel stock. The vertical supports were constructed from 12 inch long pieces of 4 x 4 inch stock. Each support had a $2 \frac{1}{8} \times 1 \frac{1}{2}$ inch section removed to form a "U" shaped structure. Two $\frac{1}{2} \times 2 \times 12$ inch pieces of steel stock (referred to as "flats") were designed to fit into the "U" of the vertical supports. The "flats" provided 2 inches of clamping surface on each side of the panel and were tightened along their length by two rows of set screws. For the experimental analysis previously conducted by Walley [42], Cyr [13], and Goodwin [19], these "flats" were indeed flat on both sides and did not allow for panel curvature. When the panels were mounted into the fixture, they were flattened over the 2 inches of clamping surface. This introduced unwanted bending stresses into the panels. Therefore to improve the clamp, the interior surfaces of the "flats" were machined to fit the curvature of the

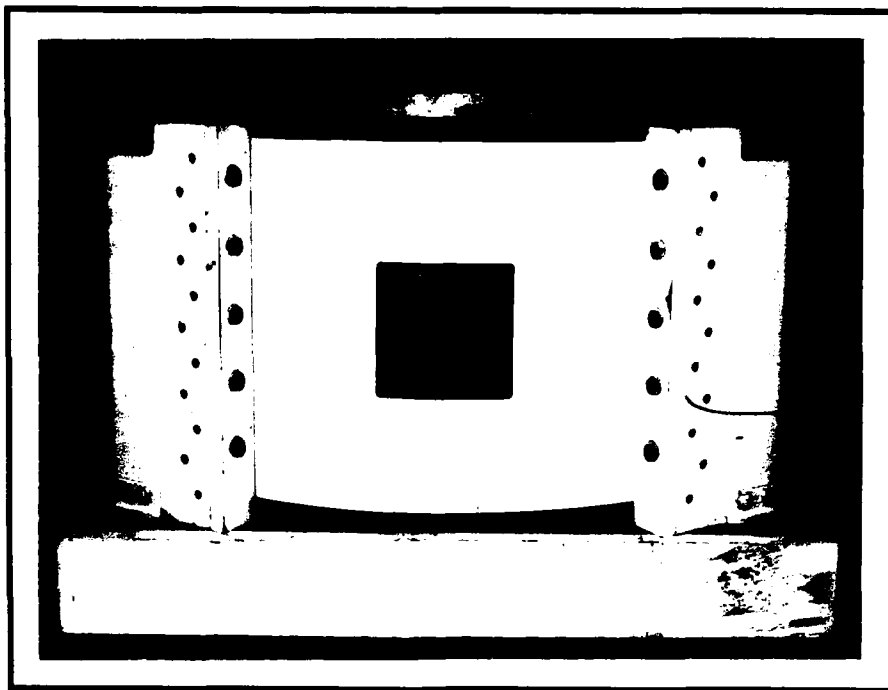


Figure 4-1. Front View of Test Fixture

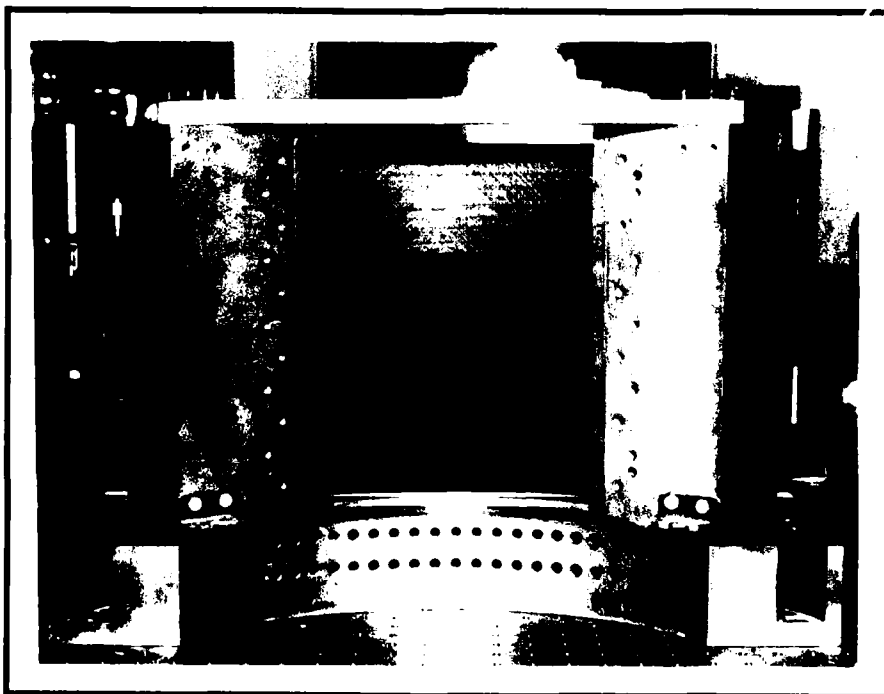


Figure 4-2. Back View of Test Fixture

panel. Figure 4-3 describes this improvement to the fixture. A uniform distribution of clamping pressure was required to achieve the appropriate boundary condition. While mounting the panels, great care was necessary when tightening the set screws against the "flats" to achieve this uniform pressure. A specific tightening sequence was developed to insure uniformity of the clamping pressure and to insure a consistent clamp was obtained between panels. Based on previous experience, the set screws used to clamp the panel were uniformly tightened to a torque of 36 in-lbs [13; 19]. For all panels tested, no fringe lines ever extended from the clamped edge indicating motion of the boundary. The way the fixture was designed (tightening the "flats" against the panels using set screws), rotation about the x-direction was believed to be the weakest degree of freedom (DOF). A special test was conducted to investigate whether the fixture was allowing rotational motion (θ_x) at

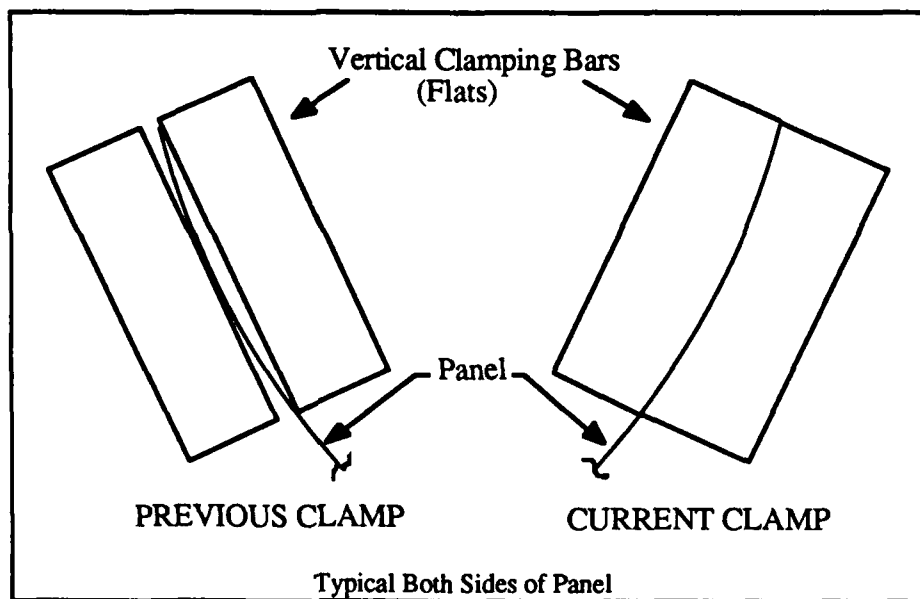


Figure 4-3. Improvement to Test Fixture Clamp

the clamped edge. A *piece of metal* was fixed to the top of one of the "flats" while a panel was mounted in the fixture. During normal testing, any movement of the *piece of metal* would have indicated rotational freedom at the boundary in the θ_x direction. No θ_x rotation was detected using the holography equipment (no fringes were observed on the *piece of metal*). Since this was believed to be the weakest DOF, the fixture was presumed to accurately simulate the clamped boundary condition.

(2) Holography Equipment and Setup. The experimental analysis was conducted using video holography equipment provided by the Flight Dynamics Laboratory. All equipment used is commercially available. The equipment consisted of a Retra 1000 holography unit (hereafter referred to as the holography unit), a Wavetek model 650 variable phase digital synthesizer, a McGohan MS1004 power amplifier, a University ID60CB Horn Driver, a Polaroid Freeze Frame unit, a video monitor, and a stable table. The stable table was used for convenience but is not a necessity for the video-holography equipment used. Figure 4-4 is a schematic of a typical video-holography setup. The portion inside the dotted line was contained within the Retra 1000 unit. Because all of the optics are packaged inside the holography unit, little or no optical alignment and cleaning is required. Figure 4-5 shows the test setup used. The holography unit contains a HeNe laser which provides the monochromatic, coherent light required. Basically the unit operates using a split-beam holography technique with a video detector recording the interference pattern created by the interaction of the object and reference beam. This interference pattern is integrated over 1/30 of a second (camera frame rate) to produce the image of the hologram viewed on the monitor. The freeze frame unit was used to record the desired mode shapes for future reference.

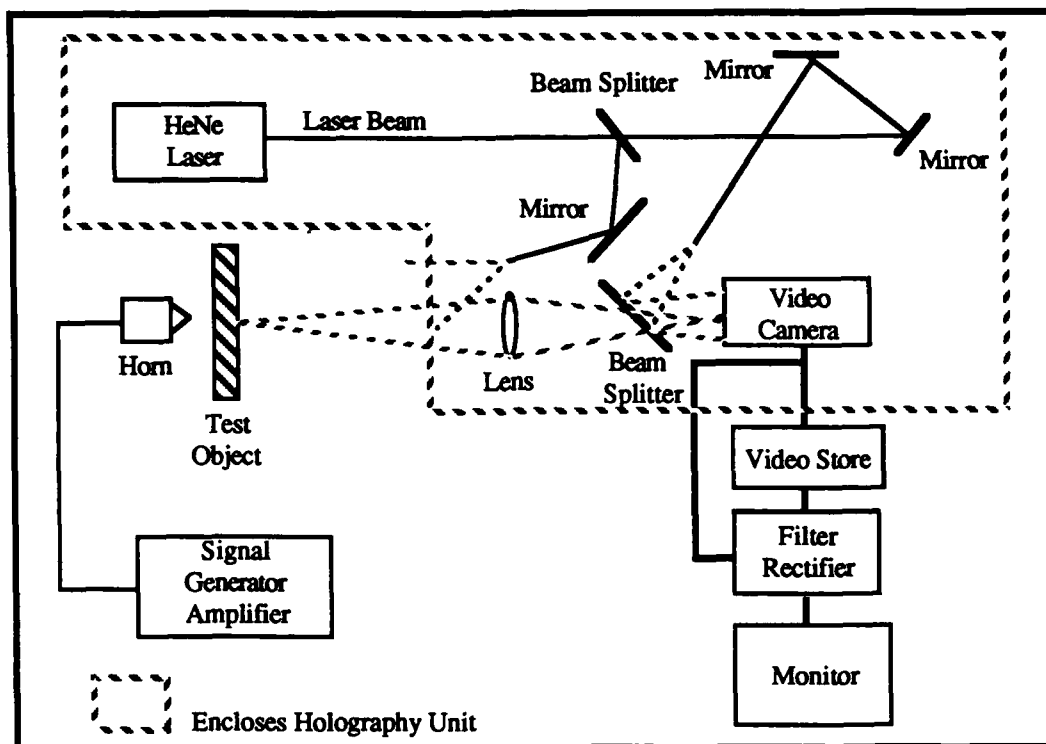


Figure 4-4. Schematic of Typical Video Holography Setup

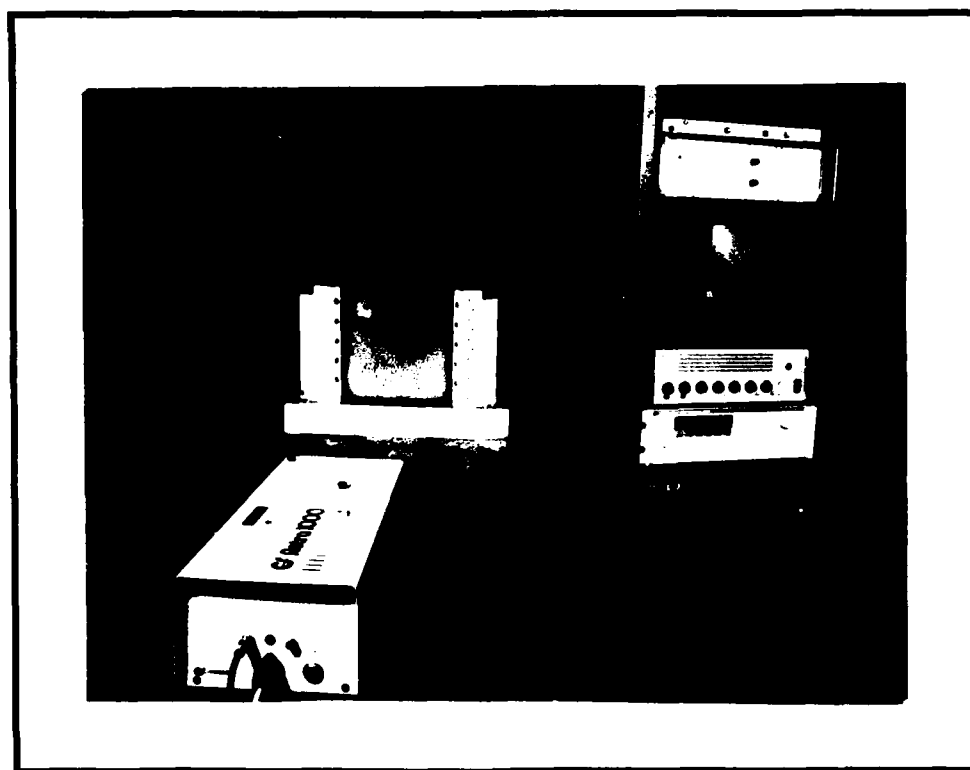


Figure 4-5. Video Holography Setup

The video holography method used for this thesis required very little effort to setup. The holography unit was placed on the stable table. The signal generator, amplifier, monitor and freeze frame unit were connected to each other and to the holography unit using appropriate input/output connectors. These connections had been made by Mr. Maddux [26] prior to the beginning of this thesis and were not altered. The panel was mounted into the fixture using a consistent tightening sequence. The fixture was laid on its side so that the convex side of the panel faced upwards. A very thin coat of all purpose oil was applied to the panel. The oil served as a type of adhesive for a retroreflective coating that was used. The oil was sprayed onto a paper towel then carefully wiped on the panel. Oil was used over an actual adhesive because it allowed the retroreflective material to be removed when the testing was completed. The retroreflective coating material was a type of glass bead which was in the form of a fine powder. The coating was lightly sprinkled onto the panel where it adhered to the oil. The fixture was then placed in the upright position and the back of the panel was tapped to liberate excess coating. The excess was then vacuumed from the table. This application procedure was selected by Mr. Maddux and was based on many hours of experience. The Gr/Ep panels are black, and the video quality is poor unless a coating is used. The coating was necessary to increase the reflected intensity of the object beam which substantially improved the video image and allowed the photographing of the mode shapes. The improved contrast and resolution also aided in determining the precise frequency of resonance and whether or not contamination from an adjacent mode was present. After the panel was mounted and coated the holographic analysis could be performed.

B. Holography Procedure

Model surveys were performed on the eleven Gr/Ep panels. The video holography equipment shown in Figure 4-5 was used. The electronic equipment and the laser were allowed to warm up for at least five minutes so that they could stabilize. Next, the panel was being mounted in the fixture and the retroreflective coating was being applied. The coated panel was then placed at the proper coherence length from the front of the holography unit. This insured the best video image. A horn driver, with an exponential cone mounted onto it, was used to excite the panel; the signal generator was set to provide sinusoidal excitation. The cone caused the excitation to better represent a point source. The horn was placed behind the panel so that the end of the cone was approximately 1/8 inch away from the panel at an antinode location. Only one horn driver was used for this thesis. Frequency sweeps were performed by gradually varying the excitation frequency from 50 to 500 hertz (Hz) and examining the panel response via the monitor. These sweeps were made at relative high excitation amplitudes. This improved the chances of detecting weak modes and it helped to increase the response of modes for which the horn location was not optimum so that they could also be detected. If the horn location was near a node line for a given mode, then the higher amplitude would help indicate the presents of a possible mode. If the horn happened to be located right at a node line then detection of that mode was unlikely. For each sweep the horn location was changed in an attempt to uncover previously undetected modes. For the first few panels numerous horn locations were examined because panel response characteristics were unknown. The horn was moved laterally and vertically to obtain optimum driving locations. As experience was gained the number of horn locations examined were reduced. During the first few sweeps of a panel only approximate locations of resonance was determined. Next, the excitation amplitude was lowered and at the approximate resonance locations the frequency was

slowly and carefully rocked above and below the resonance point until the precise resonant frequency was determined. Usually the first few antisymmetric modes were obtained, then the horn repositioned and the first few symmetric modes recorded. If the mode showed signs of contamination from an adjacent mode, the horn had to be repositioned before the resonant frequency or mode shape could be determined. Resonance was defined as the frequency yielding a local maximum displacement of the panel. The maximum displacement was determined by observing the fringe patterns making up the mode shape. The mode shapes consisted of a pattern of fringe lines. The fringe lines represented lines of constant displacement similar to the lines on a contour map. Maximum displacement occurred when the largest number of fringes were present. As previously mentioned, the maximum displacement experienced by the panels was approximately 50.0 microinches or about 1/100 of a ply thickness. The experimental frequencies were recorded to the nearest tenth of a hertz. The system is capable of much greater sensitivity, but generally the human eye was not. In fact for some cases a variation over a range of 0.5 Hz resulted in no detectable variation in fringe pattern. Therefore, to record the frequency to a large number of decimal places would have been meaningless. After all the desired frequencies had been obtained, a sine dwell was performed at each resonant frequency. The amplitude was adjusted to yield good fringe resolution, and a photograph was taken to permanently record the mode shape. This procedure was repeated for each panel tested.

C. Retroreflective Coating Effects

The retroreflective coating was required to improve the intensity of the object beam. Unfortunately the coating added mass to the panel which effectively changed the panels density and caused a decrease of all resonant frequencies. A sample piece of Gr/Ep was weighed, then coated in the same manner as the panels and then reweighed so that an

approximation to the increase in panel density could be determined. This provided only an approximation because due to the inexact method used to apply the coating, its weight could vary from panel to panel. The panel density was measured to be $0.0583 \text{ lb}_f/\text{in}^3$ (see Chapter III). From the sample tested, the increase in density due to the oil and retroreflective coating material was $4.823 \times 10^{-3} \text{ lb}_f/\text{in}^3$ ($4.812 \times 10^{-3} \text{ lb}_f/\text{in}^3$ due to the coating and $1.1 \times 10^{-5} \text{ lb}_f/\text{in}^3$ due to the oil). This resulted in an effective density for the panel of $0.0631 \text{ lb}_f/\text{in}^3$ or a difference of about eight percent. Thus the change in effective density due to the coating was too large to be ignored. On average the coating lowered the natural frequencies by about 3.5 percent; however the mode shapes were unaffected. Leissa [25] defines a frequency parameter, Ω , for an orthotropic material of the form

$$\Omega = \omega R \sqrt{\frac{\rho (1 - \nu_x \nu_\theta)}{E_x}} \quad (4.1)$$

where ρ is density, R is radius of curvature, ω is circular natural frequency, E is Young's modulus, ν is Poisson's ratio, and, x and θ , are coordinates of the structural axis system. Although the laminate used was anisotropic it is reasonable to assume that an appropriate frequency parameter would be of the form

$$\Omega_A = \omega R \sqrt{\rho C} \quad (4.2)$$

where C is a constant which incorporates panel stiffness and Poisson's ratio effects. Therefore the uncoated natural frequency could be found from the coated natural frequency

by setting equal the frequency parameters for the coated and uncoated panel. The following relationship results [26]

$$\omega_u R \sqrt{\rho_u C} = \omega_c R \sqrt{\rho_c C} \quad (4.3)$$

where u and c represent the uncoated and coated panel characteristics respectively.

Equation 4.3 can be rearranged to give

$$\omega_u = \omega_c \sqrt{\frac{\rho_c}{\rho_u}} \quad (4.4)$$

Therefore, if the panel's natural frequency with the coating and the densities of the coated and uncoated panels are known, then the uncoated panel's natural frequency can be determined. Because of the inexact methods used to apply the coating for this study, the panel's effective density (ρ_c) varied somewhat from panel to panel. Therefore, ρ_c was not constant and Equation 4.4 could not be used reliably. To accurately determine a panel's natural frequencies, ultimately required that it be tested without the coating present. Once the uncoated and coated panel frequencies were known, a ratio of the two frequencies was established. The results indicated that Equation 4.4 was indeed valid. Although not useful for this thesis, use of Equation 4.4 could prove beneficial for future testing in which the coating density was known and consistent. The panels would then only need to be tested once with the coating. This would save time and make the testing easier. For purposes of this thesis, the panels were tested first with the coating applied. This was advantageous because the enhanced video quality allowed precise mode shapes to be recorded using

sketches and photographs and allowed the user to assess whether modal contamination (discussed below) was present. Horn locations for most efficient and effective excitation of the desired modes could also be determined. Finally, the approximate location of the resonant frequency was known. The coating was then wiped off the panel. It was observed that most of the oil came off with the coating due to the nature in which the powdered coating clumped together. Any remaining oil would have truly a negligible effect (see beginning of this section). Now the panel was tested without the coating present. Knowing the precise mode shapes, excitation locations, and approximate resonant frequencies made obtaining the "true" resonant frequencies feasible even though video quality was poor for the uncoated panels. Testing the panels uncoated first would have proved much more difficult.

D. Contamination

This section is included for the benefit of the reader. No contamination of modes was observed for the panels investigated in this study.

A real structure responds to random excitation by moving in a combination of all of its modes. Generally, the normal vibration modes may be isolated by exciting the structure at the natural frequencies of each of its modes; however, some structures may respond in more than one mode, even when excited at the natural frequency of a particular mode [36:199]. This combining of the modes will be referred to as contamination.

Contamination is most commonly observed if the two combining modes are very close in frequency and if there is a significant amount of damping present within the structure. If a mode shape indicates signs of contamination, then a systematic method of modal separation is required to obtain the response of the individual modes. The presence of contamination is determined by observing the fringe patterns as the driving frequency is slightly varied

above and below the apparent resonance. If the number of fringes increases and decreases without shifting of the nodal lines and the node lines remained fixed and only grow narrower as the frequency is tuned through resonance, then the mode shape represents a true resonance or response of a single mode [36:202]. Also, the fringe pattern should increase and decrease at more or less a uniform rate. If the node lines undergo movement in a normal direction (normal to curve generated by node line), shift unexpectedly, or change shape suddenly, then modal contamination is present [27:10,12]. To remedy this situation the horn driver (excitation source) should be located as closely as possible to the antinode of the desired mode while simultaneously being located as near as possible to a node line of the contaminating mode [26]. The horn location is varied until no contamination is present. At this time an accurate frequency and mode shape can be recorded. In most cases, varying the horn location will be sufficient to separate the response of each mode. If not, a dual driver arrangement may be necessary.

This chapter has presented a summary of the experimental analysis conducted for this thesis. Completion of this thesis also required that an analytical analysis be performed using a finite element method. The next chapter describes the analytical analysis conducted using the STAGSC-1 finite element program.

V. Finite Element Analysis

This chapter discusses the procedure used to develop the finite element models. The Structural Analysis of General Shells version C-1 (STAGSC-1) finite element program was used exclusively for this thesis. The STAGSC-1 code was developed by Lockheed Palo Alto Research Laboratory.

A. STAGSC-1 Program

As its name implies, the major emphasis of the STAGSC-1 program is on shell analysis. STAGSC-1 element library contains several families of flat triangular and quadrilateral elements. To date, no curved shell elements have been incorporated into STAGSC-1 [6:6-48]. The shell geometry is therefore modeled by flat elements which produce a multifaceted approximation of the original shell surface. Therefore, when shells are modeled the elements meet at an angle and are no longer coplanar as would be the case when modeling plates. When two flat plate elements meet at an angle, potential rotational and displacement incompatibility problems arise at the interface of the two elements. The QUA4 410 and QUA4 411 quadrilateral elements in STAGSC-1 have been specifically developed to address these incompatibilities. STAGSC-1 handles the rotational incompatibility by including the normal rotation, θ_z , at each corner node. For the QUA4 elements, this normal rotation is the average in-plane rotation of the two adjacent edges of the plate element [15:24]. The displacement incompatibility arises because the lateral displacement, w , is represented by a cubic polynomial in order to handle the second derivatives associated with bending, while the in-plane u and v displacements are usually linear. To overcome this displacement nonconformity, the lateral and in-plane displacements must be represented by a polynomial of the same order [6:6-37,40; 5:6-16,17]. The QUA4 410 element has been formulated so that the in-plane displacement

normal to the element's edge is cubic and the other in-plane displacement is linear. The details of how the QUAF elements overcome the above mentioned compatibility problems have been well documented by many sources and additional discussion here was deemed unnecessary [6; 13; 15].

STAGSC-1 has been used extensively at the Air Force Institute of Technology for the static and dynamic analysis of composite shell structures; however, the majority of the effort has dealt with static analysis. Therefore, this thesis will serve to further validate the dynamic modeling capabilities of the STAGSC-1 program. At the onset of the modeling effort, the STAGSC-1 free vibration option was available at AFIT only on the CDC Cyber machine. In June of 1989, a Vax 11/785 version of STAGSC-1 containing the free vibration option was obtained. Originally it was believed that the Cyber would yield better results because of its larger word length, but similar runs made on both machines resulted in identical answers. The Cyber account required special funding, whereas the student account on the Vax machine was made available at no charge. Also, the Vax environment was more user-friendly than the Cyber. Therefore, most of the analysis for this study was conducted using the Vax machine.

A linear, free vibration analysis was conducted on the Gr/Ep circular cylindrical panels using STAGSC-1. Damping effects were assumed negligible. The panel geometries, material properties, and boundary conditions considered were discussed previously in Chapter III. In STAGSC-1, the free vibration option is selected by setting the INDIC variable equal to 2 ($INDIC = 2$), on the B-1 (Analysis Type Definition Record) input card. This option assumes small vibrations (linear) and assumes no prestress exists within the panel. This is consistent with the experimental procedure used. For free vibration analysis, STAGSC-1 outputs the desired natural frequencies and corresponding eigenvectors. The eigenvectors represent the mode shapes of the panel. STAGSC-1

normalizes the eigenvector by setting the maximum displacement component equal to 1 (or -1) and appropriately scaling the remaining components [6:7-17].

For purposes of this thesis the first five natural frequencies and mode shapes were desired. The material properties (see Chapter III) input into STAGSC-1 were for each ply. Each individual ply was treated as an orthotropic material. The number of plies, ply orientations, and ply thicknesses were input, and STAGSC-1 performed all necessary calculations to determine laminate properties. Care should be exercised when inputting ν_{12} into STAGSC-1. STAGSC-1 defines the reciprocity relation as, $\nu_{12} E_1 = \nu_{21} E_2$, which is contrary to the conventional relation given by, $\nu_{21} E_1 = \nu_{12} E_2$. Thus, the Poisson's ratio required by STAGSC-1 is related to the conventional Poisson's ratio by

$$\nu_{12})_{\text{STAGS}} = \nu_{21})_{\text{convention}} \quad (5.1)$$

To select a circular, cylindrical shell geometry, the ISHELL variable was set to 5 (ISHELL = 5) on the M-1 (Shell Type Definition Record) input card. The built in mesh generator was used to establish the finite element grid for all panels. The user determines the grid spacing in the x and y coordinate directions (Figure 3-1) and STAGSC-1 determines the nodal coordinates and connectivity matrix. The N-8 (Mesh Irregularity Record) input card is used to define a cutout in the shell's surface. This card defines the boundary grid lines of the cutout. All elements contained within these boundary lines are removed from the model. Because of the nature in which cutouts are defined, only rectangular cutouts can be introduced using the N-8 input card. For the type of analysis performed and the panel geometries investigated, STAGSC-1 proved straight forward to implement.

B. Element Selection

As mentioned earlier, STAGSC-1 only incorporates flat plate elements. Two of these elements are the QUAF 410 and QUAF 411 elements. The QUAF 410 quadrilateral element is a four noded element. It has three translational and three rotational degrees of freedom (DOF) at each node [5:6-17]. Therefore, the element contains six DOF per node for a total of 24 DOF. The QUAF 411 is a quadrilateral element which has midside nodes on all four sides and represents an enhanced version of the 410 element. The 411 element has four rotational and three translational DOF at each node and an in-plane tangent displacement at each midside node for a total of 32 DOF [5:6-17]. Both element are nonconforming [6:6-35].

The element selected to model the Gr/Ep panels for this thesis was the QUAF 410 element. The 410 element is shown in Figure 5-1. The selection of this element was based on analysis performed by Walley [42] and later substantiated by Cyr [13]. Both Walley and Cyr performed a free, undamped vibration analysis of similar Gr/Ep panels with fully clamped boundary conditions. Walley found that for the same mesh, the 410 and 411 elements resulted in essentially the same natural frequencies, but the 411 element required as much as 48% more CPU time because of its slower convergence rate (due to the higher number of DOF). Walley concluded that the improvements of the 411 element over the 410 element dealt mainly with in-plane displacements. However, the linear free vibration problem of a clamped shell is primarily concerned with out-of-plane displacements. Thus, no advantage was gained by the 411 element [42:29]. Although a CFCF boundary condition (Figure 3-2) was used, this conclusion is equally applicable to the panels investigated in this study and a similar result should be expected. To remove all doubt, a comparison between the 410 and 411 elements was performed for the solid panel [Panel 1]. Walley showed that the 411 element's performance was similar to 410 element's

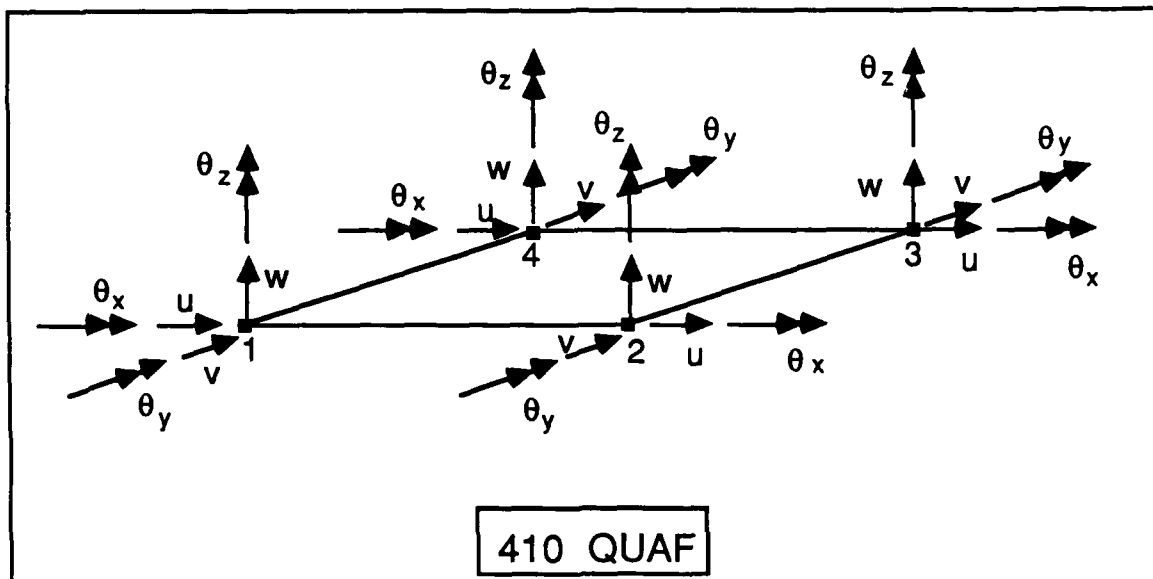


Figure 5-1. Degrees of Freedom for STAGSC-1 410 QUAF Element

performance irrespective of the mesh size [42:28]. Therefore, an element mesh was first determined using the 410 element and then this mesh size used for the comparison. (The mesh size selection is discussed in the next section.) The results of the 410 element and 411 element comparison are shown in Table 5-1. Similar to Walley's findings, both elements yielded essentially the same frequencies but the 411 element required 2.4 times as much CPU time. No further consideration was given to the 411 element.

C. Convergence Study

Walley [42] had previously conducted a convergence study using the 410 element with a similar Gr/Ep panel and fully clamped boundary condition. Because a different boundary condition was used for this thesis, good engineering practice required that the convergence study be reaccomplished. The convergence study had to be conducted early into the thesis. The current Gr/Ep panel material properties were unavailable at the time the convergence

Table 5-1. Comparison of the 410 and 411 Elements for Panel 1

Mode Number	410 Element Frequency (Hz)	411 Element Frequency (Hz)
1	117.839	117.838
2	217.351	217.349
3	247.956	247.950
4	368.235	368.167
5	393.148	393.144

study was performed; therefore, the same Gr/Ep material properties which had previously been used by Walley [42], Cyr [13], and Goodwin [19] for their vibration analysis were used. There were no extreme changes between the past and current material properties, so reaccomplishment of the convergence study with the new properties was deemed unnecessary. The convergence study is the only analysis contained within this thesis which did not use the material properties presented in Chapter III. The material properties used for the convergence study are documented by Walley [42:19].

The convergence study was conducted using the 410 element and Panel 1. The STAGSC-1 built-in grid generator was used to create all element meshes for this thesis. This resulted in uniform meshes composed of square elements. Element edge sizes of 1.0", 1/2", 1/3", and 1/4" were considered resulting in element meshes of 11 x 12, 22 x 24, 33 x 36, and 44 x 48 elements, respectively. The convergence study results for the first 5 modes are presented in Table 5-2.

Next, to insure that the discontinuity caused by a cutout would not alter the mesh selection, Panels 9 and 11 were checked using 1/2" and 1/4" elements. The results are presented in Table 5-3 and Table 5-4, respectively. Panel 9 and 11 were selected because

Table 5-2. Resulting Frequencies (Hz) from Convergence Study for Panel 1

Mode Number	1 inch elements	1/2 inch elements	1/3 inch elements	1/4 inch elements
1	120.1542	120.0670	120.0425	120.0294
2	221.2529	221.4443	221.4527	221.4496
3	259.7459	251.9366	250.6289	250.1732
4	395.4464	374.3312	370.9715	369.8239
5	398.3057	400.3557	400.6051	400.6821

Table 5-3. Resulting Frequencies (Hz) from Convergence Study for Panel 9

Mode Number	1/2 inch elements	1/4 inch elements
1	121.7101	121.5738
2	214.6801	214.4525
3	240.3943	238.6372
4	293.4082	290.6273
5	385.9062	385.0136

Table 5-4. Resulting Frequencies (Hz) from Convergence Study for Panel 11

Mode Number	1/2 inch elements	1/4 inch elements
1	115.0160	114.6769
2	228.0940	227.5142
3	253.3054	251.3746
4	272.9417	269.4845
5	392.6746	393.5623

they contained the largest cutout at the two largest eccentricities and were therefore believed to represent the worst possible cases. Element sizes of 1" and 1/3" were not used for Panels 9 and 11 because they would have required a user generated grid. This would have required a substantial effort and after the results for the 1/2" and 1/4" element meshes were obtained, it was apparent that the two additional grid sizes would not contribute to the overall decision. If one compares Tables 5-2 through 5-4, several observations can be made. First, convergence is adequately satisfied by the 1/2" element. The fourth mode for all cases represents the largest difference between the 1/2" and 1/4" elements. This difference represents just over a 1 percent change which did not justify the substantial increase in CPU time required for the 1/4" element. Secondly, the second and fifth modes did not converge uniformly from above. This can be attributed to the fact that nonconforming elements do not guarantee monotonic convergence from above [12:97,99]. The final observation is that the cutout location did not affect the mesh size selection. As a result of the convergence study, a uniform mesh of 22 x 24, 1/2" square elements was selected. This mesh was used to model all Gr/Ep panels studied. The panel mesh is shown in Figure 5-2 for the panel viewed as a flat plate and in Figure 5-3 as an

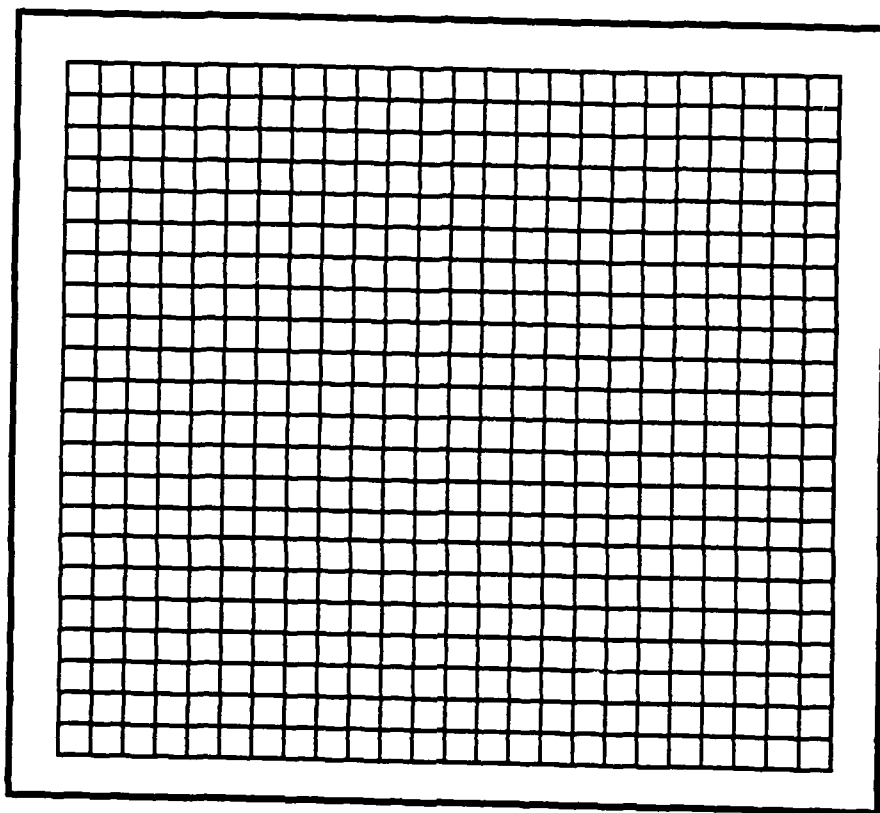


Figure 5-2. Typical Element Mesh Used for Finite Element Models (22 x 24)

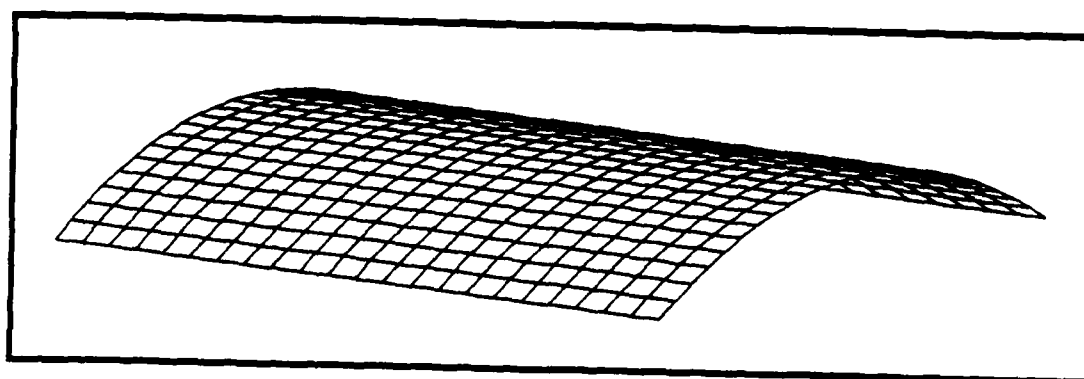


Figure 5-3. Orthographic View of Finite Element Mesh (22 x 24)

orthographic projection. One should notice (Figure 5-3) how well the 22 x 24 mesh represents the true surface curvature. After completion of the convergence study, panel modeling could begin.

D. Panel Modeling

Using the STAGSC-1 program, a linear undamped free vibration analysis was performed on the Gr/Ep panels considered in this thesis. The assumptions applicable to this analysis were presented in the beginning of Chapter II. The particular panel geometries and individual ply material properties were given in Chapter III. Also given in Chapter III was a description of the CFCF boundary condition used. The finite element meshes were generated using the STAGSC-1 grid generator and the QUAF-410 element. The N-8 (Mesh Irregularity Record) input card was used to define cutout sizes and locations. A Vax 11/785 was used to execute the STAGSC-1 program although the capability existed for execution on a CDC Cyber machine. The output from STAGSC-1 was the first five natural frequencies and their corresponding eigenvectors (mode shapes). To allow for comparison with the holograms obtained from the experimental analysis, the eigenvectors were plotted as contour plots. Also, orthographic views of the mode shapes for Panels 1 and 7 were plotted to help visualize the panel's deformed geometry (Appendix D). Due to time constraints, the mode shapes were not plotted for the panels with 3 inch and 5 inch square cutouts. To generate the contour and orthographic plots, the TOPO and SURF routines within the SURFER program were used, respectively. SURFER is an IBM-PC compatible plotting package which is copyrighted by Golden Software Incorporated. SURFER was selected because it produced better quality contour plots than the standard STAGS plotting routine (STAPL) and because it had the capability to produce the orthographic views. To use SURFER required two things. First, the STAGSC-1 output had to be converted into

the SURFER format. This was accomplished by a FORTRAN program which was written to extract the necessary data from the STAGSC-1 output and then convert it to the required format. Second, the data then had to be down loaded from the Vax onto floppy disks so that it could be input into the SURFER program. Although the use of SURFER resulted in good plots, the overall plotting process proved to be very time consuming. The analytical results obtained for the Gr/Ep panels, along with the experimental results, are presented in Chapter VI.

VI. Results and Discussion

This chapter both presents and discusses the experimental (Chapter IV) and analytical (Chapter V) results of this study. The primary objective of this thesis was to examine the eccentricity effects of a square cutout on the dynamic response (natural frequencies and mode shapes) of a circular, cylindrical Gr/Ep composite panel. To the best of the author's knowledge, eccentrically located cutouts have not been previously documented for such a panel. Previous analyses at AFIT, concerning the dynamic response of cylindrical composite panels with cutouts, have considered fully clamped boundary conditions with centrally located cutouts [13; 19; 42]. Simulating the fully clamped condition using the test fixture described in Chapter IV, had in the past proven to be an extremely awkward process. The CFCF boundary condition was selected to simplify the experimentation and panel mounting procedure. In addition, based on the literature search conducted, it appears that boundary conditions other than all edges simply supported or clamped have attracted a smaller amount of documented research. Therefore, it is hoped that this study will extend previous work performed concerning the dynamic response of composite panels and also encourage future research in this areas.

As discussed in Chapter IV, a video holography technique was used to perform the experimental analysis. Holography is an extremely accurate and effective method for obtaining the resonant frequencies and mode shapes of a structure. Thus, it is believed that the experimental results closely represent the "true" panel characteristics and will therefore be used for most comparisons made in this chapter. If experimental error was present, the two most likely sources would be: 1) The lack of the actual boundary condition, achieved by the fixture, adequately simulating the clamped condition desired (including the possibility of induced stress within the panel when clamped into the fixture), and 2) The misreading of the mode shapes (fringe pattern) when determining the precise resonant

frequencies. A test was conducted to insure that the fixture was adequately restraining motion of the panel's edge (see Chapter IV). Also, all frequency readings were carefully made and several frequency sweeps were performed for each panel to insure the "true" resonant frequencies had been found. Neither source is believed to have contributed significantly, and therefore the experimental results are thought to accurately represent the "true" panel characteristics [26]. The experimental results included herein are for the first five resonant frequencies and mode shapes for the 11 panel geometries described in Chapter III. The mode shapes were recorded by photographing the time-average holograms for each panel at the appropriate resonant frequencies. All photographs of mode shapes within this thesis represent experimental results. The video camera used for this study caused a distortion of the mode shape in the vertical direction. Therefore, the experimental mode shapes presented in this chapter are elongated in the vertical direction but still accurately represent the panel's behavior. When viewing the experimental mode shapes (via the monitor), the brightest fringe lines represent node lines, while each subsequent light fringe represents a line of constant panel displacement. The difference in displacement between adjacent light fringes is equal to approximately 6.23 microinches. For the results presented in this chapter, any reference to the number of node lines present within a given mode shape will intentionally not include the obvious node lines along the two clamped boundaries.

A single panel (Panel 7) was also tested using a conventional holography technique, in which the hologram is recorded on a thermoplastic plate. This was done so that a comparison of the video holography and the conventional holography techniques could be performed. The natural frequencies obtained by the conventional approach were, as expected, consistent with those found by the video holography experiment. Because the frequencies were consistent with the video holography results and were not needed for the comparison, they were not included in this thesis. The resolution of the holograms (mode

shapes) is the only difference in results between the two techniques. The mode shapes for Panel 7 are presented in Appendix B, along with a comparison of the two holography techniques.

The analytical analysis was performed using the STAGSC-1 finite element program. This study continued the validation of the dynamics capabilities of the STAGSC-1 program at AFTT which was initiated by Walley [42]. A linear, free vibration analysis was performed on each panel and damping effects were assumed negligible. From studying the mode shapes, resonance was found to be present over a very narrow frequency range. This is characteristic of lightly damped structures [36]. Therefore, observations made during experimentation indicate that neglecting damping was a reasonable assumption. The analytical analysis treated the Gr/Ep as a homogeneous material and did not consider any effects due to possible surface imperfections. The material properties, boundary conditions, and panel geometries were presented in Chapter III. Finite element models were developed for all panel geometries (presented in Chapter III) which were experimentally tested. In addition, cutout sizes of 3" x 3" and 5" x 5" were also analytically modeled (Panels 12 through 21 described in Table 3-3). Three inch and five inch square cutouts were selected because the panels with 3 inch cutouts would provide data points in between the two cutout sizes experimentally examined and the panels with 5 inch cutouts would extend the experimental data and would help determine when cutout size began to cause substantial frequency changes to other than the fourth mode. The same eccentricity amounts and directions were used for the 3" and 5" square cutouts as was used for the 2" and 4" cutouts (see Chapter III).

The analytical results included herein are for the first five resonant frequencies and mode shapes (eigenvectors) for Panels 1 through 11. The mode shapes were created by plotting a contour plot of the eigenvector output by STAGSC-1. The numerical values on the analytical mode shapes represent normalized displacements. For the plotting software

used (SURFER), the maximum amplitude of displacement (in absolute value) is taken as 1 (or -1) and the remaining displacements are normalized accordingly. To help visualize the mode shapes, orthographic views of the mode shapes for Panels 1 and 7 are included in Appendix D. Because the eigenvector only includes information concerning the panel's deformed geometry, the eigenvector was superimposed on top of the panel's undeformed geometry to create the orthographic views. Only the first five resonant frequencies are included for Panels 12 through 21. As mentioned in Chapter V, the plotting of the analytical mode shapes was a time consuming process. Because Panels 12 through 21 were additional panels (not part of the original thesis), they were not analyzed until all required analytical work was totally completed. Unfortunately, time did not permit the plotting of the mode shapes for Panels 12 through 21 (panels with 3" and 5" square cutouts) or the examination of additional eccentricity values.

The resulting experimental and analytical natural frequencies for this study are compared using a percent difference approach. In all cases, the percent difference for a given mode was calculated using the following relation

$$\text{Percent Difference} = \frac{f_A - f_E}{f_E} \times 100\% \quad (6.1)$$

where f_A is the analytical resonant frequency and f_E is the experimental resonant frequency. Both frequencies are given in Hertz (Hz). All percent differences reported will be positive, since STAGSC-1 yielded results which were consistently higher than experimental results.

It was first expected that the percent difference would be lowest for the first mode and increase with increasing mode number. However, this was not the case with any of the panels tested. The use of nonconforming elements may have contributed to the fact that

often in this study higher modes were predicted closer to experimental values than were lower modes. This same occurrence was also noticed in Walley's [42] and Cyr's [13] results.

Before discussing the individual panels, some initial insights should be presented regarding the effects of the inclusion of a cutout into a panel. In general, these effects can be quite complex, however, for purposes of this study only a simple explanation is attempted. Rayleigh's quotient will provide the bases for this discussion. The expression of Rayleigh's quotient for a continuous system is given by [29:191]

$$\omega^2 = \frac{\int_D u L[u] dD}{\int_D u M[u] dD} \quad (6.2)$$

where ω is a circular natural frequency of the system, L is the differential operator related to stiffness, M is the differential operator related to mass, u is a comparison function (any arbitrary function which satisfies all geometric and natural boundary conditions of the system), and D is the domain of the system. As an example, equation 6.2 can be used to obtain an estimate of the system's fundamental frequency. The accuracy of this estimate is dependent on how well the comparison function represents the actual eigenfunction. If u identically represents the eigenfunction, then Equation 6.2 will yield the "true" fundamental frequency [29:191,192]. For purposes of this thesis, the cutout effects are better illustrated if a discrete system is considered. Rayleigh's method for a discrete system is given by [29:208]

$$\omega^2 = \frac{\{u\}^T [K] \{u\}}{\{u\}^T [M] \{u\}} \quad (6.3)$$

where $\{u\}$ is a trial vector and $[K]$ and $[M]$ (hereafter K and M for simplicity) are the overall system stiffness and mass matrices, respectively. As before, if the trial vector is identical to the first eigenvector, then Equation 6.3 will yield the "true" fundamental frequency. Equation 6.3 will give a good approximation to the natural frequency even if $\{u\}$ does not closely represent the eigenvalue [29:208]. From Equation 6.3 it can be seen that for a given mode (and therefore given mode shape or eigenvector) the natural frequency is dependent on the ratio K/M . When a cutout is introduced into the panel, both K and M are reduced. Therefore for a given mode, if the overall panel stiffness and mass are affected such that the K/M ratio is approximately constant and assuming that the eigenvector (mode shape) does not change dramatically, then from Equation 6.3 the resonant frequency for the given mode should remain relatively unchanged. That is, the natural frequency of the panel with and without the cutout will be essentially the same. If the frequency changes then Equation 6.3 indicates that the K/M ratio for the panel has changed. If for a given mode the frequency increases, then that mode is more sensitive to the mass removed by the cutout and not the stiffness reduction. On the other hand, if the frequency decreases for a given mode, then that mode is more sensitive to the loss of stiffness as opposed to the mass removed. The location of the cutout with respect to node lines and antinodes may help determine whether K or M will contribute more to the panels response for a given mode. Node lines represent lines of zero displacement within a given mode shape. Therefore, excitation provided at a node line, for a given mode, will not excite that mode. Antinodes are points of maximum displacement within a given mode shape. Therefore, regions near antinodes will experience relatively large velocities and bending moments. Bending moment is inversely proportional to the radius of curvature of the deformed shape or can be thought of as proportional to the rate of change in slope of the deformed geometry (for small displacements) [34:354]. For the present argument, let mass be thought of as a forcing function ($F = ma$) and assume that nodal lines possess a small

finite width. Thus, mass added at or removed along a node line will not alter the panel's dynamic response. In reality, because cutouts are wider than node lines they may still have a small effect even if located on a node line. In general, a node line will be a line of contraflexure for the curves defining the deformed geometry of the structure. For this case, the amount of bending moment will decrease as the node line is approached. Thus, at node lines both the effects of reduced mass and stiffness will be less significant. The one affected the most will depend on many factors including, cutout size, the geometry of the mode shape and properties of the material. Both stiffness and mass will be important near antinodes and the one which contributes the most will depend, among other things, on the properties of the given material and the geometry of the mode shape. Because the effects of mass and stiffness (due to a cutout) are coupled, a cutout may affect a panel's response for a particular mode in a way contrary to how another mode is affected. These factors will be discussed further for individual panels.

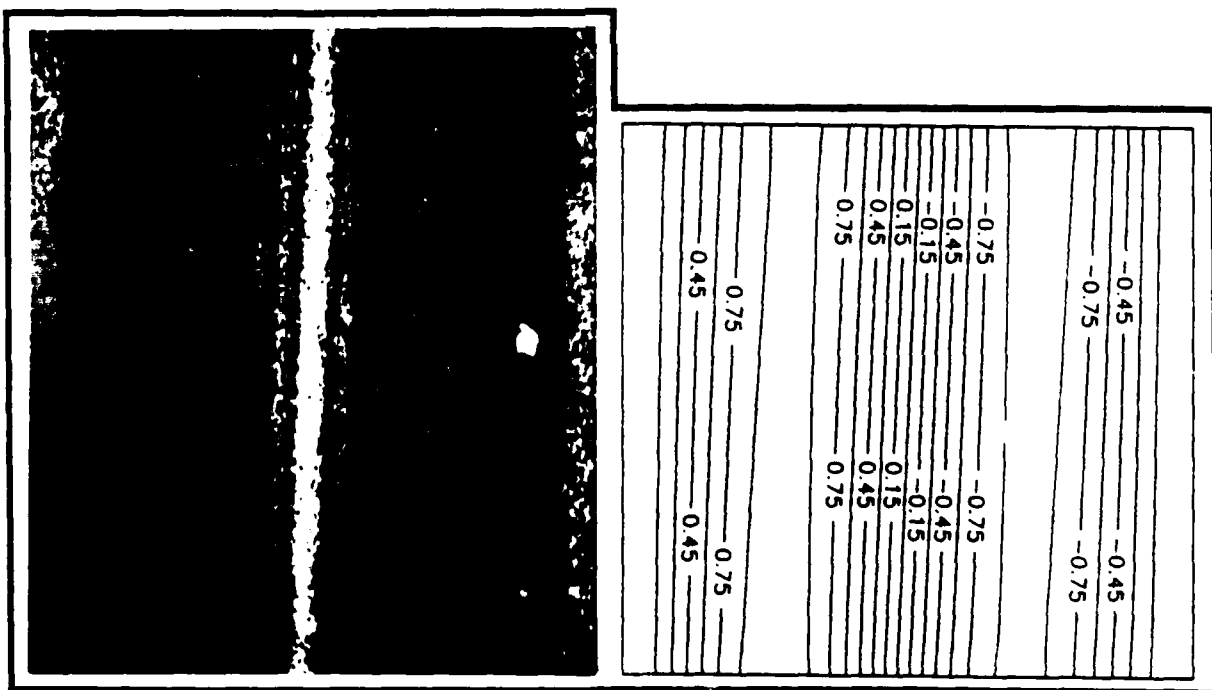
The remainder of this chapter is broken down into six major sections. The first section presents the experimental and analytical results obtained for Panel 1 (solid panel). The second section contains the experimental and analytical results for all panels with 2 inch square cutouts (Panel 2-6), while the third section contains the results for all panels with 4 inch square cutouts (Panels 7-11). Table 3-2 summarizes the configurations for these panels. The fourth section discusses STAGSC-1's performance as compared to the experimental results. In the fifth section, the results for the panels with 3 inch square cutouts (Panels 12-16) and 5 inch square cutouts (Panels 17-21) are presented together. Only analytical results are available for Panels (12-21) because no panels with these size cutouts were constructed. Table 3-3 summarizes the configurations for Panels 12 through 21. Finally, section six summarizes the cutout effects and eccentricity effects for all panels considered in this study.

A. Panel 1

This panel did not contain a cutout and was used as a baseline against which cutout effects could be compared. A summary of the experimental and analytical resonant frequencies, along with the corresponding percent differences are shown in Table 6-1. Figures 6-1 through 6-3 present the experimental (photographs) and analytical (plots) mode shapes for Panel 1. The node lines in the experimental mode shapes are represented by the brightest fringe lines. The analytical node lines are located at the point where displacements shift from positive to negative values. When comparing mode shapes, it is the overall shape which is important. The number of fringe lines (experimentally) is a function of the excitation amplitude and will increase or decrease with increasing or decreasing amplitude. The number of fringe lines (analytically) will change depending on what contour interval is selected. Therefore for the type of analysis conducted, the density of fringe lines is not important and no comparison of the actual number of fringe lines contained in the experimental mode shapes verses the analytical mode shapes should be considered. Orthographic views of the mode shapes for Panel 1 are presented in Figures 6-4 and 6-5 and in Appendix D, Figures D-1 through D-5. If one inspects Figures 6-4 and 6-5, an observation can be made which is not readily apparent from the contour plots. For the third and fourth mode shapes, due to the free edge condition, axial lines which ran along the panels surface remained relatively straight (lines are not truly straight but actually resemble two quarter sine waves) as the panel deformed. This implied that the radial distribution of displacement along the longitudinal direction of the panel was caused more by a rotational characteristic (around the horizontal node line) rather than an actual bending characteristic of the panel. The radial distribution of displacement along the circumferential direction resembled the familiar half wave pattern.

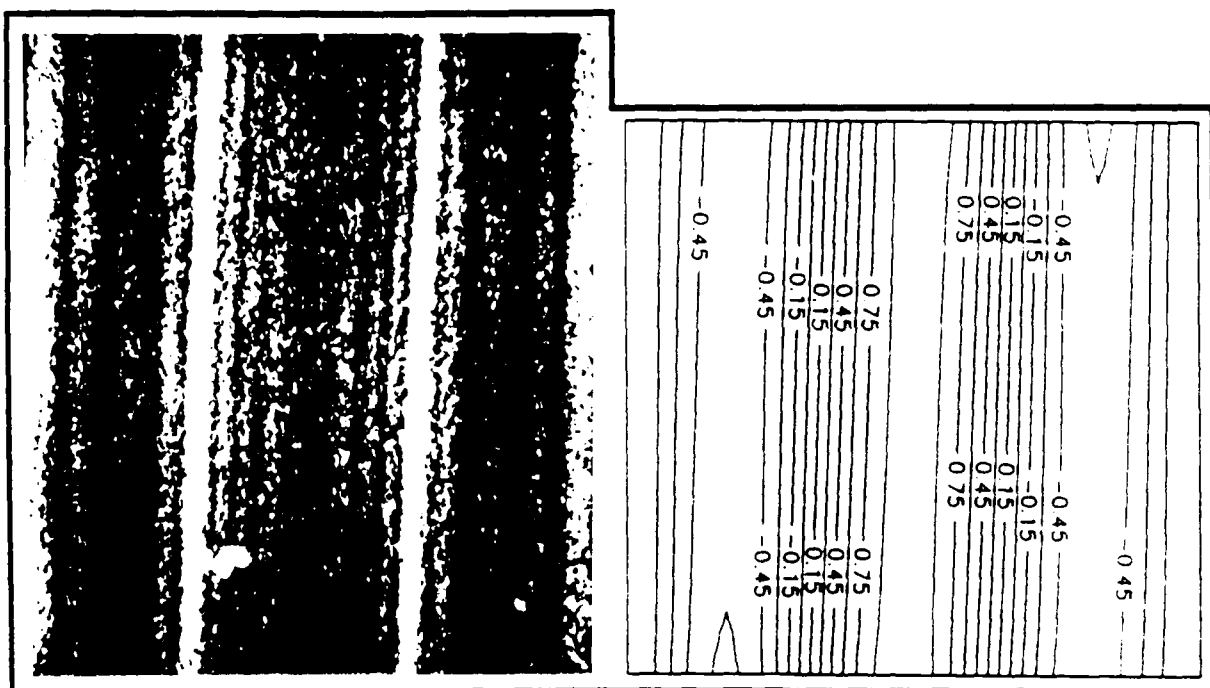
Table 6-1. Comparison of Experimental and Analytical Resonant Frequencies for Panel 1

Mode	Experiment (Hertz)	STAGSC-1 (Hertz)	Percent Difference
1	108.7	117.84	8.41
2	203.3	217.35	6.91
3	235.1	247.96	5.47
4	349.4	368.24	5.39
5	369.3	393.15	6.46

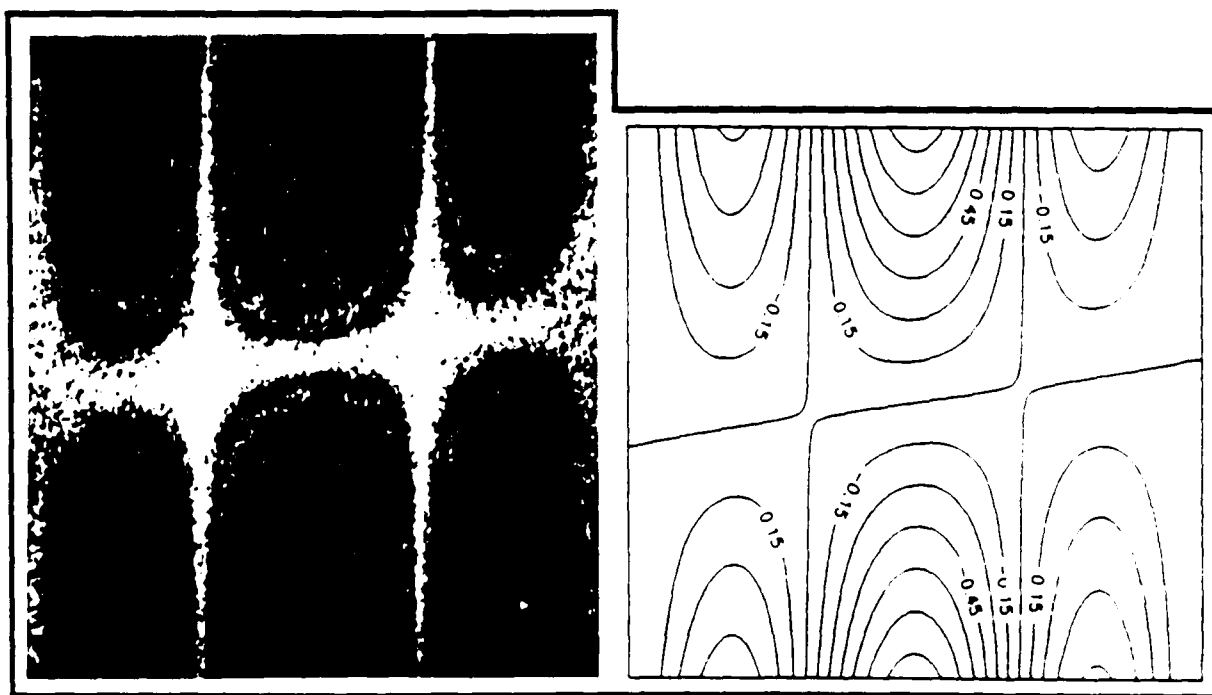


Mode 1

Figure 6-1. First Mode Shape for Panel 1

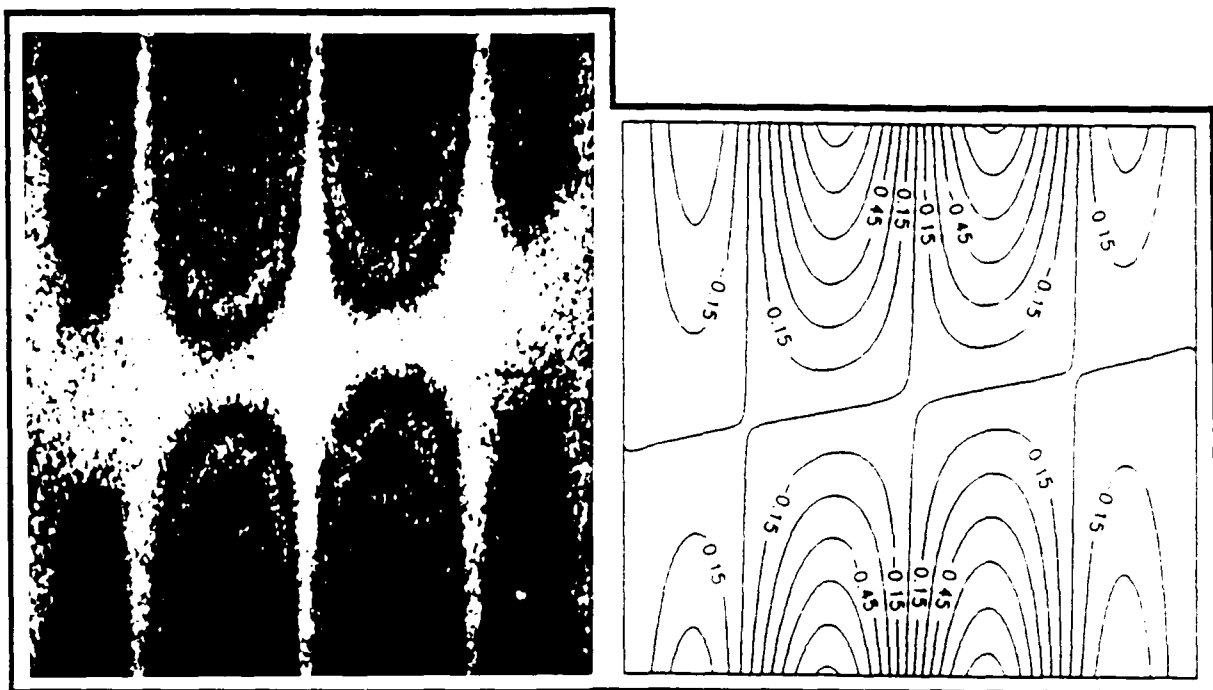


Mode 2

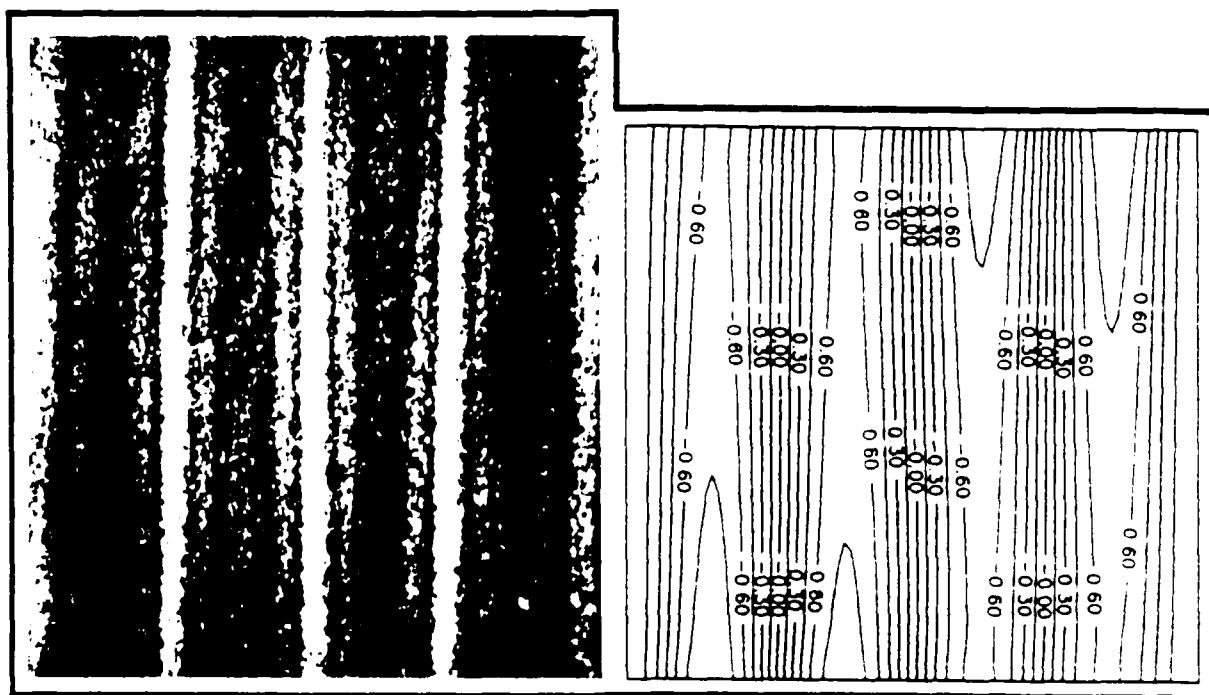


Mode 3

Figure 6-2. Second and Third Mode Shapes for Panel 1



Mode 4



Mode 5

Figure 6-3. Fourth and Fifth Mode Shapes for Panel 1

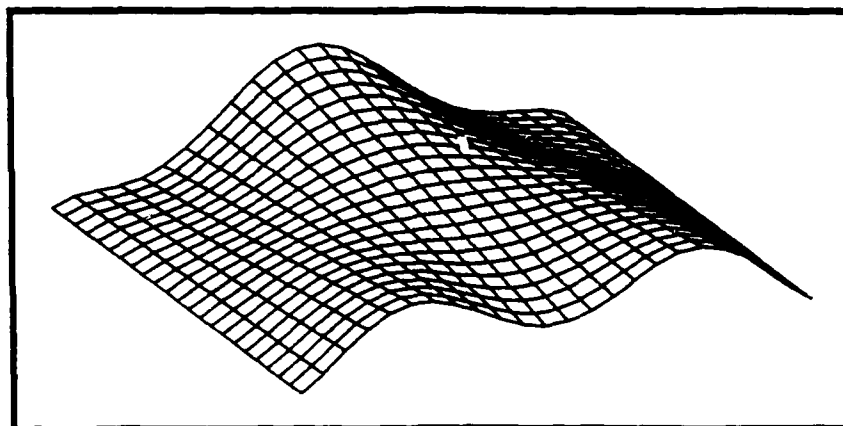


Figure 6-4. Orthographic View of the Third Mode Shape for Panel 1

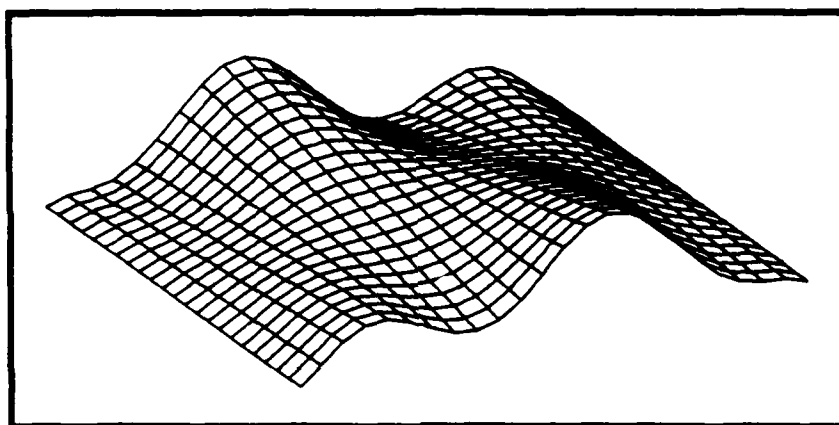


Figure 6-5. Orthographic View of the Fourth Mode Shape for Panel 1

Table 6-1 shows that STAGSC-1 provided good predictions for Panel 1's first five resonant frequencies. The largest percent difference was 8.41% for the first mode and the smallest was 5.39% for the fourth mode. For Panel 1, a graphical representation of the resonant frequencies are presented in Figure 6-6. In Figure 6-6, it can be seen how well STAGSC-1's results track the experimental findings. More interestingly, the following observation concerning the relationship between frequencies of antisymmetric and

symmetric modes was made. In Figure 6-6, the first mode is followed by a substantial increase in frequency to a relatively closely spaced second and third modes, followed by another substantial increase in frequency to a relatively closely spaced fourth and fifth modes. By referring to Figures 6-1 through 6-3, it can be seen that mode 1 was antisymmetric, modes 2 and 3 were symmetric, and modes 4 and 5 were antisymmetric. Therefore, transition from antisymmetric to symmetric modes and visa versa was accompanied by a large increase in frequency, whereas adjacent modes which are closely spaced in frequency were either both symmetric or both antisymmetric. Modes 6 and 7 were measured experimentally and both found to be symmetric and occur at 556 Hz and 569 Hz, respectively. Thus the trend was applicable up to the seventh mode. (No

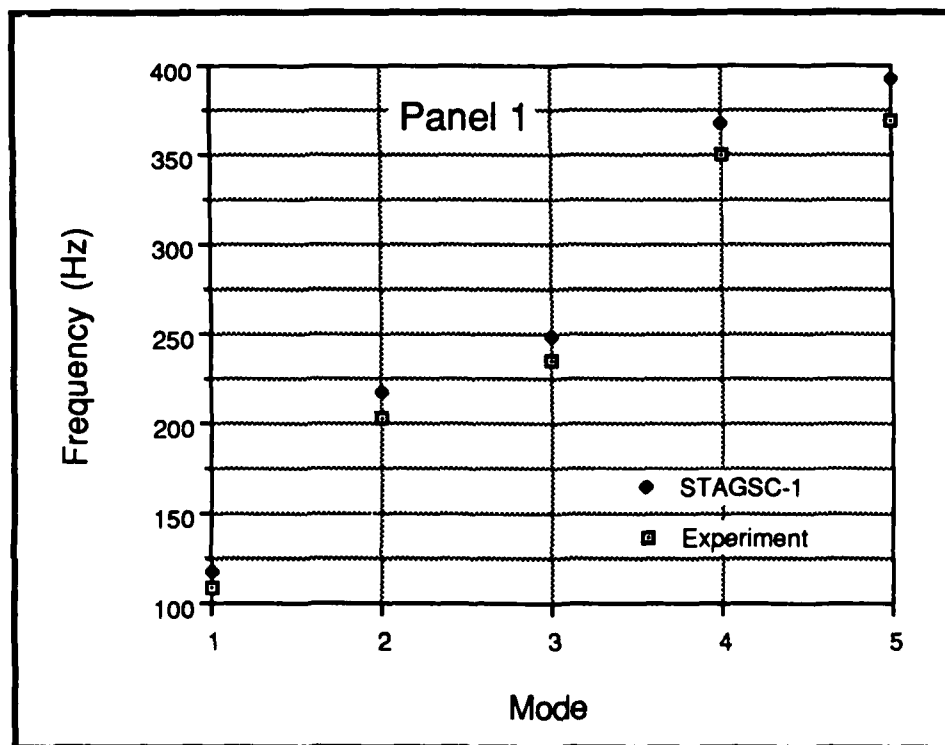


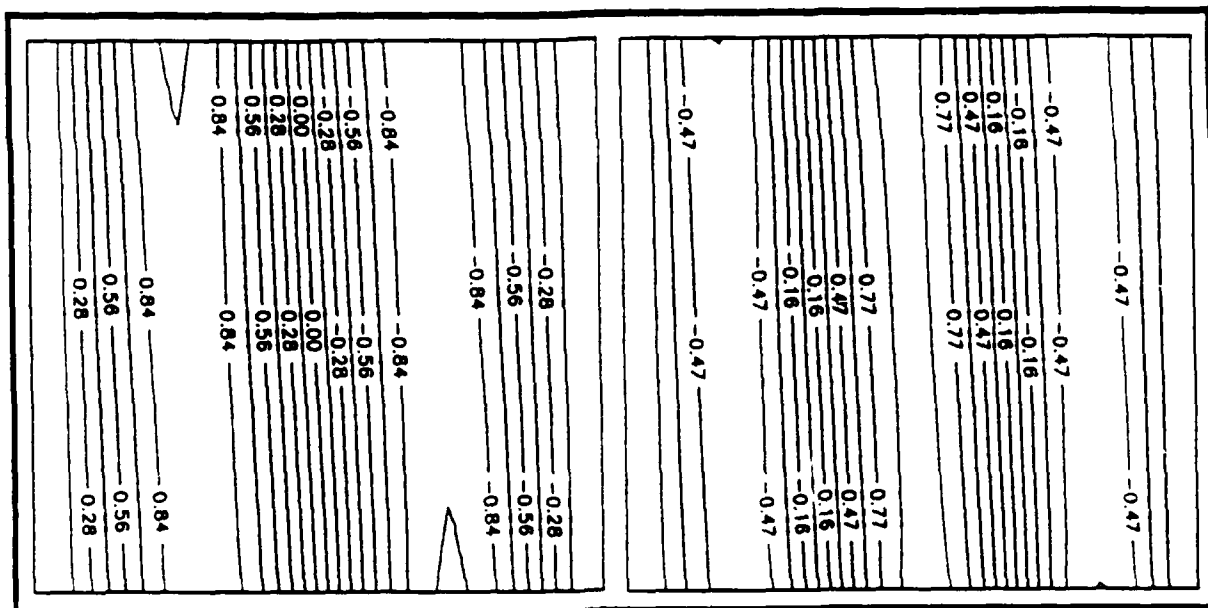
Figure 6-6. Frequency versus Mode for Panel 1

higher modes were recorded.) If one compares the results for Panel 1 with those obtained by Walley [42] and Cyr[13], the significant increase in overall stiffness which the fully clamped panel has over the CFCF condition (Chapter III) becomes obvious. Walley's and Cyr's fundamental modes for the solid panel were at 525 Hz and 516 Hz, respectively. For Panel 1 the first 5 modes were significantly below 500+ Hz, indicating a large reduction in overall panel stiffness due to the two free edges. A comparison of the experimental and analytical mode shapes is presented next.

STAGSC-1 did an excellent job of predicting the mode shapes for Panel 1, as shown in Figures 6-1 through 6-3. From Figure 6-1, it can be seen that the first modes for Panel 1 is antisymmetric. Inexperienced researchers may initially find this puzzling, especially if their past work has dealt primarily with flat plates. However, it turns out that asymmetry of the first mode is common behavior for the circular cylindrical panel geometry investigated by this study. Close inspection of the first two modes revealed a distinct tilt or bias in the vertical node lines towards the right side of the panel. This phenomena was less noticeable in the third and fourth modes and was not visible in the fifth mode. A similar occurrence was noted by Cyr [13:57] and he determined it was caused by a biasing towards the -45° ply (outer most angle ply) [13:58]. Based on Cyr's findings, the biasing of the vertical node lines for Panel 1 was believed due to ply layup and not the panel geometry or boundary conditions. Figures 6-2 and 6-3 also indicated an upward slanting (going left to right) of the horizontal node lines of modes 3 and 4. Originally, this was thought to be due to poor boundary conditions. The panel was remounted into the fixture but the same upward slant was still present. Later, it was found that the analytical data predicted this same slanting of the horizontal node line. Cyr had not documented any biasing of horizontal node lines for the fully clamped panel. However, this phenomena was hypothesized to also be caused by a biasing towards the -45° fiber direction. To confirm this hypothesis, the solid panel with a $[0/+45/-45/90]_s$ layup, was modeled using

STAGSC-1. Altering the ply layup did not affect the resonant frequencies. The resonant frequencies obtained from this run were identical to those presented in Table 6-1. Figures 6-7 and 6-8 show the first four mode shapes for the solid panel with this new layup. The fifth mode was not included because the node lines were nearly vertical and were not noticeably altered. Comparing Figures 6-7 and 6-8 with the previous mode shapes for Panel 1, indicated that the hypothesis was correct and that the biasing of the horizontal and vertical node lines was caused by the ply layup and was towards the fiber direction of the outer most angle ply. The reason the biasing was towards the outer most angle ply direction is because this ply was further than the inner angle ply from the middle surface of the laminate (by the thickness of the inner ply). This caused the outer most angle plies to have a slightly increased contribution to the bending-twisting stiffness of the panel which manifested itself by effecting the signs of the D_{16} and D_{26} terms of the Bending Stiffness Matrix, $[D]$ (see Chapter II). When the outer most ply was the -45° ply, the D_{16} and D_{26} coefficients were negative. Similarly, when the outer most ply was the $+45^\circ$ ply, the D_{16} and D_{26} coefficients were positive. The $[D]$ matrix is a key element of the moment equations (see Equation 2.21) and therefore the difference in biasing between the two ply layups was caused by the variation in the moment equations due to the different signs for the D_{16} and D_{26} terms. It should be stated that this biasing effect was noticeable because the panel thickness for this study was very small (0.04 inches). As panel thickness increases the biasing effect should rapidly diminish.

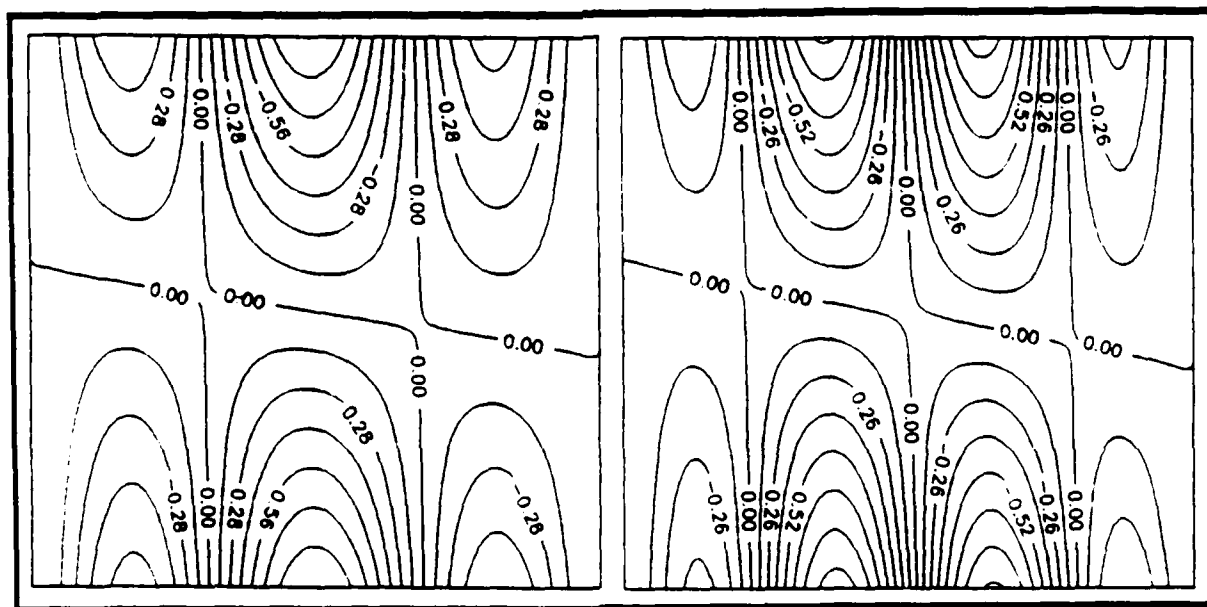
This section has presented the results for Panel 1 (solid panel). This panel will be used as a baseline for comparison with the remaining panels with centered cutouts. Panels with 2" square cutouts are discussed in the next section.



Mode 1

Mode 2

Figure 6-7. First and Second Mode Shapes for Panel With $[0/+45/-45/90]_s$ Layup



Mode 3

Mode 4

Figure 6-8. Third and Fourth Mode Shapes for Panel With $[0/+45/-45/90]_s$ Layup

B. Panels With 2" Square Cutouts

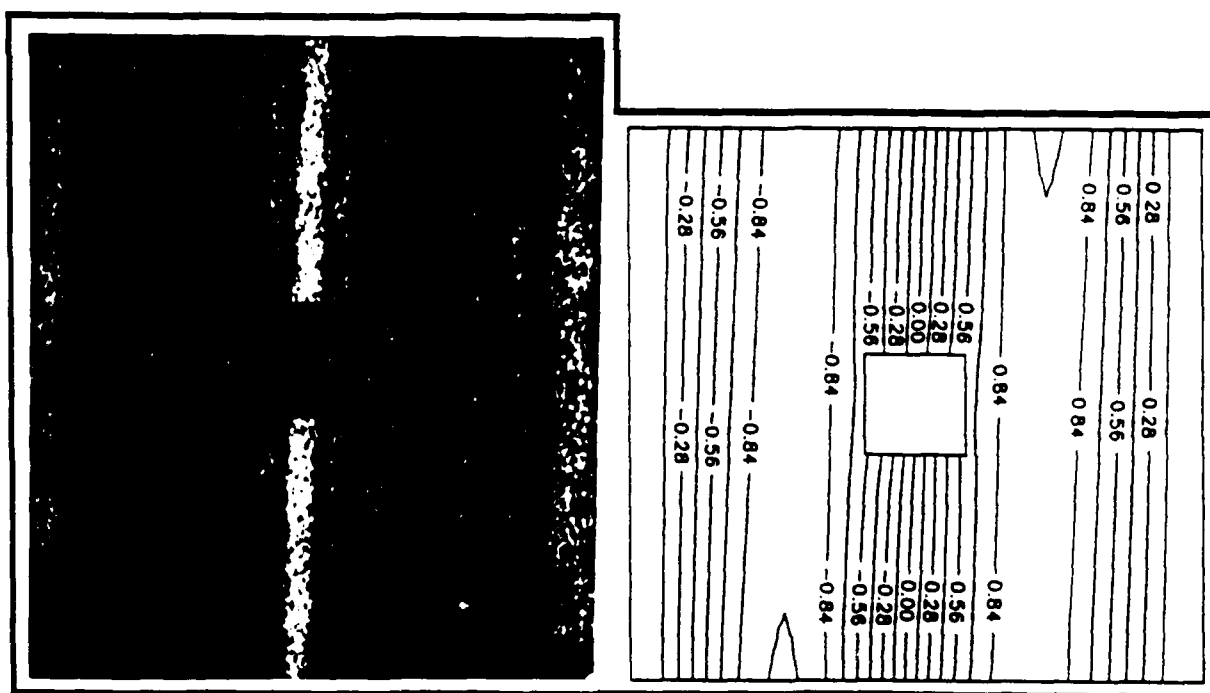
The panels with 2 inch square cutouts correspond to Panels 2, 3, 4, 5, and 6 as described in Table 3-2. This section is broken up into three parts. First, the panel with the centered cutout (Panel 2) is discussed. Next, the results for the two panels with circumferentially eccentric cutouts (Panels 3 and 4) are presented. Finally, results are given for the two panels with tangentially (axially) eccentric cutouts (Panels 5 and 6).

(1) Panel 2. This panel contained a centered 2 inch square cutout. The resonant frequencies for Panel 2 are presented in Table 6-2, followed by the mode shapes in Figures 6-9 through 6-11. Comparing experimental and analytical frequencies for Panel 2, it can be seen that the two methods correlated well, although the percent differences did increase in most cases as compared to Panel 1. The first mode was the only mode for which the percent difference decreased. As shown in Table 6-2, STAGSC-1 consistently predicted frequencies which were higher than those obtained experimentally. Figure 6-12 contains a graphical representation of the experimental and analytical frequencies for Panel 2. (Figure 6-12 is also representative of the trend found for all panels with 2" square cutouts, therefore similar plots for Panels 3 through 6 will not be included.) The same relationship between symmetric and antisymmetric modes, as noticed for Panel 1, was present in Panel 2. Inspection of Figures 6-9 through 6-11 revealed that STAGSC-1 did a very good job of predicting the mode shapes for Panel 2. As with Panel 1, Panel 2 exhibited the same biasing of the vertical and horizontal node lines due to the -45° ply. This effect was most predominate in the vertical node lines of modes 1 and 2 and in the horizontal node lines of modes 3 and 4.

Comparing Panel 2 to Panel 1, the cutout caused the experimental frequencies to change by -0.1%, +1.1%, -2.2%, -6.0%, and -2.2% for modes 1 through 5, respectively.

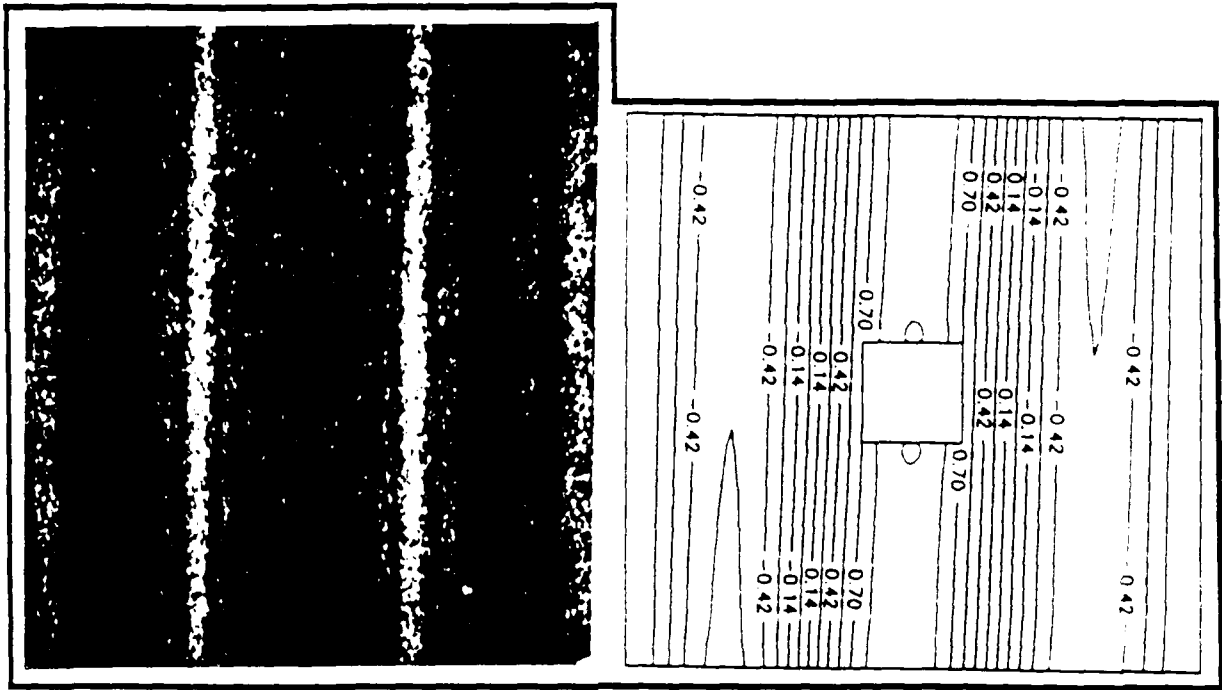
Table 6-2. Comparison of Experimental and Analytical Resonant Frequencies for Panel 2

Mode	Experiment (Hertz)	STAGSC-1 (Hertz)	Percent Difference
1	108.6	117.32	8.03
2	205.6	220.44	7.22
3	230.0	247.36	7.55
4	328.3	357.36	8.85
5	361.2	386.81	7.09

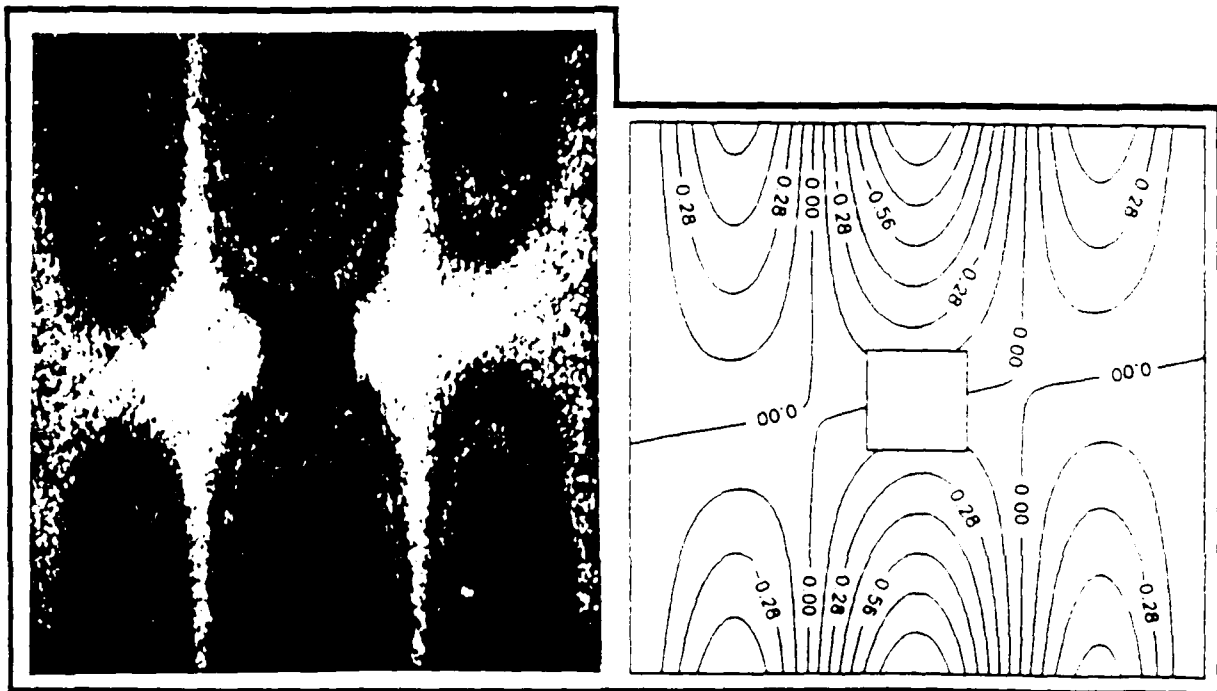


Mode 1

Figure 6-9. First Mode Shape for Panel 2

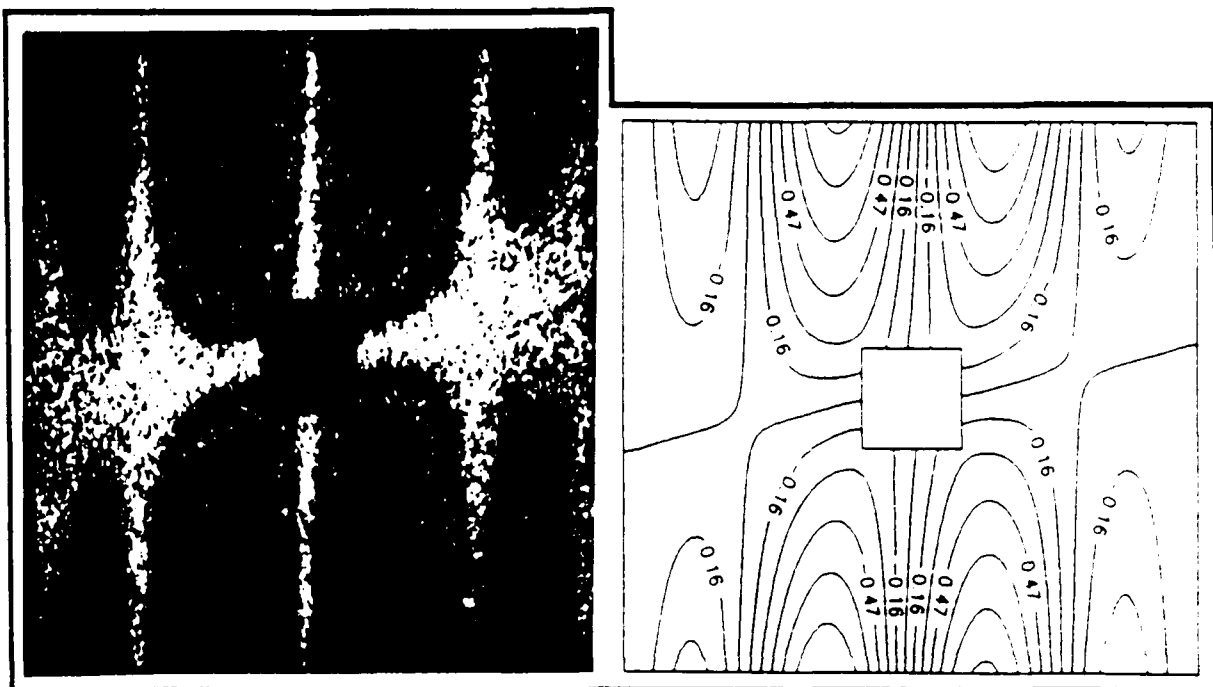


Mode 2

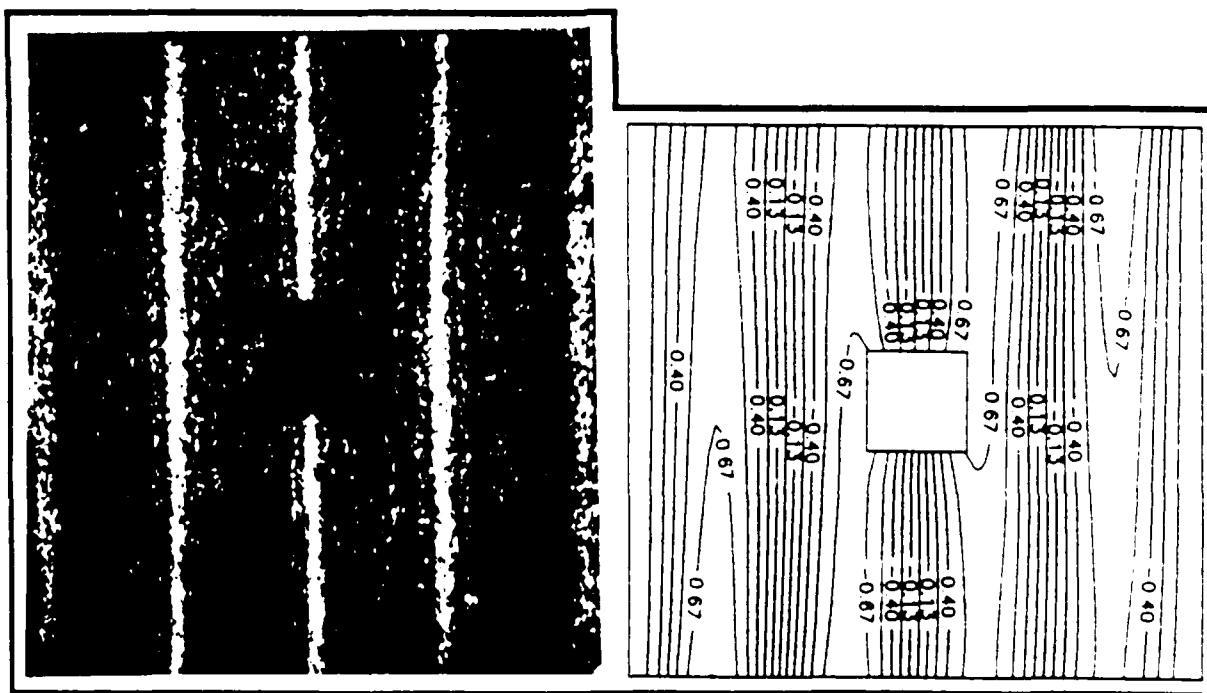


Mode 3

Figure 6-10. Second and Third Mode Shapes for Panel 2



Mode 4



Mode 5

Figure 6-11. Fourth and Fifth Mode Shapes for Panel 2

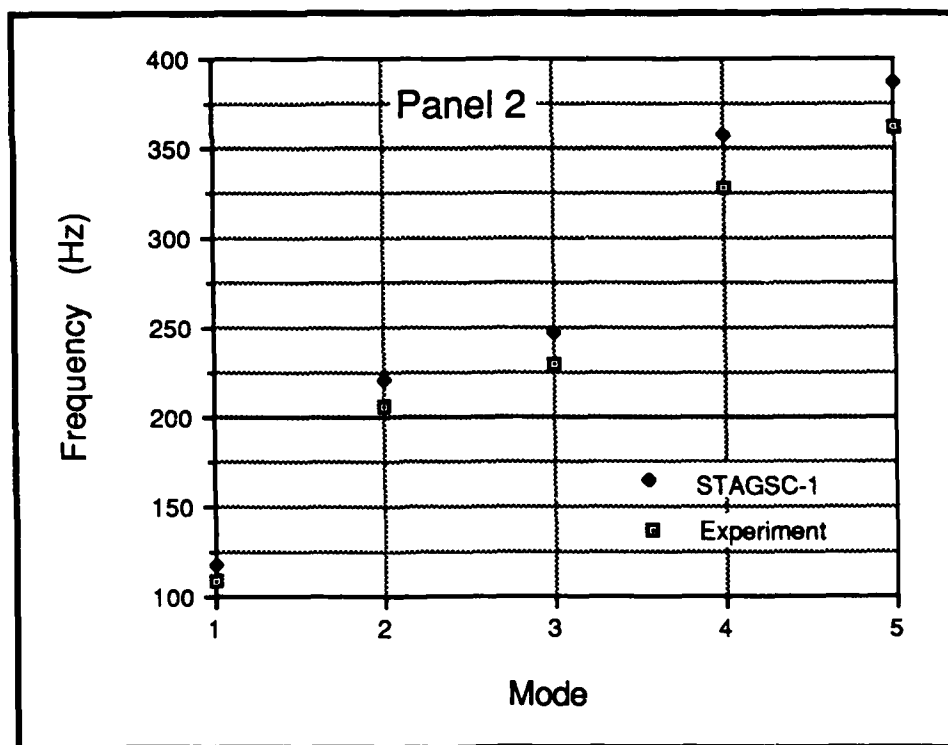


Figure 6-12. Frequency versus Mode for Panel 2

The same comparison for the analytical frequencies resulted in changes of -0.4%, +1.4%, -0.2%, -3.0%, and -1.6% for modes 1 through 5, respectively. Although not by the same magnitude, STAGSC-1 predicted increases and decreases in resonant frequencies consistent to those obtained from experimental data. These differences are shown graphically in Figures 6-13 and 6-14. The additional data presented in these figures, which as not be previously discussed, will be discussed in the next two sections. Figures 6-13 and 6-14 are presented now to provide a graphical tool which the reader can use for comparison of the panels as they are discussed (instead of after they have been discussed). It should be noted that panel to panel frequency variations for any two panels of similar geometry could conservatively be one percent (based on experience not actual data) [26]. Therefore, frequency variations between panels may not be entirely due to the

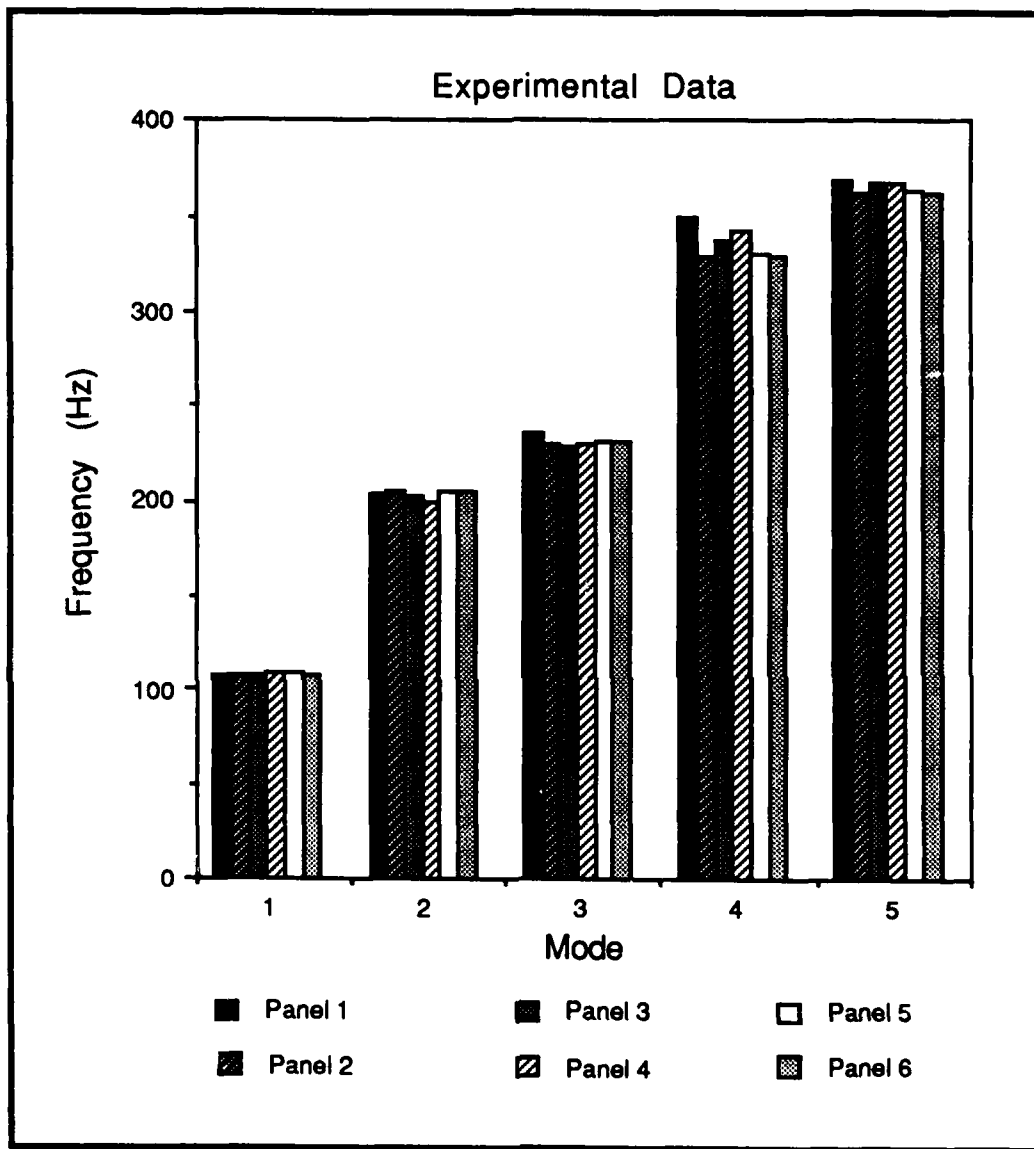


Figure 6-13. Experimental Frequency versus Mode for Panels 1, 2, 3, 4, 5, and 6

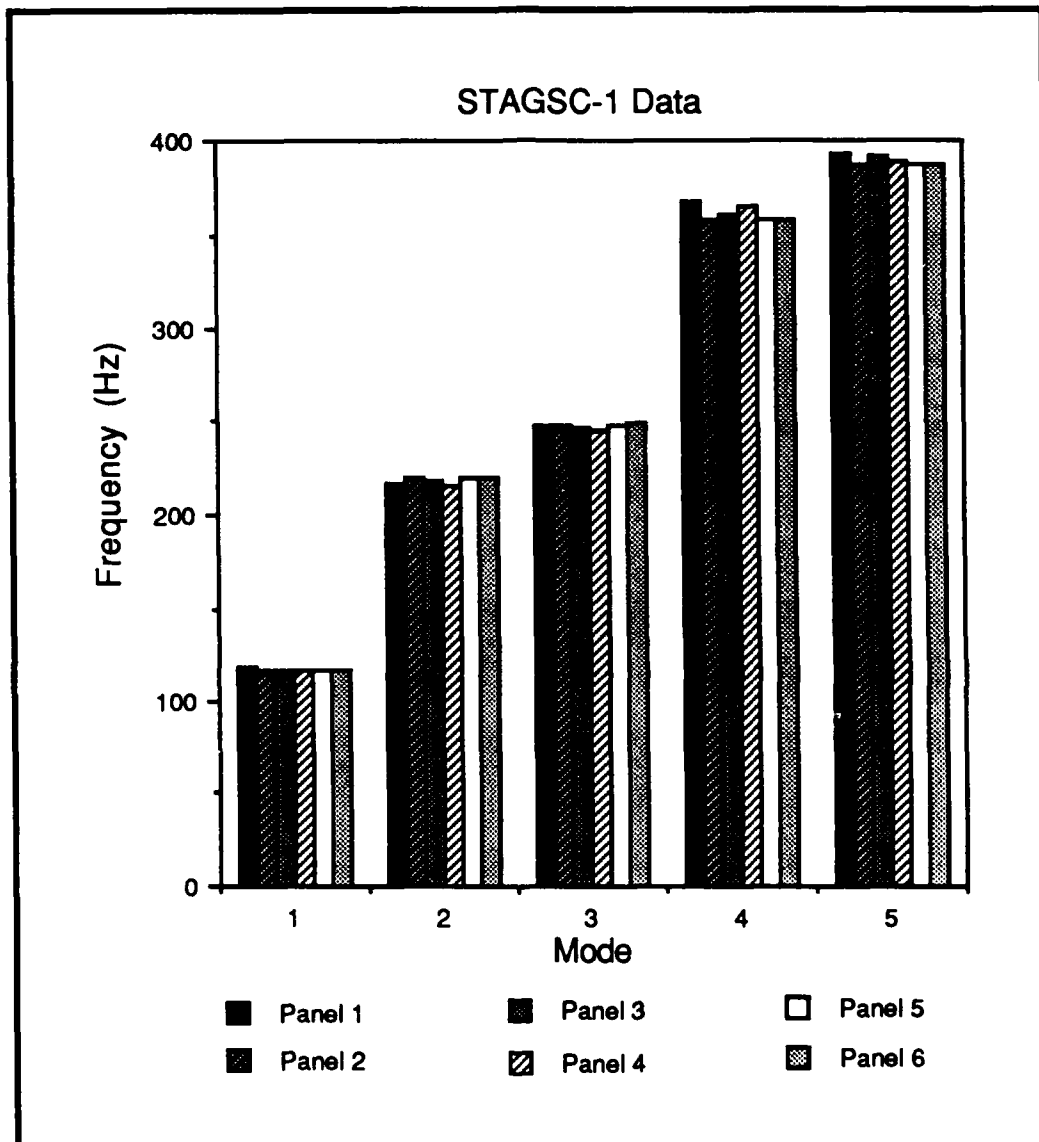


Figure 6-14. Analytical Frequency versus Mode for Panels 1, 2, 3, 4, 5, and 6

cutout effects, but may also be due to changes in density, thickness, and other similar minor imperfections. Also, experimental error could be a factor (eg., inconsistency in boundary conditions between panels due to fixture). For minor frequency variations of less than one percent, it was impossible to distinguish conclusively whether the changes were caused by the cutouts or panel variations. For purposes of this thesis, the analytical frequency variations (trends) were used to help determine whether small changes in frequency were due to "real" behavior caused by the cutouts or anomalous behavior resulting from experimental error and/or panel variations. Because the same trends were noticed experimentally and analytically for Panel 2, the frequency variations are considered "real" panel behavior resulting from the cutout. Therefore, the 2" cutout caused the second mode frequency to slightly increase and the frequencies for all remaining modes to decrease. Keep in mind, the largest variation was a decrease in the fourth mode frequency by 6%. Thus, only minor changes in frequency were noticed. Likewise, when comparing the mode shapes for Panels 2 to those for Panel 1, only small changes were visible. In fact, the first, second, third, and fifth mode shapes indicated no detectable changes even though the first, third, and fifth modes had node lines which past through the cutout. This was a strong indication that the discontinuity caused by the 2" square cutout had little effect on overall panel stiffness to mass ratio (K/M) [26]. The fact that the horizontal node line for mode 3 was wider for Panel 2 than that observed for Panel 1, indicated that different excitation amplitudes were used when the two mode shapes were recorded and was not related to cutout effects. Although slight, the fourth mode shape did show distortion. Without the cutout, the two center lobes on both the top and bottom of the panel passed near where the corners of the cutout would be. With the cutout, these lobes were "drawn" towards the cutout (since the cutout had zero stiffness) as shown in Mode 4 of Figure 6-11.

An interesting observation was made by comparing Panel 2's results to a similar fully clamped panel with a 2 inch square cutout as investigated by Walley [42]. Walley found

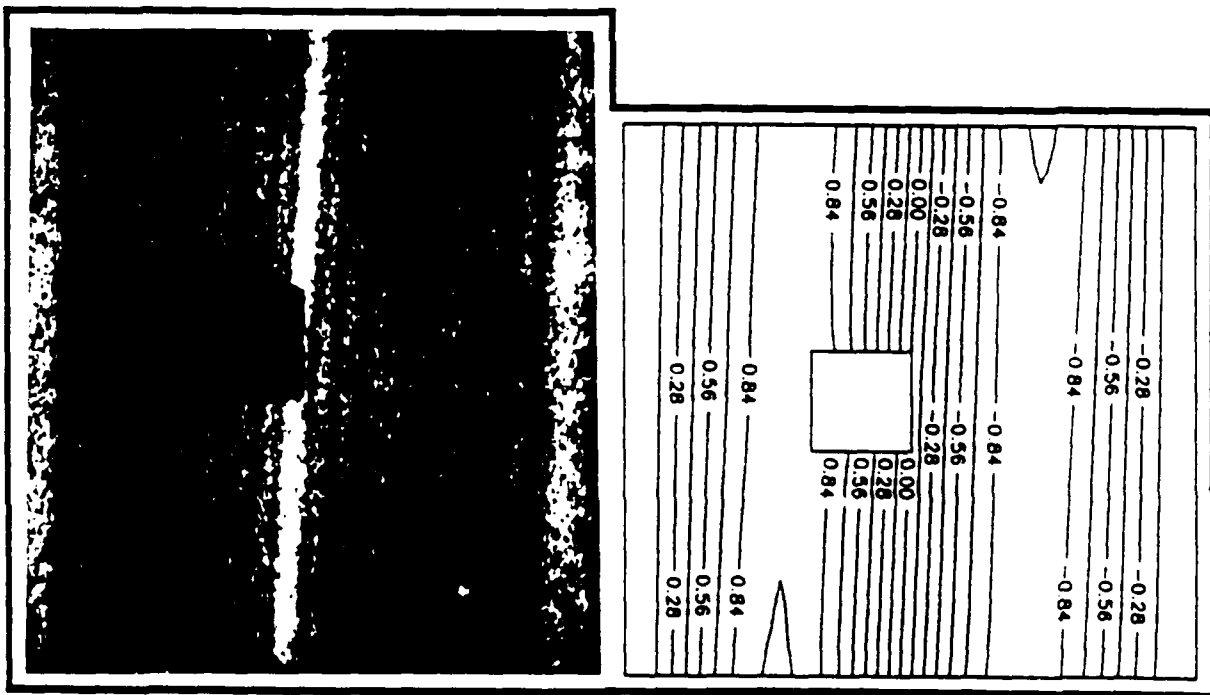
that the 2 inch cutout caused a reduction in the experimental frequency for the first five modes of -2.9%, +2.2%, -2.6%, -0.7%, and -12.3%, respectively. Interestingly enough, the second mode for the fully clamped plate was also the only one which increased. Except for the fifth mode, the frequency changes for the fully clamped panel were relatively small as observed for in Panel 2. For Panel 2 and the panel investigated by Walley, the location of the centered cutout corresponded to the center of an antinode (region of relatively large velocity, displacement, and bending moment) for mode 2 while the cutout was located on a node line(s) for all other modes. This suggested that at an antinode region the loss of mass, as opposed to stiffness, had a preponderant effect for the 2" square cutout. That is, the K/M ratio increased causing frequency to increase as well. (As cutout size increases, the relationship between mass and stiffness should not be expected to be linear and a totally opposite effect may appear for larger cutouts.) Walley also noticed a phenomena called mode switching, in which the mode shapes for the third and fourth modes switched order when the cutout was introduced. As previously mentioned, the 2 inch cutout only caused a slight variation in the fourth mode shape for Panel 2.

The panels with circumferentially eccentric 2 inch cutouts will be discussed in the next section. Their results will be compared to Panel 2.

(2) Panels 3 and 4. These panels contained 2 inch square cutouts which had been eccentrically located in the circumferential direction (Figure 3-3). The amounts of eccentricity were 1 inch and 2 inches for Panels 3 and 4, respectively. A comparison of the experimental and analytical resonant frequencies for Panel 3 is found in Table 6-3 and a comparison of the corresponding mode shapes can be found in Figures 6-15 through 6-17. Similar comparisons for Panel 4 are found in Table 6-4 and in Figures 6-18 through 6-20. Graphically, the frequencies for Panels 3 and 4 are presented in Figure 6-13 for the experimental results and in Figure 6-14 for the analytical results. STAGSC-1 did a

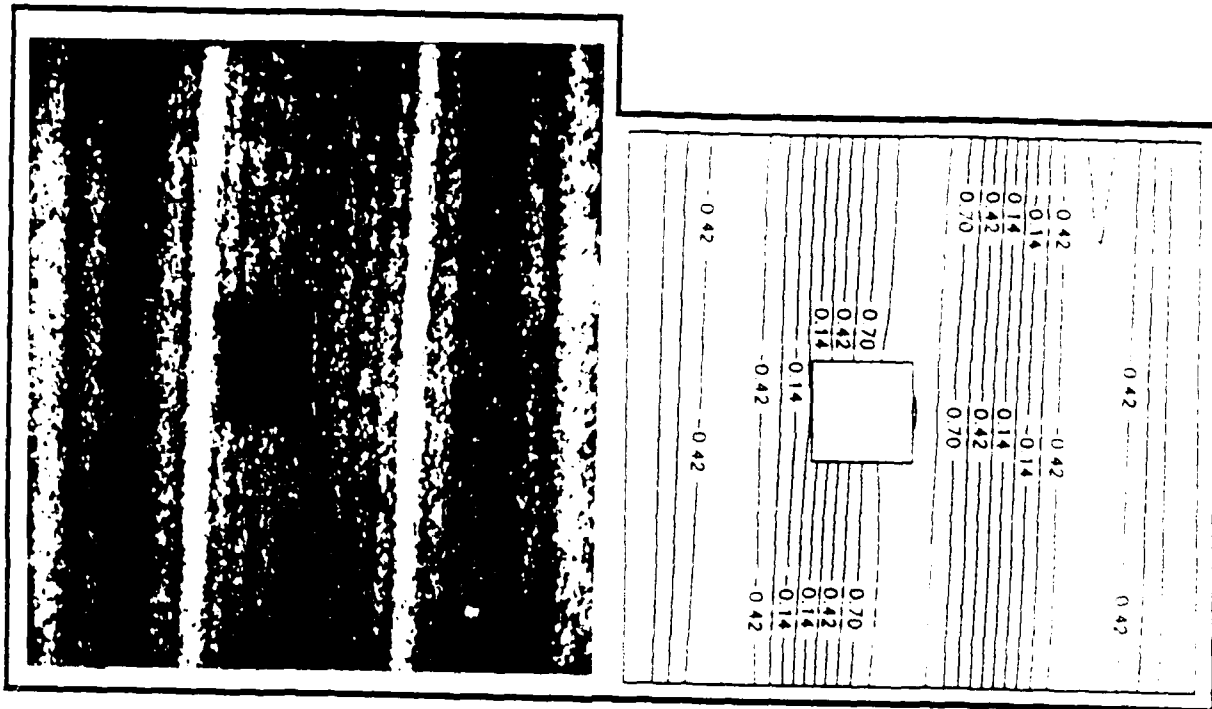
Table 6-3. Comparison of Experimental and Analytical Resonant Frequencies for Panel 3

Mode	Experiment (Hertz)	STAGSC-1 (Hertz)	Percent Difference
1	108.7	117.35	7.96
2	202.4	218.29	7.85
3	228.9	246.02	7.48
4	336.8	361.03	7.19
5	366.4	390.88	6.68

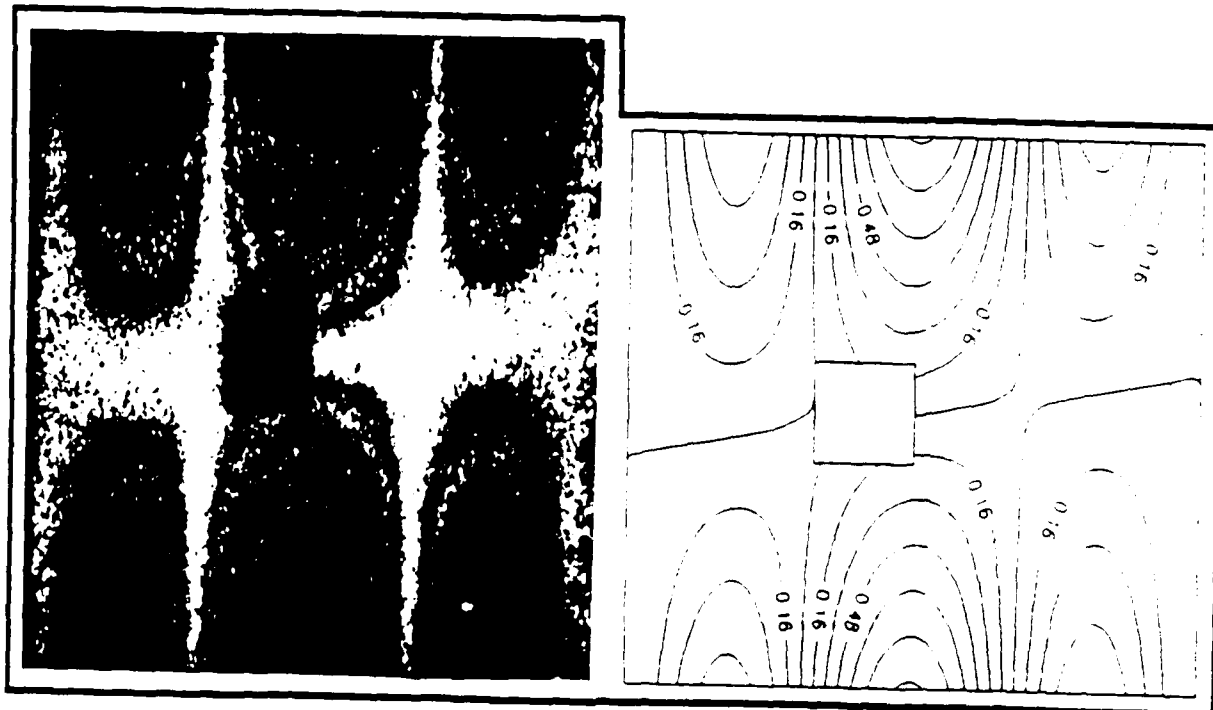


Mode 1

Figure 6-15. First Mode Shape for Panel 3

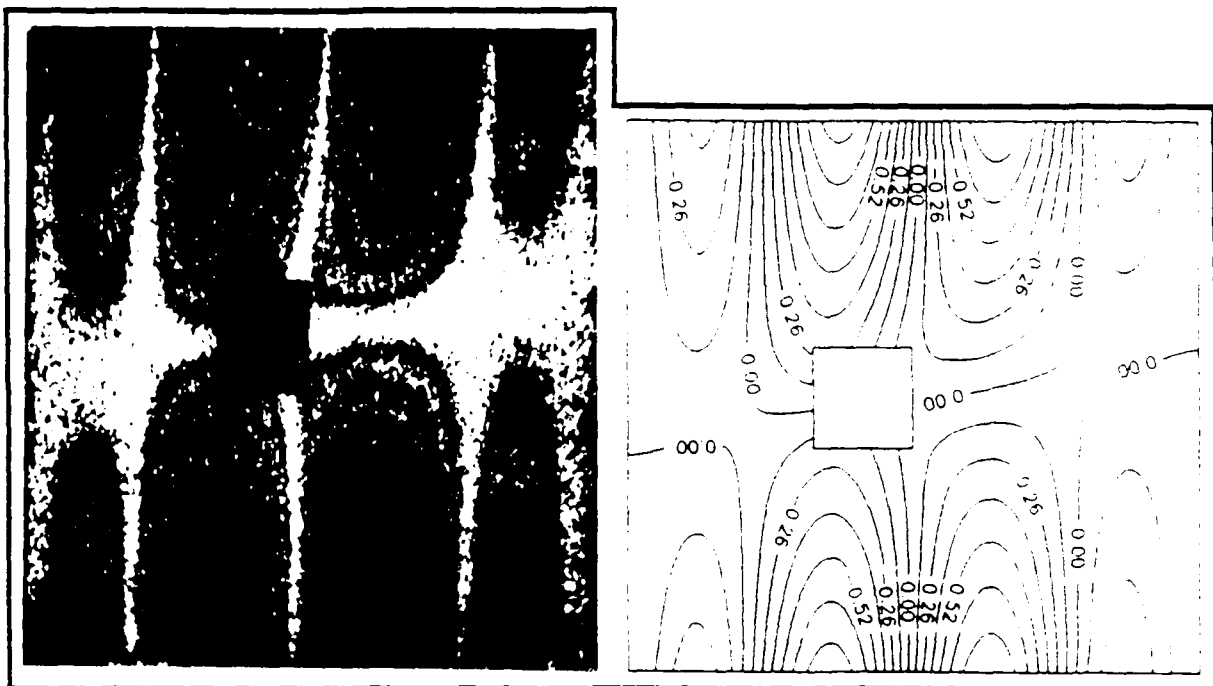


Mode 2

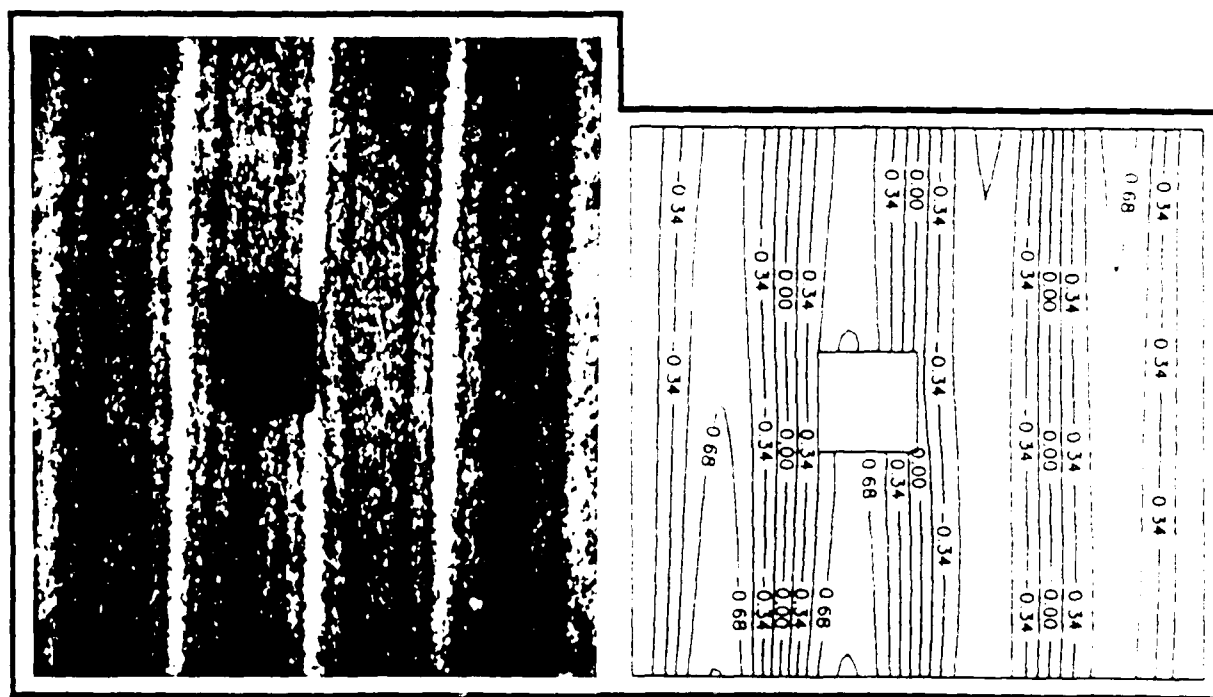


Mode 3

Figure 6-16. Second and Third Mode Shapes for Panel 3



Mode 4

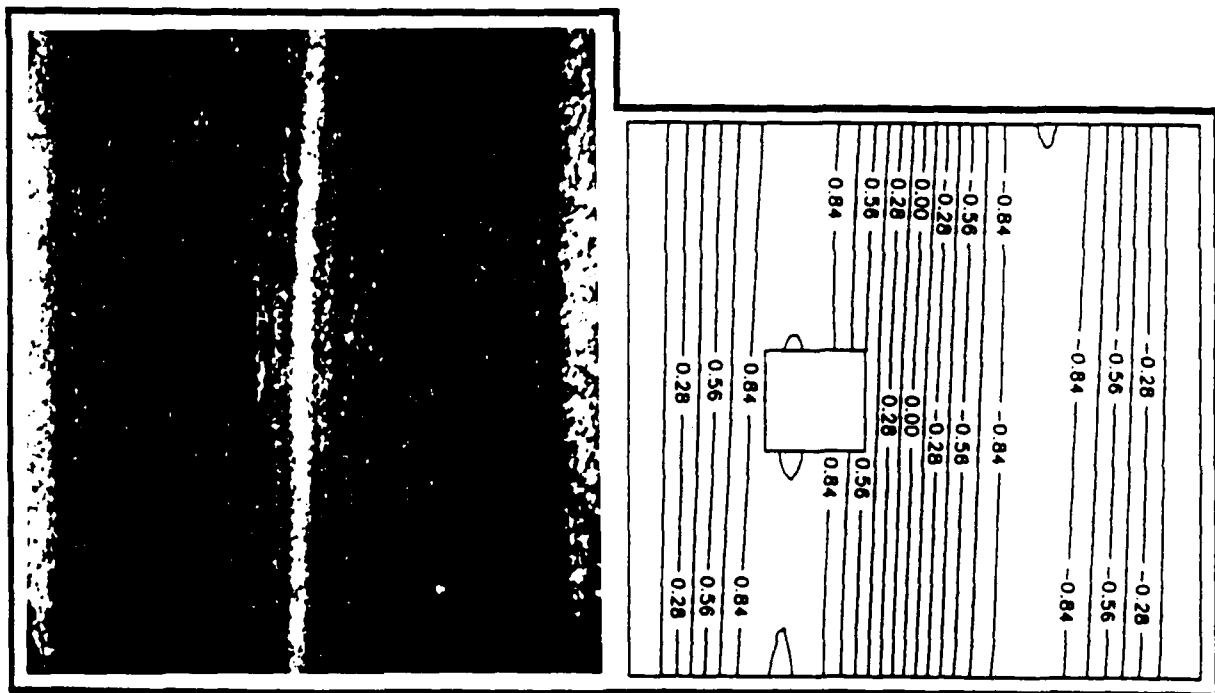


Mode 5

Figure 6-17. Fourth and Fifth Shapes for Panel 3

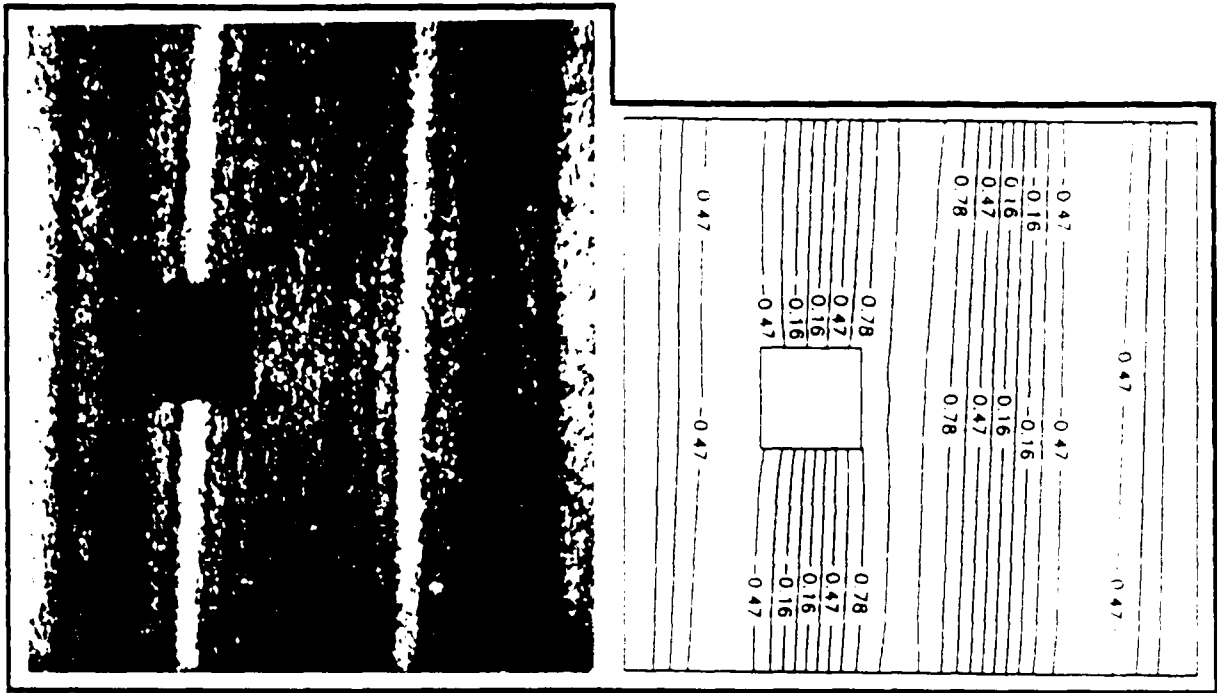
Table 6-4. Comparison of Experimental and Analytical Resonant Frequencies for Panel 4

Mode	Experiment (Hertz)	STAGSC-1 (Hertz)	Percent Difference
1	109.1	117.59	7.79
2	200.1	215.10	7.50
3	229.5	245.05	6.77
4	341.7	364.59	6.70
5	365.9	389.43	6.43

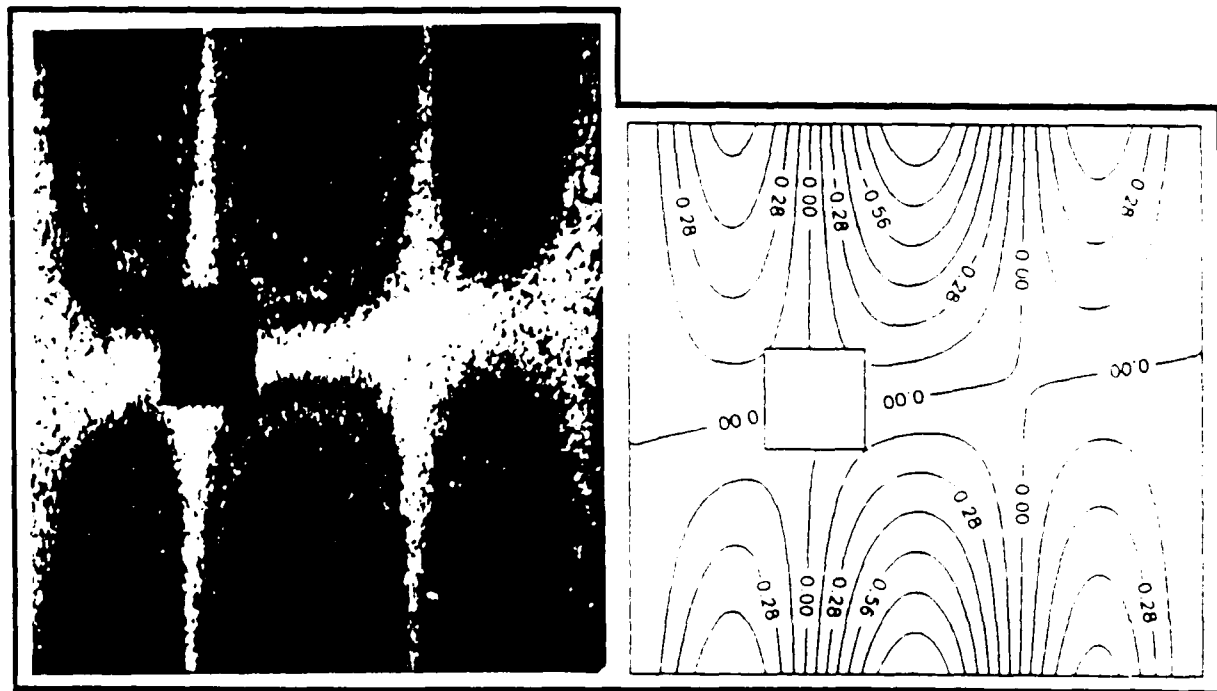


Mode 1

Figure 6-18. First Mode Shape for Panel 4

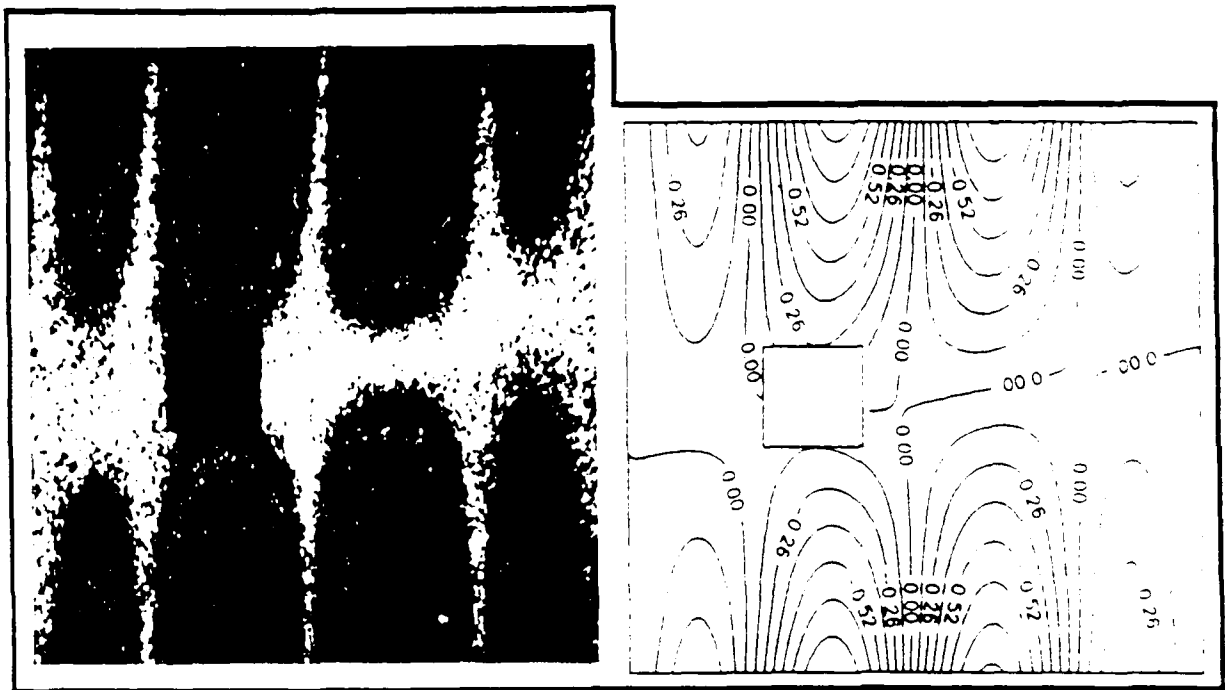


Mode 2

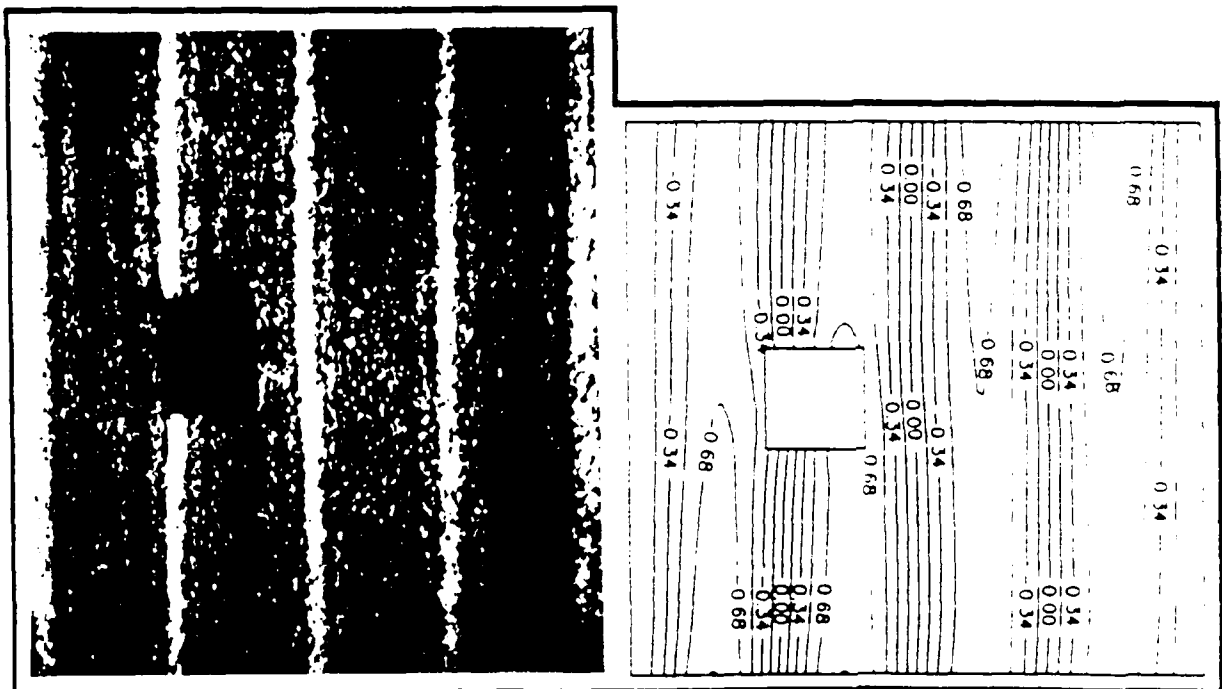


Mode 3

Figure 6-19. Second and Third Mode Shapes for Panel 4



Mode 4



Mode 5

Figure 6-20. Fourth and Fifth Shapes for Panel 4

good job of predicting the natural frequencies with the largest percent difference for these panels being 7.96%. As before, STAGSC-1 consistently predicted higher frequencies than those obtained through experimentation. Figures 6-13 and 6-14 show that the frequency variations (compared to Panels 1 or 2) caused by the 1 inch and 2 inch circumferential eccentricity values were small.

Comparison of the mode shapes in Figures 6-15 through 6-20 showed that the experimental and analytical data correlated well. For both panels the same basic mode shapes, seen in Panels 1 and 2, were present. The biasing towards the -45° ply direction, as mentioned for the previous panels was present in Panels 3 and 4 although a new observation was made. Close inspection of the fifth mode shape for Panel 3, shows a biasing or tilting of the vertical node lines which was not apparent in Panels 1 and 2; however, as circumferential eccentricity was increased (Panel 4), the biasing became no longer observable. No explanation was available as to why the fifth mode behaved in this manner. Compared to Panels 1 and 2, very little distortion was observed for the mode shapes of Panels 3 and 4. In most cases, the node lines remained unchanged for the cutout locations given by Panels 3 and 4. The most notable distortion was in the fourth mode for Panel 3. The loss in stiffness, due to the cutout, caused the two large lobes on the right side of the cutout to distort in the direction of the discontinuity (cutout). This resulted in a bending of the inward edges of the center node line in the direction of eccentricity (see Mode 4 of Figure 6-17). As the cutout was moved further to the left (Panel 4), the center of the panel regained stiffness and the mode shape resumed the same pattern that was observed for the solid panel (Mode 4 of Figure 6-3). The fact that neither the frequencies nor the mode shapes changed significantly with the circumferential eccentricity introduced, indicated that the overall stiffness to mass ratio of the panel was not particularly sensitive to the circumferential eccentricity of the 2 inch cutout. More precisely it may be stated that the 2 inch cutout had little effect on the stiffness to mass ratio, and eccentrically locating the

cutout did not substantially alter this effect. Changes did occur, but it should be kept in mind that these changes amounted to only minor variations in frequencies and mode shapes.

The circumferential eccentricity effects of the 2" square cutout can best be visualized graphically as shown in Figure 6-21. Figure 6-21, compares Panels 2, 3, and 4. The following observations are based on the data presented in Figure 6-21 and are not meant to imply panel behavior for circumferential eccentricities larger than 2 inches. Also, to establish trends, the data was fitted with a least square curves; however, the reader should be aware that the panel's behavior between the eccentricities investigated may not be represented precisely by these curves. In Figure 6-21, the first and second mode frequencies were shown to be insensitive to circumferential eccentricity of the 2 inch square cutout. The second mode frequency decreased slightly with increasing cutout eccentricity. This trend was nearly linear and resulted in decreases in experimental frequency of 1.6% and 2.7% for Panels 3 and 4, respectively. The fourth mode frequency increased with increasing circumferential eccentricity and experienced the largest sensitivity to the eccentricity. Interestingly, the fourth mode also proved the most sensitive to the introduction of the centered 2 inch cutout, although then the effect was a decrease in frequency due to circumferential eccentricity. The fourth mode increase in frequency was also nearly linear and resulted in experimental frequency increases of 2.6% and 4.1% for Panels 3 and 4, respectively. The fifth mode showed an initial increase in experimental frequency of 1.4% for Panel 3 as compared to Panel 2. This was followed by a slight decrease for Panel 4. The fifth mode experimental frequency for Panel 4 was 1.3% higher than for Panel 2 with the centered cutout. Although consistently high, STAGSC-1 predicted the frequency trends cause by the circumferential eccentricity quite well, as indicated in Figure 6-21. The following observations attempt to relate the location of the 2" cutout, with respect to node lines and antinodes of a given mode, with the frequency trends

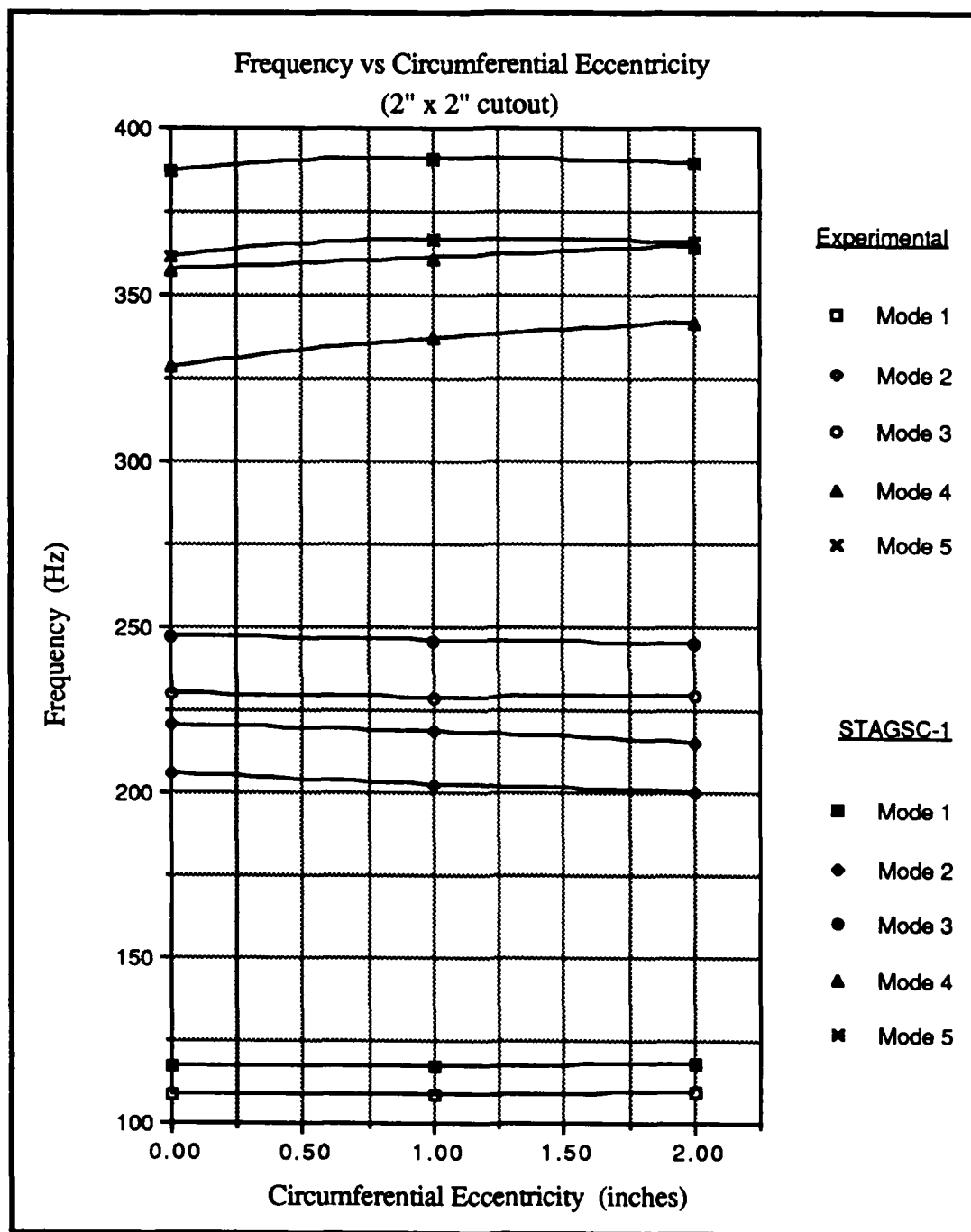


Figure 6-21. Frequency versus Circumferential Eccentricity for 2" Square Cutout

presented in Figure 6-21. The factors which determine how a cutout will effect the dynamic response of a structure for a given mode are quite complex and often complete explanation is not possible. Only a simplified stiffness to mass ratio concept, as previously discussed, was considered when making observations. The reader should be aware that the following observations (including similar observations for all panels) could only be made after the actual frequency trends were known.

The first mode frequency is only slightly decreased by the introduction of the 2 inch square cutout. For the first mode, the node line passes near the middle of the centered 2 inch cutout as shown in Figure 6-9 (Panel 2). As circumferential eccentricity was introduced, the cutout moved away from the node line towards an antinode. As this occurred, the cutout moved into a region where both the effects of bending as well as local velocities of the panel increase. Therefore, the loss of stiffness would be expected to cause a decrease in frequency, while simultaneously the loss of mass should cause the frequency to increase. For the first mode, these two phenomena appear to have a cancelling effect which resulted in a relative insensitivity of the first mode frequency to cutout location (very slight increase observed). Also, for the first mode the $1/2$ waves (regions of displacement between node lines) were considerably larger than the discontinuity created by the cutout. This allowed the effects of the larger $1/2$ wave pattern to dominate any discontinuity effects from the cutout [26]. Therefore, circumferential eccentricity of the 2 inch cutout had a negligible effect on the first natural frequency and mode shape of the panel.

The second mode frequency increased slightly when the 2 inch cutout was introduced in Panel 2. Originally for the second mode, the cutout was located at an antinode (region where large bending moment and high velocities are present). The increase in second mode frequency indicated that percentage wise, the 2 inch cutout affected (decreased) the mass more so than the stiffness. As the circumferential eccentricity is increased, the center of the cutout moves closer to a node line resulting in a decrease in frequency. One possible

explanation is that in the vicinity of a node line (for the second mode), the loss of stiffness contributes more to panel dynamic behavior than the loss of mass. For mode 1, the cutout moved from a node line towards an antinode and the frequency was essentially unaffected. For mode 2, the cutout moved from an antinode towards a node line and the frequency decreased (remember the loss of mass will have less of an effect near node lines). Thus, the loss of stiffness for mode 2 was more pronounced than for mode 1. This was apparently due to the increased number of half waves in the circumferential direction for mode 2, which resulted in a more severe bending situation. For a given cutout size, the influence of the cutout will tend to increase as the half wave size decreases [26]. Overall, the circumferential eccentricity of the 2 inch cutout caused a slight decrease in the second mode frequency and had no visible effect on the mode shape.

The third mode resonant frequency decreased for the centered 2 inch cutout and then remained relatively unchanged for increasing circumferential eccentricity. The cutout was first introduced on a node line between regions of relatively large displacement. With the cutout on the node line the loss of mass contributed very little to panel dynamics. Thus, the reduction in stiffness was predominate and the third mode frequency reduced. Although the two center lobes represented regions of relatively large displacements, axial lines running between the two lobes remained fairly straight due to the free edge condition (Figure 6-4). Therefore, the frequency was only reduced by a small amount. As the cutout was moved circumferentially, it remained on the horizontal node line (minimizing mass effects) but moved towards an area in which two directional bending was present. The fact that the third mode frequency did not increase indicated that the panel's sensitivity to the loss of stiffness did not change significantly along the horizontal node line. Therefore, circumferential eccentricity of the 2 inch cutout, as shown in Figure 6-21, had only a minor effect on the third mode natural frequency and mode shape.

For the fourth mode, the centered 2 inch square cutout was located at the intersection of the center vertical and horizontal node lines. This region of the panel experienced complex bending behavior (bending in two directions) due to the fact that half waves and quarter waves were present in the circumferential and tangential directions, respectively. Also, as shown by the large number of fringe lines for the four lobes nearest the cutout, these regions were undergoing relatively large displacements. Figure 6-5 helps visualize the complex bending in this region of the panel. Although, axial lines between the top and bottom lobes remained fairly straight, twisting occurred at the center of the panel since adjacent lobes were out of phase. The loss of stiffness in this region of the panel accounted for the 6.0% loss in the fourth mode resonant frequency for the centered cutout. This represented the largest loss in frequency and was apparently due to the cutout (loss of stiffness) interrupting the two directional bending which occurred at the center of the panel for this mode. As the circumferential eccentricity was increased, the cutout moved away from the center of the panel allowing the stiffness to be restored and therefore for the fourth mode frequency to increase. The outer most lobes of the fourth mode frequency were areas of relatively small displacement which led to a less severe state of bending away from the center of the panel. The effect of the reduction in mass was believed minimal since the cutout follows the horizontal node line (region where panel motion was small) for all circumferential eccentricity values. Overall, circumferential eccentricity of the 2 inch cutout resulted in an increase in the fourth mode natural frequency.

The fifth mode for the panel with the two inch centered cutout, contained a node line which passed through the middle of the cutout. The introduction of the cutout caused the fifth mode frequency to decrease. Because the cutout was on a node line, the loss of stiffness apparently contributed more to panel dynamics than did the loss of mass. The difference in frequency behavior between the fifth and first modes was believed due to the increase in panel bending (number of half waves) for the fifth mode. This caused the loss

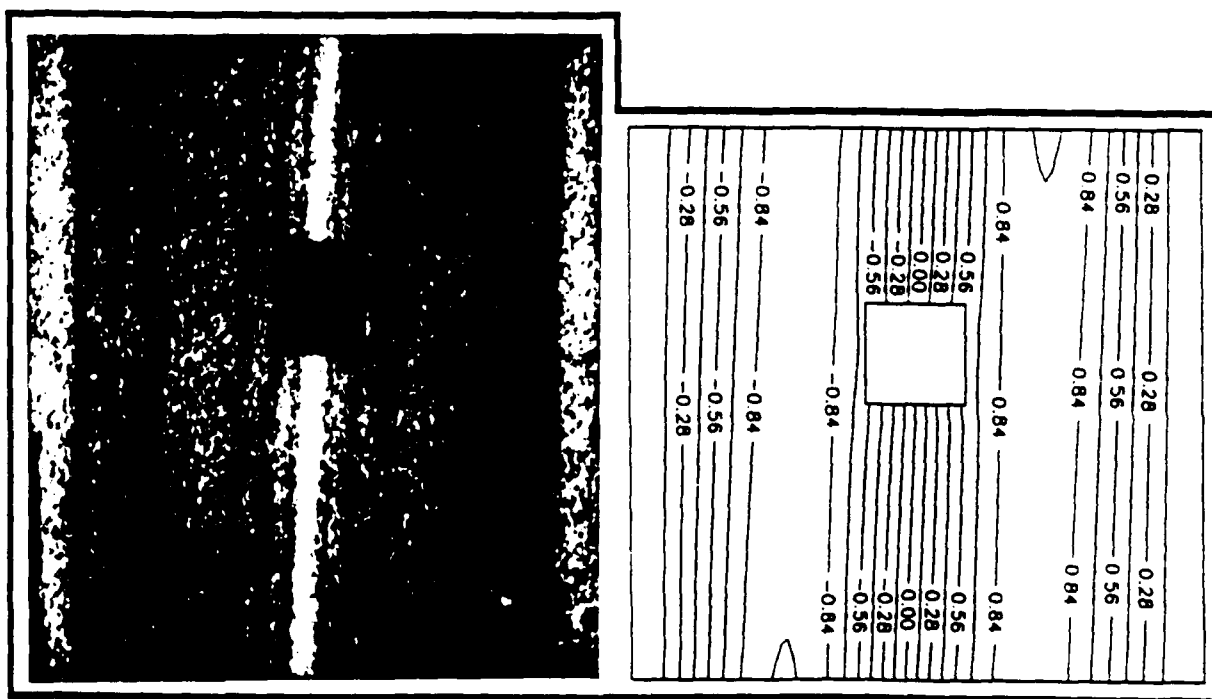
of stiffness to be more predominate. Also, the size of the half waves for the fifth mode allowed the cutout to span the majority of a half cycle and therefore this region would normally be exposed to a significant amount of bending with each end of the cutout region being bent simultaneously in opposite directions. As circumferential eccentricity was increased, the cutout first moved to a position adjacent to a vertical node line. The loss of the cutout's mass now contributed more to the panel's dynamics and resulted in an increase in frequency. When the cutout was moved to the two inch circumferential eccentricity location, the cutout was now adjacent to another node line but still within the same half wave. With respect to panel dynamics, the two eccentricity values appeared similar and therefore the fifth mode frequency remained relatively constant. Therefore, circumferential eccentricity of the 2 inch cutout, initially increased for the 1 inch eccentricity value and then remained relatively constant at the 2 inch value.

The panels with tangentially eccentric 2 inch cutouts will be discussed in the next section. Their results will be compared to Panel 2.

(3) Panels 5 and 6. These panels contained 2 inch square cutouts which had been eccentrically located in the tangential direction (Figure 3-3). The amounts of eccentricity were 1 inch and 2 inches for Panels 5 and 6, respectively. A comparison of the experimental and analytical resonant frequencies for Panel 5 is found in Table 6-5 and a comparison of the corresponding mode shapes can be found in Figures 6-22 through 6-24. Similar comparisons for Panel 6 are found in Table 6-6 and in Figures 6-25 through 6-27. Table 6-5 and 6-6 show that STAGSC-1 consistently predicted higher frequencies than those obtained through experimentation. The percent differences in general were larger than for any of the previous panels, however the experimental and analytical results were considered to correlate reasonably well. The largest percent difference for these panels was 9.03% (Mode 4, Panel 6). Graphically, the frequencies for Panels 5 and 6 are presented in

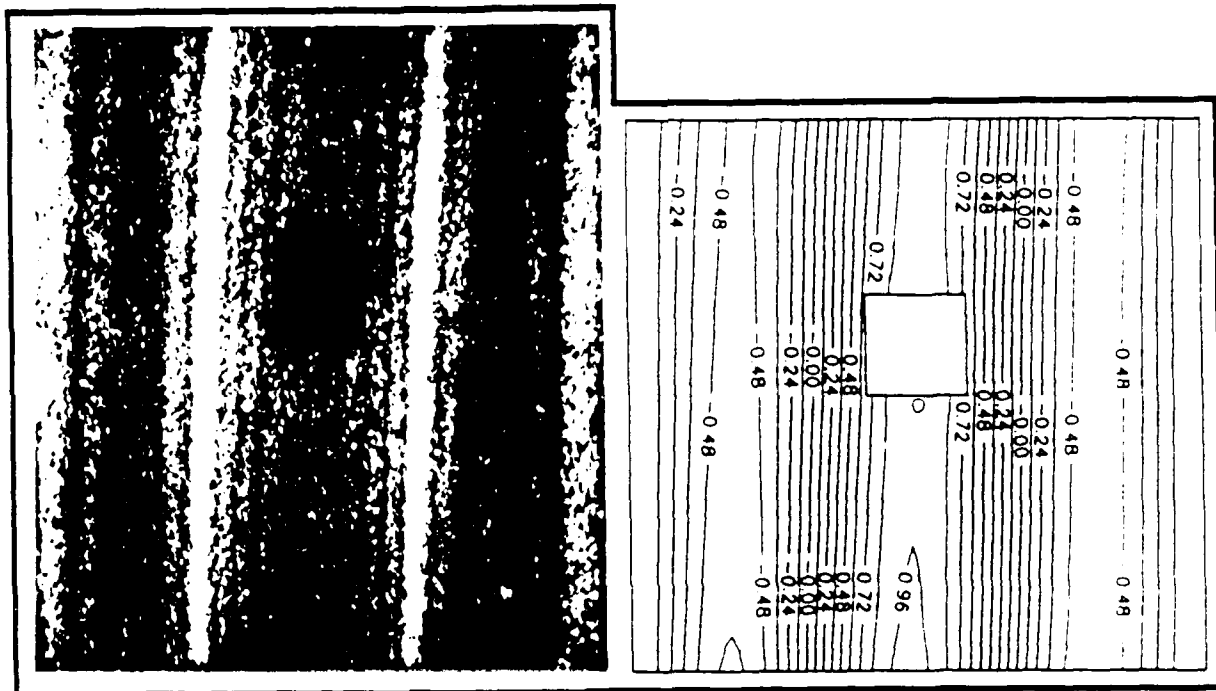
Table 6-5. Comparison of Experimental and Analytical Resonant Frequencies for Panel 5

Mode	Experiment (Hertz)	STAGSC-1 (Hertz)	Percent Difference
1	109.7	117.31	6.94
2	204.6	220.41	7.72
3	231.4	247.94	7.15
4	328.8	357.53	8.74
5	362.9	386.89	6.61

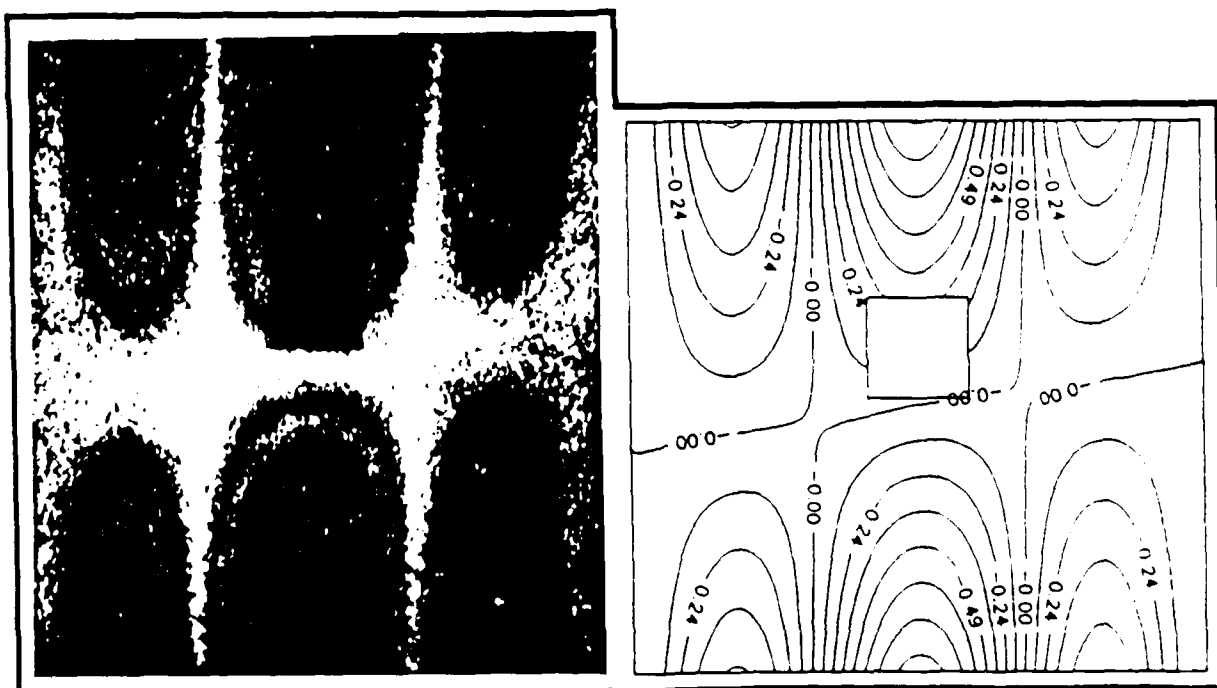


Mode 1

Figure 6-22. First Mode Shape for Panel 5

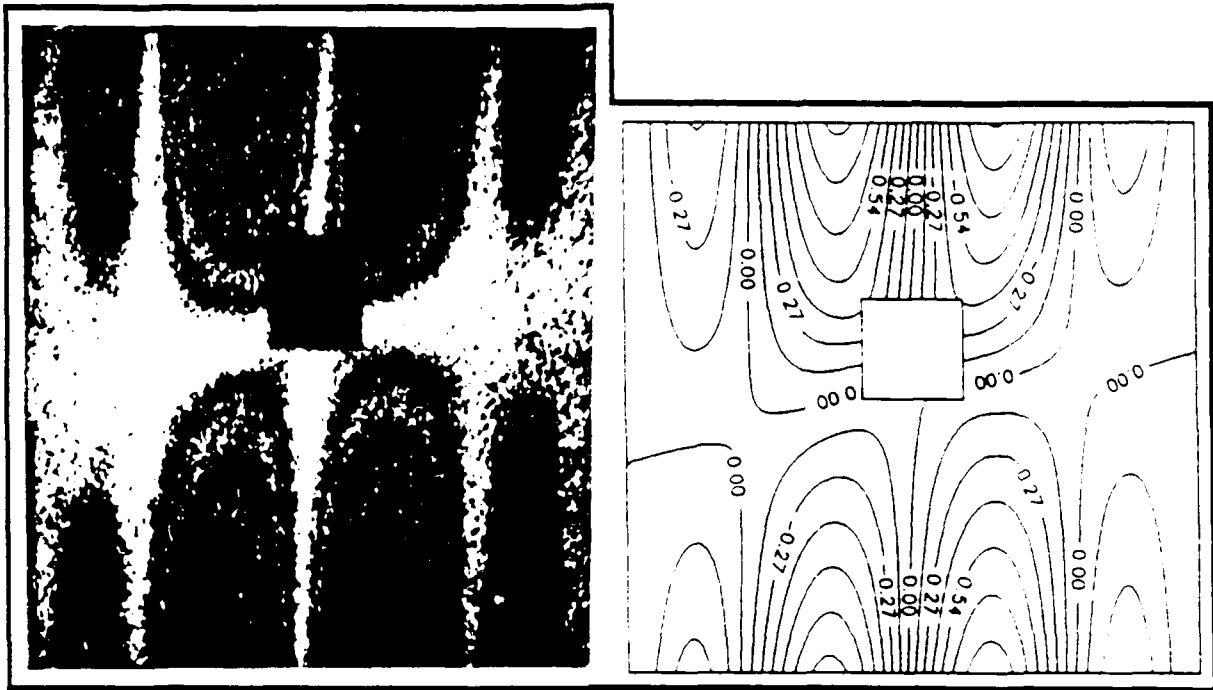


Mode 2

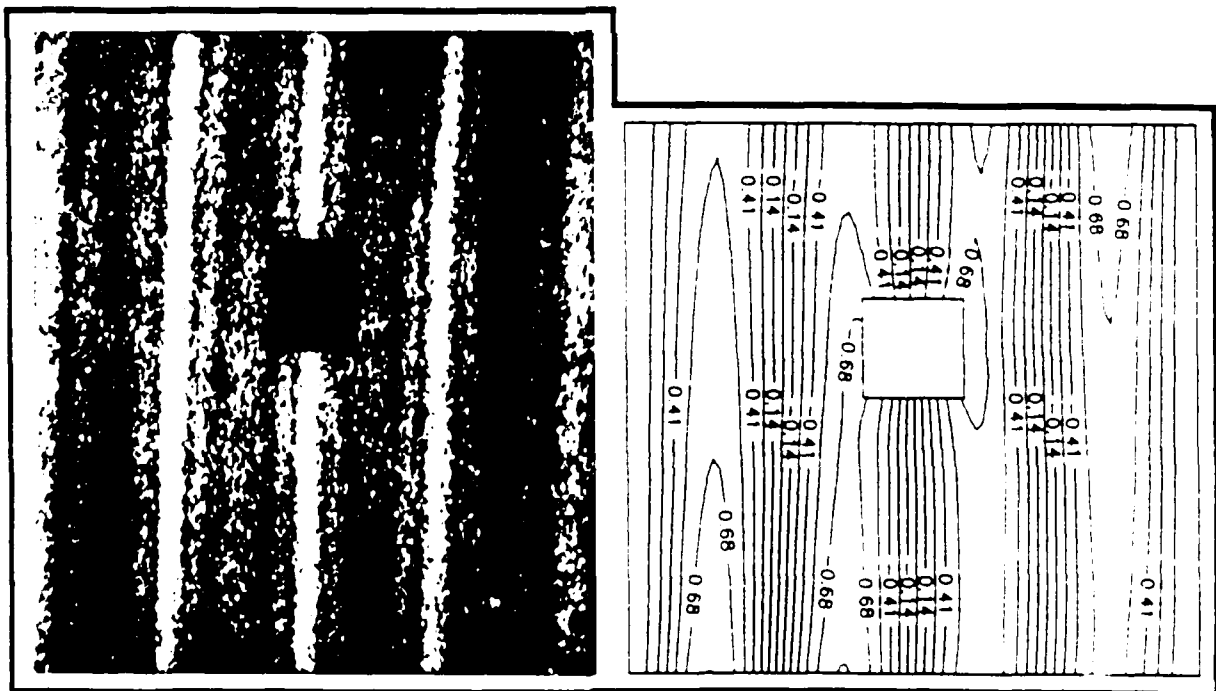


Mode 3

Figure 6-23. Second and Third Mode Shapes for Panel 5



Mode 4

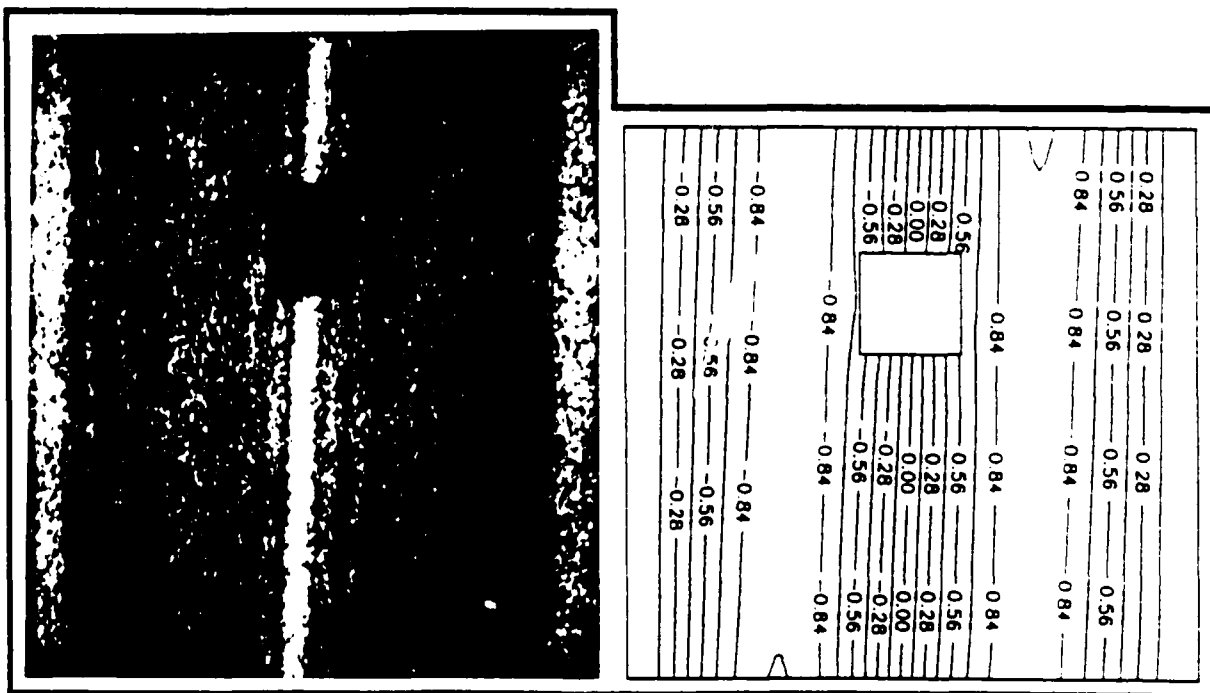


Mode 5

Figure 6-24. Fourth and Fifth Mode Shapes for Panel 5

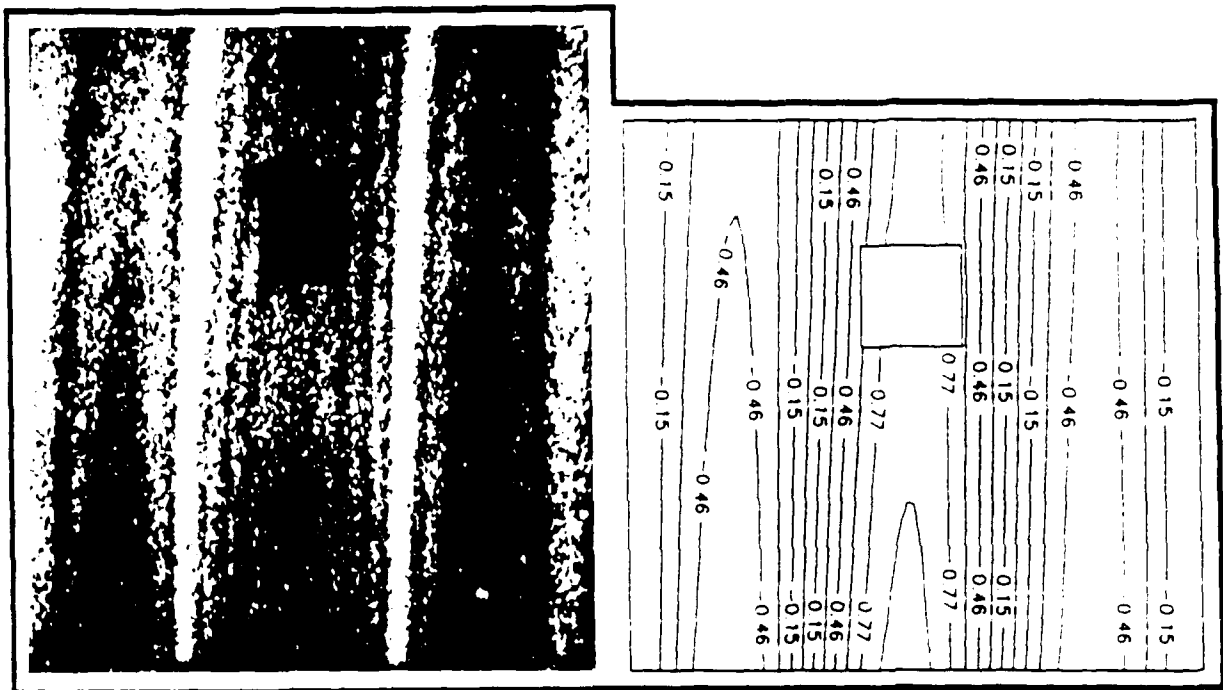
Table 6-6. Comparison of Experimental and Analytical Resonant Frequencies for Panel 6

Mode	Experiment (Hertz)	STAGSC-1 (Hertz)	Percent Difference
1	108.6	117.29	8.00
2	205.2	220.29	7.36
3	231.2	249.72	8.01
4	328.3	357.96	9.03
5	361.8	387.12	7.00

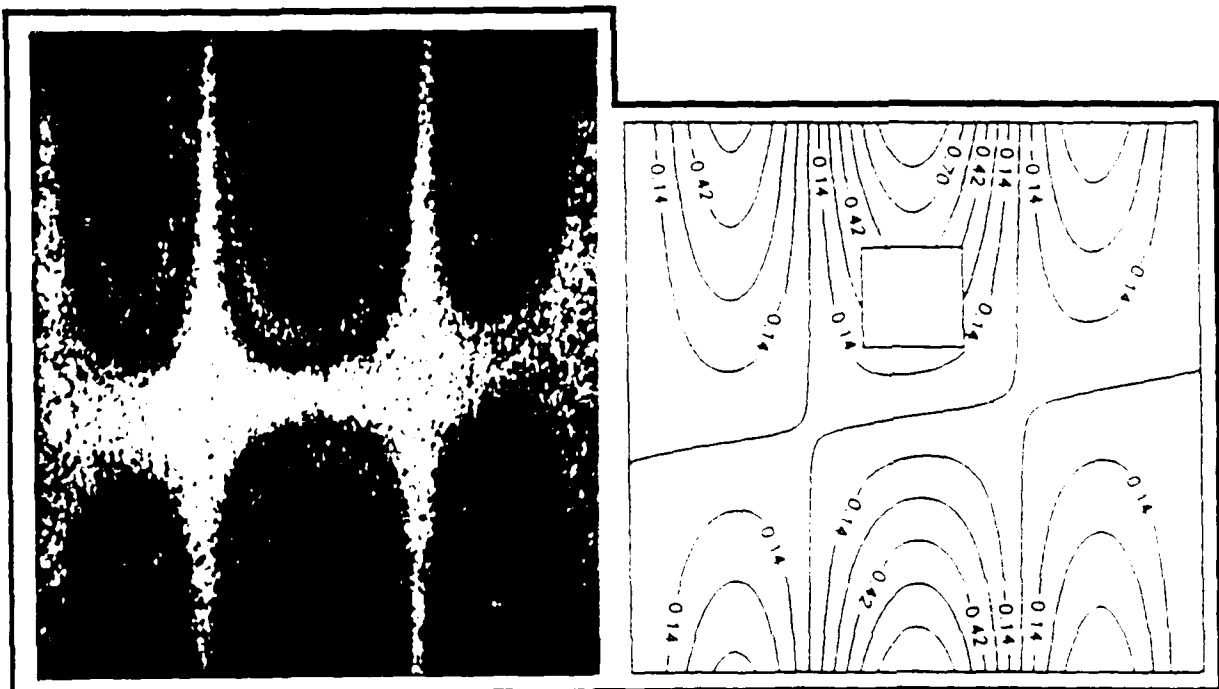


Mode 1

Figure 6-25. First Mode Shape for Panel 6

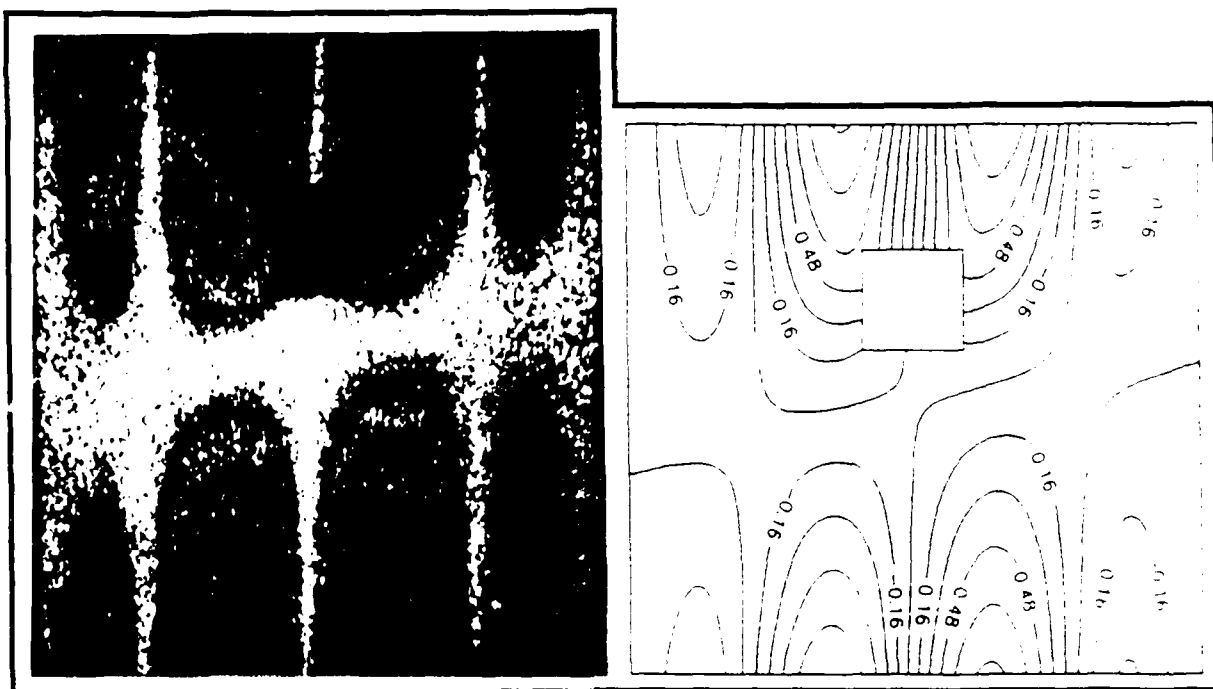


Mode 2

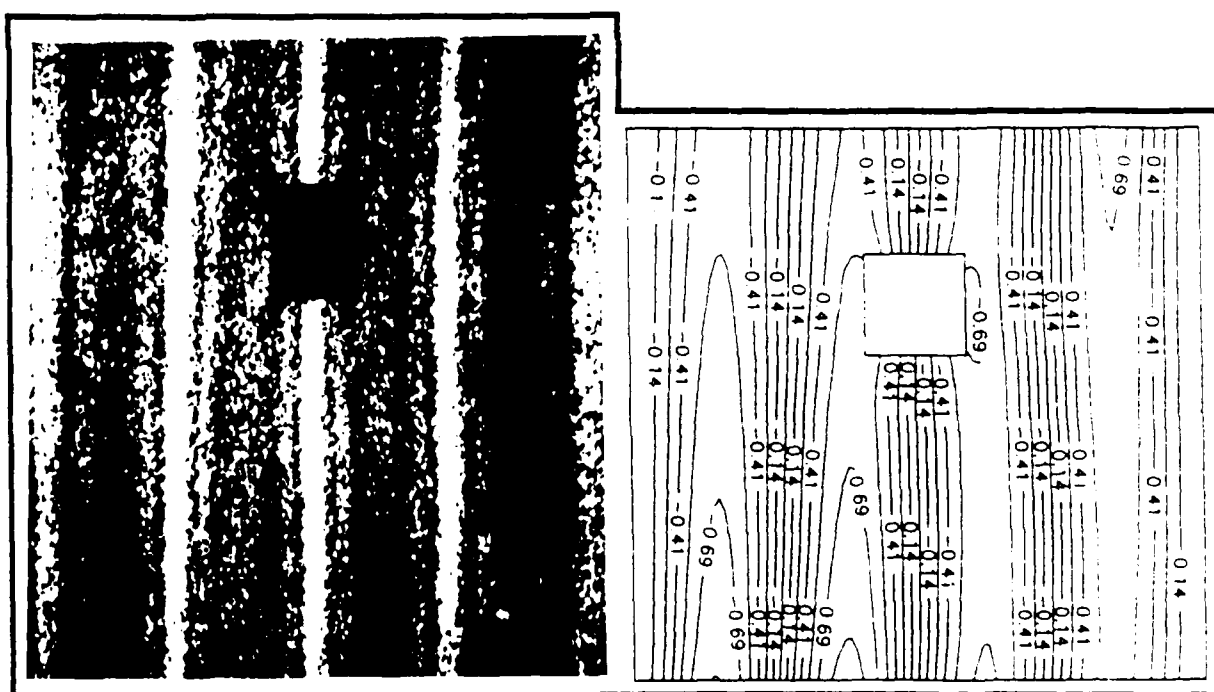


Mode 3

Figure 6-26. Second and Third Mode Shapes for Panel 6



Mode 4



Mode 5

Figure 6-27. Fourth and Fifth Mode Shapes for Panel 6

Figure 6-13 for the experimental results and in Figure 6-14 for the analytical results. From these figures it was apparent that the tangential eccentricity of the 2 inch cutout resulted in negligible frequency changes.

Comparison of Figures 6-22 through 6-27 revealed, as before, that STAGSC-1 did an excellent job of predicting the mode shapes. For both panels (Panels 5 and 6), the same basic mode shapes, as observed in the previous panels (Panels 1, 2, 3, and 4), were present. The biasing towards the -45° ply direction, as mentioned before, was apparent in Panels 5 and 6. By examining the mode shapes, it can be seen that the first, second, fourth, and fifth mode shapes were unaffected by the tangential eccentricity. At first, it was believed that the cutout location in Panel 6 had caused the shortening of the two top lobes in the center of the fourth mode shapes. After closer inspection, it was determined that the fourth mode shape had not been distorted. The appearance of a shortening of the upper lobes is believed due to an optical illusion. Also, the mode shape in question may have been recorded using a slightly lower amplitude setting than used for Panels 2 and 5. The effects of the tangential eccentricity were most obvious in the third mode for Panels 5 and 6 where the top lobes (especially the top center lobe) were elongated. As eccentricity increased, the cutout moved into the center lobe and was surrounded by an area of the panel which was all in phase. The resulting loss of stiffness allowed larger deformations in this region.

The eccentricity effects can best be visualized in Figure 6-28. For all practical purposes, the first five modes were insensitive to the tangential eccentricity considered for the 2 inch cutout. This was not surprising, because for the first five modes the radial displacements varied primarily in the circumferential direction (all modes had half waves which ran along the circumferential direction). For the first, second, and fifth modes the cutout moved along an antinode which was normal to the direction of primary displacements. The cutout's position did not change relative to node line or antinode

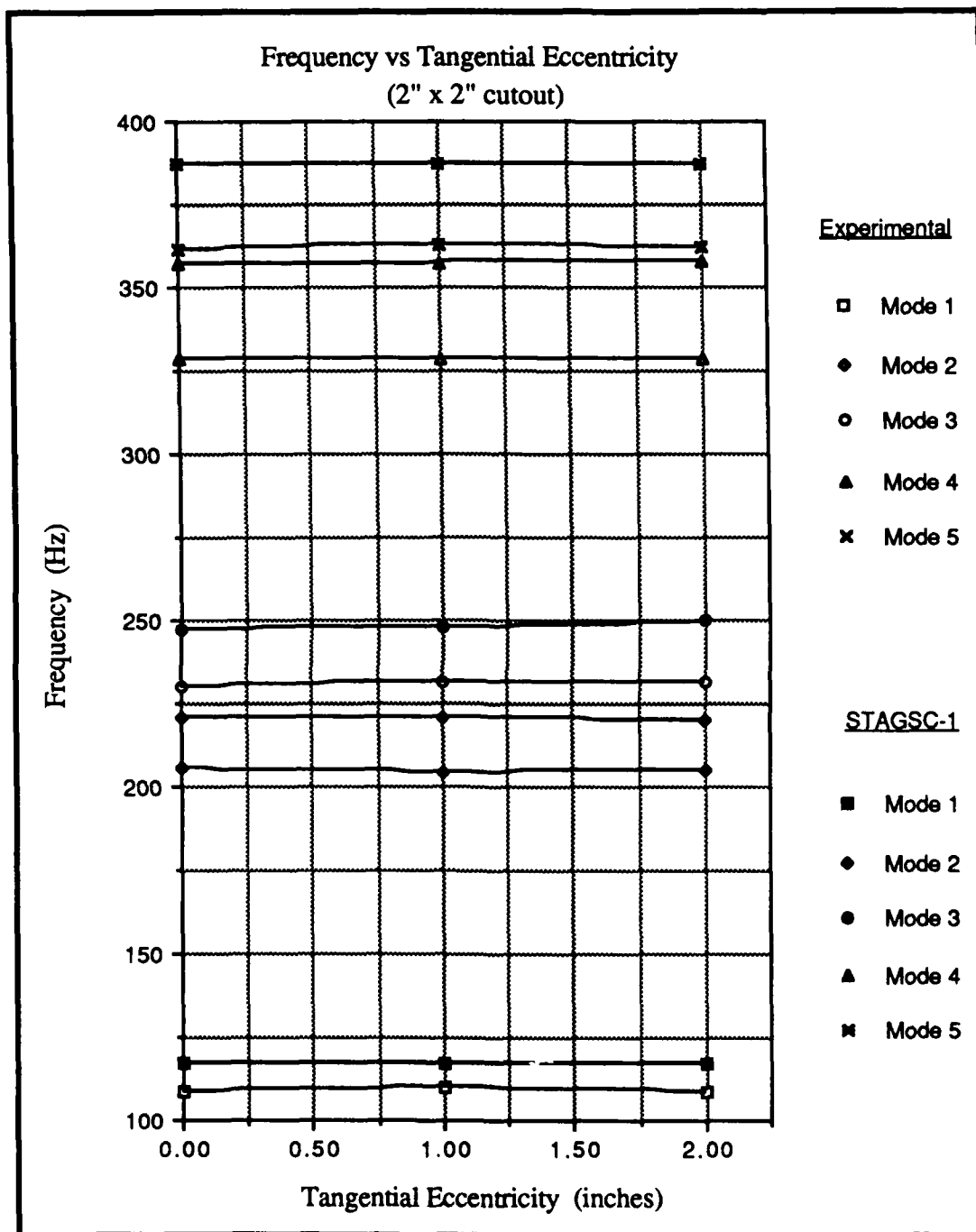


Figure 6-28. Frequency versus Tangential Eccentricity for 2" Square Cutout

locations so no distortion of the mode shapes or significant variation of the natural frequencies should be expected. The third and fourth modes also had quarter waves which ran in the tangential direction as well, however these modes remained insensitive to the tangential eccentricity. In the third mode the cutout moved off the horizontal node line. For Panels 3 and 4, it was observed that near an antinode the effects of the loss in cutout mass contributed more than the loss in stiffness (frequency increased). Due to the free edge condition, the antinode for the third (and fourth) mode was at the very edge of the panel. For Panels 5 and 6 it can be seen that even at the largest tangential eccentricity value the cutout remained far from the antinode. The mass effects contributed more but so did the stiffness due to the large amount of bending present in the center lobe (Figure 6-4). In the fourth mode, the eccentricity caused the cutout to move along a vertical node line which kept the mass effects small. The top center lobes represented areas of relatively large displacement and between these lobes the panel underwent a lot of bending. Because the frequency remained constant, it appears that the bending between center lobes and the two directional bending at the center of the panel were equally sensitive to the loss of stiffness caused by the cutout.

The 2 inch square cutout did not substantially alter the stiffness to mass ratio of the panels studied. Only slight frequency variations were noticed when the cutout was first introduced and as circumferential eccentricity was increased. The panel geometry was insensitive to the tangential eccentricity of the 2 inch cutout. For all locations, the mode shapes were relatively unaffected by the cutout. Overall, dynamic response the panels studied was not significantly effected by the 2 inch square cutout. The results for the panels with 4 inch square cutouts are discussed in the next section.

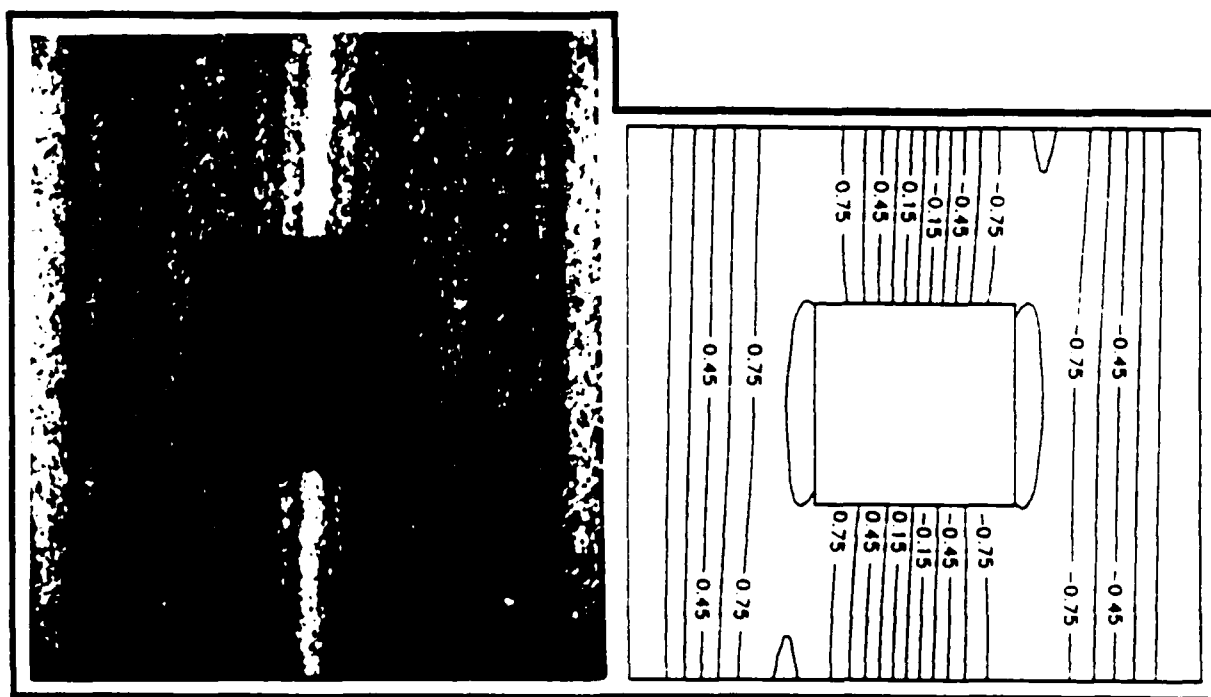
C. Panels with 4" Square Cutouts

The panels with 4 inch square cutouts corresponded to Panels 7, 8, 9, 10, and 11 as described in Table 3-2. This section is broken into three parts. First, the panel with the centered 4 inch cutout (Panel 7) is discussed. Next, the results for the two panels with circumferentially eccentric cutouts (Panels 8 and 9) are presented. Finally, results are given for the two panels with tangentially eccentric cutouts (Panels 10 and 11).

(1) Panel 7. This panel contained a centered 4 inch square cutout. The natural frequencies for Panel 2 are presented in Table 6-7. The corresponding mode shapes follow in Figures 6-29 through 6-31. As shown in Table 6-7, STAGSC-1 did a good job of predicting the first five natural frequencies. The largest percent difference was 9.34% and occurred for the first mode. As for all previous panels, the analytical frequencies were consistently higher than those obtained experimentally. Inspection of Figures 6-29 through 6-31 revealed that STAGSC-1 provided, as in the past, excellent predictions of the first five mode shapes for Panel 7. Figure 6-32 contains a graphical representation of the experimental and analytical frequencies for Panel 7. (Figure 6-32 is also representative of the trend found for all panels with 4 inch square cutouts, therefore similar plots for Panels 8 through 11 will not be included.) The relationship which existed between symmetric and antisymmetric modes as noticed for all previous panels, was disrupted by the 4 inch square cutout. The larger cutout caused a significant drop in the fourth mode natural frequency. The mode shape remained antisymmetric, however the frequency dropped to just 16 Hz above the third mode frequency. Thus, for Panel 7, the second and third modes (symmetric) were close in frequency to the fourth mode (antisymmetric). The biasing of the vertical and horizontal node lines towards the -45° fiber direction was present in Panel 7, although to a lesser extent. Biasing was mainly visible in the vertical node lines of

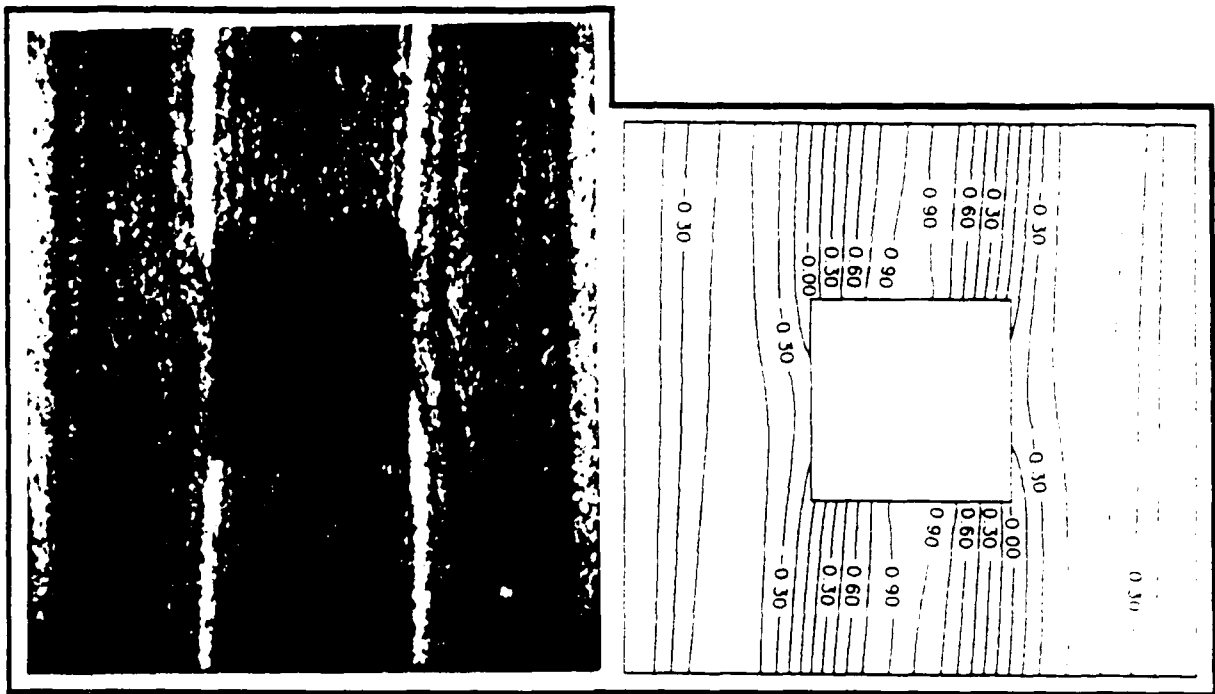
Table 6-7. Comparison of Experimental and Analytical Resonant Frequencies for Panel 7

Mode	Experiment (Hertz)	STAGSC-1 (Hertz)	Percent Difference
1	103.6	113.28	9.34
2	208.3	225.41	8.21
3	224.4	241.56	7.64
4	240.6	257.40	6.98
5	358.0	384.63	7.44

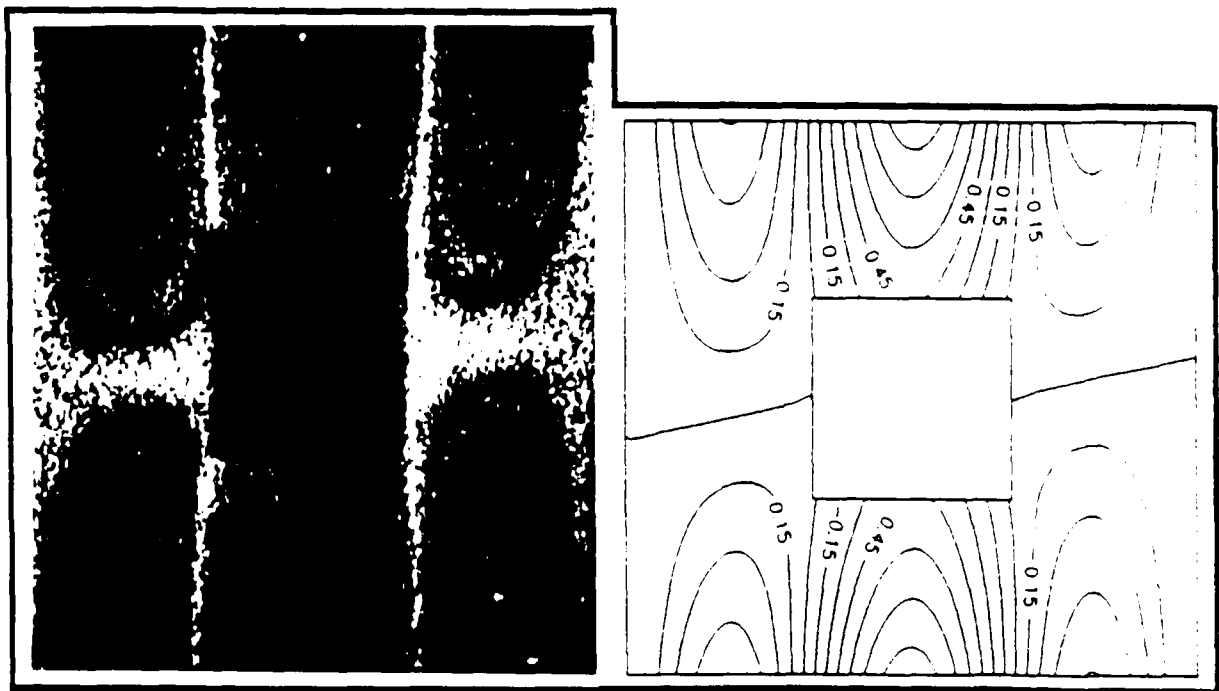


Mode 1

Figure 6-29. First Mode Shape for Panel 7

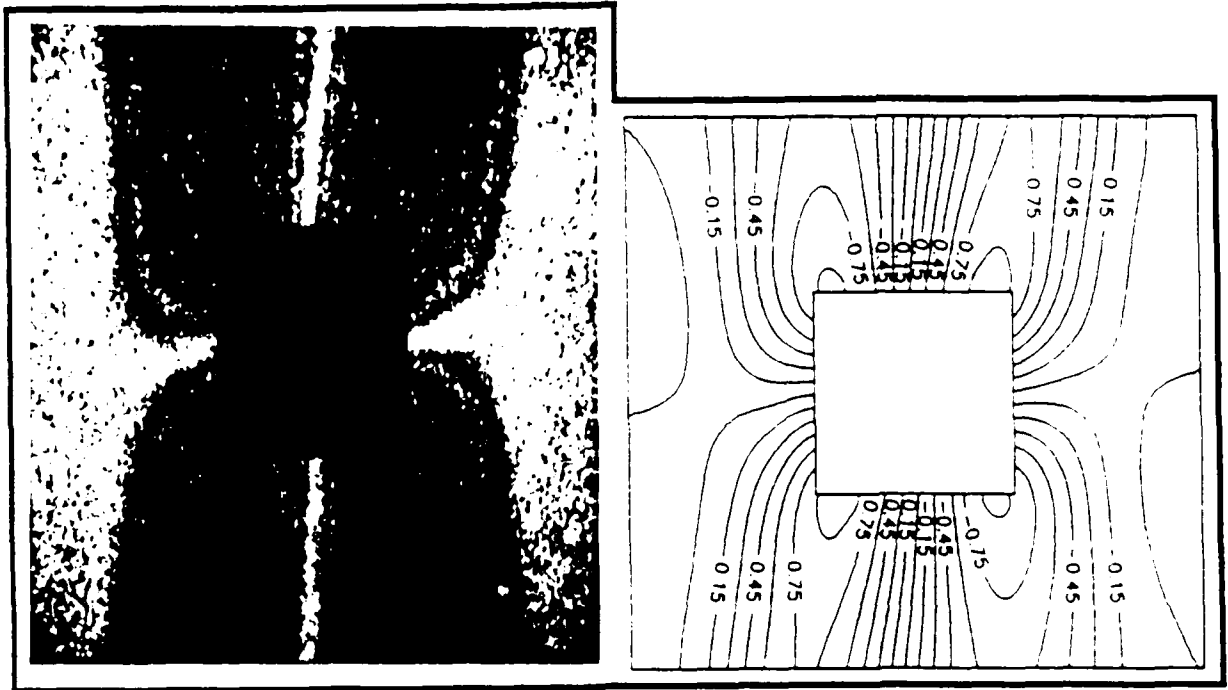


Mode 2

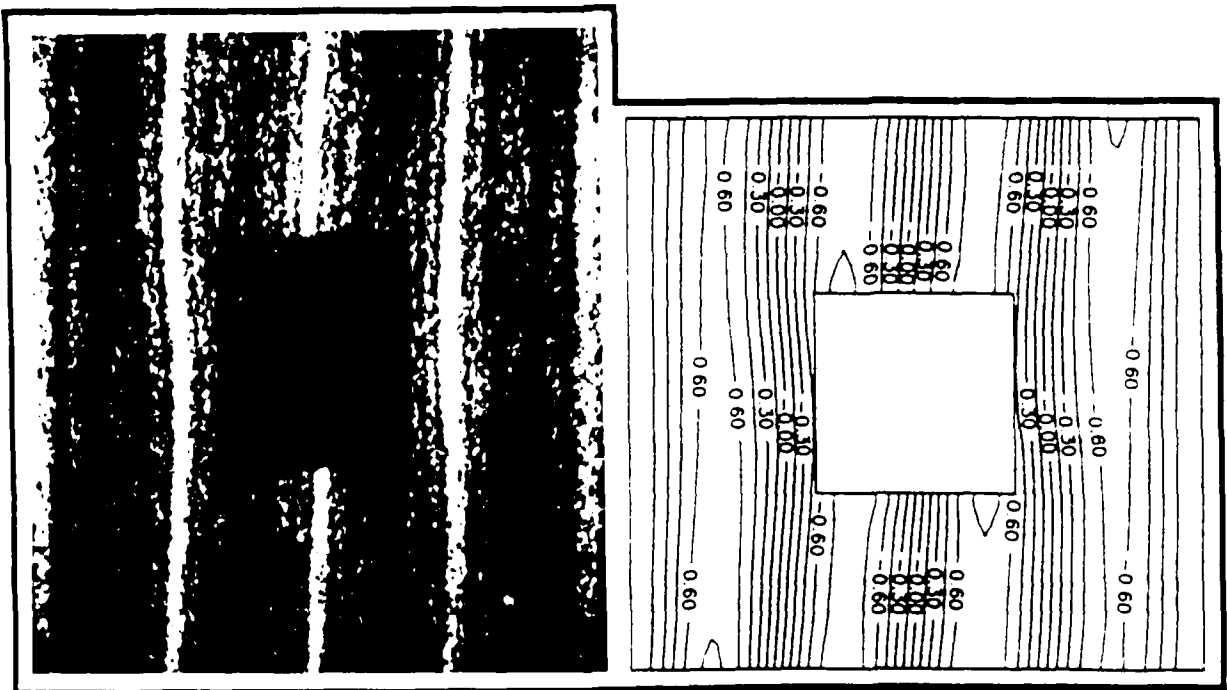


Mode 3

Figure 6-30. Second and Third Mode Shapes for Panel 7



Mode 4



Mode 5

Figure 6-31. Fourth and Fifth Mode Shapes for Panel 7

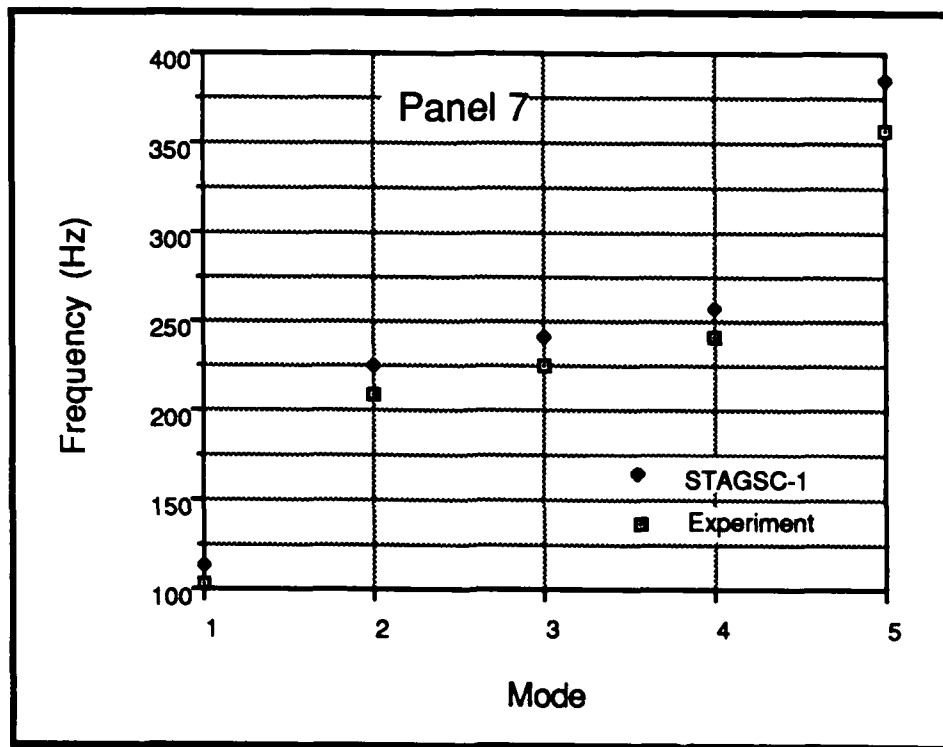


Figure 6-32. Frequency versus Mode for Panel 7

the first, fourth, and fifth modes and in the horizontal node lines of the third and fourth mode. The vertical node lines in the second and third modes were bent into the direction of the discontinuity (cutout), in effect masking any biasing present.

Comparing Panel 7 to Panel 1, the cutout caused the experimental frequencies to change by -4.7%, +2.5%, -4.6%, -31.1%, and -3.1% for modes 1 through 5, respectively. The same comparison for the analytical frequencies resulted in changes of -3.9%, +3.7%, -2.6%, -30.1%, -2.2% for modes 1 through 5, respectively. As for the 2 inch square cutout, STAGSC-1 predicted the increases and decreases in resonant frequencies consistent to those obtained from experimental data. These differences are shown graphically in Figures 6-33 and 6-34. Because similar trends were noticed both experimentally and analytically for Panel 7, the frequency variations were considered "real"

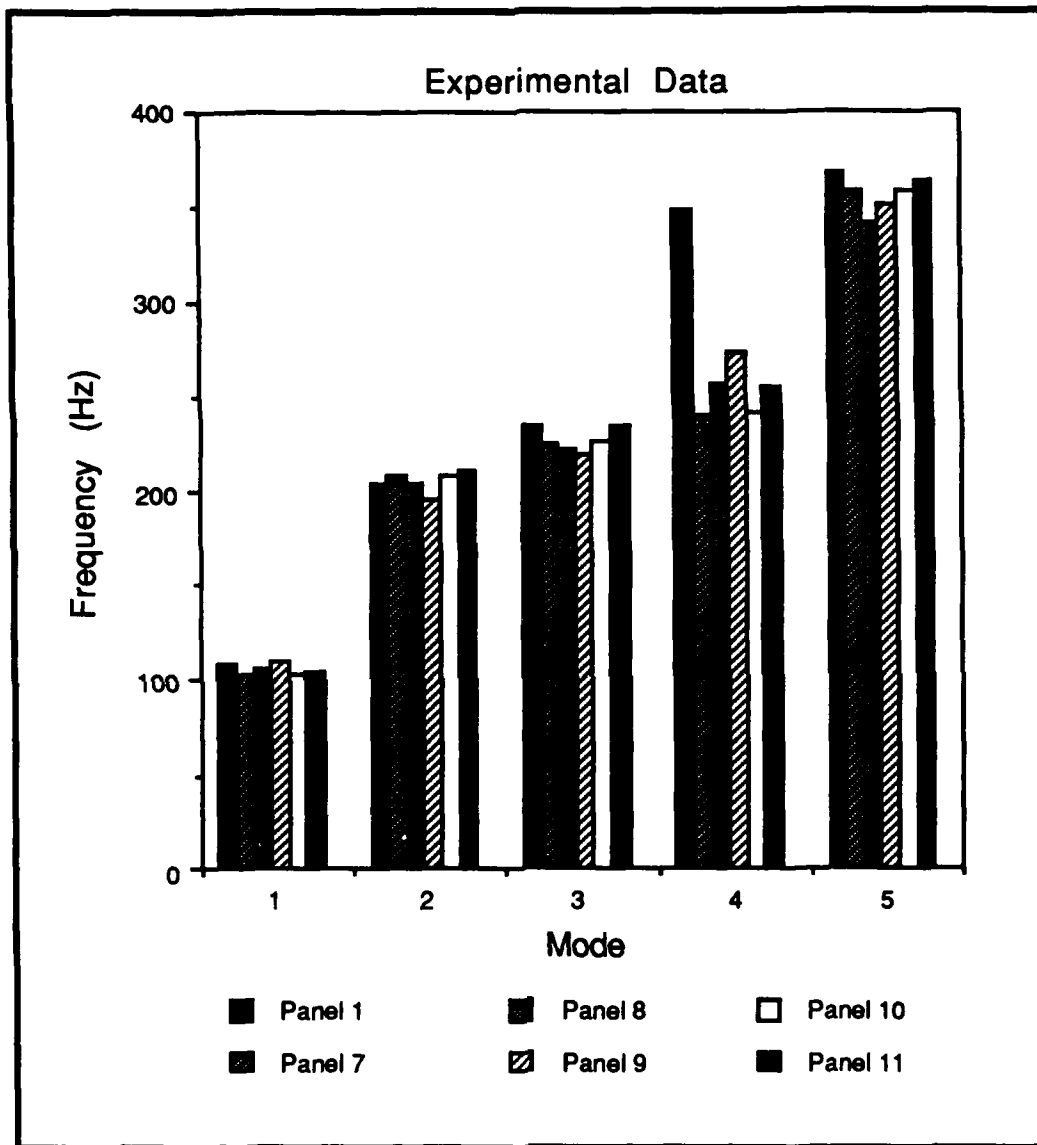


Figure 6-33. Experimental Frequency versus Mode for Panels 1, 7, 8, 9, 10, and 11

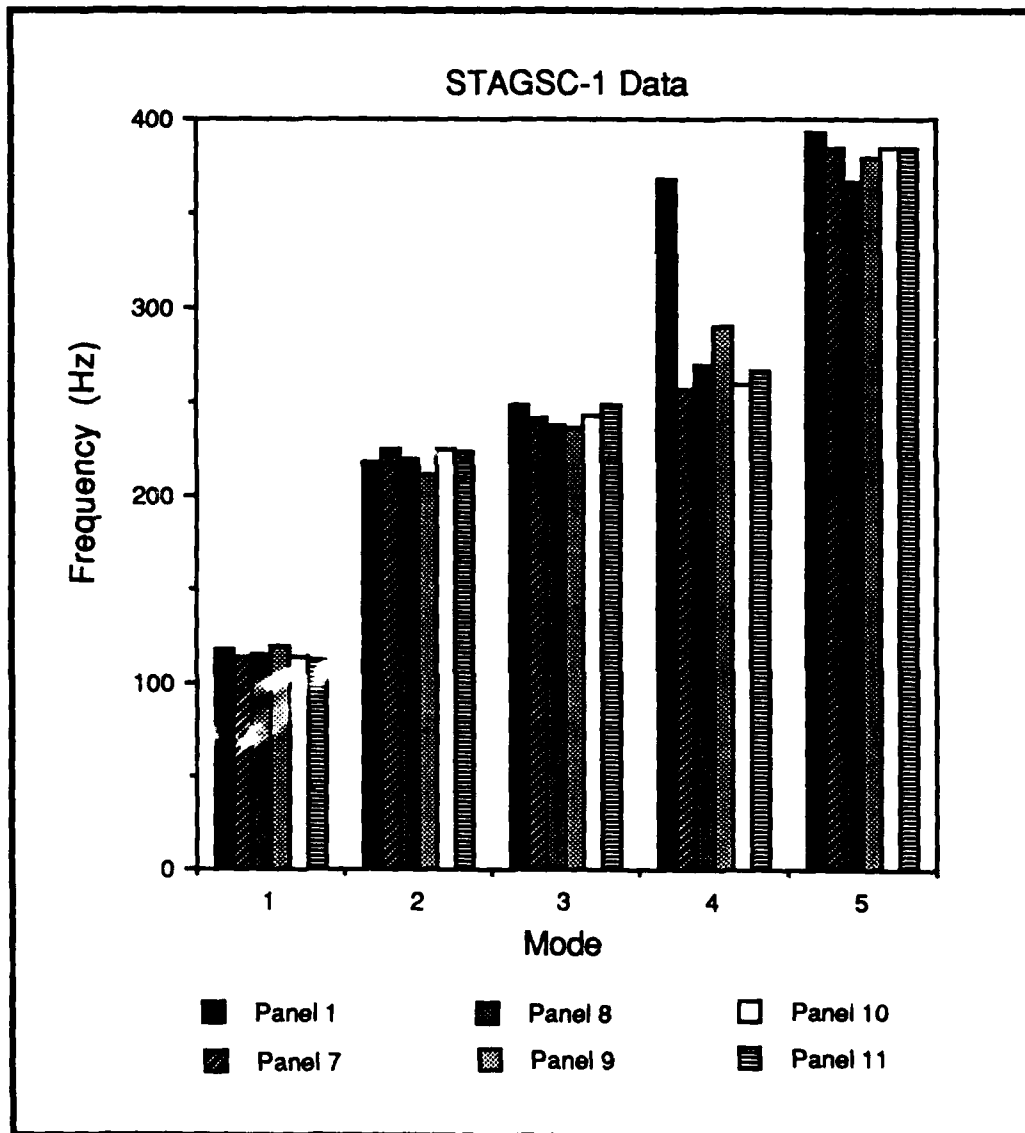


Figure 6-34. Analytical Frequency versus Mode for Panels 1, 7, 8, 9, 10, and 11

panel behavior which occurred as a result of the cutout. Similar to the 2 inch cutout, the 4 inch cutout caused the second mode frequency to increase while decreases in frequency were noticed in all other modes. As before, the loss of mass contributed more to the panels response than the loss of stiffness at the center antinode location of the second mode (K/M increased). The only significant change in frequency (due to the cutout) was noticed for the fourth mode where the natural frequency dropped over thirty percent. The fourth mode shape for Panel 7 also changed significantly as compared to Panel 1. For a given mode, if a cutout causes a large change in frequency, then a large variation in the eigenvector should also be expected.

The first mode shape was unaffected by the 4 inch square cutout; the node line which passes through the cutout remained straight. The second mode had vertical node lines which originally would have run along the edges of the cutout. Due to the loss of stiffness the vertical node lines have been "drawn" towards the cutout and become discontinuous. At first it seemed puzzling that a node line on the panel, which experienced no motion, would be "drawn" towards an area of the panel where, due to loss of stiffness, larger displacements would be expected. After discussion with Mr. Maddux [26], it was decided that this behavior could best be described graphically as presented in Figure 6-35. In Figure 6-35 an undeformed panel is shown along with geometries representing mode shapes obtained with and without the centered cutout present. Please note, the deformed geometries presented in Figure 6-35 are in no way intended to represent actual mode shapes of the panels studied. As shown in Figure 6-35, the loss of stiffness caused by the cutout allows the center of the panel to undergo larger deformations while the amplitude of the two side half waves is reduced (assuming no elongation of the neutral axis of the panel occurs). In effect, the node lines are "drawn" closer together. A similar argument can be used to explain the behavior of the vertical node lines for the third and fifth modes. In the third mode the warping of the vertical node lines was most obvious by noticing that the side

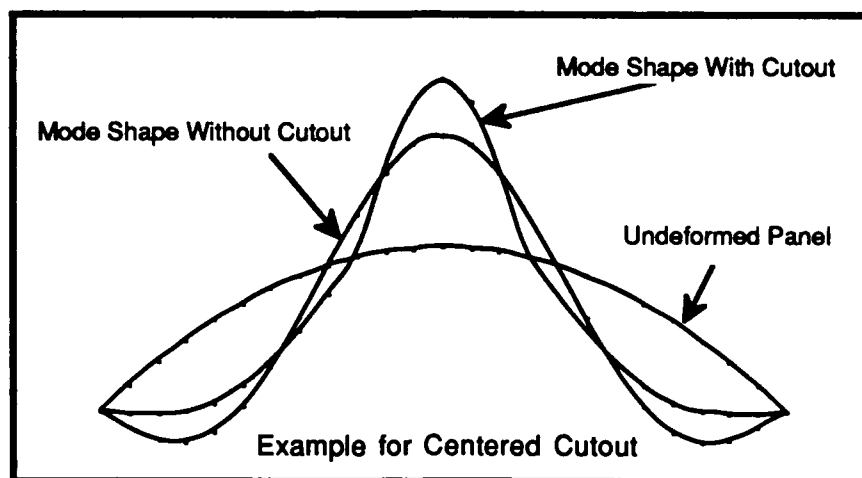


Figure 6-35. Cutout Effects on Mode Shape

lobes were tilted towards the center of the panel. For the fifth mode, the two segments of the center vertical node line no longer remained in a line. The two segments continued to have the same slope (due to -45° ply biasing) and it appeared that the bottom segment could be generated by merely translating the upper segment down. Considering the fifth mode response, apparently the bottom edge of the cutout represented a large enough free edge that behavior beneath the cutout was similar to behavior above the cutout. The fourth mode shape provided the most interesting observations. First, the mode shape changed significantly from that seen in Panel 1. Considering the fourth mode, since the panel no longer supported four half waves in the circumferential direction, it would seem natural that the overall panel stiffness had been affected. Also, the large loss of stiffness at the center of the panel had allowed the four center lobes to enlarge. Secondly, for all previous panels the antinodes for the fourth mode were located at the free edges of the panel. Close inspection of the fringe lines for the fourth mode of Panel 7 indicated that the antinodes were located at the corners of the cutout. This also suggested a large decrease in stiffness in the region of the cutout had occurred. Thirdly, the two segments of the vertical node line

were no longer linear (similar to mode 5) and also were at different slopes. No explanation can be given as to why this occurred. The changes in the fourth mode shape implied a substantial decrease in the stiffness (related to the fourth mode response) which was consistent with the large decrease in frequency observed.

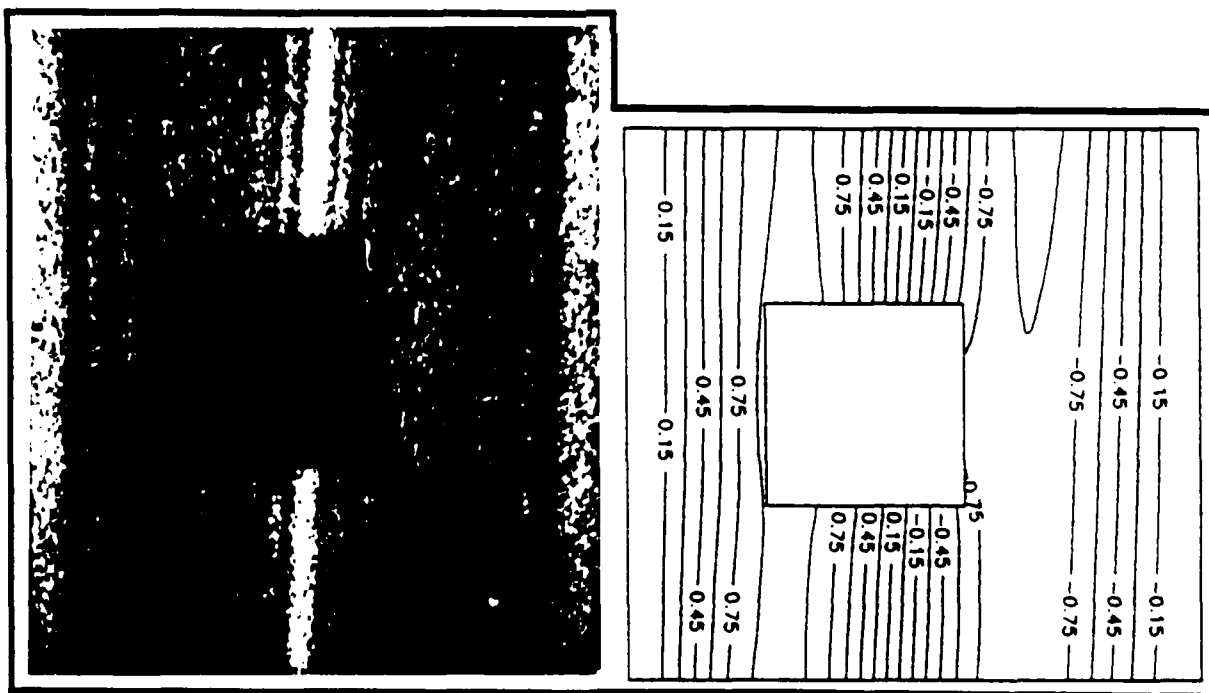
If the results from Panel 7 are compared with the results obtained by Walley [42], for a similar panel with a 4 inch square cutout and fully clamped boundary conditions, additional observations can be made. Walley found that the 4 inch cutout caused a reduction in the experimental frequency for the first five modes of -9.1%, -4.5%, -14.6%, -6.1% and -13.2%, respectively. All frequencies decreased for the fully clamped panel and except for the fourth mode the decreases were considerably larger than for Panel 7. Also all five of the mode shapes for the fully clamped panel were significantly altered. Thus, the 4 inch square cutout caused a larger overall reduction in stiffness for the fully clamped panel than it did for the panel with the CFCF boundary condition.

The panels with circumferentially eccentric 4 inch square cutouts will be discussed in the next section. Their results will be compared to Panel 7.

(2) Panels 8 and 9. These panels contained 4 inch square cutouts which had been eccentrically located in the circumferential direction (Figure 3-3). The amounts of eccentricity were 1 inch and 2 inches for Panels 8 and 9, respectively. A comparison of the experimental and analytical resonant frequencies for Panel 8 is found in Table 6-8 and a comparison of the corresponding mode shapes can be found in Figures 6-36 through 6-38. Similar comparisons for Panel 9 are found in Table 6-9 and in Figures 6-39 through 6-41. STAGSC-1 again performed well predicting the natural frequencies and mode shapes. The frequencies presented in Tables 6-8 and 6-9 correlated well with the largest percent difference being 8.28% (Mode 1, Panel 9). The analytical frequencies were consistently predicted higher than the experimental frequencies. The analytical mode shapes for Panels

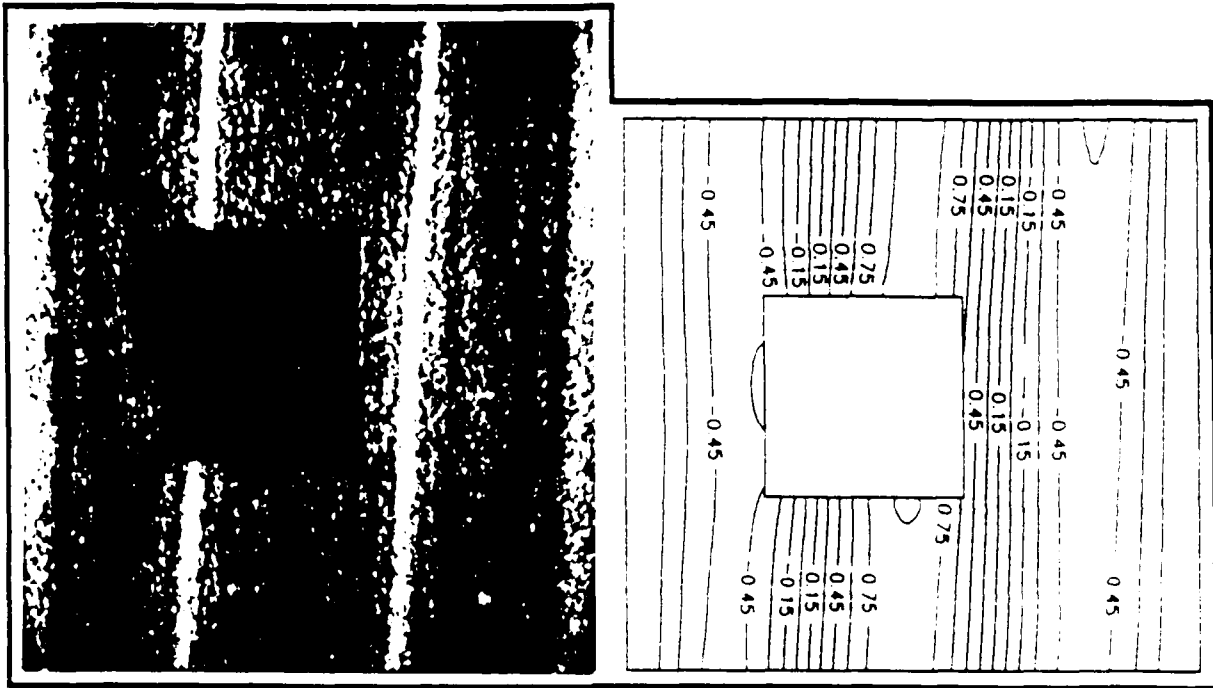
Table 6-8. Comparison of Experimental and Analytical Resonant Frequencies for Panel 8

Mode	Experiment (Hertz)	STAGSC-1 (Hertz)	Percent Difference
1	106.9	115.53	8.07
2	204.1	220.11	7.85
3	222.1	237.09	6.75
4	256.7	269.63	5.04
5	341.0	367.01	7.63

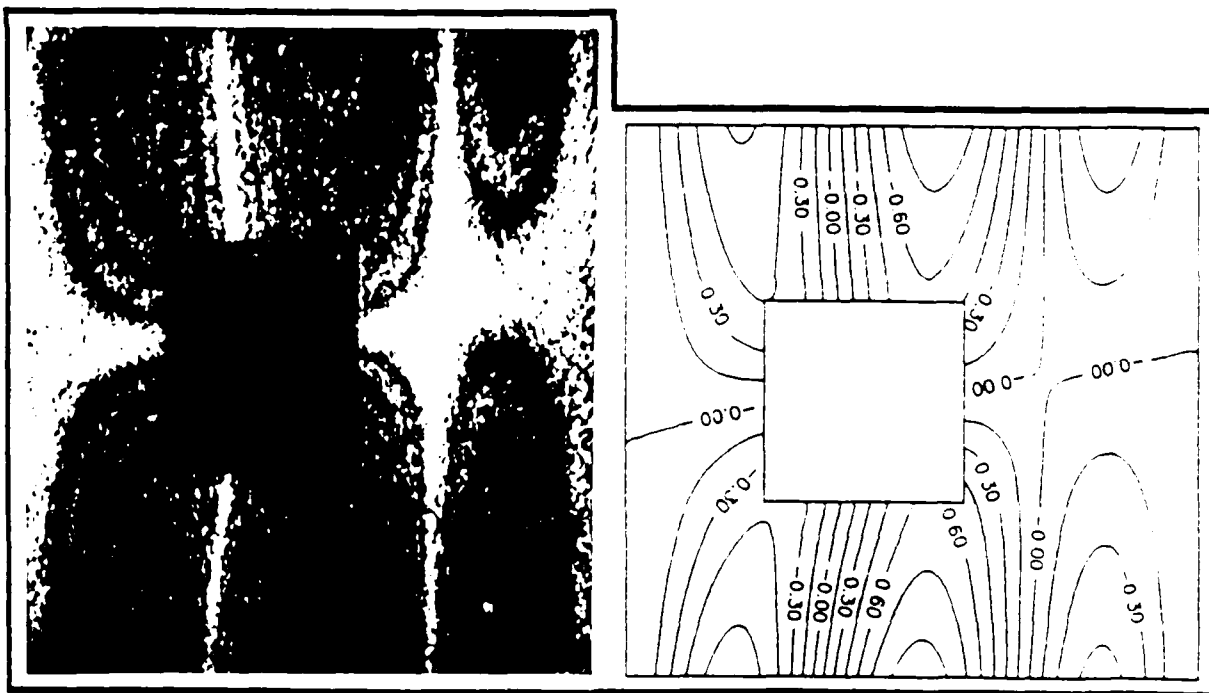


Mode 1

Figure 6-36. First Mode Shape for Panel 8

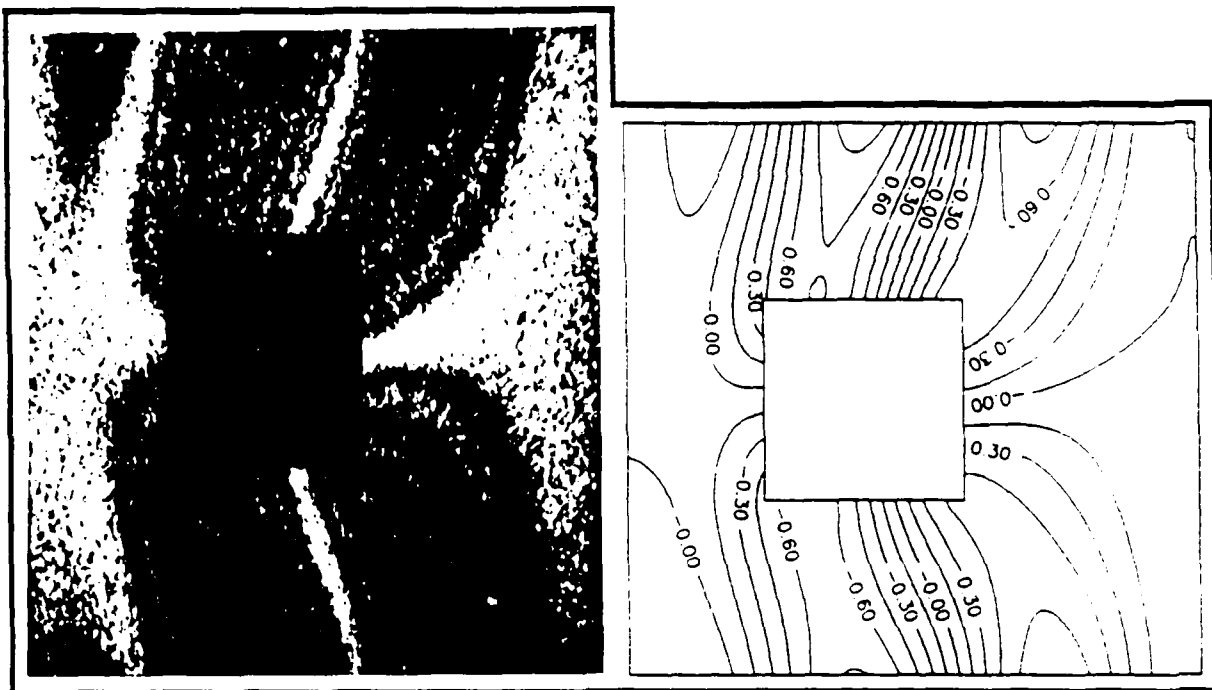


Mode 2

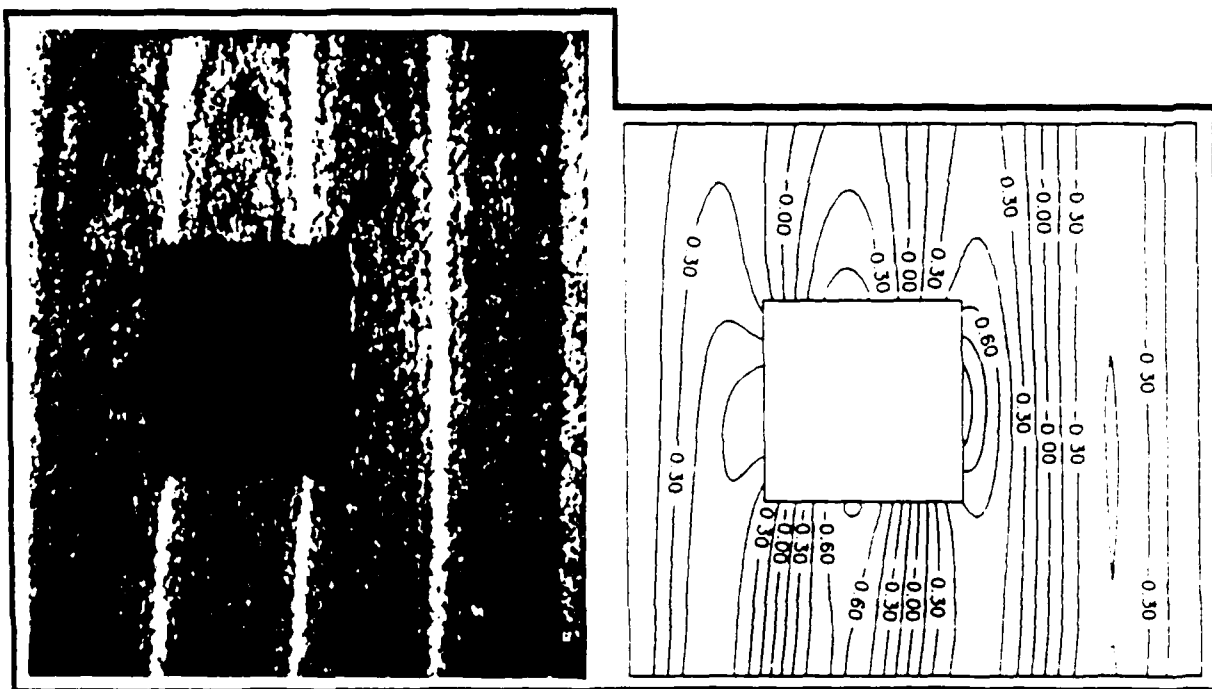


Mode 3

Figure 6-37. Second and Third Mode Shapes for Panel 8



Mode 4

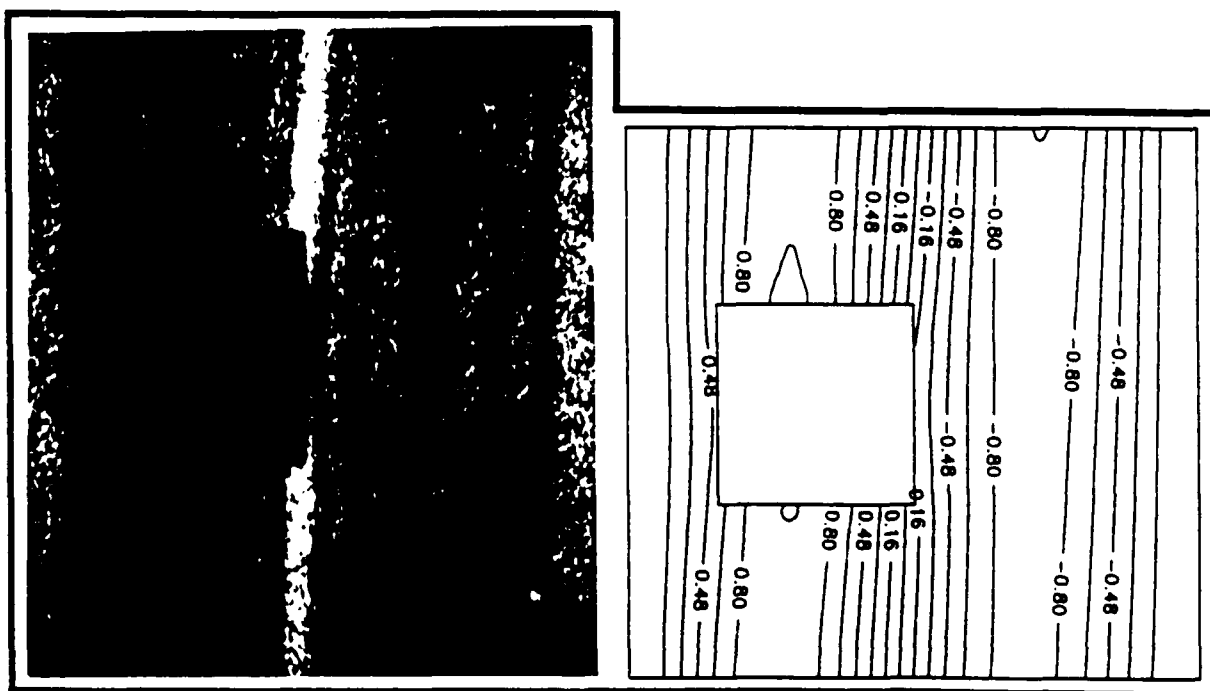


Mode 5

Figure 6-38. Fourth and Fifth Mode Shapes for Panel 8

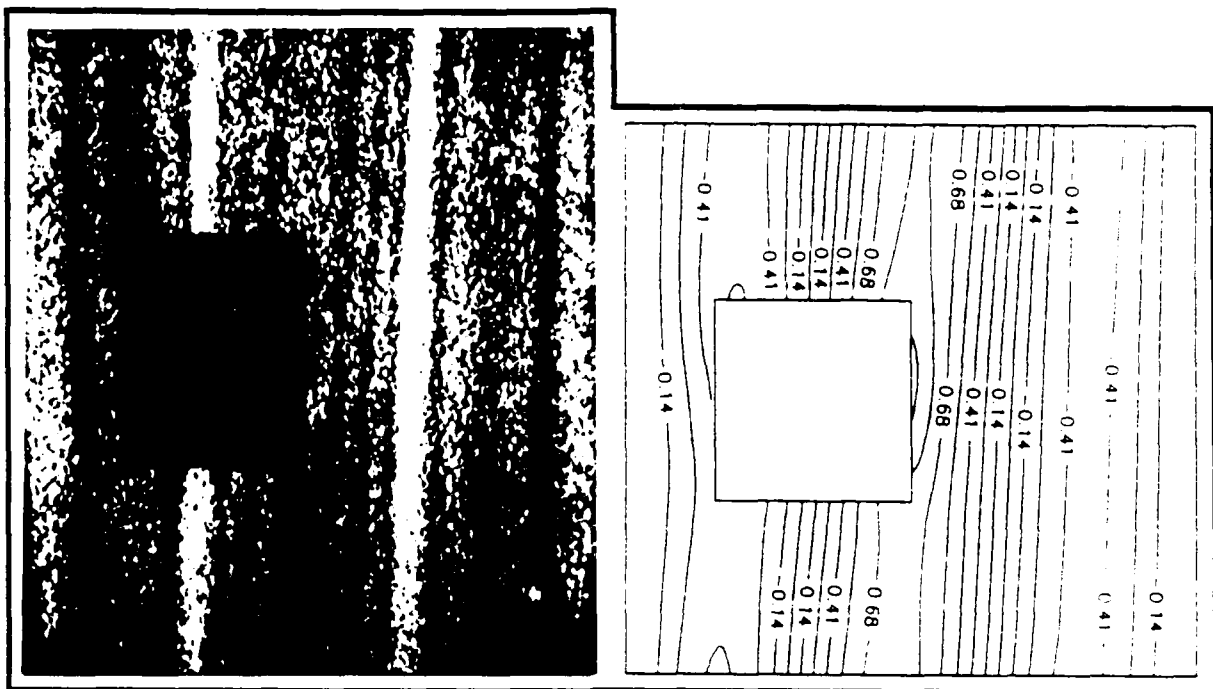
Table 6-9. Comparison of Experimental and Analytical Resonant Frequencies for Panel 2

Mode	Experiment (Hertz)	STAGSC-1 (Hertz)	Percent Difference
1	110.3	119.43	8.28
2	194.9	210.61	8.06
3	219.8	236.43	7.57
4	273.5	290.57	6.24
5	352.5	379.08	7.54

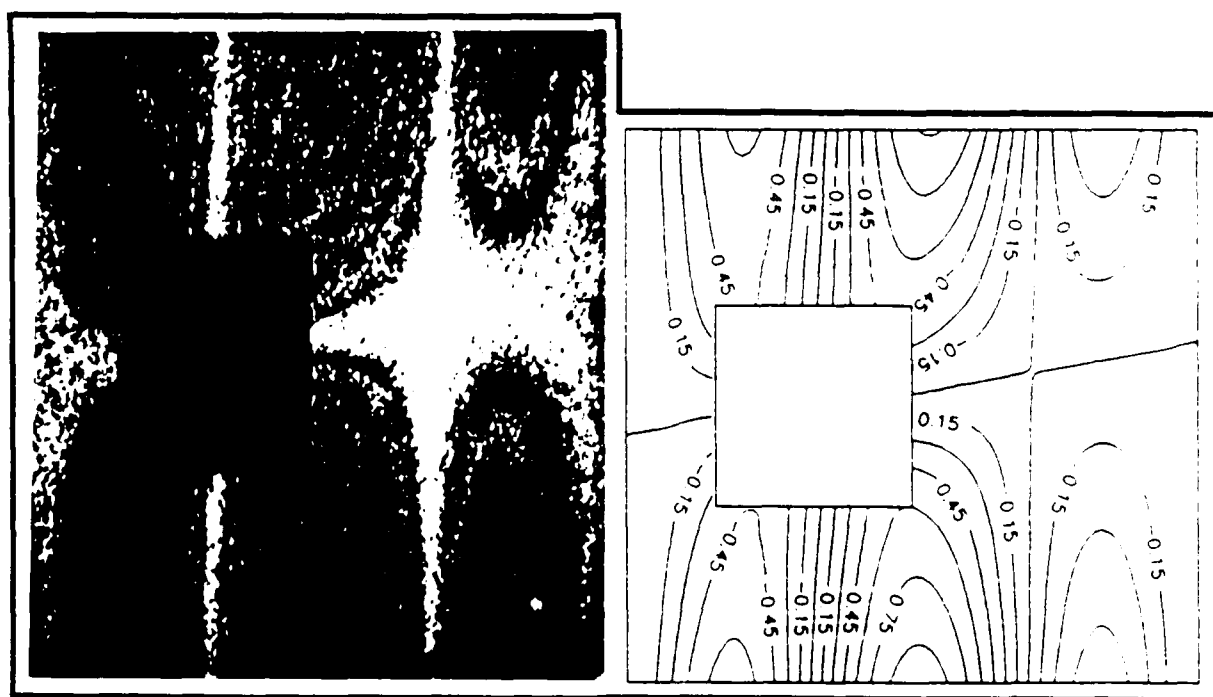


Mode 1

Figure 6-39. First Mode Shape for Panel 9

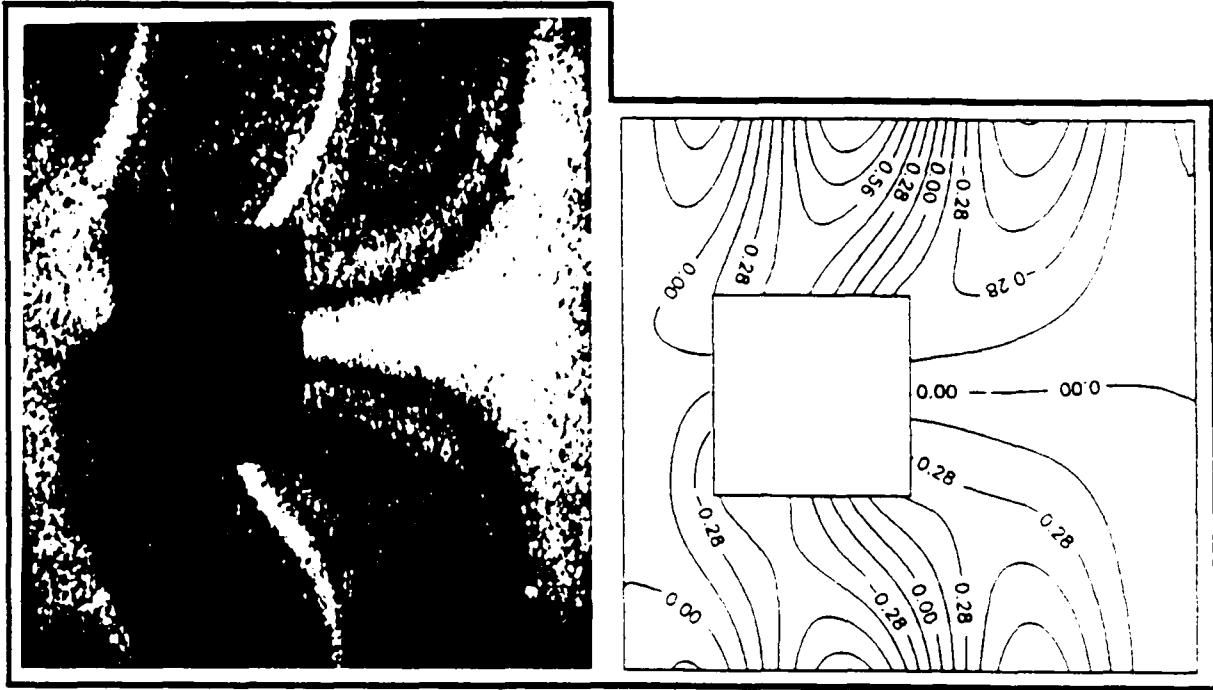


Mode 2

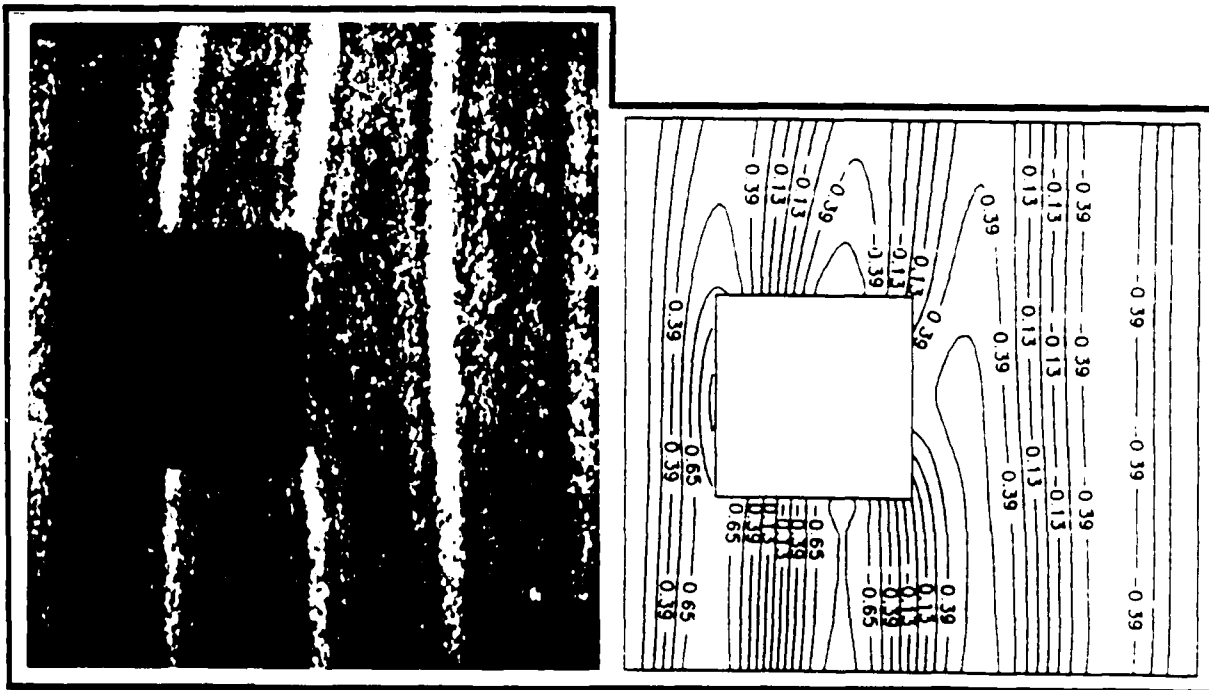


Mode 3

Figure 6-40. Second and Third Mode Shapes for Panel 9



Mode 4



Mode 5

Figure 6-41. Fourth and Fifth Mode Shapes for Panel 9

8 and 9 showed excellent agreement with those obtained experimentally. Graphically, the experimental frequencies for Panels 8 and 9 are presented in Figures 6-33 and the analytical frequencies are shown in Figure 6-34. Comparing Panels 8 and 9 to Panel 7, Figures 6-33 and 6-34 showed that the circumferential eccentricity of the 4 inch cutout caused only small frequency variations. Comparison of the mode shapes in Figures 6-36 through 6-41 revealed that for both panels the same basic mode shapes, as found for Panel 7, were present with the exception of the fourth mode. As circumferential eccentricity of the cutout increased, the fourth mode became highly distorted. Biasing towards the -45° fiber direction was present. Because the 4 inch square cutout causes some distortion of most mode shapes, the effects of biasing could only be confirmed in the first and second modes for both panels. As shown in Figures 6-36 through 6-41, the larger cutout caused most of the mode shapes to contain at least small amounts of distortion which were not present with the 2 inch cutout. This indicated that the loss of stiffness due to the 4 inch cutout was beginning to have a noticeable affect on the overall stiffness of the panel. However, the stiffness to mass ratio of the panel has still not drastically been affected, which was attested by the fact that first, second, third, and fifth mode frequencies were varied by only small amounts as compared to Panel 1. The fourth mode was believed to be somewhat of a special case which happened to be extremely sensitive to the inclusion of the cutout. The reader should recall that the fourth mode was also the most affected by the 2 inch square cutout.

The circumferential eccentricity effects of the 4 inch square cutout can best be visualized graphically as shown in Figure 6-42. Figure 6-42 compares Panels 7, 8, and 9. Based on the data presented in this figure the following observations were made. As before, in all cases STAGSC-1 did an excellent job of predicting the same frequency trends that were observed in the experimental data. For all but the fourth mode, the trends in Figure 6-42 represent only minor frequency variations.

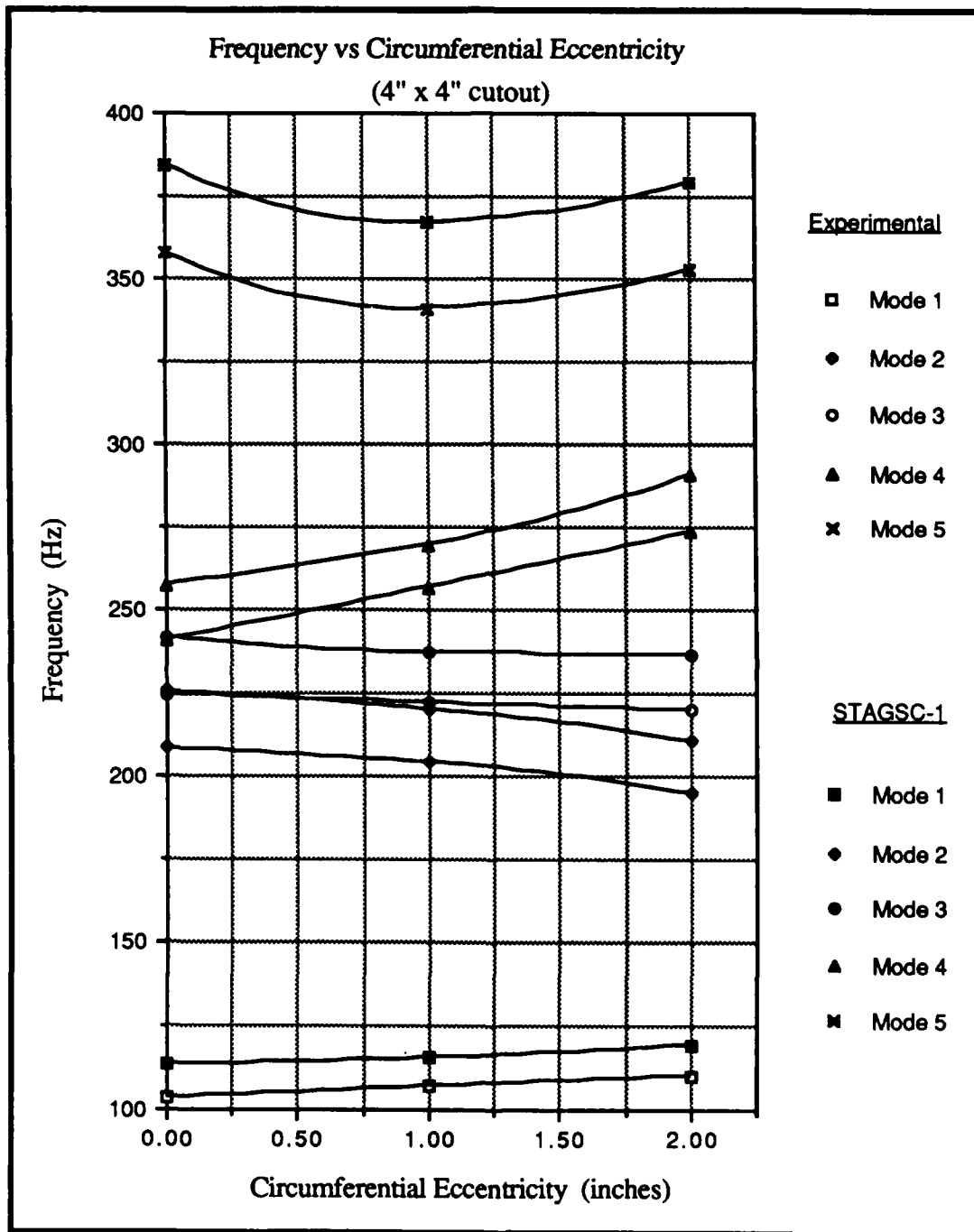


Figure 6-42. Frequency versus Circumferential Eccentricity for 4" Square Cutout

The first mode experimental frequencies increased by 3.2% and 6.5% (compared to Panel 7) for Panels 8 and 9, respectively. For the first mode, the cutout was originally located on a node line. As eccentricity was increased the cutout moved off of the node line and towards an antinode. The increase in frequency indicated that the contribution of the mass (loss of mass) increased as the antinode was approached. The first mode was more sensitive to the larger cutout, as one would expect, due to the fact that the larger cutout represented a much larger percentage of the total panel mass. Also, the larger cutout was nearly as wide as the half waves present in the first mode.

When the 4 inch cutout was introduced, the second mode frequency increased which indicated that the loss of mass, not stiffness, was predominate near the antinode. As circumferential eccentricity was increased, the second mode frequency decreased. These decreases in experimental frequency, relative to Panel 7, were 2.0% and 6.4% for eccentricity values of 1 inch and 2 inches, respectively. As shown by the mode shapes, the cutout was moved from an antinode towards a vertical node line. Near the node line, apparently the loss of cutout mass affected the panel's response less and stiffness effects became dominate. The result, as indicated in Figure 6-42, was a decrease in frequency. Similar second mode behavior was noted for both cutout sizes.

The third mode frequency decreased when the cutout was first introduced and continued to decrease slightly as the circumferential eccentricity increased. The cutout remained on the horizontal node line therefore, effects due to mass remained minimal. For Panel 8, the center of the cutout was to the right side of the left vertical node line (see Figure 6-37). The loss of stiffness caused the side lobes to be "drawn" towards the cutout and became elongated. As the side lobes were "drawn" towards the cutout, the two segments of the left vertical node line became tilted. For Panel 9, the region near the cutout closely resembled the geometry of the fourth mode shape. The loss of stiffness became obvious by observing how unproportionate the side lobes had become. For Panels 8 and 9

the displacements in the side lobes near the cutout became relatively large. This increased the amount of two directional bending present near the cutout. The small decrease in frequency, between Panels 8 and 9, apparently occurred because the cutout was moved to the center of this area of complex bending.

The 4 inch square cutout caused a large drop in the fourth mode frequency and significantly altered the mode shape. For the 1 inch and 2 inch eccentricities the fourth mode frequency with respect to Panel 7, increased by 6.7% and 13.7%, respectively. This represented the largest frequency variation due to eccentricity, experienced by any mode for either of the panels with 2 inch or 4 inch cutouts. As cutout eccentricity was increased, the mode shape experienced a lot of distortion. Describing the fourth mode frequency trend in Figure 6-42 by relating the cutout locations with respect to node line positions could not be done since the node lines moved with the cutout. The mode shapes for Panels 8 and 9 did however give an indication as to which would correspond to the higher frequency. Due to the nature of the panel's curved geometry, it could resist bending around the horizontal node line better than the vertical node lines. That is, the panel would bend easier around a vertical node line lesser than it would around a horizontal node line. As the slope of the vertical node line decreases, the mode shape will correspond to a higher frequency [26]. Therefore the fourth mode shape for Panel 9 would be expected to occur at the higher frequency.

The fifth mode frequency decreased by 4.7% for the 1 inch eccentricity and then increased so that for Panel 9 it was only 1.5% lower than for Panel 7. For Panel 8 the cutout was adjacent to the left vertical node line and extended past the center node line while in Panel 9 the cutout was adjacent to the center node line and extended past the left vertical node line. In both cases the majority of the cutout remained in the same half wave. The difference in frequency between Panels 8 and 9 was slightly over 3%. This represented

only a minor change in frequency but was larger than expected considering the similarity in the mode shapes. No explanation could be determined for this behavior.

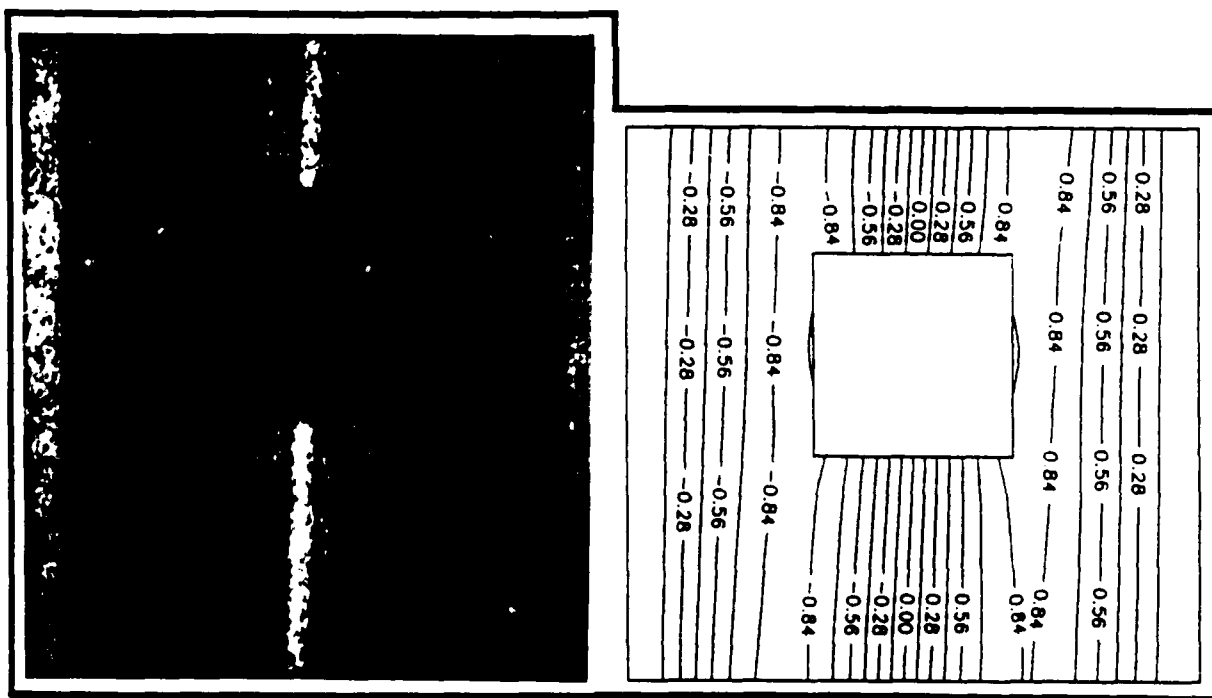
The next section discusses the panels which contained tangentially eccentric 4 inch square cutouts. Their results will be compared to Panel 7.

(3) Panels 10 and 11. These panels contained 4 inch square cutouts which had been eccentrically located in the tangential direction (Figure 3-3). The amounts of eccentricity were 1 inch and 2 inches for Panels 10 and 11, respectively. For the first five modes, a comparison of the experimental and analytical natural frequencies for Panel 10 is found in Table 6-10 and a comparison of the corresponding mode shapes can be found in Figures 6-43 through 6-45. Similar comparisons for Panel 11 are found in Table 6-11 and in Figures 6-46 through 6-48. As before, STAGSC-1 predicted frequencies and mode shapes which correlated well with the experimental data. Tables 6-10 and 6-11 show that STAGSC-1 consistently predicted higher frequencies than those obtained through experimentation. The percent differences obtained for Panel 10 were similar to those obtained for the previous panels but the percent differences for Panel 11 were much better than most. For both panels the largest percent difference was determined to be 8.62% (Mode 1, Panel 10). The resonant frequencies for Panels 10 and 11 along with the other panels with 4 inch square cutouts are presented graphically in Figures 6-33 and 6-34.

Comparison of the mode shapes for Panels 10 and 11, with those obtained for Panel 7, showed that the same basic mode shapes were present. As mentioned before, the biasing towards the -45° fiber direction was also visible in these panels. By examining Figures 6-43 through 6-48, it can be seen that the first, second, and fifth mode shapes were not changed by the tangential eccentricity. The warping of the vertical lines in the second and fifth mode translated with the cutout as would be expected. In the third mode as the cutout was moved upwards, loss of stiffness allowed larger deformations in the top half of

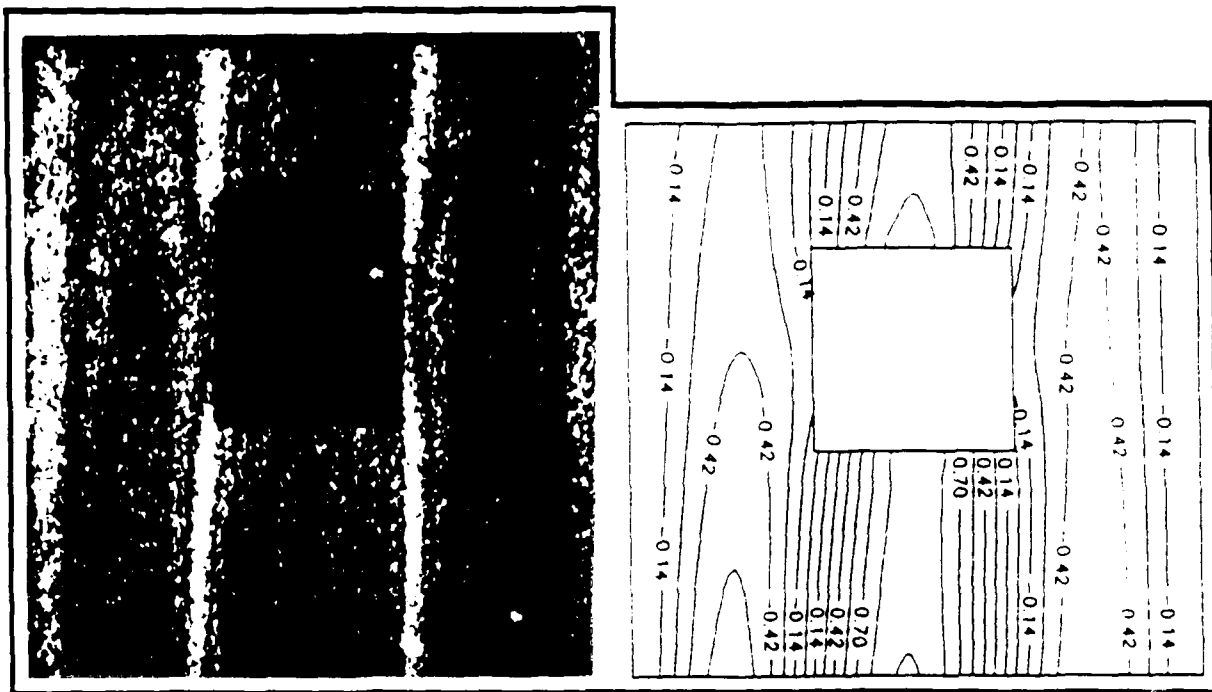
Table 6-10. Comparison of Experimental and Analytical Resonant Frequencies for Panel 10

Mode	Experiment (Hertz)	STAGSC-1 (Hertz)	Percent Difference
1	104.2	113.18	8.62
2	207.2	224.94	8.56
3	225.8	243.50	7.84
4	242.1	260.32	7.52
5	357.8	384.78	7.54

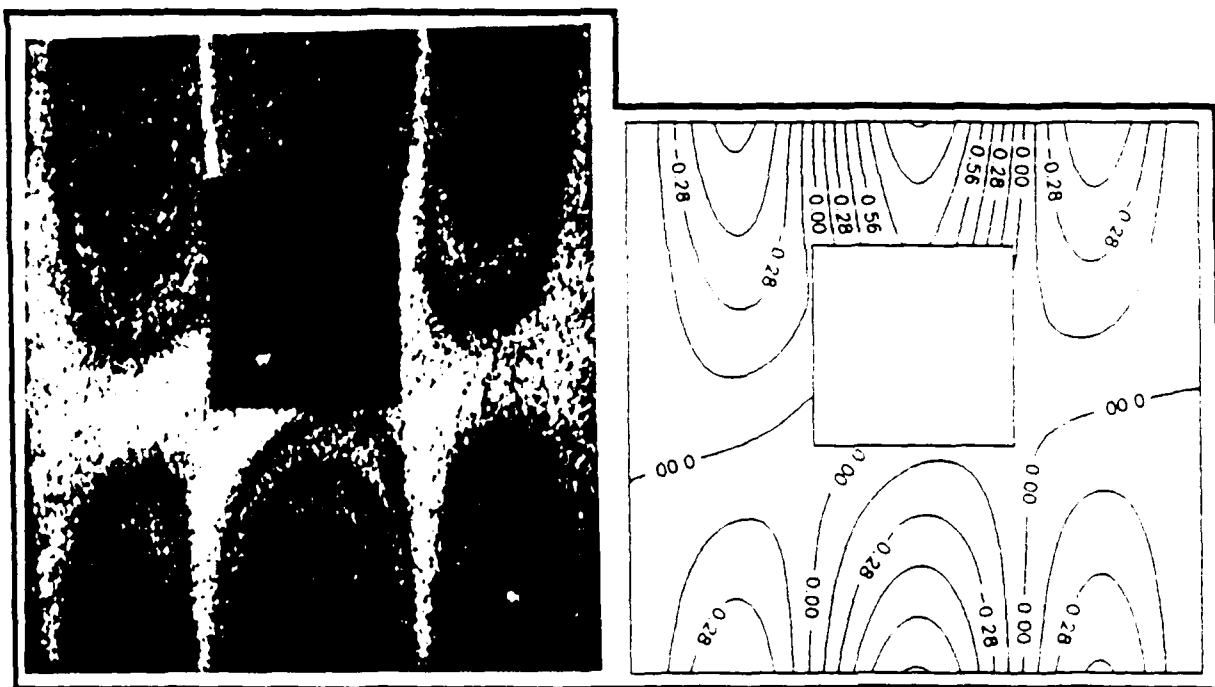


Mode 1

Figure 6-43. First Mode Shape for Panel 10

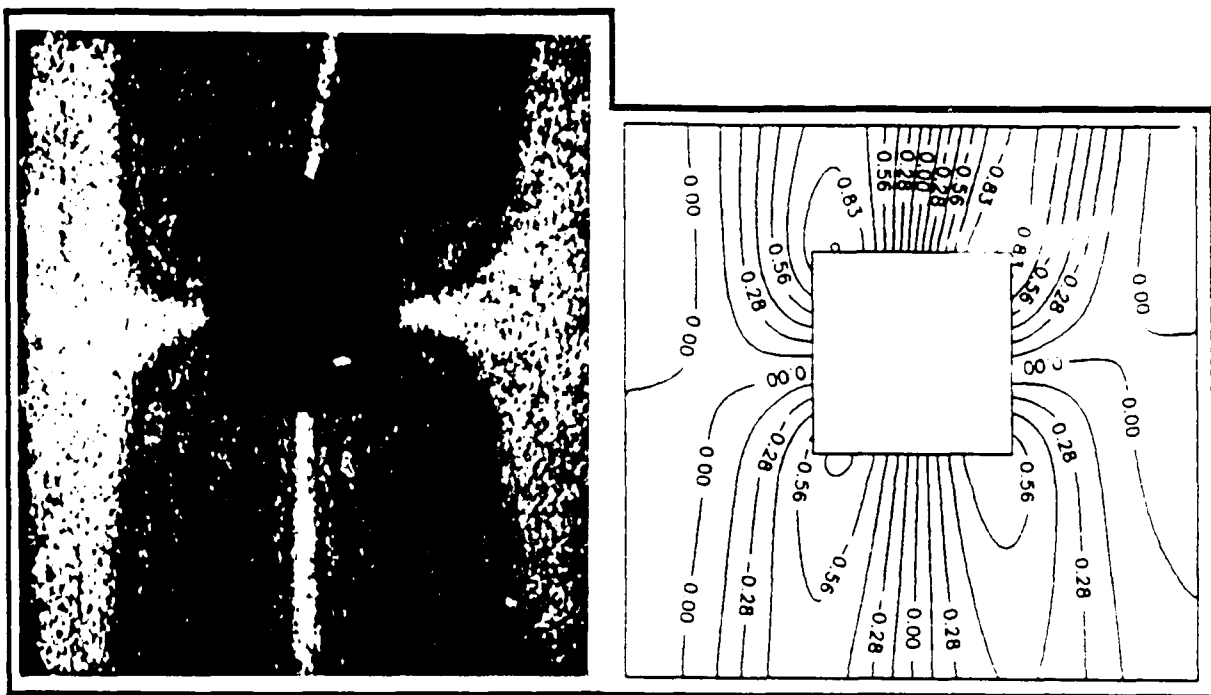


Mode 2

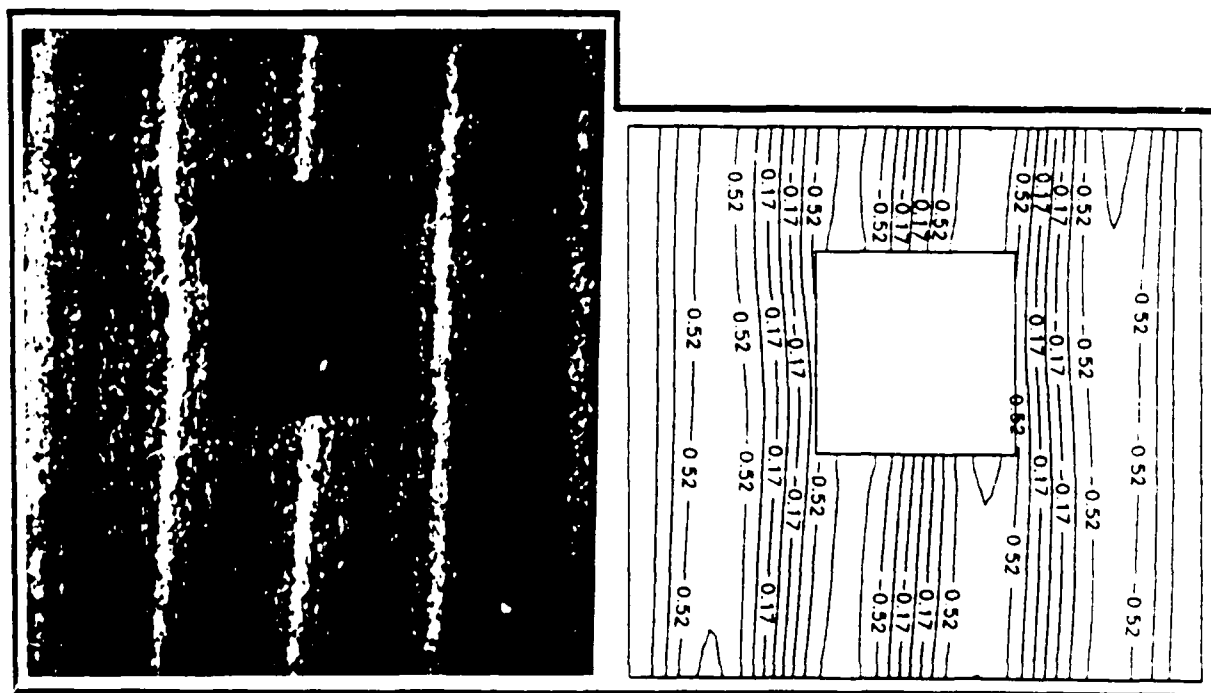


Mode 3

Figure 6-44. Second and Third Mode Shapes for Panel 10



Mode 4

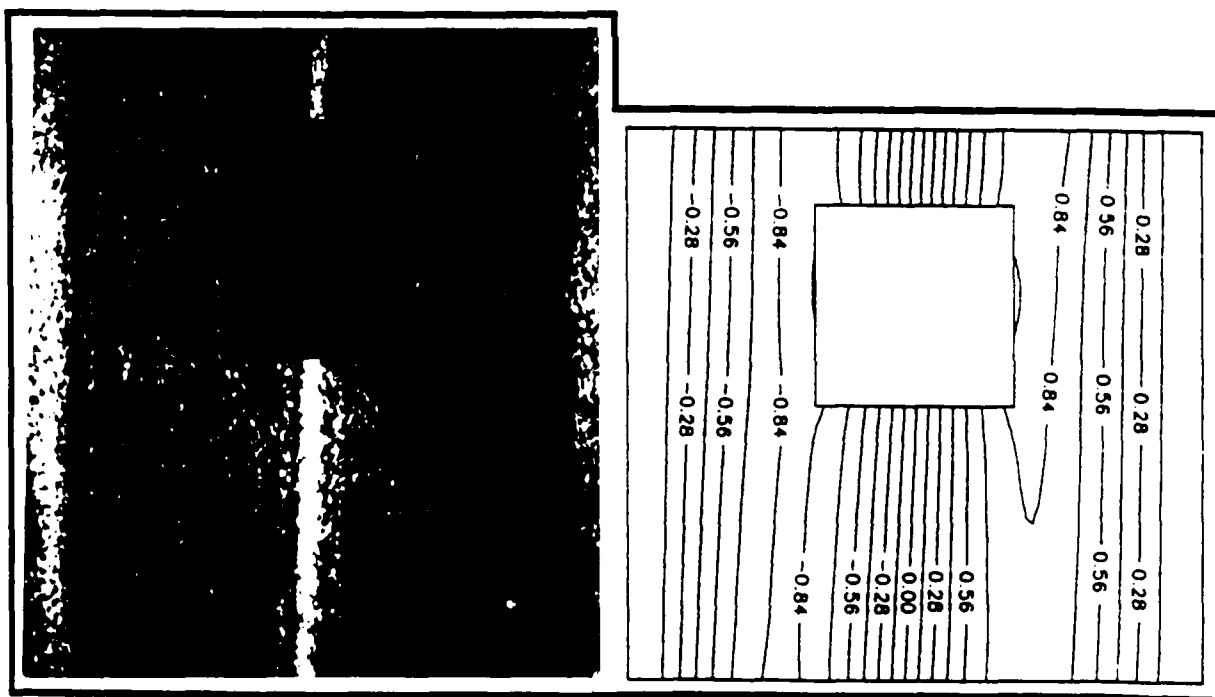


Mode 5

Figure 6-45. Fourth and Fifth Mode Shapes for Panel 10

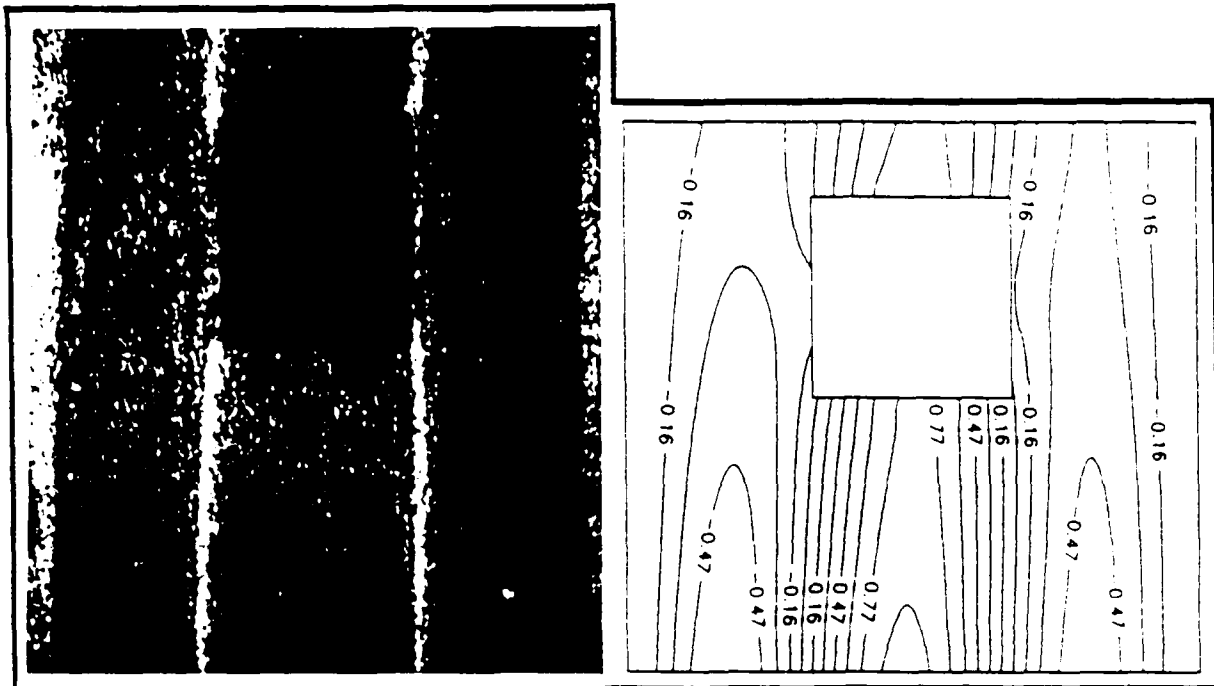
Table 6-11. Comparison of Experimental and Analytical Resonant Frequencies for Panel 11

Mode	Experiment (Hertz)	STAGSC-1 (Hertz)	Percent Difference
1	105.2	112.88	7.30
2	210.6	223.91	6.32
3	235.0	249.10	6.00
4	255.9	269.99	5.50
5	365.3	385.33	5.48

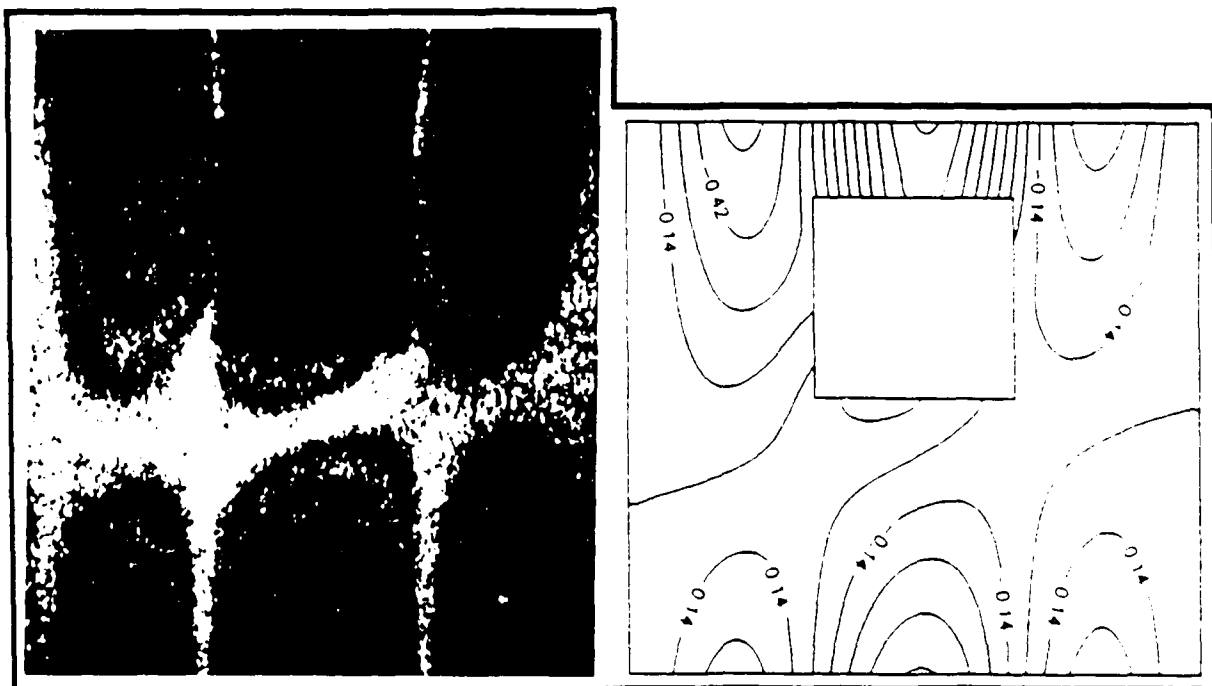


Mode 1

Figure 6-46. First Mode Shape for Panel 11

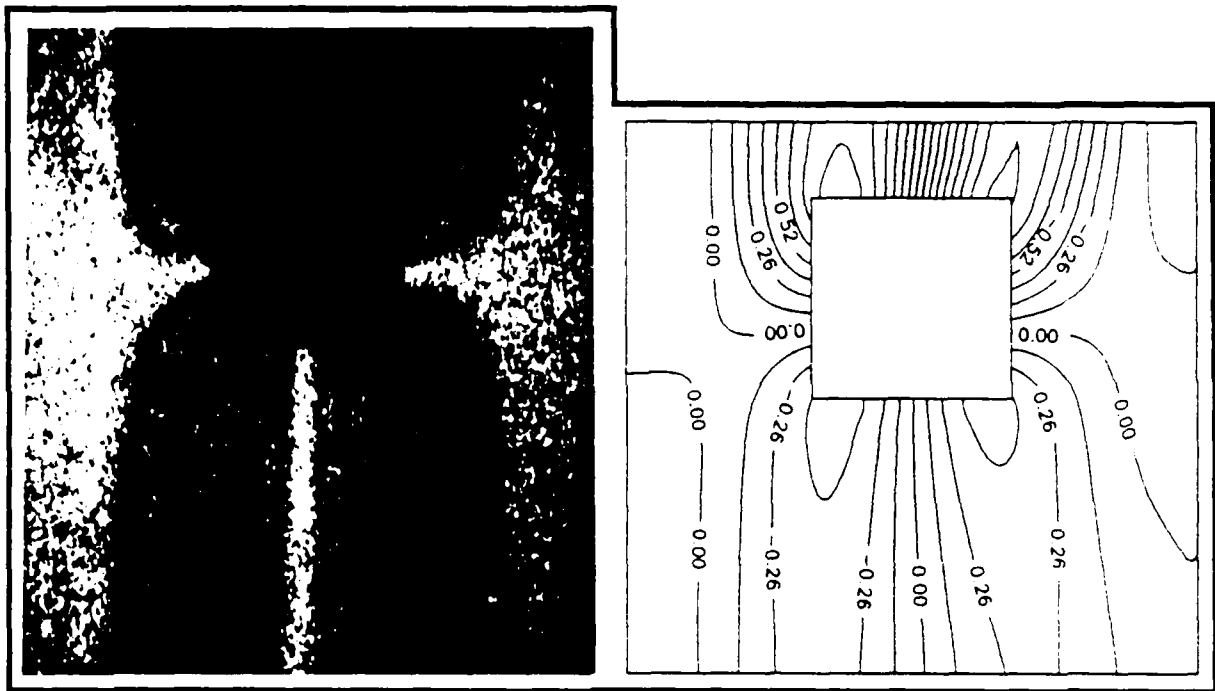


Mode 2

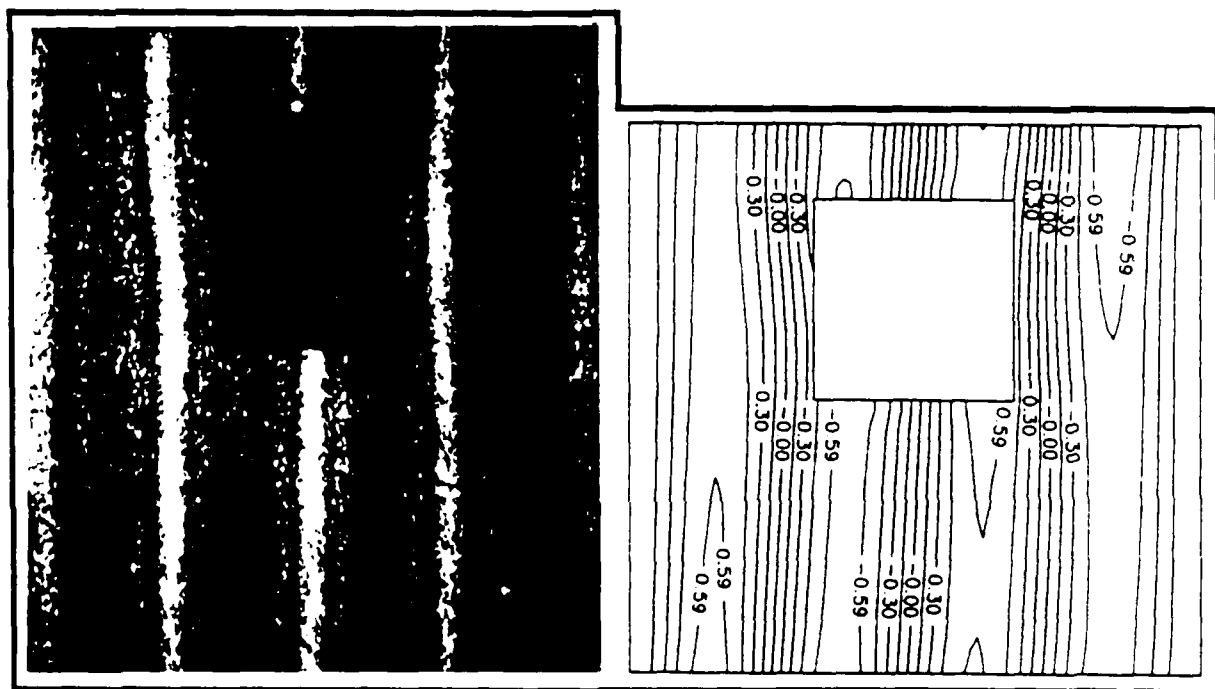


Mode 3

Figure 6-47. Second and Third Mode Shapes for Panel 11



Mode 4



Mode 5

Figure 6-48. Fourth and Fifth Mode Shapes for Panel 11

the panel which caused the bottom lobes to shorten and the top lobes to elongate. The tangential eccentricity had the largest effect on the fourth mode shape. The intersection of the vertical and horizontal node lines in the fourth mode shapes represented a region of the panel in which two directional bending was present. Normally, this intersection occurred near the center of the panel. With the 4 inch square cutout, the loss of stiffness was substantial enough that this region of complex bending now formed at the cutout (weakest part of the panel) instead of at the center of the panel. Therefore, as the eccentricity of the cutout was increased, the horizontal node line moved with the cutout and the top lobes and bottom lobes were substantially shortened and lengthened, respectively. Also for the fourth mode, as the cutout moved upward, the biasing (towards the -45° direction) of the top segment of the vertical node line was enhanced and the bottom segment appeared to be axial.

The tangential eccentricity effects on the natural frequencies of the panel can best be visualized in Figure 6-49. The first, second, and fifth modes were relatively insensitive to the tangential eccentricity. The fifth mode at first seemed to experience a notable increase between the 1 inch and 2 inch eccentricity values. However, this increase turned out to be only 2% and was thus considered insignificant. The third and fourth experimental frequencies showed no change for the 1 inch eccentricity and then at the 2 inch eccentricity they increased by 4.7% and 6.4%, respectively. After inspection of the mode shapes, no conclusive explanation could be reached as to why this increase occurred. For the 4 inch cutout, the top edge of the cutout was only 1.5 inches from the edge. Possibly, the large discontinuity caused by the larger cutout was interacting in some way with the free edge to cause the frequency increase observed. An observation concerning the trends predicted by STAGSC-1 was also made. The analytical trends for the circumferential and tangential eccentricity of the 2 inch square cutout as well as the circumferential eccentricity of the 4 inch square cutout were all very good. However, in Figure 6-49 the predicted trends

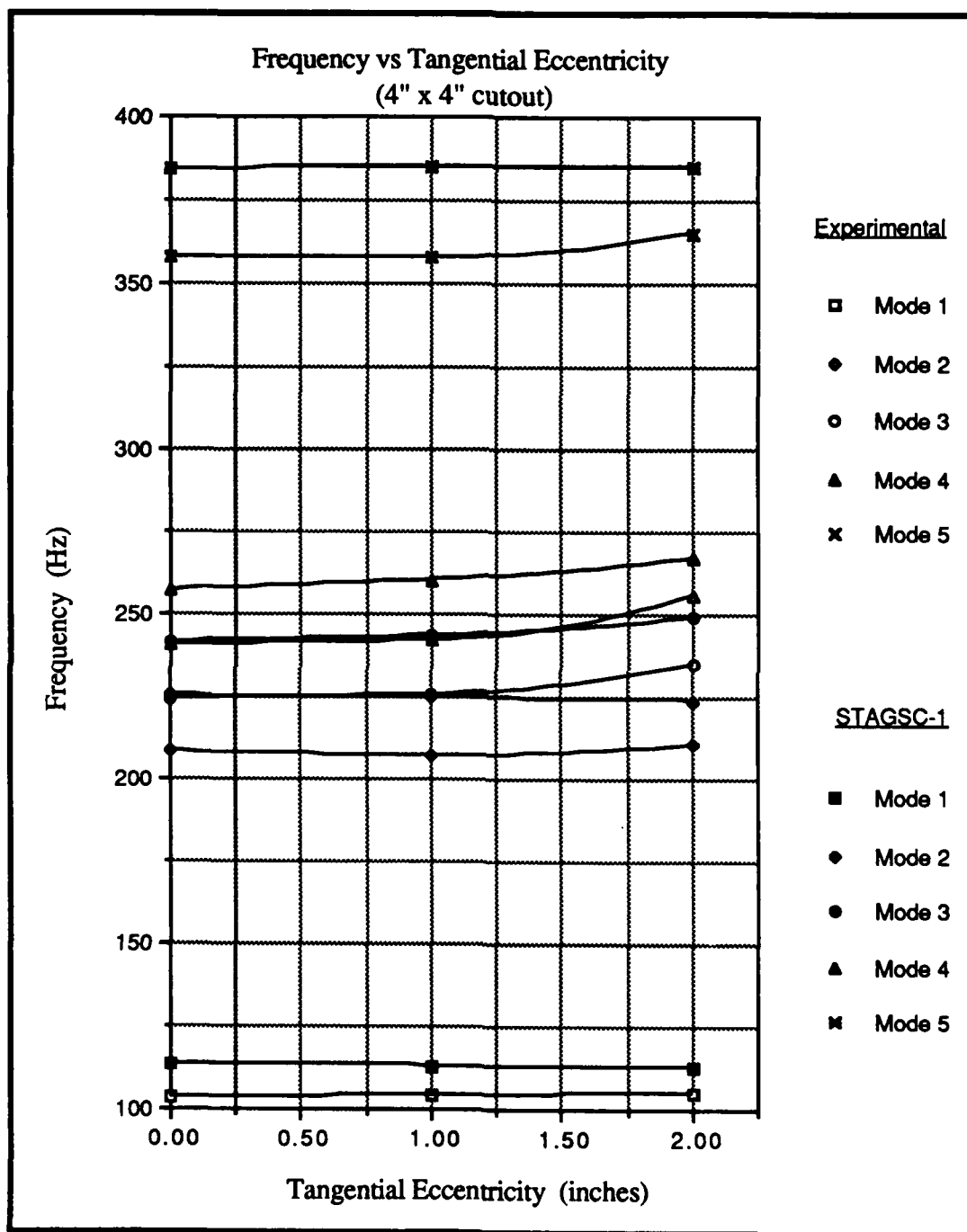


Figure 6-49. Frequency versus Tangential Eccentricity for 4" Square Cutout

deviate from the experimental trends particularly for the 2 inch eccentricity in the fourth and fifth modes. This was not expected. The circumferential direction was believed to be the worst case since all modes experienced radial variation in this direction. It was also considered that possibly the experimental data was in error due to a defect or other minor variation in Panel 11 which only became apparent at the higher modes. The fourth and fifth modes for Panel 11 were the only cases of significant deviation noticed. No firm explanation for this deviation was forthcoming.

This completes the discussion on the panels which were analyzed both experimentally and analytically. The next section presents a summary of STAGSC-1's performance.

D. STAGSC-1's Performance

The natural frequencies predicted by STAGSC-1 correlated well with those obtained experimentally. Similarly, the analytical mode shape predictions were excellent. It hardly seems necessary to devote an entire section of this chapter reiterating these two statements which have been made numerous times before. Primarily, this section was included to discuss an additional observation that was made. After reviewing the percent differences obtained for the original eleven panels investigated by this study, it was observed that they were relatively consistent between panels and averaged approximately 7.5%. Mr. Maddux [26] stated that such consistent percent differences indicated there was possibly an error in the material properties input into the STAGSC-1 program. The material properties used in the finite element models had been obtained from tensile tests of coupons. These coupons had been manufactured along with the panels (see Chapter III). The material properties obtained from these coupons represented the static behavior of the Gr/Ep from which the panels were made. However according to Mr. Maddux, the static modulus may not be representative of the dynamic modulus for the Gr/Ep material. The

dynamic modulus (stiffness) arises from the phenomena that some material responded differently when loaded dynamically as opposed to statically. Mr. Maddux has experienced materials in which the static and dynamic stiffness values differed by as much as 25% [26]. Therefore, it was speculated that the dynamic stiffness of the Gr/Ep was different from the value obtained from tensile testing. This would account for the relatively consistent percent differences observed in the data. To determine the dynamic stiffness of the Gr/Ep material would have required resources which were not available for this thesis. Mr. Maddux suggested that the frequencies be normalized in order to remove the material property dependence. The frequencies were normalized by dividing the first five experimental and analytical resonant frequencies by the corresponding fifth mode frequency. Thus, the largest normalized frequency was equal to one. The experimental and analytical normalized frequencies were compared for the solid panel (Panel 1) and the two panels with centered cutouts (Panels 2 and 7). These three panels were representative of the variation in percent differences observed for the panels and it was felt that they would be sufficient to illustrate the point intended. The normalized experimental and analytical frequencies for Panels 1, 2, and 7 are presented in Tables 6-12, 6-13, and 6-14, respectively. By definition, the fifth mode normalized frequencies were equal to unity and thus, no comparison between percent differences for this mode could be performed. The percent differences in Tables 6-12 through 6-14 are excellent. Therefore, it was believed that STAGSC-1 did an outstanding job of predicting the resonant frequencies and mode shapes and that the percent differences reported in Tables 6-1 through 6-11 would have been reduced if the material properties of the Gr/Ep had been more accurately known.

The next section presents the results for the panels with 3 inch and 5 inch square cutouts (Panels 12 through 21). These panels were not part of the actual thesis and were only studied analytically.

Table 6-12. Normalized Frequencies for Panel 1

Mode	Experiment	STAGSC-1	Percent Difference
1	0.2943	0.2997	1.83
2	0.5505	0.5528	0.42
3	0.6366	0.6307	0.93
4	0.9461	0.9366	1.00
5	1.0000	1.0000	—

Table 6-13. Normalized Frequencies for Panel 2

Mode	Experiment	STAGSC-1	Percent Difference
1	0.3007	0.3033	0.86
2	0.5692	0.5699	0.12
3	0.6368	0.6395	0.42
4	0.9089	0.9239	1.65
5	1.0000	1.0000	—

Table 6-14. Normalized Frequencies for Panel 7

Mode	Experiment	STAGSC-1	Percent Difference
1	0.2894	0.2945	1.76
2	0.5818	0.5860	0.72
3	0.6268	0.6280	0.19
4	0.6721	0.6692	0.43
5	1.0000	1.0000	—

E. Panels with 3" and 5" Square Cutouts

The analysis of the panels with 3 inch and 5 inch square cutouts was performed in addition to the required thesis. Due to time constraints, only limited analysis was possible. The panels with the 3 inch square cutouts correspond to Panels 12, 13, 14, 15, and 16, and the panels with 5 inch square cutouts correspond to Panels 17, 18, 19, 20, and 21. The panels with 3 inch and 5 inch square cutouts were studied only analytically using the STAGSC-1 program. Time did not allow for the plotting of mode shapes for the panel, therefore only the frequencies are represented. Three inch and five inch square cutouts were selected because the panels with 3 inch cutouts would provide data points in between the two cutout sizes experimentally examined and the panels with 5 inch cutouts would extend the experimental data. The following discussion includes a comparison between Panel 1 (solid panel) and the panels with centered 3 inch and 5 inch cutouts. Also included

are graphs which show the frequency variations caused by the circumferentially and tangentially eccentric cutouts.

(1) Panels 12 Through 16. Panel 12 contained a centered 3 inch square cutout. Panels 13 and 14 contained cutouts with circumferential eccentricity while Panels 15 and 16 contained cutouts with tangential eccentricity. The first five natural frequencies for these panels are presented in Table 6-15. These frequencies are shown graphically in Figure 6-50. As can be seen in Figure 6-50, the frequency variation for the panels with 3 inch square cutouts were small compared to Panel 1 for all modes but the fourth. The centered 3 inch cutout caused the analytical natural frequencies to change by -2.1%, +3.7%, -1.0%, -11.5%, and -3.0% for modes 1 through 5, respectively. As was noticed for the 2 inch and 4 inch

Table 6-15. Natural Frequencies for Panels 12 Through 16

Panel Number	Natural Frequencies for Modes 1 Through 5 (Hertz)				
	1	2	3	4	5
12	115.44	225.41	245.44	325.93	381.23
13	116.51	218.77	243.33	334.10	385.38
14	118.57	211.31	241.94	348.21	385.24
15	115.41	225.08	247.12	327.34	381.28
16	115.28	224.29	252.18	331.74	381.47

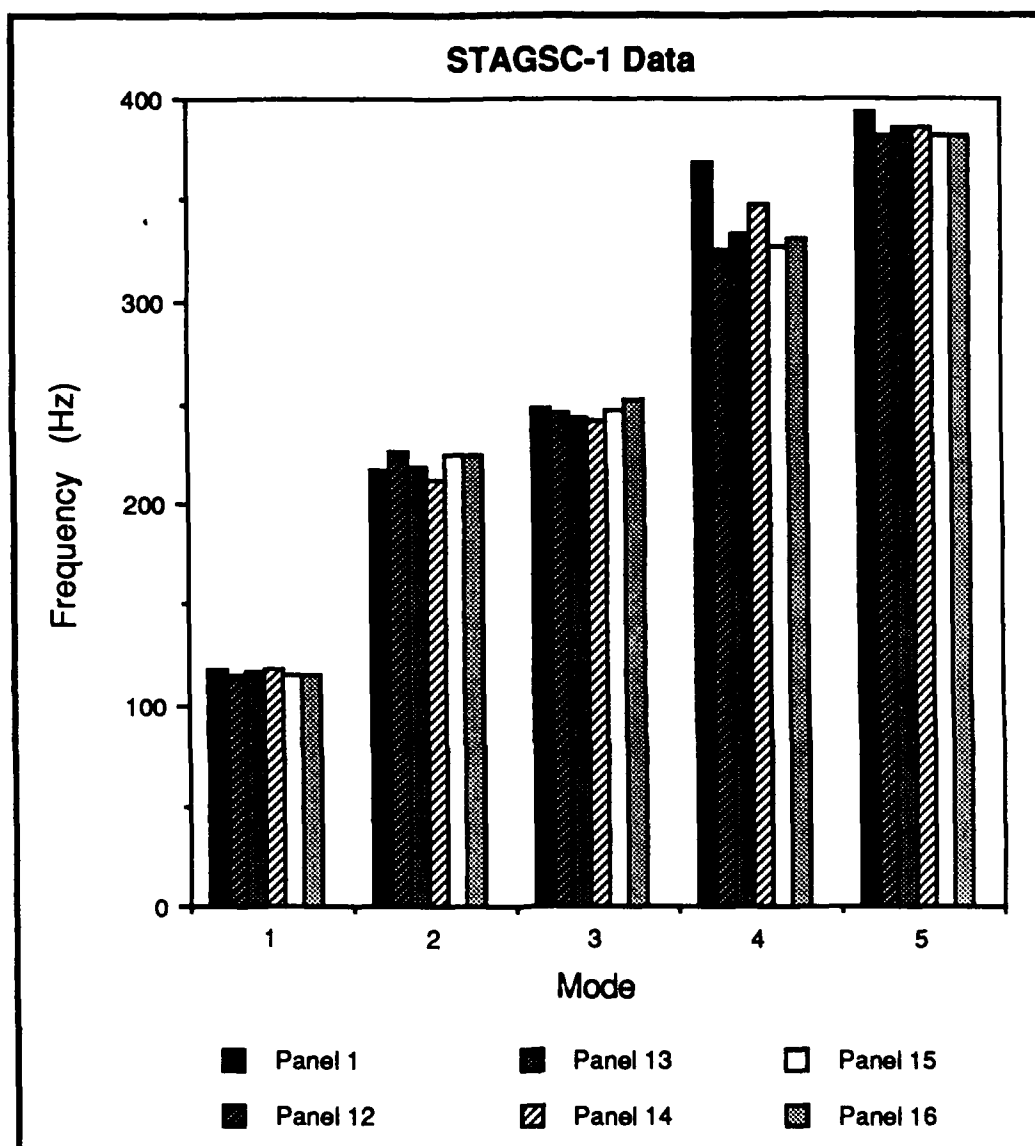


Figure 6-50. Analytical Frequency versus Mode for Panels 1, 12, 13, 14, 15, and 16

square cutouts, the second mode frequency was the only one which increased, and the fourth mode frequency showed the most sensitivity to the inclusion of the cutout.

The effects of circumferential eccentricity of the 3" square cutout can best be seen in Figure 6-51. The first, third, and fifth modes were relatively insensitive to the circumferential eccentricity. The second mode decreased and the fourth mode increased due to eccentricity. The variations in frequency at the 2 inch circumferential eccentricity location were -6.3% and +6.8% for the second and fourth modes, respectively.

The frequency variations due to tangential eccentricity are presented in Figure 6-52. As shown in Figure 6-52, none of the first five modes were sensitive to the tangential eccentricity. The largest percent change in frequency was 2.8% for the third mode of Panel 16.

The modes shapes for Panels 12 through 16 were unavailable and therefore an analysis of the mode shapes was not conducted. The first, second, third, and fifth mode shapes were basically the same for the panels with 2 inch and 4 inch cutouts. Thus, it is highly probable that these modes would have similar mode shapes for the panels with 3 inch square cutouts. The fourth mode shape changed substantially between the 2 inch and 4 inch square cutouts. The fourth mode shape for Panel 2 contained eight antinodes while Panel 7 contained four antinodes. Compared to Panel 1, STAGSC-1 predicted fourth mode frequency changes of -3.0%, -11.5%, and -30.1% for the 2 inch, 3 inch, and 4 inch centered cutouts, respectively. The -11.5% change in frequency for Panel 12 was not believed large enough to represent the substantial change in mode shape present between Panels 2 and 7. Therefore, the fourth mode shapes for the panels with 3 inch square cutouts most likely resemble those obtained for similar panels (same direction and magnitude of eccentricity) with the 2 inch cutouts.

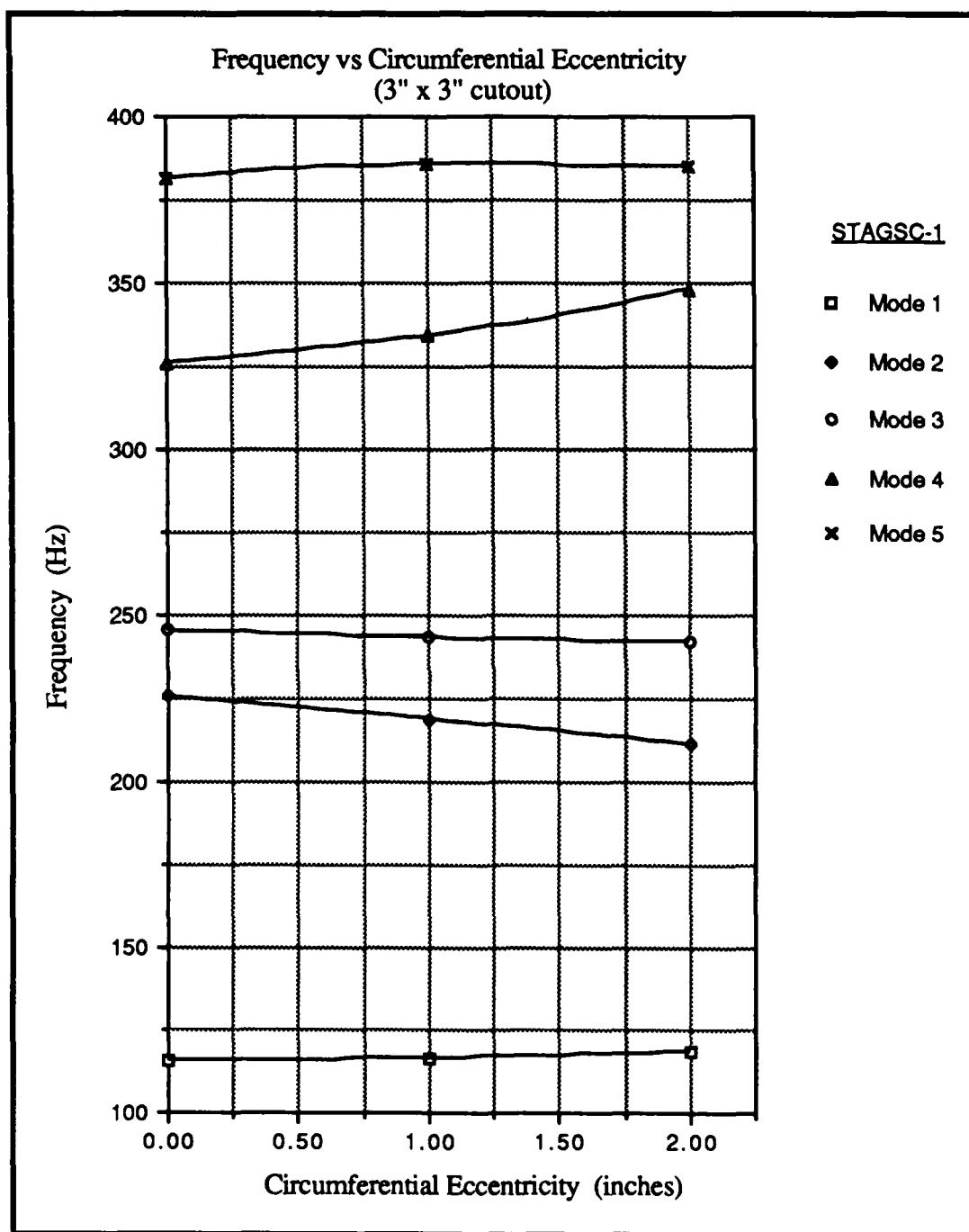


Figure 6-51. Frequency versus Circumferential Eccentricity for 3" Square Cutout

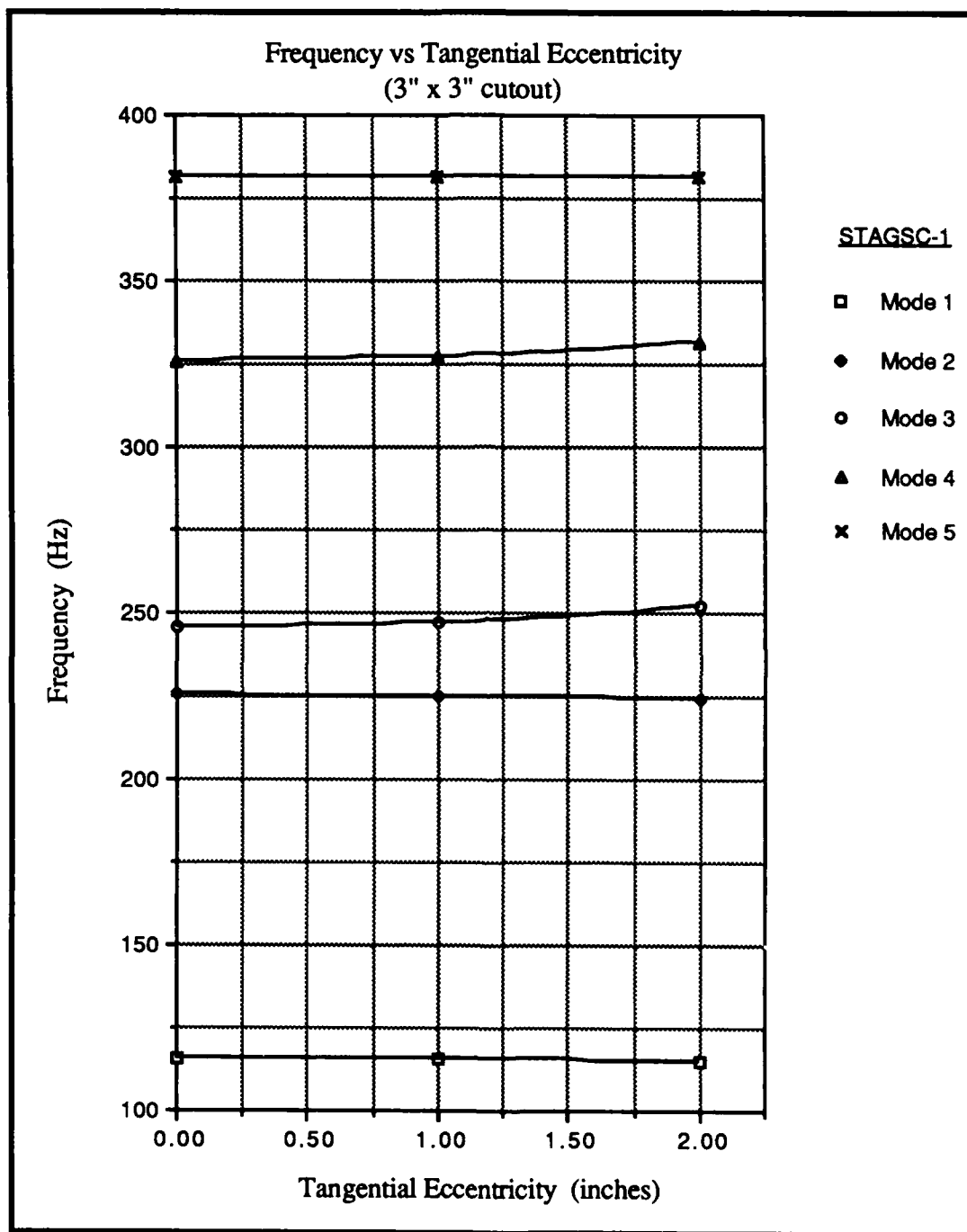


Figure 6-52. Frequency versus Tangential Eccentricity for 3" Square Cutout

At most, only small frequency changes were observed by eccentrically locating the 3 inch square cutout in the circumferential and tangential directions. The panels with 5 inch square cutouts are discussed in the next section.

(2) Panels 17 Through 21. Panel 17 contained a centered 5 inch square cutout. Panels 18 and 19 contained cutouts with circumferential eccentricity while Panels 20 and 21 contained cutouts with tangential eccentricity. The first five natural frequencies for these panels are presented in Table 6-16. These frequencies are shown graphically in Figure 6-53. One should notice in Figure 6-53 that the fourth mode frequency was the most sensitive to the introduction of the cutout and shows a dramatic drop in frequency for all panels with the 5 inch square cutouts. This was similar to the behavior observed for the panels with 4 inch square cutouts. Also, the second and third mode frequencies showed a notable decrease in frequency due to 5 inch cutout while the first and fifth mode frequencies were relatively unchanged. The 5 inch cutout was the only cutout considered (experimentally or

Table 6-16. Natural Frequencies for Panels 17 Through 21

Panel Number	Natural Frequencies for Modes 1 Through 5 (Hertz)				
	1	2	3	4	5
17	113.11	193.49	215.67	235.56	376.59
18	115.04	196.83	221.31	239.92	354.81
19	117.15	207.54	220.43	248.62	371.21
20	112.98	196.56	215.49	236.17	377.15
21	112.67	206.57	214.91	237.89	379.90

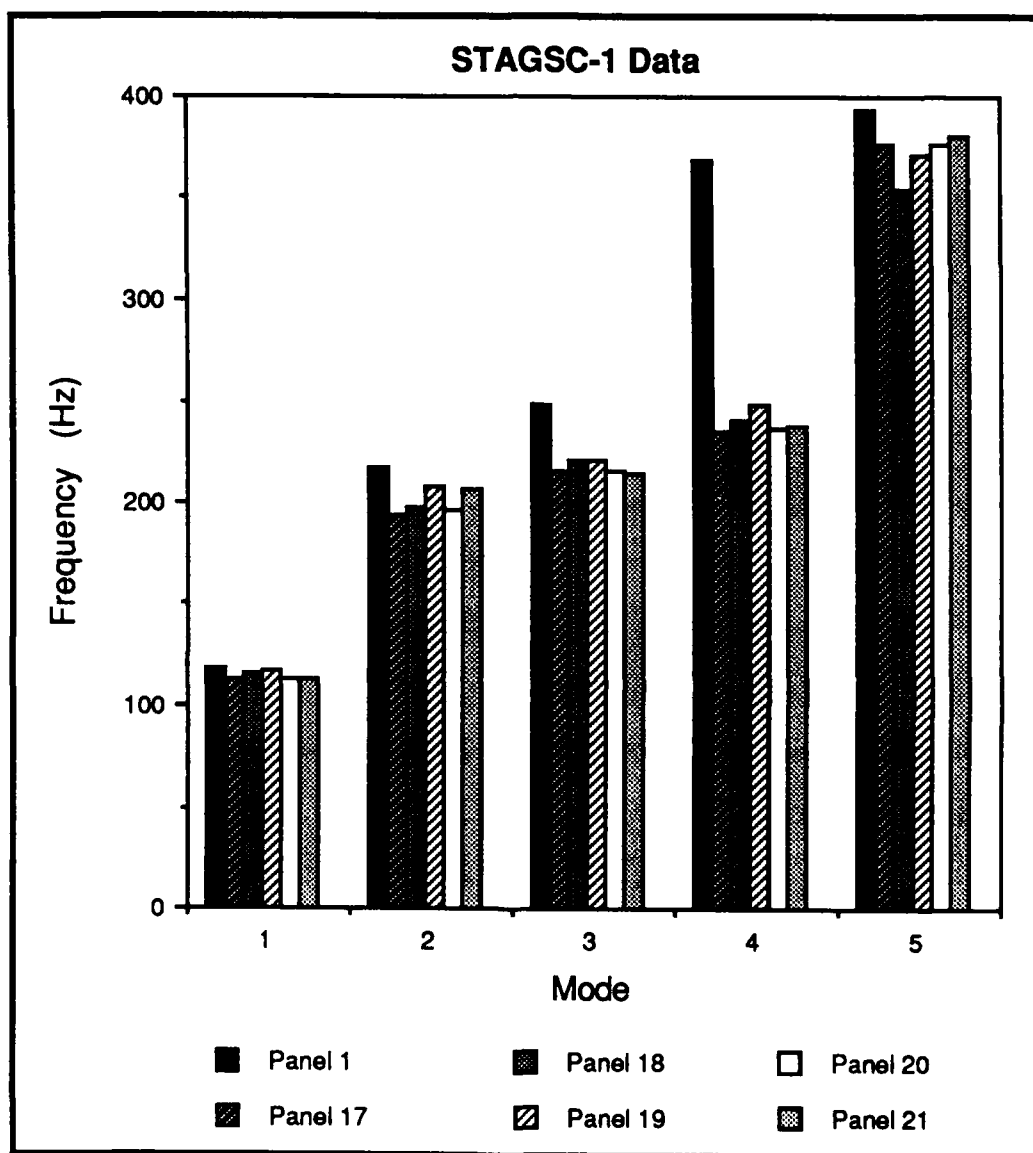


Figure 6-53. Analytical Frequency versus Mode for Panels 1, 17, 18, 19, 20, and 21

analytically) which caused the second mode frequency to decrease when it was introduced. If one compares Figure 6-53 to similar figures for previous panels (Figures 6-14, 6-34, and 6-50) the variations in frequency are seen to be much larger indicating that the loss of stiffness due to the cutout was becoming more predominate than the loss of mass as the cutout size increased.

The centered 5 inch cutout caused the analytical natural frequencies to change by -4.0%, -11.0%, -13.0%, -36.0% and -4.2% for modes 1 through 5, respectively. The effects of circumferential eccentricity of the 5 inch cutout can best be seen in Figure 6-54. The first, third, and fifth modes were relatively insensitive to the circumferential eccentricity. From Figure 6-54, the variations in fifth mode at first appeared notable. However, the largest change shown in fifth mode frequency was -3.5%, at the 1 inch circumferential eccentricity value. This represented only a minor change in frequency and the fifth mode was considered relatively insensitive. The second and third mode frequencies were the most affected by the circumferential eccentricity. Still only small frequency changes were observed. At the 2 inch circumferential eccentricity value, the second and fourth mode frequencies increased by 7.2% and 5.5%, respectively.

The frequency variations due to tangential eccentricity are presented in Figure 6-55. As shown in Figure 6-55, the second mode frequency experienced the largest change due to the tangential eccentricity. The change in second mode frequency progressively increased to 6.8% at the 2 inch eccentricity location (Panel 21). The first, third, fourth, and fifth mode frequencies were relatively insensitive to the tangential eccentricity.

The mode shapes for Panels 17 through 21 were unavailable and therefore an analysis of the mode shapes could not be conducted. It was speculated that the mode shapes for Panels 17 through 21 would resemble those obtained for similar panels with 4 inch square cutouts (Panels 7 through 11). This was based on the similarity in frequencies observed between the panels with 4 inch and 5 inch square cutouts. However, after discussion with

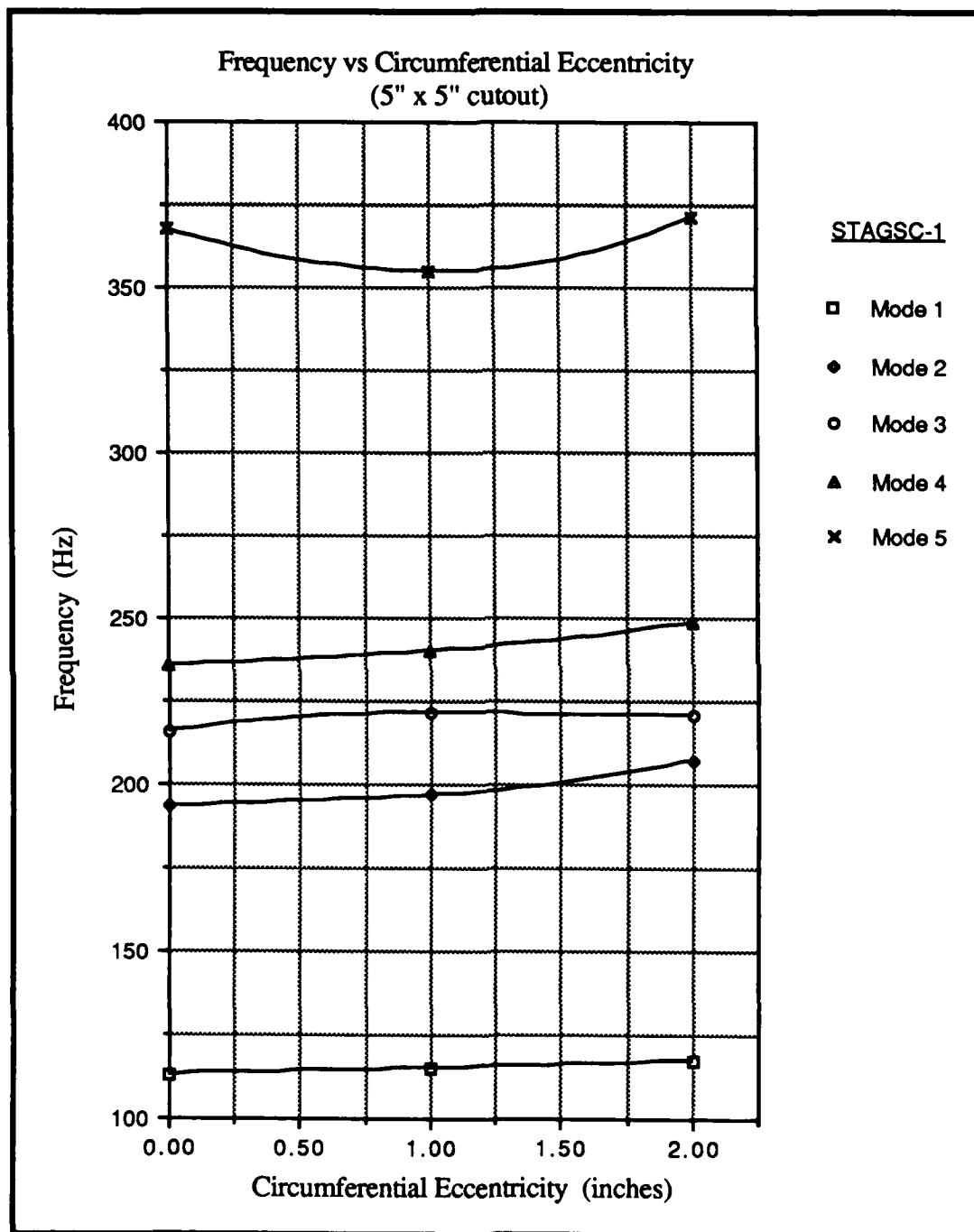


Figure 6-54. Frequency versus Circumferential Eccentricity for 5" Square Cutout

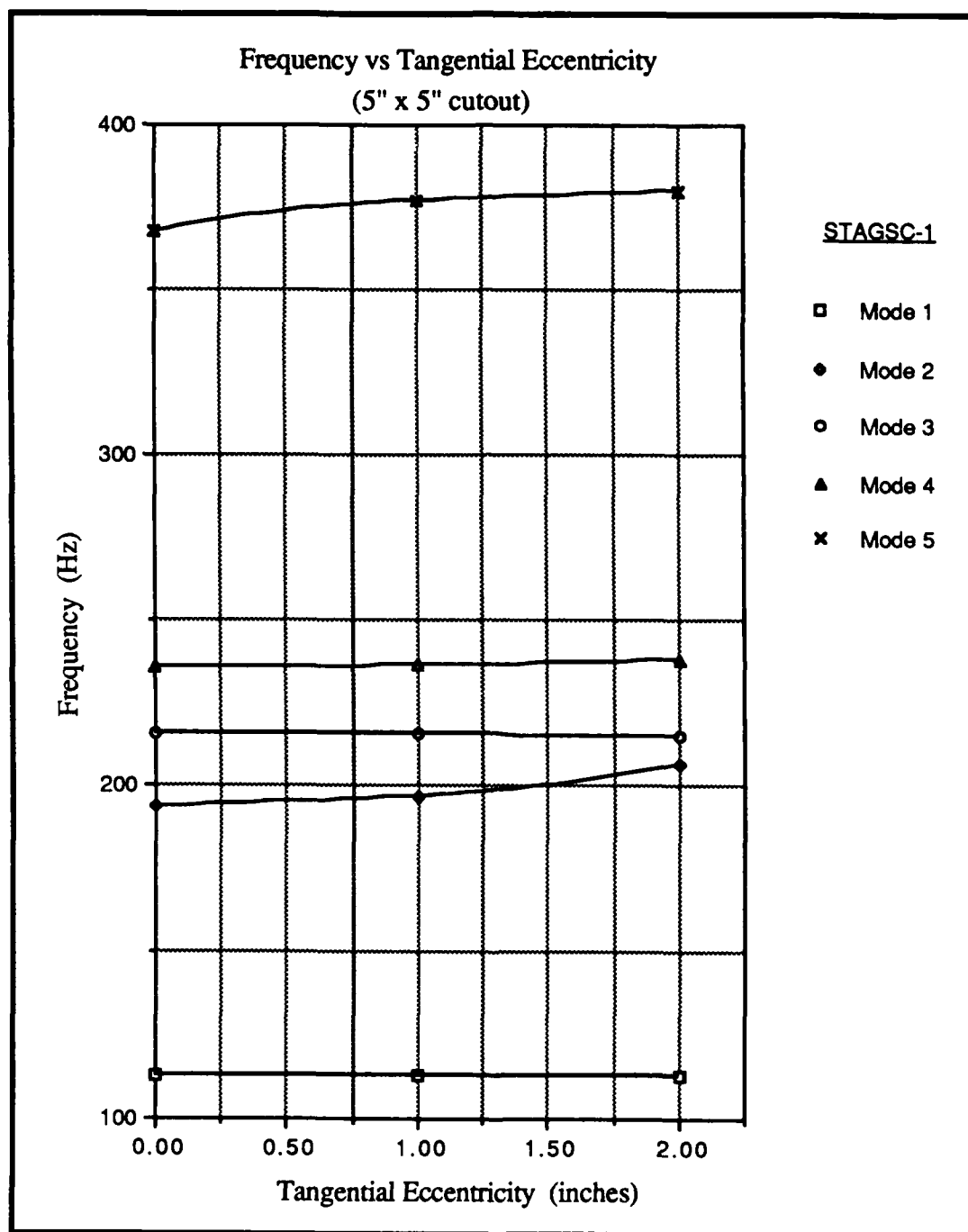


Figure 6-55. Frequency versus Tangential Eccentricity for 5" Square Cutout

Mr. Maddux [26], it was decided that while similar to the panels with 4 inch cutouts, the mode shapes for the panels with 5 inch cutouts would probably show more variation in radial displacement along the tangential direction. This was because the cutout is now large enough that the widths of the four panel sections surrounding the cutout are now substantially smaller than the width of the cutout. Thus, these four sections will want to respond more as an individual entity than as a whole panel. The bottom and top pieces would begin to respond as two thin strips of curved panel and the pieces along the side boundaries would want to behave similar to two small cantilevered panels. Therefore, no elaboration on the behavior of the panels with 5 inch square cutouts would be possible without having the mode shapes available.

The introduction of the 5 inch square cutout caused the largest drop in frequencies observed for any of the panels studied. The panel stiffness to mass ratio decreased as cutout size increased as is indicated if Figures 6-14, 6-34, 6-50, and 6-53 are compared (frequencies generally decrease). Circumferential eccentricity of the 5 inch square cutout caused only small frequency changes while the tangential eccentricity caused only minor frequency changes. The next section presents a summary on the results obtained for centered and eccentrically located cutouts.

F. Summary

This section summarizes the discussion which was presented in Sections A through D of Chapter VI. Two main areas are included in this summary. First, the effects of the introduction of a cutout are discussed. For this discussion only the centered cutouts are considered. The second area summarized will be the effects resulting from eccentrically locating a cutout on the panel. For this sub-topic, the effects of circumferential and tangential eccentricity are discussed separately.

(1) Summary of Cutout Effects. The 2 inch and 4 inch cutouts were investigated both experimentally and analytically, while the 3 inch and 5 inch cutouts were investigated only analytically. The effects the centered cutouts had on a given mode depended on several factors, some of which were the cutout size, complexity of the mode shape, and location of the cutout with respect to node lines and antinodes. The cutout size had the most significant effect on the amount of frequency change experienced by the panels; however, the reader should be aware that except for the fourth mode, the frequency variations observed were usually small ($< 10\%$). The centered 5 inch square cutout was the only centered cutout to cause frequencies, other than the fourth mode frequency, to change by over 10%. For the 5 inch cutout, the second and third mode frequencies changed by -11.0% and -13.0%, respectively. The fourth mode was found to be the most sensitive to all cutout sizes. Apparently, the complexity of the bending occurring in the fourth mode caused an increased sensitivity to the stiffness lost by adding the cutout.

The effects of the cutouts on the panel's natural frequencies can best be shown by a graph as presented in Figure 6-56. In Figure 6-56, the natural frequencies for the panels were plotted versus the percent of mass removed by the cutout. The percent mass removed was also equal to the percent of the panel's surface area removed by the cutout. The percentage of mass removed was determined by dividing the amount of mass lost due to the cutout by the total mass of the panel. The percentage of mass removed by the 2 inch (Panel 2), 3 inch (Panel 12), 4 inch (Panel 7), and 5 inch (Panel 17) square cutouts were 3.03%, 6.82%, 12.12%, and 18.94%, respectively. The data points in Figure 6-56 were connected to help the reader with the identify trends. They do not imply that the panel's behavior will follow exactly these curves. For example, the fifth mode analytical frequency decreases slightly for the 3 inch square cutout. Obviously, since no experimental data was taken for the 3 inch square cutout, no such indication was present in the fifth mode experimental frequency curve. Which curve, if either, represented the actual response was

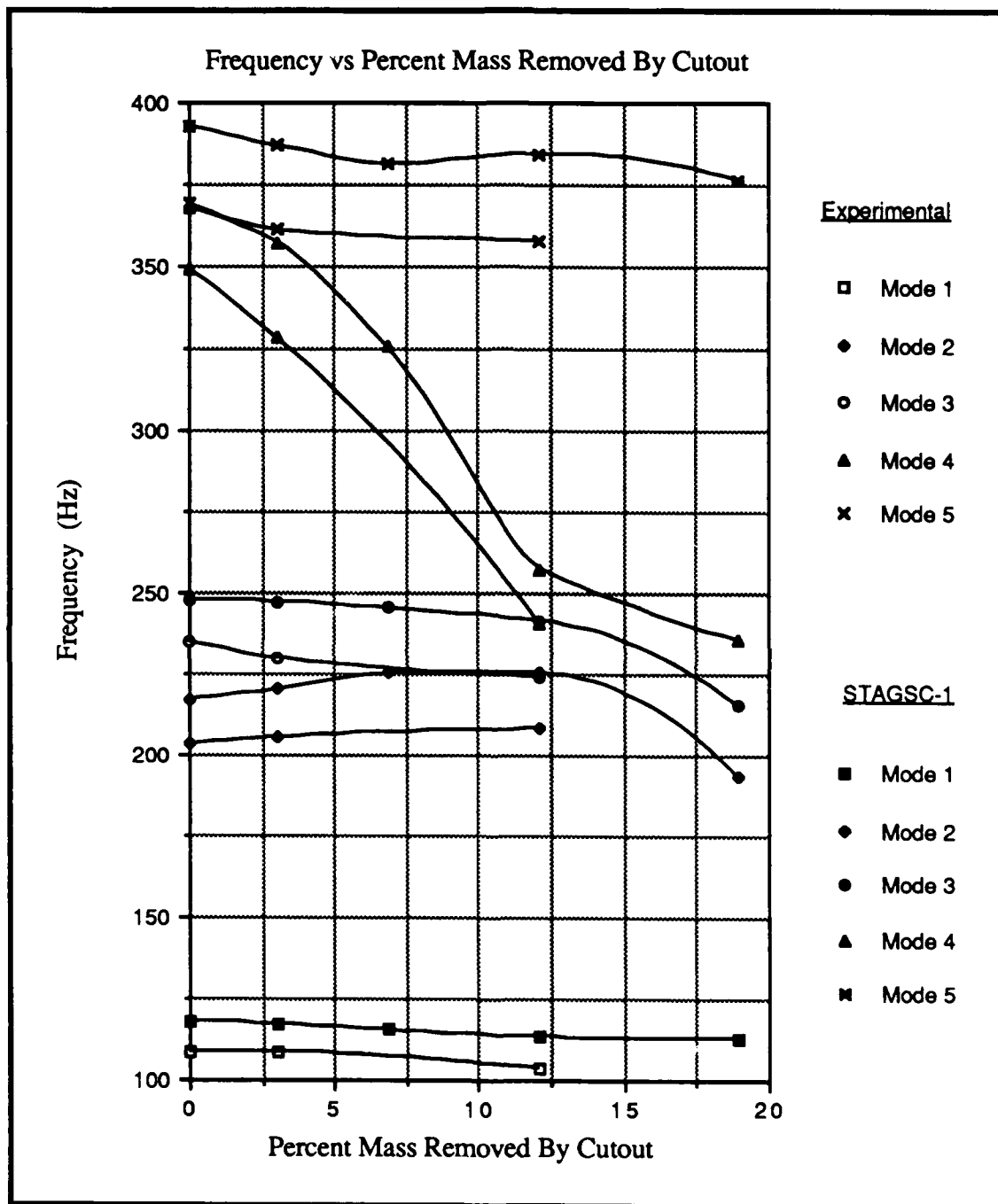


Figure 6-56. Frequency versus Percent Mass Removed By Cutout

not known. However, what could be summarized for the fifth mode was that in general, frequency decreased slightly as cutout size (percent mass removed) increased.

Modes which showed a decrease in frequency as cutout size increased, indicated that the loss of stiffness was more affected by increasing cutout size than the loss of mass for that mode (K/M decreased). Thus, considering a given modes response, loss of stiffness increased faster than the loss of mass as cutout size increased. If the frequency increased as the cutout size increased, then the loss of mass was more predominate than the loss of stiffness for the given mode (K/M increased).

The first mode frequency, as shown in Figure 6-56, consistently decreased both experimentally and analytically as the cutout size increased. The largest variation was -4.7% and was obtained experimentally for the 4 inch square cutout. Thus, the first mode experienced only small frequency variations due to the cutouts. This was consistent with the fact that the first mode shape was unaffected by the 2 inch and 4 inch square cutouts.

The second mode frequency increased as cutout size increased up to the 4 inch square cutout. For the 4 inch cutout the frequency had increased experimentally and analytically by 2.5% and 3.7%, respectively. Up to the 4 inch cutout, only small frequency changes were noticed, however, the 5 inch square cutout was analytically predicted to cause a frequency drop of 11.0% (compared to Panel 1). STAGSC-1 did a good job predicting the trends shown in Figure 6-56, and therefore a similar decrease in frequency would be expected experimentally. The 11.0% was considered significant and indicated that pertaining to the second mode behavior a large decrease in stiffness had occurred between the 4 inch and 5 inch cutouts. The second mode shape was not significantly altered by the 2 inch and 4 inch cutouts which again was consistent with the fact only small frequency variations had been observed for these cutout sizes. Overall, the second mode frequency was only significantly altered by the 5 inch square cutout.

The third mode frequency slowly decreased in frequency as the cutout size increased to the 4 inch cutout. Experimentally, a decrease of 4.6% was observed between Panels 1 and 7. The 4 inch centered cutout caused only small amounts of distortion of the third mode shape. No distortion was observed by the 2 inch cutout. The 5 inch cutout revealed a 13% decrease in third mode frequency as compared to Panel 1. Similar to what was observed for the second mode, this large decrease in frequency indicated a significant reduction of the stiffness to mass ratio, for the third mode, between the 4 inch and 5 inch cutouts.

The fourth mode frequency decreased sharply as cutout size increased. The 4 inch square cutout caused a substantial 31.1% decrease in fourth mode frequency (experimentally). Therefore the stiffness to mass ratio decreased significantly. Between the 4 inch and 5 inch cutout sizes the rate of decrease slowed forming a "knee" in the curve as shown in Figure 6-56. The sudden change in slope of the curve was believed to be associated with the drastic change in mode shape observed. Due to limited data, the "knee" appeared to occur near the 12% mass removed value (4 inch cutout). If more data were available the location of the "knee" may have changed. Projecting along the curve between the 2 inch and 3 inch cutouts and then along the segment between the 4 inch and 5 inch cutouts it was speculated that the "knee" would most likely be located between the 8% and 12% mass removed values. Figure 6-56 shows the fourth mode frequency approached the third mode value to within 16.2 Hz (experimentally) for the 4 inch cutout. Between the 4 inch and 5 inch cutouts the second, third, and fourth mode frequencies appear to maintain the same relatively spacing. This suggested that the "knee" for the fourth mode was close to the 12% mass removed value. Additional data would be needed to verify the actual shape of the fourth mode curve.

As previously mentioned, the fifth mode frequency generally decreased as the cutout size increased. The 2 inch cutout caused no distortion of the fifth mode shapes and the 4 inch cutout on slightly distorted the vertical node lines.

For the panel geometries tested, only the fourth mode was sensitive to cutout sizes up to 4 inches square. A significant drop in frequency and change in mode shape was observed for the fourth mode with the 4 inch square cutout. The first, second, third, and fifth modes experienced only small frequency variations for the 4 inch cutout and smaller. The first and fifth mode frequencies showed little variation due to the 5 inch square cutout while the second, third, and fourth modes all underwent notable decreases in frequency. The next section presents a summary of the eccentricity effects of the square cutouts studied.

(2) Summary of Eccentricity Effects. The effects of eccentrically located square cutouts are summarized in this section. The two types of eccentricity considered were circumferential and tangential as described in Figure 3-3. For the following summary, frequency changes of less than 5% will be considered minor. Changes between 5% and 10% will be considered small and only changes larger than 10% will be considered significant. The discussion presented in this section is broken into two parts. First, the effects of circumferential eccentricity are summarized followed by the effects of tangential eccentricity.

(2.1) Circumferential Eccentricity. Values of 1 inch and 2 inches circumferential eccentricity were investigated and the results for the 2 inch, 3 inch, 4 inch, and 5 inch square cutouts can be found in Figures 6-21, 6-51, 6-42, and 6-54, respectively. The 2 inch and 4 inch square cutouts were studied both experimentally and analytically while the 3 inch and 5 inch square cutouts were studied only analytically. The following summary will address each mode individually. All reference to eccentricity in this section will represent circumferential eccentricity unless otherwise stated.

The first mode frequency increased with increasing eccentricity for all four cutout sizes investigated. The eccentrically located 2 inch and 3 inch cutouts caused negligible frequency variations. As eccentricity was increased, the 4 inch cutout resulted in small frequency changes. The maximum increase in experimental frequency for the panels with 4 inch cutouts (also maximum for all panels) was 6.8% at the 2 inch eccentricity value (Panel 9). For the 5 inch cutout, increasing eccentricity caused the frequency to increase but by a lesser amount than the 4 inch cutout. As shown in the last section, as the cutout size increased the percentage of stiffness lost increased faster than the percentage of mass lost. Apparently the loss of stiffness due to the 5 inch cutout was so large that as the cutout moved off the node line the K/M ratio did not increase as much as for the smaller cutouts.

The second mode frequency decreased with increasing eccentricity for all cutout sizes except the 5 inch cutout. The 5 inch cutout was also the only centered cutout which caused the second mode frequency to decrease. This was exactly opposite from the previous observation made for the second mode with smaller cutouts and was believed due to the large loss of stiffness caused by the 5 inch square cutout. The two inch circumferential eccentricity of the 5 inch cutout, with 2 inches of circumferential eccentricity, resulted in an increase in second mode frequency of 7.2%. Eccentrically locating the 2 inch cutout caused negligible changes while the 3 inch and 4 inch cutouts showed decreases in frequency of 6.3% (analytical) and 6.4% (experimental), respectively at the two inch eccentricity value. The circumferential eccentricity resulted in at most small frequency variations for the second mode.

The third mode frequency behaved similar to the second mode in that all cutout sizes except the 5 inch showed decreases in frequency as circumferential eccentricity increased. For the 5 inch cutout this again indicated that the loss of mass was more predominate to third mode behavior than loss of stiffness. For all cutout sizes the variation in third mode frequency was less than 3% and thus considered negligible.

As circumferential eccentricity increased, the fourth mode frequency increased for all cutout sizes. At the 2 inch eccentricity values these increases were determined to be 4.1%, 6.8%, 13.7%, and 5.5% for the 2 inch, 3 inch, 4 inch, and 5 inch cutouts, respectively. The fourth mode frequency was the most sensitive to circumferential eccentricity yet only the 4 inch square cutout caused significant frequency variation and only at the largest eccentricity investigated.

The fifth mode only experienced small frequency variations due to circumferential eccentricity and only for the 4 inch and 5 inch cutouts. Eccentricity of the 2 inch and 3 inch cutouts only caused minor frequency variations. For these two cutout sizes, the fifth mode frequency increased slightly for the 1 inch eccentricity value then remained relatively constant at the 2 inch eccentricity. The larger cutouts resulted in a different frequency trend as eccentricity increased. For the 4 inch and 5 inch cutouts, the 1 inch eccentricity caused a decrease in frequency followed by an increase in frequency at the 2 inch eccentricity. It was speculated that the larger cutouts experienced different behavior because the cutouts were large enough to interact with both node lines simultaneously.

The frequency variations caused by eccentrically locating the square cutouts in the circumferential directions were discussed in this section. In general, the variation in frequency increased as cutout size increased for all but the 5 inch cutout. Also, the variations in frequency increased as the eccentricity increased for all modes except the fifth mode. For the fifth mode the largest frequency variation was observed at the 1 inch eccentricity value. The fourth mode was observed to be the most sensitive to eccentricity of the cutouts and the only one to experience a significant frequency variation ($> 10\%$). The largest experimental frequency variation (fourth mode) resulted in a increase in frequency of 13.7% (Panel 9). The largest analytical variation was 12.9% and occurred for the same conditions.

This section summarized the resulting frequency variation due to circumferential eccentricity of various size square cutouts. The next section will present a summary of the effects caused by tangential eccentricity of the same square cutouts.

(2.2) Tangential Eccentricity. The values of tangential eccentricity investigated were 1 inch and 2 inches. Figures 6-28, 6-52, 6-49, and 6-55 contain the results for the 2 inch, 3 inch, 4 inch, and 5 inch square cutouts, respectively. The 2 inch and 4 inch square cutouts were studied both experimentally and analytically. The 3 inch and 5 inch cutouts were studied only analytically. In the following summary, the information will be presented according to individual modes. All reference to eccentricity in this section will represent tangential eccentricity unless otherwise stated.

The first mode frequency for all cutout sizes considered was insensitive to tangential eccentricity. The largest variation in frequency was only 1.5% and occurred with the 4 inch cutout at the 2 inch tangential eccentricity value (Panel 11). As eccentricity was increased the cutout moved along the vertical node line for the first mode and its position relative to node line and antinode locations did not change. Thus, little or no frequency variation was expected.

The second mode frequency was also insensitive to tangential eccentricity for cutout sizes through 4 inches square. For these panels, the most variation was 1.1% which was observed for Panel 11. The 5 inch cutout caused a 6.8% increase in second mode frequency at the 2 inch eccentricity value (Panel 21). Most of the increase occurred between the 1 inch and 2 inch eccentricity positions. As tangential eccentricity increased, the cutouts moved along the center half wave of the panel. As with the first mode, the cutouts position did not change relative to node lines. The mode shapes were unavailable for the panels with 5 inch cutouts and the reason this panel behaved differently was not known. Possibly the increase loss of stiffness for the 5 inch cutout caused additional radial

variation of displacement in the tangential (axial) direction than was not present with the smaller cutouts; however, no firm explanation was available.

The third mode showed little sensitivity to tangential eccentricity of the cutout. The panels with 2 inch and 5 inch cutouts experienced negligible frequency variations due to eccentricity while the panels with 3 inch and 4 inch cutouts experienced a slight rise in frequency which grew larger as the eccentricity and cutout size increased. The majority of the increase in frequency occurred between the 1 inch and 2 inch eccentricity values. Apparently, the loss of mass contribution increased as the antinode was approached. The panels with 5 inch cutouts deviated from the pattern established by the smaller panels. This was possibly due to the larger reduction of stiffness as compared to mass. The largest frequency variation resulting from tangential eccentricity was 4.7% (experimentally) for Panel 11 at the 2 inch tangential eccentricity value. Overall, tangential eccentricity of all square cutouts investigated resulted in very little variation in the third mode frequency.

The fourth mode frequency experienced sensitivity to tangential eccentricity for only the panels containing the 4 inch cutouts. All other cutout sizes studied showed only negligible frequency changes due to eccentricity. Eccentricity of the 4 inch cutout caused only small variations in frequency with the largest observed being 6.4% for Panel 11. The frequency trend predicted by STAGSC-1, for the 4 inch cutout with tangential eccentricity, represented the first time a notable difference between the experimental and analytical trend was observed. STAGSC-1 predicted that the increase in frequency due to eccentricity of the 4 inch cutout would be nearly linear but experimentally the majority of the frequency increase occurred between the 1 inch and 2 inch eccentricity values. A similar observation was made concerning the fifth mode trends for the panels with 4 inch cutouts. In both cases the differences were small but obvious.

The fifth mode frequency varied only slightly due to eccentricity of the 4 inch and 5 inch cutouts and negligibly due to the eccentricity of the smaller cutouts. The 4 inch cutout

eccentrically located 2 inches (Panel 11) caused the experimental frequency to increase by 2.0%. The same eccentricity for the 5 inch cutout analytically caused a 3.3% increase. Thus, tangential eccentricity effects on the fifth mode frequency were negligible.

As can be derived from this summary, circumferential eccentricity generally caused larger frequency variations than did tangential eccentricity. The mode shapes revealed that for the panel geometry and boundary conditions tested, most of the radial distribution of displacement occurred in the circumferential direction. Thus, a greater sensitivity to the circumferential eccentricity should be expected. In all but one case, both types of eccentricity resulted in small or negligible frequency variations. The only exception was the fourth mode for Panel 11 (4 inch square cutout with 2 inches of circumferential eccentricity) in which a 13.7% increase in experimental frequency was observed.

This concludes the formal discussion of the results for this study. The next chapter (Chapter VII) presents the conclusions drawn from the data and observations of this study.

VII. Conclusions

This study investigated the eccentricity effects of square cutouts on the natural frequencies and mode shapes of circular, cylindrical Gr/Ep composite panels. Eccentricity was examined in both the circumferential and tangential directions as defined in Figure 3-3. The experimental results were obtained using a video-holography technique and the STAGSC-1 finite element program was used to determine the analytical predictions.

The following represents a summary of the conclusions which were drawn from the data and observations presented in this study:

1) The CFCF boundary condition and the geometry of the curved panels studied, resulted in mode shapes in which the distribution of radial displacements varied primarily in the circumferential direction. The CFCF boundary condition represented a simpler boundary condition than the fully clamped panel which had previously been studied at AFIT [13; 19; 42] and as a result, geometrically simpler mode shapes were observed.

To simulate the fully clamped condition, using the available test fixture, would have required an awkward mounting procedure which was believed to most often result in localized bending (induced stress) of the panel due to the fixture. Because of the available fixture's design, the CFCF boundary condition could be achieved easier and more reliably than could the fully clamped condition. To further reduce the amount of bending induced by the fixture, the clamping surfaces were machined to fit the curvature of the panels. This improved the clamped condition and significantly lowered the amount of bending caused by the fixture. Overall, the CFCF boundary condition resulted in a simpler mounting procedure and less probability of prestress on the panels.

2) The introduction of a cutout into a panel reduces both the overall stiffness and mass of the panel. Thus, the response of the panel will reflect this coupling of the mass and

stiffness. For a given mode, if the effective K/M ratio decreased (due to cutout), then the stiffness loss was preponderate and the resulting frequency also decreased. However, if the mass loss dominated, then both the K/M ratio and the frequency increased. How the cutout affected a particular mode's response depended on many factors, some of which were, the amount of relative displacements and the particular bending characteristics present at the location in which the cutout was introduced. For different mode shapes, the velocities, displacements, and amounts of bending within the panels varied. Therefore, the cutout often affected individual modes in different ways.

3) The introduction of the centered cutouts (up to 4 inches square) into the Gr/Ep panels caused a decrease in natural frequency for all but the second mode. For the first, third, fourth, and fifth modes the effective K/M ratio for the panel was reduced which resulted in the drop in frequency. For the second mode, the loss of mass was predominate and the frequency increased.

Cutout sizes up to 4 inches square resulted in only small frequency variations for all but the fourth mode. This indicated that for cutouts 4 inches square and smaller, the percentages of stiffness and mass lost due to the cutout were similar. The fourth mode represented a special case because of the complex two directional bending which was present. Therefore, the fourth mode was extreme sensitivity to the loss of stiffness resulting from the cutouts.

4) The 2 inch square cutout caused only minor changes in the panel's mode shapes. Except for the fourth mode, the 4 inch cutout resulted in only small distortion in the mode shapes. The 4 inch cutout caused the fourth mode to change drastically. The fourth mode shapes were also sensitive to eccentricity (circumferential and tangential) of the 4 inch cutout and varied considerably as eccentricity increased. As previously mentioned, the

fourth mode was sensitive to the loss of stiffness due to the two directional bending present. This sensitivity resulted in the large fourth mode shape variations observed.

5) The 5 inch square cutout caused a decrease in frequency for all five of the modes with the second, third, and fourth modes experiencing significant reductions. The 5 inch cutout represented a cutout in which the percentage of stiffness loss was much larger than the percentage of mass loss. The behavior of the panels with 5 inch square cutouts deviated significantly from that noticed for the smaller cutouts. It was speculated that this deviation resulted from the cutout being large enough to allow the remaining portions of the panel not only to respond as a whole, but also to begin to respond as individual entities. The mode shapes would have been needed to confirm this speculation.

6) Primarily, eccentricity affected the panel's natural frequencies (changes effective K/M ratio) by changing the cutouts location relative to node lines and antinode, or by moving the cutout either towards or away from regions of the panel experiencing relatively high bending moments.

7) The panel geometry and boundary conditions studied were most sensitive to eccentricity in the circumferential direction. Eccentricity of the cutouts (circumferential and tangential) caused both increases and decreases in frequency depending on the particular mode. In most cases the effects of eccentricity were small. Although small, often these variations were as large as those noticed when the cutout was first introduced into the panel.

8) In general, circumferential eccentricity of the square cutouts resulted in only small frequency variations. In only one case did circumferential eccentricity cause a significant frequency variation. This occurred for the fourth mode of Panel 9 in which a 13.7% increase in frequency was observed.

9) Due to the boundary conditions and the geometry of the resulting mode shapes, tangential eccentricity of the square cutouts caused little variation in frequency of the panels. Tangential eccentricity of the 2 inch and 3 inch cutouts resulted in negligible frequency changes, while the panels with 4 inch and 5 inch cutouts experienced only small changes.

10) This study contributed to the verification of the STAGSC-1 finite element program and demonstrated its ability to handle problems with unsymmetrical geometries and free-edge boundary conditions. STAGSC-1 was a very useful engineering tools for this study. The analytical frequencies predicted by STAGSC-1 correlated well with experimental results. Also, STAGSC-1's mode shape predictions were in excellent agreement with those obtained experimentally. A better understanding of the Gr/Ep's material properties would have resulted in more accurate finite element models and lower percent differences between experimental and analytical frequencies. Although the frequency variations (due to eccentricity) observed in this study were small, STAGSC-1 did a good job of predicting the same trends obtained experimentally.

..... One area of the STAGSC-1 program which should be improved upon is its post-processing capabilities. STAGSC-1 does possess some post-processing capabilities but they are extremely limited. To obtain the plots included in this thesis, data had to be downloaded to a personal computer for processing. To improve the usefulness of the STAGSC-1 program, improvements of its post-processing capabilities should seriously be considered.

VIII. Recommendations

This chapter lists some recommendations for future research based on knowledge gained while conducting this study.

- 1) The current test fixture was difficult to use and highly susceptible to variation of the boundary condition between panels. Mounting the panels was time consuming and extreme care was necessary to reduce the amount of stress (bending) induced into the panels by the clamp. Therefore, a new test fixture design is recommended for future studies of curved panels with clamped boundary conditions.
- 2) An obvious extension of this work would be to use different shaped cutouts (rectangular, circular, etc.) to further study the effects of eccentric cutouts on a panel's response. Also, a study could be conducted in which cutouts are eccentrically located in the circumferential and tangential directions simultaneously.
- 3) A similar study could be conducted using different materials, ply layups, and laminate thicknesses to investigate how they affect a panel's sensitivity to eccentric cutouts.
- 4) A similar study could consider eccentric cutouts with alternate boundary conditions, such as, a fully clamped panel or a panel clamped at the two edges along its arclength and free along the two axially oriented edges. Also, how a panel's response is affected as a cutout approaches a boundary could be investigated.
- 5) A similar study could be conducted in which the mass is allowed to vary without changes in stiffness occurring. Different size distributed masses could be investigated at various panel locations so that the mass effects can be observed without the stiffness coupling which results from a cutout. If possible, reducing the stiffness without affecting the mass may also prove useful.

This thesis has investigated the eccentricity effects of square cutouts on the dynamic response of circular, cylindrical composite panels. Documented research concerning the vibration analysis of curved composite panels with eccentrically located cutouts and mixed boundary conditions is limited. It is hoped that this study will not only make a useful contribution to the research community but will also encourage additional work in similar areas.

Bibliography

1. Alam, Naiyar, and Asnani, N.T. "Vibration and Damping Analysis of a Multilayered Cylindrical Shell. Part II: Numerical Results," AIAA Journal, Volume 22, No. 7, pages 975-981, July 1984.
2. -----, "Vibration and Damping Analysis of a Multilayered Cylindrical Shell, Part I: Theoretical Analysis," AIAA Journal, Volume 22, No. 6, pages 803-810, June 1984.
3. -----, "Vibration and Damping Analysis of Fibre Reinforced Composite Material Cylindrical Shell," Journal of Composite Materials, Volume 21, No. 4, pages 291-393, April 1987.
4. Almroth, B.O., and F.R. Brogan. Numerical Procedures for Analysis of Structural Shells. AFWAL-TR-80-3129. Wright-Patterson Air Force Base, Ohio: Air Force Wright Aeronautical Laboratory, March 1981.
5. Almroth, B.O., F.A. Brogan, and G.M. Stanley. Structural Analysis of General Shells, Volume II User Instructions for STAGSC-1. LMSC-D633873. Applied Mechanics Laboratory, Lockheed Palo Alto Research Laboratory, January 1983.
6. -----, STAGS Theory Manual, Cosmic Program No. HQN-10960. Structural Mechanics Laboratory, Lockheed Palo Alto Research Laboratory, March 1978.
7. Ashton, J.E., and J.M. Whitney. "Theory of Laminated Plates," Progress in Material Science Series, Volume IV. Stanford: Technomic Publishing Company, Inc., 1970.
8. Bathe, Klaus-Jürgen. Finite Element Procedures in Engineering Analysis. New Jersey: Prentice-Hall, Inc., 1982.
9. Bert, C.W., J.L. Baker, and D.M. Egle. "Free Vibrations of Multilayer Anisotropic Cylindrical Shells," Journal of Composite Materials, Volume 3, No. , pages 480-499, July 1969.
10. Bicos, Andrew S., and George S. Springer. "Vibrational Characteristics of Composite Panels with Cutouts," AIAA Journal, Volume 27, No. 8., 1988.
11. Caulfield, Henry J., and Sun Lu. The Applications of Holography. New York: Wiley-Interscience, 1970.
12. Cook, Robert D. Concepts and Applications of Finite Element Analysis (Second Edition). New York: John Wiley and Sons, 1981.
13. Cyr, Capt Garry J. Effects of Cutout Orientation on Natural Frequencies and Mode Shapes of Curved Rectangular Composite Panels. Master's Thesis, AFTT/GAE/AA/86D-3. School of Engineering, Air Force Institute of Technology, (AU), Wright-Patterson Air Force Base, Ohio, December 1986.

14. Cyr, G.J., R.L. Hinrichsen, and R.A. Walley. "Effects of Cutouts on the Dynamic Response of Curved Rectangular Composite Panels," AIAA Journal, Volume 26, No. 5, pages 582-588, May 1988.
15. Egan, Captain Gregory S. Nonlinear Finite Element Analysis of a General Composite Shell. Master's Thesis, AFIT/GAE/AA/88D-12. School of Engineering, Air Force Institute of Technology (AU), Wright-Patterson Air Force Base, Ohio, December 1988.
16. Ennos, A.E., Research Techniques in Nondestructive Testing, edited by R.S. Sharpe. London: Academic Press, Inc., 1970.
17. Francon, M. Holography. New York and London: Academic Press, 1974.
18. Gibson, J.E. Thin Shells Computing and Theory. Oxford: Pergamon Press, 1980.
19. Goodwin, Major William P. Effects of Battle Damage Repair on the Natural Frequencies and Mode Shapes of Curved Rectangular Composite Panels. Master's Thesis, AFIT/GAE/AA/88D-18. School of Engineering, Air Force Institute of Technology, (AU), Wright-Patterson Air Force Base, Ohio, December, 1988.
20. Hornbeck, Robert W. Numerical Methods. New York: Quantum Publishers, Inc., 1975.
21. Huebner, Kenneth H., and Earl A. Thorton. The Finite Element Method for Engineers (Second Edition). New York: John Wiley and Sons, Inc., 1982.
22. Irons, Bruce, and Sohrab Ahmad. Techniques of Finite Elements. Chichester, England: Ellis Horwood Limited, 1980.
23. Jones Robert M. Mechanics of Composite Materials. New York: Hemisphere Publishing Corporation, 1975.
24. Kock, Winston E. Lasers and Holography, and Introduction to Coherent Optics. New York: Doubleday and Company, Inc., 1969.
25. Leissa, Arthur W. "Vibration of Shells," NASA SP-288, 1973.
26. Maddux, Gene, Aerospace Engineer, Flight Dynamics Laboratory, Wright-Patterson Air Force Base, Ohio. Personal interviews, March - November 1989.
27. -----. Aerospace Engineer, Flight Dynamics Laboratory, Wright-Patterson Air Force Base, Ohio. Video Holography Notes, November 1988.
28. Meirovitch, Leonard. Elements of Vibrations Analysis (Second Edition). New York: McGraw-Hill Book Company, 1986.
29. -----. Analytical Methods in Vibrations. New York: MacMillan Publishing Company, Inc., 1967.

30. Monohan, 1st Lt Jon. Natural Frequencies and Mode Shapes of Plates with Interior Cut-Outs. Master's Thesis, AFIT/GAM/MC/71-1. School of Engineering, Air Force Institute of Technology (AU), Wright-Patterson Air Force Base, Ohio, September 1970.
31. Newport Corporation. Operator's Manual for HC-300 Holographic Recording Device. Fountain Valley, California.
32. Rajamani, A., and R. Prabhakaran. "Dynamic Response of Composite Plates with Cut-Outs, Part II: Clamped-Clamped Plates," Journal of Sound and Vibration, Volume 54, No. 4, pages 565-576, 1977.
33. -----, "Dynamic Response of Composite Plates with Cut-Outs, Part I: Simply-Supported Plates," Journal of Sound and Vibration, Volume 54, No.4, pages 549-564, 1977.
34. Saada, Adel S. Elasticity Theory and Applications. Malabar, Florida: Robert E. Krieger Publishing Company, 1987.
35. Smith, J.W. Vibration of Structures: Applications in civil engineering design. London: Chapman and Hall, 1988.
36. Stetson, Karl A. "Holographic Vibration Analysis," Holographic Nondestructive Testing, edited by Robert K. Erf. New York: Academic Press, 1974.
37. Thomas, K., and L.H. Sobel. Evaluation of the STAGSC-1 Shell Analysis Program. WARD-10881. Madison, PA: Westinghouse Advanced Reactors Division, August 1981.
38. Tisler, T.A. Collapse Analysis of Cylindrical Composite Panels with Large Cutouts Under Axial Loads. Master's Thesis, AFIT/GAE/AA/86D-18. School of Engineering, Air Force Institute of Technology (AU), Wright-Patterson Air Force Base, Ohio, December 1986.
39. Unterseher, Fred, et al. Holography Handbook. Berkeley, California: Ross Books, 1982.
40. Vikhagen, Eiolf. TV-Holography in Material Evaluation. Trondheim University: June 1989.
41. Vinson, Jack R. The Behavior of Thin Walled Structures: Beams, Plates, and Shells. Dordrecht, The Netherlands: Kluwer Academic Publishers, 1989.
42. Walley, Capt Richard A. Natural Frequencies and Mode Shapes of Curved Composite Panels with Interior Cutouts. Master's Thesis, AFIT/GAE/AA/85D-16. School of Engineering, Air Force Institute of Technology, (AU), Wright-Patterson Air Force Base, Ohio, December 1985 (AD-A165 269).
43. Warlbarton, G.B. The Dynamic Behavior of Structures (Second Edition). Oxford: Pergamon Press, 1976.

44. Waters, James P. "Holography," Holographic Nondestructive Testing, edited by Robert K. Erf. New York: Academic Press, 1974.
45. -----, "Interferometric Holography," Holographic Nondestructive Testing, edited by Robert K. Erf. New York: Academic Press, 1974.
46. Yen, S.C., and F.M. Cunningham. "Vibration Characteristics of Graphite-Epoxy Composite Plates," Proceedings of the 1985 SEM Spring Conference on Experimental Mechanics. 60-67. Brookfield Center, Connecticut: Society for Experimental Mechanics, 1985.
47. Zienkiewicz, O.C. The Finite Element Method (Third Edition). London: McGraw-Hill Publishing Company Limited, 1977.

Appendix A: Eigenvalue Problem Solution Algorithms

A. Subspace Iteration

The following subspace iteration algorithm was developed by Bathe [8] and is repeated here for the benefit of the reader. The goal of the subspace iteration method is to solve for the "p" lowest eigenvalues and eigenvectors which satisfy

$$K\Phi = M\Phi\Lambda$$

where $\Phi = [\{\phi_1\} \ \{\phi_2\} \ \dots \{\phi_p\}]$, $\Lambda = \text{diag matrix of } \lambda_i \text{'s } (i = 1, 2, \dots, p)$, and K and M are the symmetric stiffness and mass matrices respectively [8:675]. First, the starting iteration vectors, x_1 , which span the subspace (eigensubspace), E_1 , are selected. (E_∞ is the p-dimensional subspace spanned by the "p" lowest eigenvectors). The starting iteration vectors should be chosen to excite those degrees of freedom possessing large mass and small stiffness [8:682]. One method for obtaining x_1 , which has been effectively used, begins by letting the first column of $[M] x_1$ be the major diagonal of $[M]$. This establishes excitation of all degrees of freedom possessing mass. The other columns of $[M] x_1$ are unit vectors with a "1" at locations with the smallest K_{ii}/m_{ii} ratios. Therefore, all locations but one within these columns contains zeros. The last column in $[M] x_1$ can be a random vector [8]. After the starting iteration vector is determined, iteration begins from E_k to E_{k+1} (E_∞ is the eventual desired result), where $k = 1, 2, \dots, n$, by applying [8]

$$K \bar{x}_{k+1} = M x_k \tag{A.1}$$

As used here, "n" is the number of iterations required to obtain convergence. Equation A.1 is solved for \bar{x}_{k+1} by premultiplication of both sides of the equation by $[K]^{-1}$ to yield

$$\bar{x}_{k+1} = K^{-1} M x_k \quad (A.2)$$

Next, the projections of the K and M operators on the E_{k+1} subspace are determined by [8]

$$K_{k+1} = \bar{x}_{k+1}^T K \bar{x}_{k+1} \quad (A.3)$$

$$M_{k+1} = \bar{x}_{k+1}^T M \bar{x}_{k+1} \quad (A.4)$$

By using the above relations for K_{k+1} and M_{k+1} , the eigensystem of the projected operators can be solved by [8]

$$K_{k+1} Q_{k+1} = M_{k+1} Q_{k+1} \Lambda_{k+1} \quad (A.5)$$

Equation A.5 represents the reduced eigenvalue problem for the E_{k+1} subspace and can be solved by any popular technique (STAGSC-1 uses Householder's Method followed by a LR algorithm) to obtain values for Q_{k+1} and Λ_{k+1} . An improved approximation to the eigenvectors is found next from [8]

$$X_{k+1} = \bar{X}_{k+1} Q_{k+1} \quad (A.6)$$

This procedure is iterated until the desired convergence is obtained. This X_{k+1} is now substituted into Equation A.1 in place of X_k and the algorithm iterated until sufficient convergence has been obtained. Figure A-1 presents a flow chart of the subspace iteration algorithm incorporated in STAGSC-1. In subspace iteration, the iteration vectors are ordered such that the vectors converging to $\phi_1, \phi_2, \dots, \phi_p$ are stored as the first, second, ..., p^{th} columns of X_{k+1} , respectively. As long as no vector contained within X_1 is orthogonal to any of the required eigenvectors, then as k tends to infinity Λ_{k+1} approaches to Λ (the required diagonal matrix of "p" eigenvalues) and X_{k+1} approaches $[\phi]$ (the required column matrix of "p" eigenvectors) [8].

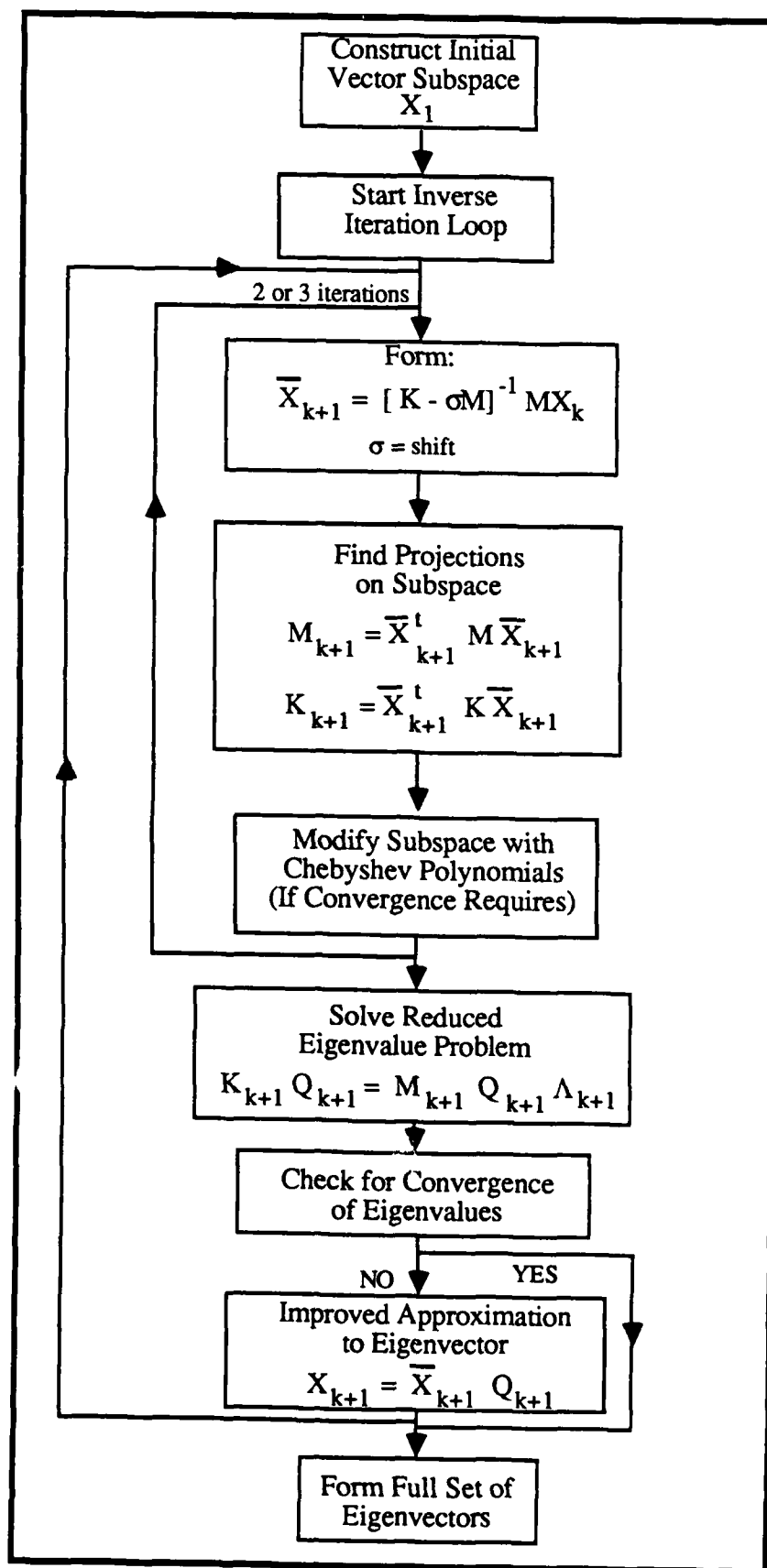


Figure A-1. Subspace Iteration Algorithm

B. Householder's Method

Householder's Method is an extremely effective technique for tridiagonalizing a symmetric matrix. It is based on orthogonal transformations, in which each transformation yields a large number of zeros in a given row and column [20:241].

Consider a symmetric ($n \times n$) matrix, $[H_1]$. For purposes of illustration a 4×4 matrix will be used. Therefore $[H_1]$ is given by

$$[H_1] = \begin{bmatrix} h_{11} & h_{12} & h_{13} & h_{14} \\ h_{21} & h_{22} & h_{23} & h_{24} \\ h_{31} & h_{32} & h_{33} & h_{34} \\ h_{41} & h_{42} & h_{43} & h_{44} \end{bmatrix} \quad (\text{A.7})$$

The objective is to find a symmetric orthogonal matrix, $[T_1]$, such that [20:241]

$$[T_1][H_1][T_1]^T = \begin{bmatrix} h'_{11} & h'_{12} & 0 & 0 \\ h'_{21} & h'_{22} & h'_{23} & h'_{24} \\ 0 & h'_{32} & h'_{33} & h'_{34} \\ 0 & h'_{42} & h'_{43} & h'_{44} \end{bmatrix} \quad (\text{A.8})$$

where $[T_1]^T = [T_1]$ due to symmetry. In the above expression the product $[T_1][H_1]$ yields the zeros resulting in the first column and the postmultiplication by $[T_1]^T$ yields the first row zeros. The product in Equation A.8 is symmetric because the transformation is

orthogonal. For this first orthogonal transformation, the general form of $[T_1]$ is given by [20:241]

$$[T_1] = \begin{bmatrix} 1 & 0 & 0 & 0 \\ 0 & & & \\ 0 & [P] & & \\ 0 & & & \end{bmatrix} \quad (A.9)$$

where the symmetric (3×3) , orthogonal submatrix, $[P]$, is selected so that the desired first column zeros result in $[H_1]$. Considering Equations A.7 and A.9, the product of $[T_1][H_1]$ becomes

$$[T_1][H_1] = \begin{bmatrix} 1 & 0 & 0 & 0 \\ 0 & & & \\ 0 & [P] & & \\ 0 & & & \end{bmatrix} \begin{bmatrix} h_{11} & h_{12} & h_{13} & h_{14} \\ h_{21} & h_{22} & h_{23} & h_{24} \\ h_{31} & h_{32} & h_{33} & h_{34} \\ h_{41} & h_{42} & h_{43} & h_{44} \end{bmatrix} \quad (A.10)$$

The premultiplication by $[T_1]$, causes no changes between the first rows of $[H_1]$ and $[T_1][H_1]$. Therefore, $[P]$ acts only on the lower $(n-1)$ rows of $[H_1]$. Considering $[P]$ times the first column of $[H_1]$, the required result is a vector with zeros in the last two element locations as shown in Equation A.9 [20:241]. Thus,

$$[P] = \begin{bmatrix} h_{21} \\ h_{31} \\ h_{41} \end{bmatrix} = \begin{bmatrix} h'_{21} \\ 0 \\ 0 \end{bmatrix} = h'_{21} \begin{bmatrix} 1 \\ 0 \\ 0 \end{bmatrix} \quad (A.11)$$

Due to the orthogonality of [P], the length of the original vector is preserved. This length, S, is given by [20:242]

$$S = \sqrt{h_{21}^2 + h_{31}^2 + h_{41}^2} = h_{21}' \quad (\text{A.12})$$

The desired results are obtained if [P] is of the form

$$[P] = [I] - \frac{\{U\}\{U\}^T}{S^2 \pm h_{21}S} \quad (\text{A.13})$$

where [I] is an (n-1) x (n-1) identity matrix and {U} is given by

$$\{U\} = \begin{Bmatrix} h_{21} \pm S \\ h_{31} \\ h_{41} \end{Bmatrix} \quad (\text{A.14})$$

The correct sign to use in Equations A.13 and A.14 is the one which maximizes $|h_{21} \pm S|$. Substituting [P], as given by Equation A.13, into Equation A.7 yields the necessary $[T_1]$ matrix. Just as the first row of $[H_1]$ was unchanged by the product $[T_1][H_1]$, so to the first column of $[T_1][H_1]$ is unchanged by the postmultiplication $[T_1][H_1][T_1]$. Thus, the objective has been satisfied [20:242].

Next, it is necessary to create zeros in the second row and column such that

$$[T_2][H_2][T_2] = \begin{bmatrix} h'_{11} & h'_{12} & 0 & 0 \\ h'_{21} & h''_{22} & h''_{23} & 0 \\ 0 & h''_{32} & h''_{33} & h''_{34} \\ 0 & 0 & h''_{43} & h''_{44} \end{bmatrix} \quad (A.15)$$

where $[H_2] = [T_1][H_1][T_1]$ and $[T_2]$ is given by [20:242]

$$[T_2] = \begin{bmatrix} 1 & 0 & 0 & 0 \\ 0 & 1 & 0 & 0 \\ 0 & 0 & [P] & \\ 0 & 0 & & \end{bmatrix} \quad (A.16)$$

Again, $[T_2]$ is an orthogonal matrix. The submatrix $[P]$ is now a (2×2) matrix and is formed exactly as previously done, except that the $\{U\}$ vector is constructed from the second column of $[H_2]$, omitting the top two elements [20:242]. Notice that $[H_3] = [T_2][H_2][T_2]$.

This is as far as Householder's Method can be carried for a (4×4) matrix. For an $(n \times n)$ matrix, the method is carried out $n-2$ times. The resulting matrix will be tridiagonal and symmetric. Householder's Method does not yield the eigenvalues, but reduces the original fully populated matrix into a special form which is easier to handle [20:242].

C. LR Algorithm

The LR algorithm is an effective method for obtaining the eigenvalues for the symmetric, tridiagonal matrix which Householder's Method yields [20:246]. "The LR algorithm is based on the fact that virtually any matrix can be decomposed into a product of lower triangular and upper triangular matrices" [20:244]. The "L" denotes a lower triangular matrix (or left) and the "R" denotes an upper triangular matrix (or right). Therefore the original matrix, $[H_1]$ can be written as [20:244]

$$[H_1] = [L_1] [R_1] \quad (A.17)$$

Solving for $[R_1]$ gives

$$[R_1] = [L_1]^{-1} [H_1] \quad (A.18)$$

Postmultiplying both sides of Equation A.18 by $[L_1]$ yields

$$[R_1] [L_1] = ([L_1]^{-1} [H_1]) [L_1] \quad (A.19)$$

Comparing Equations A.17 - A.19, it can be seen that the product $[R_1] [L_1]$ represents a similarity transform of $[H_1]$ and therefore the eigenvalues will be preserved. For $[H_2] = [R_1] [L_1]$, decomposition can be carried out, similar to the procedure for $[H_1]$, to obtain

$$[H_2] = [L_2] [R_2] \quad (A.20)$$

Now, $[H_3]$ can be determined from [20:244]

$$[H_3] = [R_2] [L_2] \quad (A.21)$$

The process described above is repeated until the desired results are obtained. If $[H_1]$ is symmetric and positive definite, then the method converges. As "k" proceeds to infinity, $[H_k]$ approaches a lower triangular matrix with the eigenvalues in order of decreasing magnitude along the main diagonal [20:244].

Appendix B: Comparison of Holography Techniques

This appendix provides a comparison between the video holography technique used for this study and a conventional split-beam holography technique in which a thermoplastic plate is used to record the holograms (hereafter referred to as conventional holography). Video holography was the experimental procedure primarily used for this thesis, although one panel (Panel 7) was tested using the conventional approach to allow for an accurate comparison. The conventional holography equipment is setup in one of the AFIT laboratories located in the AFIT Engineering Building. This appendix is broken down into three sections. First, information on the experimental procedure for performing the conventional holographic analysis is provided. Included is a list of the equipment used, photographs of the conventional holography test setup, the general procedure used for performing holographic analysis with the Newport Research Corporation Model HC-300 System, and the results obtained for Panel 7. Secondly, the procedure used for performing the video holograph analysis is presented. Although the procedure was discussed in Chapter III, an actual list of the steps was not provided. The procedures are included so that the reader can appreciate the efficiency of the video holography technique. Finally, a listing of the advantages and disadvantages of both holography techniques is presented. The list comprises the majority of the comparison contained in this Appendix.

A. Conventional Holography

(1) **Holography Test Equipment.** The following is a list of the equipment used in conducting the conventional holographic analysis for this thesis.

Atlas Sound Horn
60 Watts

Bogen MOS-FET High Performance Power Amplifier
Model HTA-125

Coherent Radiation Laboratories Power Meter
Model 202; S/N 118

Hewlett-Packard Function Generator
Model 3310B; S/N 1201A06275

Hewlett-Packard Universal Counter
Model 5316A; S/N 2308A04211

Newport Research Corporation Beam Splitter (2 each)
Model 960A

Newport Research Corporation Holographic Camera
Model HC 310; S/N 7090034

Newport Research Corporation Holographic Camera Controller
Model HC 320; S/N 7090034

Newport Research Corporation Mirror
Model 630A-2

Newport Research Corporation Shutter
Model 884

Newport Research Corporation Spatial Filter (2 ea)
Model 900

Newport Research Corporation Universal Shutter System
Model 880; S/N 1154.1121

Spectra-Physics Exciter
Model 261; S/N 3110390

Spectra-Physics Laser
Model 125A; S/N 3610621

Spectra-Physics Power Meter
Model 401C; S/N 1627

Stable Table

Tektronix Dual Trace Amplifier (2 ea)
S/N 116125 and S/N BO86362

Tektronix Oscilloscope
Model 7603

The above equipment is located in the AFIT Holography Laboratory. Figures B-1 and B-2 provide two views of the conventional holography test setup. The test setup for the video holograph equipment is shown in Figure 4-5. Comparison of the two test setups reveals the simplicity and therefore one of the significant advantages of the video holography technique. When performing conventional holography analysis, a stable table is required. The stable table isolates the test object and optical setup from vibrations present in the surrounding environment. Because of the precise optical setup and the necessity of a stable table, conventional holography is generally only practical in a laboratory environment. For convenience, a stable table was also used with the video holography technique, although it was not required. Also, the video holography equipment is compact and can easily be used outside the laboratory environment.

The next section discusses the test procedure used to perform the conventional holography equipment with the NRC HC-300 system.

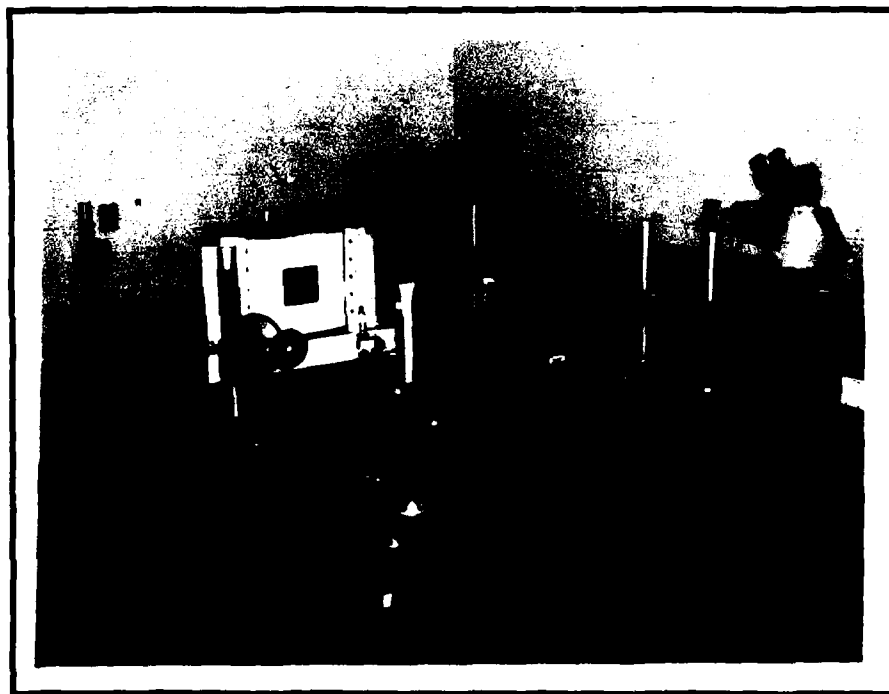


Figure B-1. Conventional Holography Test Setup (Front)

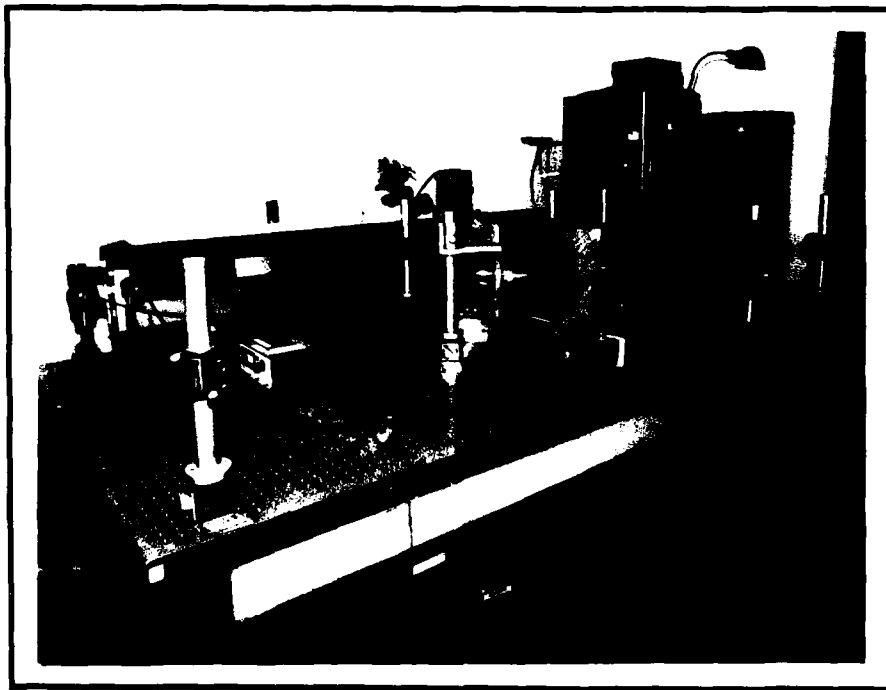


Figure B-2. Conventional Holography Test Setup (Back)

(2) Holography Procedure with NRC HC-300 System. Holography procedures vary with the type of system and setup being used. The following steps are applicable for the NRC HC-300 Thermoplastic Holography System. The setup is similar to that used for the traditional wet chemical process. The essential difference is the use of a thermoplastic plate for making the hologram recordings instead, of a photographic emulsion. This results in a much-simplified procedure. This procedure assumes the optic setup is already complete.

1. CAUTION: A laser eye exam is required before using a laser. Instructions for the setup, care, and use of the laser should be received prior to its first use to prevent personal injury or equipment damage.

2. Mirrors and lenses must be clean of all dirt and dust particles. If not, the quality of the laser light will be severely degraded and, consequently, so will the quality of the

holograms. If cleaning is necessary, consult an AFIT laboratory technician for proper cleaning instructions and supplies. Remember, optical equipment should be treated with extreme care.

3. The stable table must be charged (supplied with pressurized air at approximately 60-70 psi) so that the table is "floating" or isolated from vibrations in the room and building. Also, a source of clean, dry compressed air at 5 to 10 psi must be connected through the HC-300 Controller Unit to the HC-300 Camera Unit. This provides cooling for the thermoplastic plate.

4. Turn on the laser with the toggle switch on the Spectra-Physics Exciter and allow it to warm up. No adjustments should be made to the laser during the required 15-30 minute warm-up period.

5. After the laser is warmed up, turn on the NRC Universal Shutter System and set it to the manual position. Trigger the shutter open, so that the laser beam passes through the shutter opening.

6. Place the power meter in the laser beam path and insure that the output is at least 50 milliwatts (mW). If the power level is less than 50 mW, adjustment or cleaning of the laser is necessary.

7. Next, set the intensities of the reference beam and the object beam so that a 10:1 ratio is obtained at the thermoplastic plate (intensity of reference beam equals ten times the intensity of the object beam). A 10:1 ratio was recommended for the thermoplastic plates used. The adjustment of this ratio is an iterative process, with the ratio being adjusted using one or both of the variable beam splitters. This adjustment must be made in total darkness (except for laser light).

8. When the light intensities are correct, trigger the shutter closed. Now, set the shutter to the automatic mode and pre-select the desired exposure time. The exposure time will vary according to the intensity of the light and the quality of the resulting holograms desired. The light intensity levels for this study averaged 0.3 microwatts and 0.03 microwatts for the reference and object beams, respectively. Exposure times of 45 to 85 seconds were used for both real time and time average holograms. The exposure time appeared to increase with age of the plate.

9. Place the horn (with exponential cone mounted) to within approximately 3/16" of the back of the panel at an antinode of the desired mode.

10. For time average holograms, set the excitation frequency to the natural frequency of the desired mode. The power level is set to yield a hologram with adequate fringe resolution. Too low of an amplitude will result in too few fringes and too large an amplitude will cause so many fringes that they will be indiscernible.

11. Remove the polarizing cover and insert a thermoplastic plate into the camera mount. Replace the polarizing cover. With all lights turned off (laser light included), press the "Erase" button on the HC-300 Controller Unit. The automatic erase cycle will begin. When this is complete, the "Expose" button followed by the "Busy" button will be illuminated. The plate is now ready to make a new recording. Next, activate the shutter to automatically expose the plate for the predetermined amount of time. When the exposure has completed, the laser beam will be turned off. At this time, press the "Busy" button to activate the develop cycle. This takes about 10 to 15 seconds. When complete, the "Erase" button illuminates to indicate that the hologram recording cycle has completed and the system is prepared for the next hologram. If the "Fault" light comes on, repeat the hologram recording process beginning with the erasing of the holographic plate. Usually

the fault can be corrected by repositioning the holographic plate to allow for proper electrical connection. If the fault persists, consult the operator's manual.

12. After the hologram has been recorded, it can now be viewed. Trigger the shutter in the manual mode, allowing laser light to pass through the shutter. Block the object beam and allow only the reference beam to illuminate holographic plate. View the hologram by peering "through" the holographic plate. The reconstructed image (hologram) is now visible. This procedure is repeated for each mode of interest.

(3) Panel 7 Results. Panel 7 contained the 4 inch centered cutout and was the only panel tested using the conventional holography technique. As expected, the natural frequencies and mode shapes agreed favorably with those obtained using video holography. The primary advantage of the conventional holography technique is its capability to produce high quality holograms (higher resolution than video holography). This aspect became apparent when the time average holograms were made. Figures B-3 through B-7 present the time-average holograms photographed for Panel 7. If these figures are compared with Figures 6-29 through 6-31 in Chapter VI, the increased resolution is obvious. The fringe lines are easier to distinguish in the conventional holograms. Although this feature is more aesthetically appealing, it is not required for the type of modal analysis performed in this study. The natural frequencies and mode shapes are the data sought, and they will be the same no matter what holography technique is used. As mentioned earlier, the resonant frequencies obtained were consistent with those reported in Chapter VI and will therefore not be included here.

The next section provides a step by step procedure for the video holography technique used in this thesis.

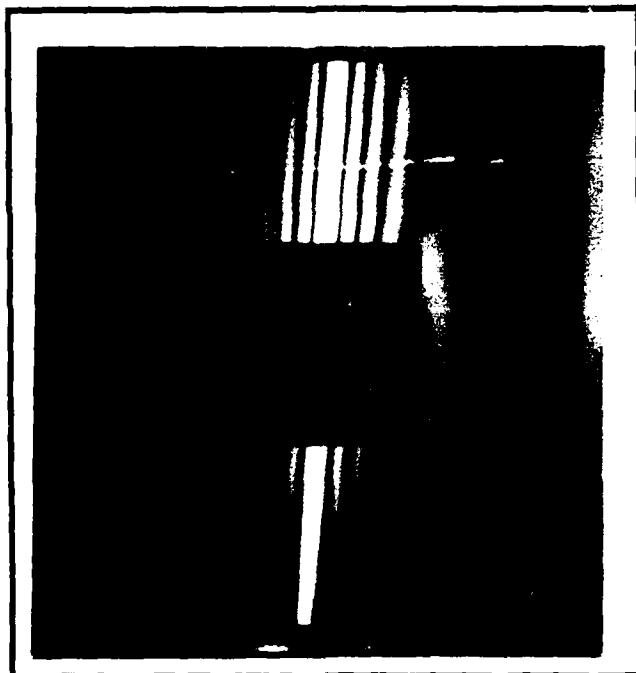


Figure B-3. First Mode Shape For Panel 7

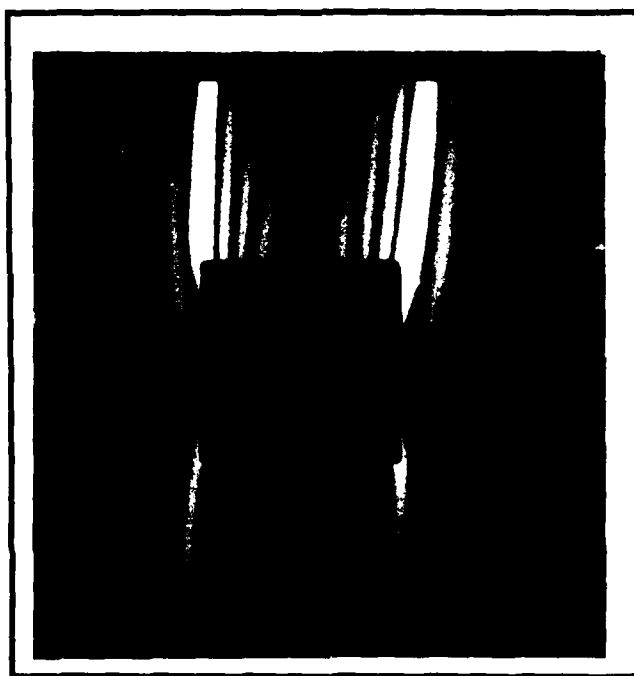


Figure B-4. Second Mode Shape For Panel 7

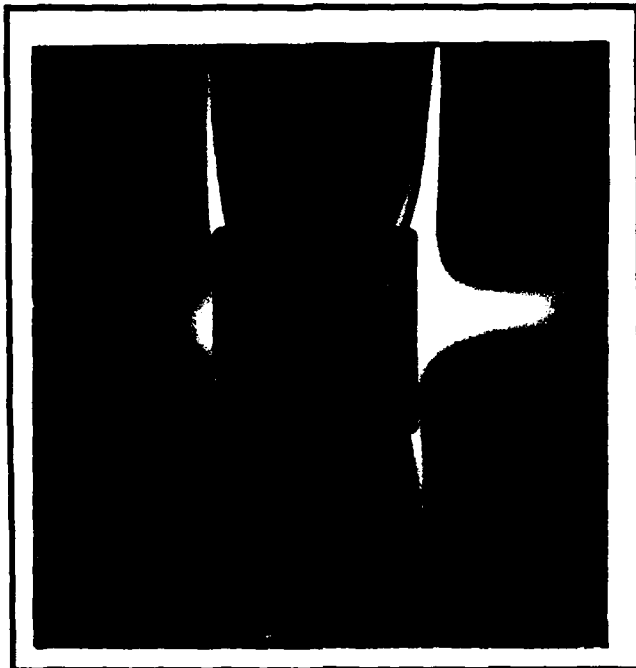


Figure B-5. Third Mode Shape For Panel 7

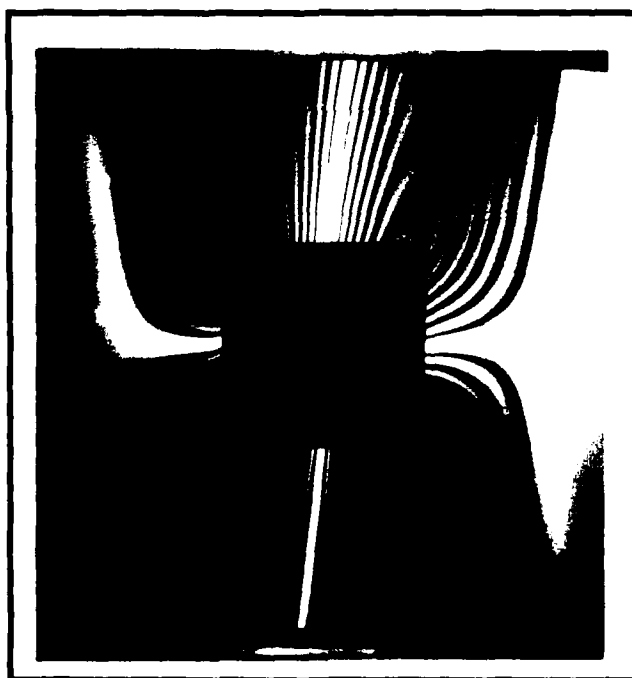


Figure B-6. Fourth Mode Shape For Panel 7

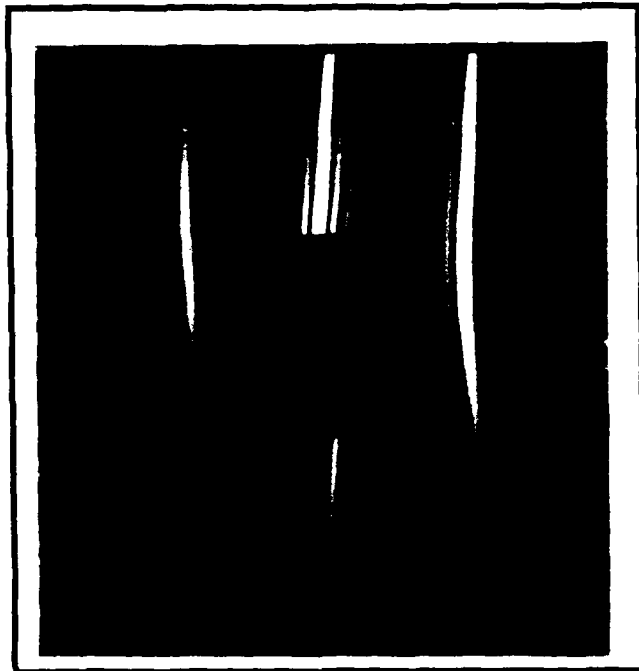


Figure B-7. Fifth Mode Shape For Panel 7

B. Video Holographic Procedure

The following procedure was used to perform the conventional holography equipment with the Retra 1000 system.

1. CAUTION: A laser eye exam is required before using a laser. Instructions for the setup, care, and use of the laser should be received prior to its first use to prevent personal injury or equipment damage.
2. Turn on the laser and the electronic equipment. Allow all components to warm up for at least 5 minutes. Set the amplitude of the signal generator to 0.5 volts peak-to-peak and set the output to 50.0 ohms.

3. Measure the distance between the Retra 1000 unit and the center of the panel and insure that the distance is near the coherence length of the laser.

4. Adjust laser so that panel is completely illuminated.

5. Place the horn (with exponential cone mounted) to within about 3/16" of the back of the panel at an antinode of the desired mode.

6. While adjusting the frequency output by the signal generator, view the hologram on monitor. In effect, 30 holograms per second are taken to produce the image on screen. Record the natural frequencies of the desired modes.

7. To photograph the desired mode shapes, first adjust the excitation amplitude so that the desired panel displacements are obtained (fringe resolution). Next, press the button on the freeze frame unit and a photograph of the mode shape visible on the monitor will be taken. Insure that no loud noise, such as a door shutting or a phone ringing, occurs while the mode shape is being recorded. If this happens, the photograph should be retaken.

8. This procedure is repeated for each mode of interest.

C. Comparison

The following list provides a comparison of the advantages and disadvantages of the video and conventional holography techniques. A list format was selected since it allows for an efficient comparison of the two techniques and because the differences are self-explanatory and do not require additional discussion. One technique's advantage will usually be another technique's disadvantage and this is reflected in the data which follows.

VIDEO HOLOGRAPHY

Disadvantages

1. Resolution of hologram lower than conventional holography.
2. High initial investment (\$ 100k+).

Advantages

1. Stable table not required.
2. Can be used outside of laboratory environment.
3. 5 pieces of equipment to monitor.
4. Set up time measured in minutes.
5. Laser light emitted from Retra 1000 unit is eye safe.
6. Can be performed in normal room light.
7. Can be used in a relatively confined area.
8. Not sensitive to bumping of equipment or test fixture.
9. Time required for a single hologram approximately 5 minutes.
10. Hologram conveniently viewed on a monitor.
11. Lenses and mirrors enclosed in Retra 1000 unit and therefore protected from environment.
12. Photographing mode shapes amounts to pushing a button.
13. Allows for continuous feedback as horn is repositioned. (ex. when attempting to find the optimum driving location for a given mode.)
14. Experimental procedure is simple.

CONVENTIONAL HOLOGRAPHY

Advantages

1. Higher resolution holograms.
2. Moderate initial investment (\$ 50k+).

Disadvantages

1. Stable table required.
2. Limited to laboratory environment.
3. 18+ pieces of equipment to monitor.
4. Set up time measured in hours.
5. Laser light has potential to cause serious eye damage.
6. Must be performed in total darkness.
7. Due to optical setup, more room is required.
8. Highly susceptible to even slight bumping of equipment or test fixture.
9. Time require for a single hologram approximately 20-30 minutes (assuming optics already setup).
10. Hologram viewed by peering "through" the holographic plate (approximately 1 square inch in size).
11. Lenses and mirrors exposed to room environment.
12. Photographing mode shapes requires support from Tech Photo Lab.
13. Hologram recording procedure must usually be repeated for each horn location.
14. Experimental procedure is more complicated and time consuming.

Appendix C: Sample Input Files

This appendix present some sample inputs for the STAGSC-1 finite element program along with some Cyber and Vax command files necessary to execute STAGSC-1.

A. STAGSC-1 Input File For Panel 1

```
CASE PANEL 1, SOLID PANEL, NEW MATL PROP, 410 ELEMENT
2,1,1,0,0,0,1,0,0      $B1 SMALL VIBS, FULL OUTPUT
1,0,0                  $B2 ONE SHELL
1,0,1,0                $B3 ONE MATL, ONE WALL TYPE
1                      $C1
1,0,7000,1             $D2 7000 CPU SEC
8,0,0,0                $D3 # OF EIGENVALUES
23,25                  $F1 ROWS,COLS
1,0                    $I1 MATL #
20.46E06,0.0205,0.8638E06,0.0583,0.0216,1.34E06,15.2 $I2 MAT;L PROPS
1,1,8                  $K1 GEN LAYERED WALL, 8 LAYERS
1,0.005,0,0,0          $K2 PLY DATA
1,0.005,-45,0,0        $K2
1,0.005,45,0,0         $K2
1,0.005,90,0,0         $K2
1,0.005,90,0,0         $K2
1,0.005,45,0,0         $K2
1,0.005,-45,0,0        $K2
1,0.005,0,0,0          $K2
5,0                    $M1 CYL, LOCAL & GLOBAL COORDS SAME
0,0,11,0,0,0,57.29578,12.0 $M2A PANEL GEOMETRY
1,0                    $M5 NO IMPERFECTIONS
410,0,0,1,0,0,0        $N1 410 ELEMENT GRID
3,2,3,2                $P1 BOUNDARY CONDITIONS
0                      $Q1 LOADS SUMMARY
1,1,0,1,0,0,0,0,0,0,0 $R1 PRINT DISPL & STRESS
```

B. STAGSC-1 Input File For Panel 2

CASE PANEL 2, CENTERED 2" SQUARE CUTOUT NMP, 410 ELEMENT	
2,1,1,0,0,0,1,0,0	\$B1 SMALL VIBS, FULL OUTPUT
1,0,0	\$B2 ONE SHELL
1,0,1,0	\$B3 ONE MATL, ONE WALL TYPE
1	\$C1
1,0,7000,1	\$D2 7000 CPU SEC
8,0,0,0	\$D3 # OF EIGENVALUES
23,25	\$F1 ROWS,COLS
1,0	\$I1 MATL #
20.46E06,0.0205,0.8638E06,0.0583,0.0216,1.34E06,15.2	\$I2 MAT;L PROPS
1,1,8	\$K1 GEN LAYERED WALL, 8 LAYERS
1,0.005,0,0,0	\$K2 PLY DATA
1,0.005,-45,0,0	\$K2
1,0.005,45,0,0	\$K2
1,0.005,90,0,0	\$K2
1,0.005,90,0,0	\$K2
1,0.005,45,0,0	\$K2
1,0.005,-45,0,0	\$K2
1,0.005,0,0,0	\$K2
5,0	\$M1 CYL, LOCAL & GLOBAL COORDS SAME
0,0,11,0,0,0,57.29578,12.0	\$M2A PANEL GEOMETRY
1,0	\$M5 NO IMPERFECTIONS
410,0,0,1,0,0,0	\$N1 410 ELEMENT GRID
10,14,11,15	\$N8 CUTOUT LOCATION
3,2,3,2	\$P1 BOUNDARY CONDITIONS
0	\$Q1 LOADS SUMMARY
1,1,0,1,0,0,0,0,0,0,0	\$R1 PRINT DISPL & STRESS

C. STAGSC-1 Input File For Panel 9

CASE PANEL 9, 4" SQUARE CUTOUT OFFSET 2" LEFT, NMP, 410 ELEMENT	
2,1,1,0,0,0,1,0,0	\$B1 SMALL VIBS, FULL OUTPUT
1,0,0	\$B2 ONE SHELL
1,0,1,0	\$B3 ONE MATL, ONE WALL TYPE
1	\$C1
1,0,7000,1	\$D2 7000 CPU SEC
8,0,0,0	\$D3 # OF EIGENVALUES
23,25	\$F1 ROWS,COLS
1,0	\$I1 MATL #
20.46E06,0.0205,0.8638E06,0.0583,0.0216,1.34E06,15.2	\$I2 MAT;L PROPS
1,1,8	\$K1 GEN LAYERED WALL, 8 LAYERS
1,0.005,0,0,0	\$K2 PLY DATA
1,0.005,-45,0,0	\$K2
1,0.005,45,0,0	\$K2
1,0.005,90,0,0	\$K2
1,0.005,90,0,0	\$K2
1,0.005,45,0,0	\$K2
1,0.005,-45,0,0	\$K2
1,0.005,0,0,0	\$K2
5,0	\$M1 CYL, LOCAL & GLOBAL COORDS SAME
0,0,11,0,0,0,57.29578,12.0	\$M2A PANEL GEOMETRY
1,0	\$M5 NO IMPERFECTIONS
410,0,0,1,0,0,0	\$N1 410 ELEMENT GRID
8,16,5,13	\$N8 CUTOUT DEFINITION
3,2,3,2	\$P1 BOUNDARY CONDITIONS
0	\$Q1 LOADS SUMMARY
1,1,0,1,0,0,0,0,0,0,0	\$R1 PRINT DISPL & STRESS

D. Command File For Executing STAGSC-1 on the Cyber

This procedure assumes that the STAGSC-1 input file is called CASE1. The output file will not be saved, but only printed by this procedure. The command file will be called BCASE1.

BCASE1 contents are as follows:

```
/JOB
ujn,P3.
/USER
CHARGE,*
RFL=325000.
SETTL(*).
ATTACH,STAGS1/UN=T890071.
GET,CASE1.
REWIND,*
STAGS1,CASE1,OUT1.
RETURN,STAGS1.
RFL=325000.
ATTACH,STAGS2/UN=T890071.
REWIND,*
STAGS2,OUT1,OUT2.
RETURN,STAGS2.
REWIND,*
COPYSBF,OUT1,POUT1.
COPYSBF,OUT2,POUT2.
REWIND,*
ROUTE,POUT1,ST=CSA,DC=PR,UN=AL,UJN=ujn.
ROUTE,POUT2,ST=CSA,DC=PR,UN=AL,UJN=ujn.
/EOR
```

To execute BCASE1, enter the following command at the prompt.

```
submit,BCASE1,rb=al
```

E. Command File For Executing STAGSC-1 on the Vax

To execute STAGSC-1 the input and output files must be "(...).INP" and "(...).OUT" files, respectively. This procedure assumes that the STAGSC-1 input file is called SAMPLE.INP and the output file is SAMPLE.OUT. Also, it is assumed the input file is located in a subdirectory call [.STAGS]. The command file will be called BATSAM.COM.

BATSAM.COM contents are as follows:

```
$ set def [.STAGS]
$ assign SAMPLE.INP FOR005
$ assign SAMPLE.OUT FOR006
$ run $1$dja13:[STAGS88.GILLIAN.STAG88]STAGS1.EXE
$ run $1$dja13:[STAGS88.GILLIAN.STAG88]STAGS2.EXE
$ exit
```

To execute BATSAM.COM, enter the following command at the \$ prompt.

```
$ submit BATSAM.COM
```

Appendix D: Orthographic Views of Mode Shapes for Panels 1 and 7

This appendix contains orthographic views of the mode shapes for Panels 1 and 7. These figures were included to help the reader visualize the panel's deformed geometry for the first five mode shapes.

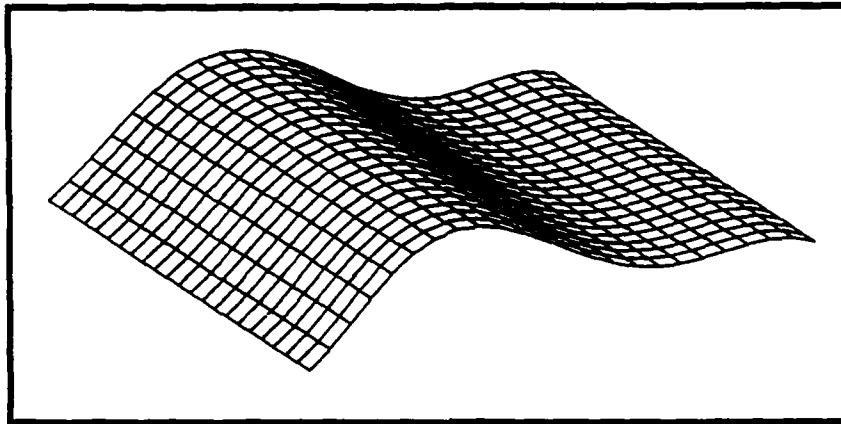


Figure D-1. First Mode Shape for Panel 1

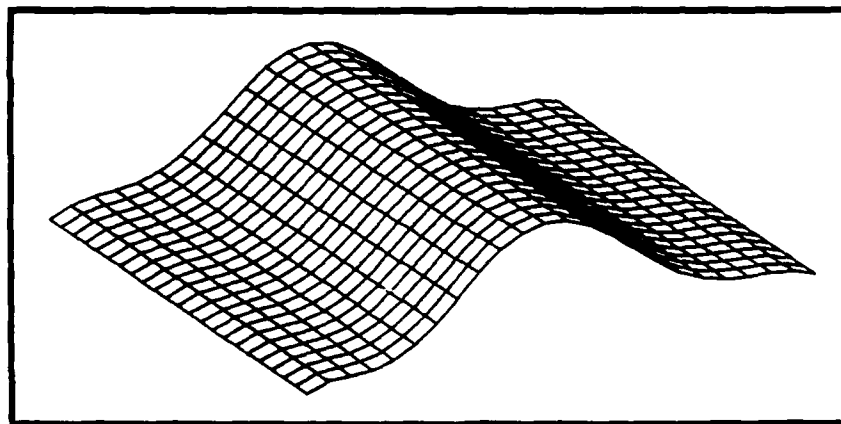


Figure D-2. Second Mode Shape for Panel 1

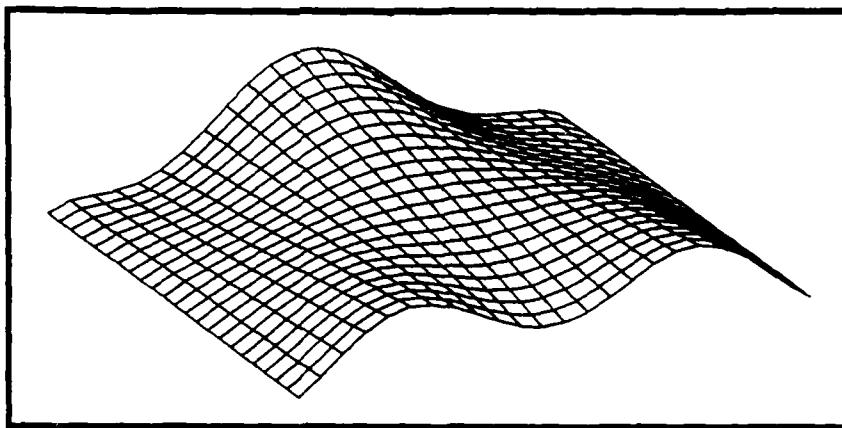


Figure D-3. Third Mode Shape for Panel 1

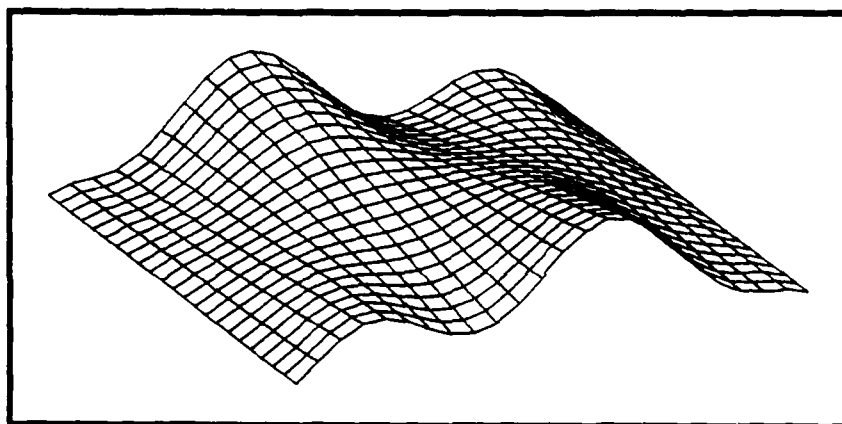


Figure D-4. Fourth Mode Shape for Panel 1

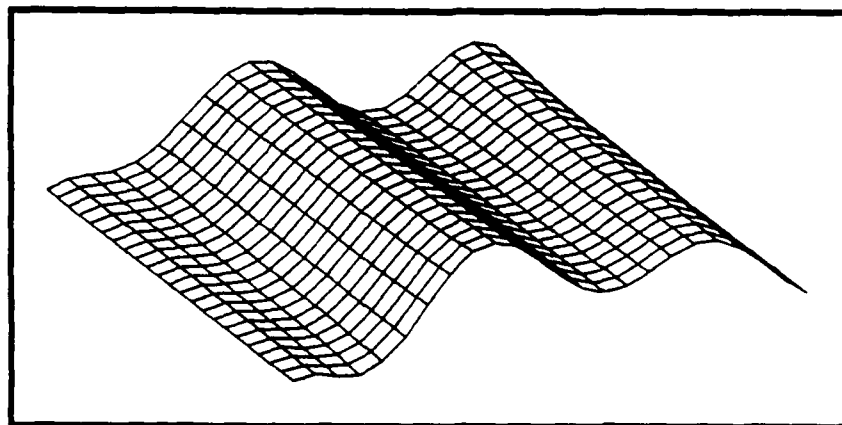


Figure D-5. Fifth Mode Shape for Panel 1

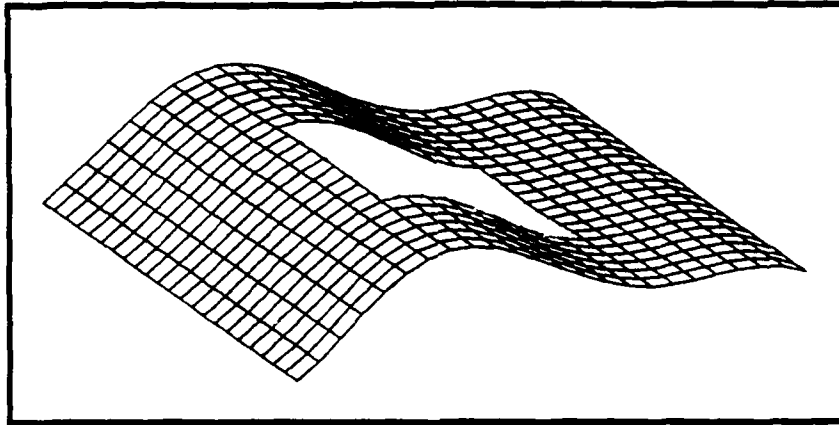


Figure D-6. First Mode Shape for Panel 7

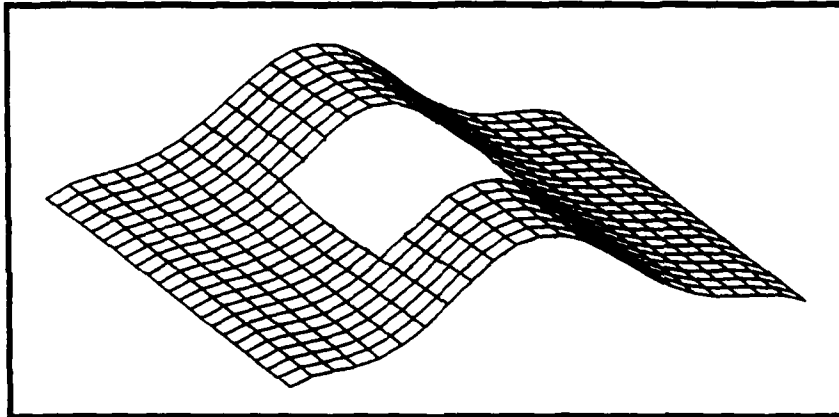


Figure D-7. Second Mode Shape for Panel 7

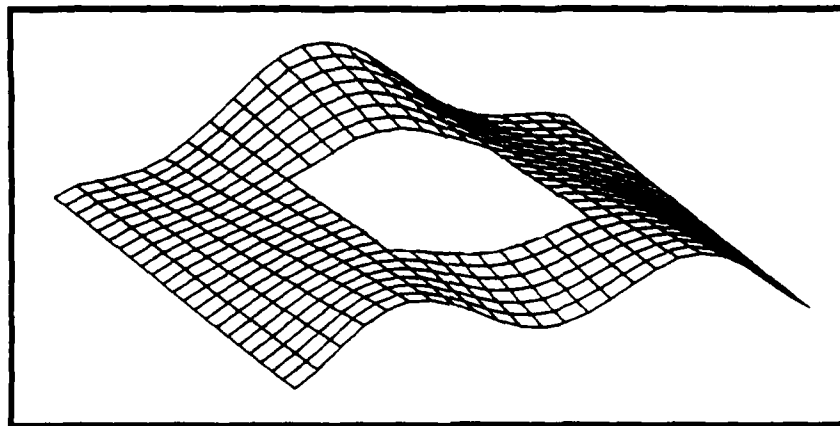


Figure D-8. Third Mode Shape for Panel 7

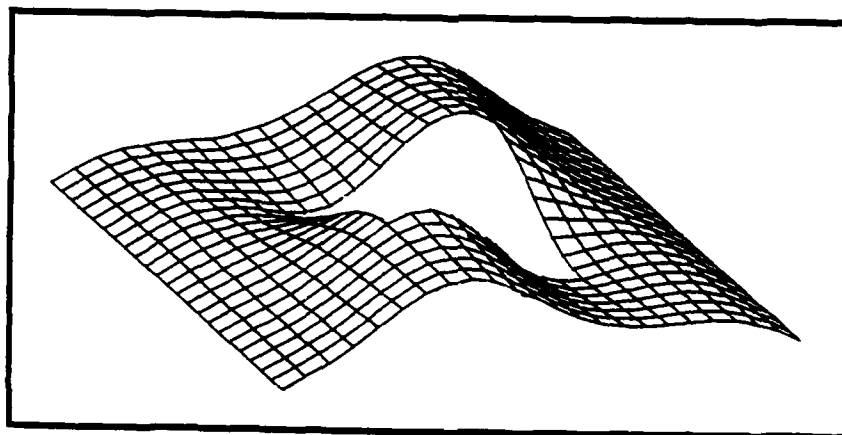


Figure D-9. Fourth Mode Shape for Panel 7

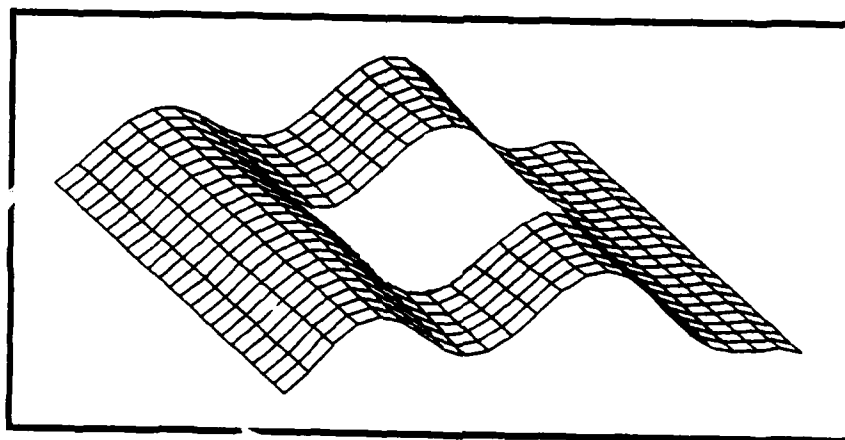


Figure D-10. Fifth Mode Shape for Panel 7

Vita

Vincent Joseph Levraea, Jr. [REDACTED]

[REDACTED]. Following graduation from Redemptorist High School in 1978, he attended Louisiana State University. There he received a Bachelor of Science degree in Mechanical Engineering in May of 1983. After graduation from LSU, he attended Officer Training School in San Antonio, Texas and upon completion was commissioned a 2nd Lieutenant in the United States Air Force. In September of 1983 he was assigned to the Deputy for Engineering at Eglin Air Force Base, Florida. There he worked on several projects, including the Sensor Fused Weapon and AGM-130 programs. In 1986, he was collocated to the Deputy for Development Plans to serve as Lead Missile Engineer for the Hypervelocity Missile program. He entered the School of Engineering at the Air Force Institute of Technology in June of 1988.

[REDACTED]

[REDACTED]

[REDACTED]

Unclassified

SECURITY CLASSIFICATION OF THIS PAGE

REPORT DOCUMENTATION PAGE

Form Approved
OMB No. 0704-0188

1a. REPORT SECURITY CLASSIFICATION Unclassified			1b. RESTRICTIVE MARKINGS		
2a. SECURITY CLASSIFICATION AUTHORITY			3. DISTRIBUTION / AVAILABILITY OF REPORT Approved for public release; distribution unlimited		
2b. DECLASSIFICATION / DOWNGRADING SCHEDULE					
4. PERFORMING ORGANIZATION REPORT NUMBER(S) AFIT/GAE/ENY/89D-20			5. MONITORING ORGANIZATION REPORT NUMBER(S)		
6a. NAME OF PERFORMING ORGANIZATION School of Engineering		6b. OFFICE SYMBOL (If applicable) AFIT/ENY		7a. NAME OF MONITORING ORGANIZATION	
6c. ADDRESS (City, State, and ZIP Code) Air Force Institute of Technology (AIU), Wright-Patterson AFB, Ohio 45433-6583			7b. ADDRESS (City, State, and ZIP Code)		
8a. NAME OF FUNDING / SPONSORING ORGANIZATION Air Force Office of Scientific Research		8b. OFFICE SYMBOL (If applicable) AFOSR		9. PROCUREMENT INSTRUMENT IDENTIFICATION NUMBER	
8c. ADDRESS (City, State, and ZIP Code) Bolling AFB Washington, D.C. 20332			10. SOURCE OF FUNDING NUMBERS		
			PROGRAM ELEMENT NO.	PROJECT NO.	TASK NO.
11. TITLE (Include Security Classification) Eccentricity Effects of Square Cutouts on the Natural Frequencies and Mode Shapes of Curved Rectangular Composite Panels					
12. PERSONAL AUTHOR(S) Vincent J. Levraea, Jr. M.S., Capt USAF					
13a. TYPE OF REPORT Thesis		13b. TIME COVERED FROM _____ TO _____		14. DATE OF REPORT (Year, Month, Day) 1989 December	
15. PAGE COUNT 221					
16. SUPPLEMENTARY NOTAT ON					
17. COSATI CODES			18. SUBJECT TERMS (Continue on reverse if necessary and identify by block number)		
FIELD	GROUP	SUB-GROUP	Composites, Vibrations, Holography, STAGSC-1, Finite Elements, Natural Frequencies, Mode Shapes, Modal Analysis		
11	04				
20	11				
19. ABSTRACT (Continue on reverse if necessary and identify by block number) Thesis Advisor: Dr. Anthony N. Palazotto The purpose of this study was to investigate the eccentricity effects of square cutouts on the natural frequencies and mode shapes of circular, cylindrical composite panels. A video holographic interferometry technique was used to determine the first five natural frequencies and mode shapes of the panels. Analytically, predictions for this same data were obtained using the STAGSC-1 finite element program. The primary objective was to examine how cutout eccentricity (over)					
20. DISTRIBUTION / AVAILABILITY OF ABSTRACT <input checked="" type="checkbox"/> UNCLASSIFIED/UNLIMITED <input type="checkbox"/> SAME AS RPT. <input type="checkbox"/> DTIC USERS			21. ABSTRACT SECURITY CLASSIFICATION unclassified		
22a. NAME OF RESPONSIBLE INDIVIDUAL Anthony N. Palazotto, PhD			22b. TELEPHONE (Include Area Code) (513)255-2998		22c. OFFICE SYMBOL AFIT/ENY